CHARACTERIZATION AND IN-SITU MODIFICATION OF HYBRID PLASMONIC NANOSYSTEMS

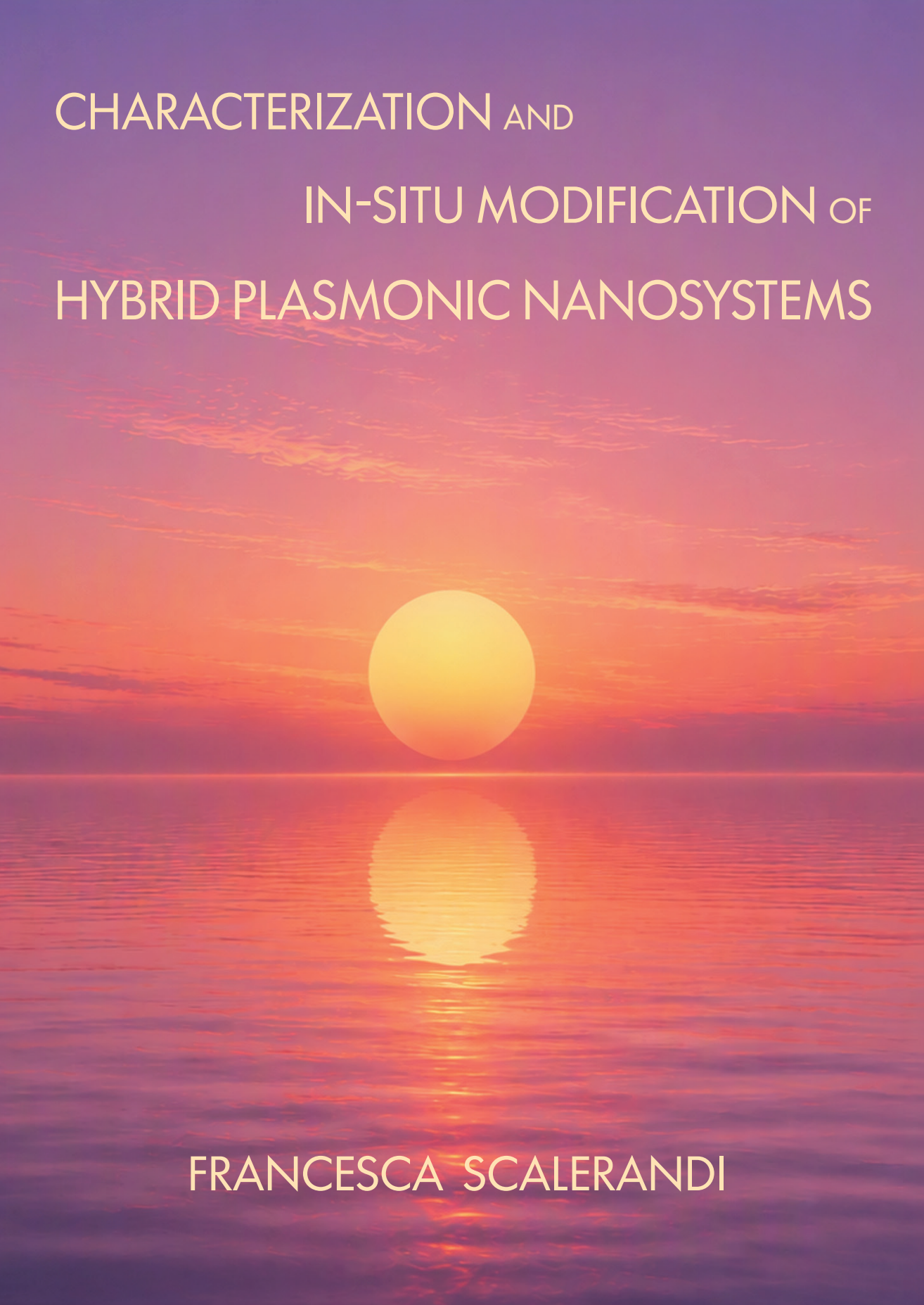

FRANCESCA SCALERANDI

Characterization and in situ modification of hybrid plasmonic nanosystems

Ph.D. Thesis, University of Amsterdam, September 2026
Characterization and In Situ Modification of Hybrid Plasmonic Nanosystems
F. Scalerandi

Cover design: AI-generated artwork depicting a sunset reflected on a calm sea. The composition is inspired by a plasmonic nanosystem, resembling a nanosphere dimer separated by a nanogap. The bright reflection evokes the localized electromagnetic field enhancement that arises within the gap due to plasmonic coupling.

ISBN: 978-94-6537-852-7

The work described in this thesis was performed between September 2021 and June 2026 at AMOLF, Science Park 104, 1098XG Amsterdam, The Netherlands, an institute of the Dutch Research Council (NWO).

A digital version of this thesis is available at `https://ir.amolf.nl`.

Printed by Ridderprint

Characterization and In Situ Modification of Hybrid Plasmonic Nanosystems

Academisch Proefschrift

ter verkrijging van de graad van doctor

aan de Universiteit van Amsterdam

op gezag van de Rector Magnificus

ten overstaan van een door het College voor Promoties ingestelde commissie,

in het openbaar te verdedigen in de Aula der Universiteit

op vrijdag 11 september 2026, te 11.00 uur

door Francesca Scalerandi

geboren te Torino

Promotiecommissie

Promotor:	prof. dr. E.C. Garnett	Universiteit van Amsterdam
Copromotor:	dr. W. Albrecht	AMOLF
Overige leden:	dr. S.A. Mann	Universiteit van Amsterdam
	dr. S. Grecea	Universiteit van Amsterdam
	prof. dr. A. Polman	Universiteit van Amsterdam
	prof. dr. G. Tagliabue	EPFL École Polytechnique Fédérale
	dr. A. Baldi	Vrije Universiteit Amsterdam

Faculteit der Natuurwetenschappen, Wiskunde en Informatica

Contents

1 Introduction **1**

1.1 Plasmonic nanoparticles . . . 2

1.1.1 Plasmonic excitations . . . 2

1.1.2 Surface-plasmon decay . . . 3

1.1.3 Hybrid plasmonic nanosystems . . . 5

1.1.4 Photo-thermal stability and reshaping of plasmonic NPs . . . 7

1.2 Single particle correlation . . . 7

1.2.1 Single-particle optical spectroscopy . . . 8

1.2.2 Simulations of plasmonic optical properties . . . 9

1.2.3 Transmission electron microscopy . . . 10

1.2.4 Other e-beam techniques and electron beam damage . . . 13

1.3 This thesis: Motivation and outline . . . 15

2 Dimer synthesis in solution and correlation of dark-field scattering and 2D morphology **17**

2.1 Introduction . . . 18

2.2 Methodology . . . 20

2.2.1 Self-assembly of gold nanoparticles . . . 20

2.2.2 Quasi-dark-field scattering setup . . . 21

2.2.3 Correlation procedure . . . 22

2.2.4 Optical simulations . . . 24

2.2.5 Electron microscopy . . . 24

2.3 Results and discussion . . . 24

2.3.1 Dimers yield optimization . . . 24

2.3.2 2D-correlation . . . 28

2.3.3 The gap size from 2D STEM images . . . 29

2.3.4 The gap size from optical measurements 33
2.3.5 Electromagnetic models for plasmonic nanogaps: the dielectric environment uncertainty 34
2.4 Conclusion 38
2.5 Appendix 39
2.5.1 Junction models for plasmonic nanogaps 40
a. Classical framework with effective medium . 40
b. Quantum-Corrected Model (QCM) 40
c. Molecular transport 41
d. Effective conductance 42
e. Ohmic conductivity 43

3 Reliable determination of sub-nanometer gaps in plasmonic gold dimers 45

3.1 Introduction 46
3.2 Methodology 47
3.2.1 Nanodimers colloidal assembly 47
3.2.2 Electron tomography 47
3.2.3 Reconstruction of tomography data 48
3.2.4 Simulation of STEM projections 48
3.2.5 Surface meshing of tomography data 49
3.2.6 BEM optical simulations 50
3.2.7 Convolution fit 50
3.3 Results and discussion 52
3.3.1 3D experimental data 52
3.3.2 Simulated data and convolution method 56
3.3.3 Convolution on experimental data 59
3.3.4 Transferring 3D morphological insights to 2D STEM images . . 62
3.4 Conclusion 64
3.5 Appendix 65

4 Synthesis and crystallization pathways of $Au@TiO_2$ NRs 73

4.1 Introduction . . . 74
4.2 Methodology . . . 77
4.2.1 Chemicals . . . 77
4.2.2 Electron Microscopy . . . 77
4.3 Results and discussion . . . 79
4.3.1 Design of the initial $Au@TiO_2$ interface and morphology: role of ligand and precursor chemistry . . . 79
4.3.2 Controlled synthesis of amorphous $Au@TiO_2$ nanorods . . . 81
a. Titanium (IV) isopropoxide precursor . . . 82
b. Titanium (III) chloride precursor . . . 83
4.3.3 Crystallization strategies . . . 89
4.3.3.A Low temperature hydrothermal crystallization . . . 90
a. Titanium (III) chloride precursor . . . 90
4.3.3.B Laser induced crystallization . . . 95
a. Titanium (IV) isopropoxide precursor . . . 96
b. Titanium (III) chloride precursor . . . 99
4.3.4 Conclusion and Outlook . . . 104
4.4 Appendix . . . 106
4.4.1 Details on synthesis . . . 106
4.4.1.A TiO_2 volume fraction estimation . . . 108
4.4.2 Further analysis on hydrothermal crystallization . . . 110
4.4.3 Details on laser induced crystallization . . . 111

5 Optically driven AuCu alloying in single nanoparticles revealed by in situ TEM 113

5.1 Introduction . . . 114
5.2 Methodology . . . 116
5.2.1 Light in-coupling . . . 116
5.2.2 Diffraction and 4D-STEM data analysis . . . 117
5.2.3 Heat simulations . . . 117
5.3 Results and discussion . . . 118
5.3.1 Copper incorporation under laser illumination . . . 118

5.3.2 Volume evolution and spatial distribution 121
5.3.3 Composition control and alloy homogeneity 125
5.3.4 Diffraction-based analysis of composition dynamics and kinetics 128
5.4 Conclusion 133
5.5 Appendix 134

Bibliography **139**

Author contributions and publications **155**

Summary **157**

Samenvatting **161**

Sommario **165**

Acknowledgment **169**

About the author **175**

1 Introduction

Meeting the growing global energy demand while reducing the use of fossil fuels is one of the main challenges of our time. Figure 1.1 shows the global energy consumption by source up to 2025, highlighting a continuous increase in demand. According to NASA's Earthdata program, an average of 342 $\mathrm{W\,m^{-2}}$ of solar energy reaches Earth every day over the entire year. This corresponds to a total of 44 quadrillion W (44000 TW) of power. In comparison, global energy consumption in 2025 was 20 TW [1]. This means that harvesting only 0.1-0.4% of the solar power reaching the planet would be sufficient to meet the global energy demand. A significant part of this demand stems not from electricity but from the production of fuels and chemicals, which today relies almost entirely on fossil resources. Harvesting, storing, and converting sunlight into usable energy is therefore at the heart of the energy transition. Sunlight can be converted into electricity through photovoltaic technologies [2]. Furthermore, it can be used directly to drive the catalytic reactions needed to produce these fuels and chemicals from biomass or harmful compounds, reducing our dependence on fossil feedstocks at the source. Compared to conventional thermal catalysis, which requires high temperatures and pressures, photocatalytic processes can operate under milder conditions, either driven by sunlight or by LEDs and lasers powered by photovoltaic technologies. In addition, light can selectively drive specific reaction pathways, potentially reducing unwanted byproducts and improving efficiency.

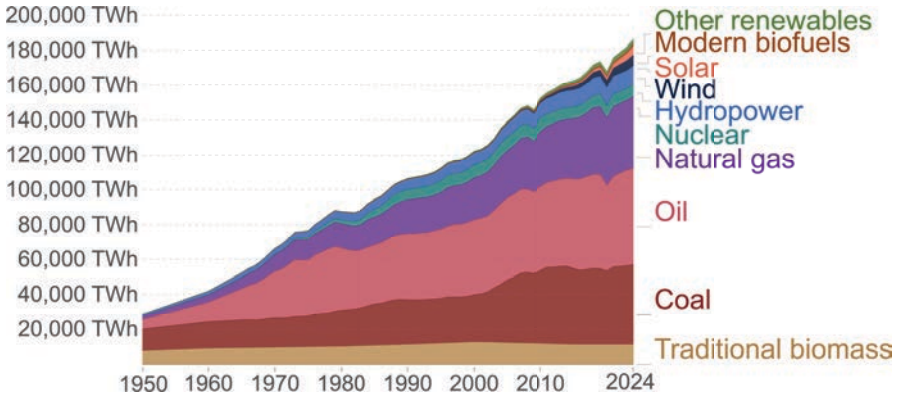

Figure 1.1: *Global energy consumption by source up to 2025. Data adapted from the Energy Institute Statistical Review of World Energy (2025) [1].*

Despite these advantages, several challenges remain. Current photocatalysts absorb visible light inefficiently, and the charge carriers generated upon absorption are often lost to recombination before they can drive useful chemistry. Enhancing light absorption and charge generation is key for the future scalability of photocatalytic technologies. Plasmonic nanoparticles (NPs) are particularly promising in this context. They absorb light with exceptionally high efficiency across the visible range and can convert this energy into reactive charge carriers, driving chemical transformations at the nanoscale. Coupling these nanoparticles to molecular or semiconductor interfaces opens up additional pathways for light-driven energy conversion. Charge carriers can be transferred to and stabilized by the adjacent material, extending their lifetime and increasing the probability of driving a useful chemical reaction. In this thesis, we focus specifically on gold nanoparticles coupled to molecules or semiconductors, as will be discussed in the next section.

1.1 Plasmonic nanoparticles

1.1.1 Plasmonic excitations

Plasmons are collective oscillations of conduction electrons. Upon light excitation, if the nanostructure is much smaller than the wavelength of the incident light, a localized surface plasmon resonance (LSPR) can be excited. Under this resonant condition, in the far-field absorption and scattering reach a maximum [3, 4]. In the near-field, the resonance manifests as an enhancement of the incident electric field in localized "hot spots" at the nanoparticle surface. Through this near-field confinement, plasmonic nanostructures concentrate light into extremely small volumes, surpassing the diffraction limit [5, 6]. Furthermore, when two plasmonic nanoparticles are positioned close to each other, their electromagnetic fields couple, modifying the optical properties of each individual particle and producing hybridized plasmonic modes with shifted resonance energies.

In 1908, Gustav Mie derived the exact analytical solution to Maxwell's equations for spherical plasmonic particles [7], explaining the relationship between nanoparticle morphology and the observed color. Solving Maxwell's equations results in the definition of the extinction cross-section (σ_{ext}) as the sum of absorption (σ_{abs}) and scattering (σ_{sca}) [3, 4].
An analytical solution of the LSPR exists only when the particle size is much smaller than the wavelength of light. In this regime the quasi-static approximation applies, the extinction cross-section is governed by the particle polarizability and can be expressed as:

$$\sigma_{\text{ext}} \propto \text{Im}\left\{\frac{\varepsilon(\omega) - \varepsilon_m}{\varepsilon(\omega) + 2\varepsilon_m}\right\} \tag{1.1}$$

where $\varepsilon(\omega)$ is the complex dielectric function of the metal and ε_m is the dielectric constant of the surrounding medium. The LSPR occurs at resonance, which is achieved when:

$$\mathrm{Re}\left(\varepsilon(\omega)\right) = -2\varepsilon_m \tag{1.2}$$

This analytical solution is limited to spherical particles in the quasi-static regime. It can be extended to ellipsoidal particles by introducing shape-dependent depolarization factors. For more complex geometries or bigger particles, retardation effects cannot be neglected and Maxwell's equations have to be solved numerically, as discussed in *Section 1.2.2*. Equation 1.2 shows that the behavior of plasmonic nanostructures under incident light depends on both the material, through $\varepsilon(\omega)$, and the environment, through ε_m. The dielectric function $\varepsilon(\omega)$, describes how the material polarizes in the presence of an electric field:

$$\varepsilon(\omega) = \varepsilon^{'} + i\varepsilon^{''} \tag{1.3}$$

Metals have a complex dielectric function. The real part ε' largely determines the location of the plasmon resonance, while the imaginary part ε'' describes losses due to electron scattering and interband transitions. The response of free electrons in noble metals, such as gold, can be well approximated by the Drude model [8]:

$$\varepsilon_{\mathrm{Drude}}(\omega) = \varepsilon_\infty - \frac{\omega_p^2}{\omega^2 + i\Gamma\omega} \tag{1.4}$$

where ω_p is the plasma frequency, Γ is the damping rate, and ε_∞ is a constant term that partially accounts for the screening by bound electrons but does not capture the frequency dependence of interband transitions. The dielectric function $\varepsilon(\omega)$ is experimentally determined, and the Drude model parameters are obtained by fitting this model to the measured data. The Drude approximation is only valid far from interband transition energies, which however dominate a significant part of the visible (VIS) spectrum of gold. For this reason, in optical simulations usually the full experimentally measured dielectric function is used, which captures both free-electron and interband contributions. The Drude model remains useful, as it makes the role of damping explicit through Γ, which directly contributes to the broadening of the plasmon resonance.

1.1.2 Surface-plasmon decay

Upon light excitation, the collective oscillation of conduction electrons in a plasmonic nanoparticle represents a highly non-equilibrium state. The coherent plasmon oscillation decays on an ultrafast timescale of roughly 100 fs [6]. The absorbed energy then dissipates through electron-electron scattering, electron-phonon coupling, and finally heat dissipation to the environment. These processes occur on progressively longer timescales up to nanoseconds, as shown in Figure 1.2a. This decay and dephasing of

the collective plasmon oscillation is referred to as plasmon damping, driving the system back toward thermal equilibrium. The decay pathways determine how efficiently the absorbed energy can be used.

Plasmon damping occurs via several mechanisms. A plasmon may decay either radiatively by re-emitting photons, or non-radiatively, where energy is transferred to individual electron–hole pairs, generating hot carriers through Landau damping [9]. Bulk and surface damping contributions introduced below originate from Landau damping. The total damping rate is the sum of several contributions, as shown in Equation 1.5.

$$\Gamma_{\text{total}} = \Gamma_{\text{bulk}} + \Gamma_{\text{surface}} + \Gamma_{\text{radiative}} + \Gamma_{\text{CID}} \tag{1.5}$$

Each term is associated with different physical processes and characteristic timescales. Bulk damping (Γ_{bulk}) arises from electron-scattering processes in the metal and is described by the dielectric function of the metal itself. Surface scattering ($\Gamma_{surface}$) becomes relevant when the nanoparticle size approaches or is smaller than the electron mean free path (typically 20–50 nm in noble metals), leading to additional electron collisions at the particle boundary. The dielectric function of gold is typically measured on bulk materials, where surface scattering is negligible. Therefore, to account for Γ_{surface} in simulations of small particles, a size-dependent correction to the damping term Γ in the Drude model needs to be introduced [10]. Radiative damping ($\Gamma_{radiative}$) corresponds to the re-emission of photons and becomes increasingly important for larger particles. In full retarded electrodynamic simulations, it is accounted for. Chemical interface damping (CID) accounts for additional non-radiative decay pathways introduced by the local environment. CID is particularly important in systems where the nanoparticle is in close proximity or in contact with molecules, semiconductors, or other materials.

In the LSPR, plasmon damping manifests as a broadening of the resonance peak. The measured linewidth can therefore be used to estimate the total damping rate. Bulk and radiative damping can be obtained from full electrodynamic simulations using the experimental dielectric function. Surface damping can be partially accounted for by incorporating a size-dependent correction to Γ in the Drude model, though the prefactor of this correction is itself empirical and depends on particle geometry and surface termination. The total damping rate is therefore not straightforward to simulate accurately. Experimentally, CID is accessed by measuring the discrepancy between the measured linewidth when a molecule or material is brought into contact with the nanoparticle and the contributions predicted by simulations. This empirically extracted quantity provides a direct measure of the rate at which hot carriers are transferred across the interface. Quantifying and understanding CID is therefore essential for optimizing the efficiency of hybrid plasmonic nanosystems for photocatalytic applications.

1.1.3 Hybrid plasmonic nanosystems

The lifetime of electron–hole pairs generated in plasmonic nanoparticles is extremely short, resulting in poor charge-separation efficiencies. To overcome this limitation, hybrid plasmonic systems are widely explored, in which plasmonic nanoparticles are coupled to molecular or semiconductor acceptors to enable charge or energy transfer before relaxation occurs [11].

Metal–molecule interfaces

Adsorbed molecules can hybridize their HOMO (Highest Occupied Molecular Orbital) and LUMO (Lowest Unoccupied Molecular Orbital) orbitals with the electronic bands of the metal surface [12]. Hot carriers can be then transferred either directly into molecular orbitals or indirectly via excitations within the metal [11, 13]. The direct charge-transfer process enables carrier extraction before thermalization within the metal [11, 13]. This transfer of hot carriers from plasmonic nanoparticles to molecular catalysts can be exploited to drive catalytic reactions that chemically modify the adsorbates. In *Chapters 2 and 3*, we explore the metal-molecule interface using gold nanosphere dimers bridged by 1-4, benzenedithiol (BDT) as a model system.

Metal–semiconductor interfaces

When a metal forms conductive contact with a semiconductor, their Fermi levels align. This induces band bending in the semiconductor. The energy difference between the semiconductor conduction band minimum and the metal Fermi level is defined as the Schottky barrier [14]. If the hot electrons generated in plasmonic nanoparticles have sufficient energy to overcome the Schottky barrier, they can be injected into the semiconductor [9, 15]. Injection efficiencies of up to ∼50% have been experimentally reported for small Au nanoparticles, with values decreasing for larger particles due to reduced interband absorption [16]. Energy and charge can be transferred across the metal–semiconductor interface through different mechanisms as shown in Figure 1.2b and c. In plasmon-induced resonance energy transfer (PIRET), the energy is transferred through non-radiative near-field dipole–dipole interaction, directly generating electron-hole pairs in the semiconductor. This opens an additional non-radiative decay channel for the plasmon, contributing to broadening of the resonance beyond that described by Equation 1.5 [17, 18]. PIRET is governed by the spectral overlap of the LSPR and the semiconductor band gap, and can occur even for nanometers separations between the metal and the semiconductor [19, 20]. In contrast, charge transfer mechanisms involve the physical injection of hot electrons across the interface into the semiconductor conduction band, which can occur through several distinct pathways [19, 21]. In the indirect plasmon-induced charge transfer (PICT) process, hot carriers generated by plasmon decay in the metal are subsequently transferred to the semiconductor. This indirect charge transfer occurs after Landau damping and typically has low efficiency due to the ultrashort lifetime of hot carriers in the metal.

Direct interfacial charge-transfer transitions (DICTT) can also occur but are typically much weaker than plasmon driven excitations [21]. More recently, another mechanism has been proposed to explain experimentally observed charge-transfer efficiencies exceeding 40% [22–24]: plasmon-induced interfacial charge-transfer transition (PICTT), also known as direct charge transfer [19, 21]. In PICTT, optical excitation directly promotes electrons from the metal into unoccupied semiconductor states during plasmon decay itself, without requiring prior hot-carrier generation via Landau damping. According to DFT simulations, there is a ∼50% probability of instantaneous charge separation via PICTT [25]. This direct mechanism avoids the energy losses within the metal and manifests as a broadening of the plasmon resonance.

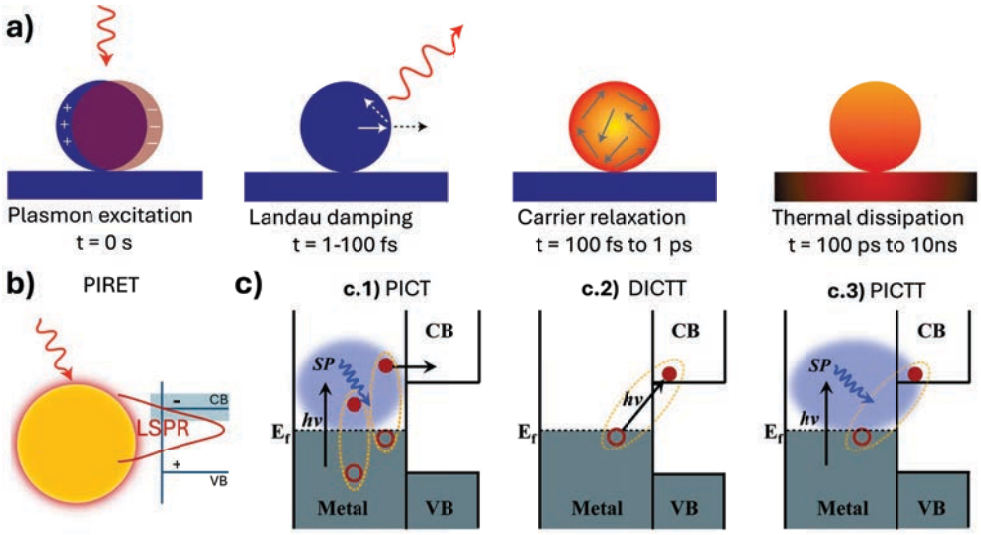

Figure 1.2: *a) Excitation of surface plasmon resonance (LSPR) and the subsequent relaxation pathways, along with their average timescales. Adapted with permission from [26]. In b) and c) the schematic representations of plasmon damping mechanisms are shown. b) Schematic of energy transfer through plasmon-induced resonance energy transfer (PIRET), in which the plasmon near-field directly excites electron-hole pairs in the adjacent semiconductor. c) Schematics of charge transfer mechanisms at a metal-semiconductor interface, adapted with permission from [21]: c.1) indirect plasmon-induced charge transfer, in which hot carriers generated by plasmon decay in the metal are subsequently injected into the semiconductor; c.2) direct interfacial charge transfer (DICTT), a direct optical transition across the interface independent of the plasmon; c.3) plasmon-induced direct charge transfer, in which the plasmon itself decays by exciting an electron directly across the metal-semiconductor interface.*

The relative contribution of direct and indirect charge-transfer pathways, as well as the overall efficiency of hot-carrier injection, are strongly governed by structural and interfacial factors including atomic-scale interface quality, electronic coupling, and defect density. These aspects, along with strategies for controlling them, will be addressed in *Chapter 4* for a $Au@TiO_2$ system.

1.1.4 Photo-thermal stability and reshaping of plasmonic NPs

When hot carriers are not harvested efficiently, the plasmon energy ultimately dissipates as heat, as illustrated in Figure 1.2a [26]. Under realistic photocatalytic operating conditions this leads to substantial temperature increases [17, 27]. The heat assists catalytic reactions but can also alter nanoparticle size, shape, and composition over time. Photo-thermal stability becomes a critical aspect. The temperature at which Au nanoparticles begin to reshape depends on factors such as particle size, shape, and environment. While bulk gold melts at 1064 °, nanoparticles exhibit a dramatically reduced melting point due to size-dependent thermodynamic effects. As shown by Foster et. al. [28], gold NP with a diameter below 5 nm can start melting at the surface below 600 °. Surface diffusion can already induce reshaping below 200 ° [29]. The specific reshaping pathway depends on laser fluence, pulse duration, environment, and initial morphology [30]. Structural transformations occur through atomic redistribution [31], defect formation [32], and the emergence of twin boundaries [32]. Understanding these light-induced structural transformations requires access to atomic-scale and ideally three-dimensional structural information. These changes can be highly heterogeneous, varying from particle to particle depending on subtle differences in initial morphology, defects, and local environment. This makes single-particle experiments essential. Furthermore, because these processes are inherently dynamic, characterization before and after reaction alone cannot reveal the underlying mechanisms. Instead, in situ, single-particle studies are required to capture the transient structural evolution. Recent progress in integrating pulsed lasers with TEM has enabled in situ time-resolved imaging, allowing direct observation of light-induced structural transformations at the single-particle level with high spatial resolution. The role of in situ single-particle TEM optical excitation in driving reshaping will be addressed in *Chapter 5*.

1.2 Single particle correlation

To capture the structural heterogeneity arising from synthesis, interfacial quality in hybrid nanosystems, and light-induced reshaping, it is essential to correlate structures and properties at the single nanoparticle level. At the nanoscale, morphology and structure fundamentally dictate material properties [4]. This relationship is particularly strong for plasmonic nanoparticles. Variations in particle shape [4],

size, elemental composition [33], surface configuration, and atomic arrangement[34] strongly influence plasmonic behavior and, consequently, the optical [35], electronic, and catalytic characteristics of these systems [36]. As discussed above, these structural parameters also govern nanoparticle stability. As increasingly complex, anisotropic, and asymmetric nanoparticle geometries emerge from modern synthesis methods, establishing detailed structure–property correlations has become an essential tool for understanding nanoscale properties and phenomena and avoiding ensemble averaging. This effect is illustrated in Figure 1.3, which shows dark-field scattering spectra measured on individual gold nanorods (AuNRs) from the same synthesis batch alongside their corresponding TEM images. Despite originating from the same batch, the particles exhibit distinct optical responses, which would not be possible to detect in an ensemble measurement. This example demonstrates both the importance and the strength of correlating structure and properties at the single particle level.

Despite this need, correlating morphology and properties at the single-particle level remains challenging. Optical properties are typically probed using spectroscopy techniques. However, the diffraction limit of light prevents direct, high-resolution correlation with nanoparticle morphology. Structural information is most accurately obtained through electron microscopy, which is on the other hand not suited for measuring optical, electronic, or catalytic responses. Overcoming these limitations requires methodologies that combine spectroscopic and electron-microscopic techniques on the same individual nanoparticles, enabling true correlative analysis.

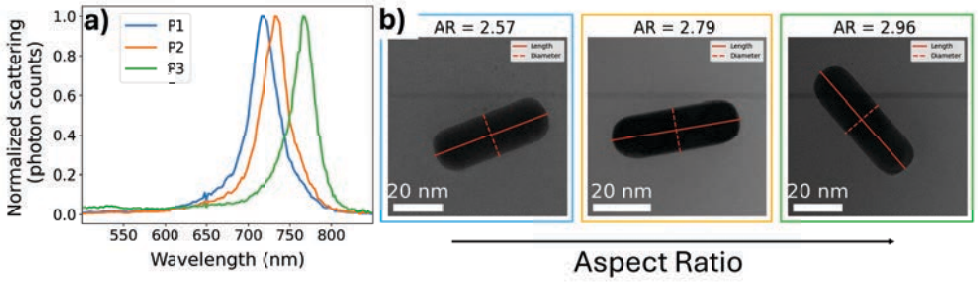

Figure 1.3: *a) Dark-field scattering spectra measured for three NRs. b) Respective TEM images and extracted aspect ratios.*

1.2.1 Single-particle optical spectroscopy

Several single-particle spectroscopy methods have been developed to optically characterize plasmonic nanoparticles. These techniques rely on detecting different optical responses, including scattering [37–39], absorption [39, 40], as in photothermal measurements [41], and extinction [39, 42]. Additional approaches include photolu-

minescence spectroscopy (PL) [43, 44] and transient absorption spectroscopy [24, 45]. Among these single-particle techniques, dark-field scattering (DFS) spectroscopy is the most widely used. It is straightforward to implement, provides high spectroscopic resolution [46], and the strong scattering cross-section of plasmonic nanoparticles allows imaging of particles down to around 10 nm in diameter. As particle size decreases, it becomes more challenging as the extinction is dominated by absorption rather than scattering. For particles smaller than ∼20 nm sensitive detectors and careful optimization of the measurement geometry are needed. DFS is also a non-destructive technique and it is compatible with a wide range of substrates. Finally, the LSPR peak position in DFS is strongly influenced by the refractive index of the environment. This strong sensitivity makes it a powerful probe of local environmental changes. Most importantly for this thesis, the LSPR peak position and linewidth give access to the resonance condition and the total damping, respectively. In this way, single-particle optical measurements can be directly linked to the physical mechanisms discussed in *Section 1.1*.

1.2.2 Simulations of plasmonic optical properties

While single-particle spectroscopy provides direct experimental access to scattering and absorption, numerical simulations are essential to disentangle the individual contributions of geometry, dielectric environment, and different plasmon damping mechanisms. In this thesis, the Boundary Element Method (BEM), implemented in the MATLAB MNPBEM (Metal NanoParticle Boundary Element Method) toolbox was used to simulate the optical properties of the plasmonic systems investigated and to support the interpretation of the optical measurements presented [47]. This method solves Maxwell's equations for objects with homogeneous and isotropic dielectric properties separated by sharp interfaces. In BEM, only the surfaces of the objects need to be discretized, which leads to comparatively high convergence with low computational cost [48]. The inputs required for these simulations include the dielectric function of gold, the dielectric environment, and the object's exact morphology in the form of a surface mesh. Accurate structural models are therefore essential, particularly for complex or asymmetric nanoparticle geometries. One central theme of this thesis is obtaining accurate input geometries for BEM simulations directly from electron microscopy and tomography data. This allows the influence of particle geometry to be systematically accounted for, enabling a cleaner disentanglement of shape contributions from other factors governing the optical response.

1.2.3 Transmission electron microscopy

In 1873, Ernst Abbe demonstrated that the spatial resolution of optical microscopes is fundamentally limited by the wavelength of visible light [49]. When illuminating in the visible range, features smaller than a few hundred nanometers cannot be resolved. To overcome this diffraction limit, researchers began exploring probes with shorter wavelengths. In 1904, Carl Zeiss commercialized the first ultraviolet (UV) microscopes, achieving about twice the resolution of visible-light instruments. A major breakthrough came in 1931, when Ernst Ruska and Max Knoll showed that electrons, which have much shorter wavelengths than photons, could be used to image materials with far better resolution. Their pioneering work led to the first transmission electron microscope (TEM) and a Nobel Prize in 1986 [50]. The underlying principle was established earlier by Louis de Broglie in 1924, who related the wavelength of electrons to their momentum [51]:

$$\lambda = \frac{h}{mv} = \frac{h}{\sqrt{2meV}} \tag{1.6}$$

Here, λ is the de Broglie wavelength of a particle with mass m and velocity v, h is Planck's constant, e is the elementary charge, and V is the accelerating potential. Increasing the accelerating voltage therefore reduces the electron wavelength, making higher resolutions achievable. However, the experimentally achievable resolution is ultimately limited by lens aberrations and is therefore lower than the theoretical values in Equation 1.6. Modern instruments equipped with aberration correctors can now routinely achieve sub-angstrom resolution[52]. A further milestone was reached in the 1980s with the advent of digital imaging, enabling direct acquisition, processing, and analysis of TEM data on computers.

When an electron beam interacts with a sample, it undergoes elastic and inelastic scattering, generating a variety of signals that can be selectively detected to extract structural, compositional, and crystallographic information. The different signals generated are schematized in Figure 1.4a. TEMs operate in two main modes. In conventional TEM, a broad, approximately parallel electron beam illuminates the specimen, producing high-resolution real-space images or diffraction patterns from the transmitted electrons. In scanning transmission electron microscopy (STEM), a focused electron probe is rastered across the sample. Different detectors collect electrons scattered into specific angular ranges. Bright-field (BF) detectors collect the transmitted and low-angle scattered electrons, while annular dark-field (ADF) detectors capture electrons scattered to intermediate and high angles, depending on the angular range selected. Electrons elastically scattered by atomic nuclei can be deflected to high angles through Rutherford scattering, and when collected at high angles the ADF detector operates in HAADF mode. HAADF-STEM contrast scales approximately with thickness and atomic number (Z^2-contrast), enabling the visual-

ization of compositional variations with high spatial resolution. Electrons interacting with crystalline planes, on the other hand, give rise to coherent Bragg scattering at low angles, detectable by BF detectors.

Electron tomography

Although TEM enables imaging down to atomic resolution, it inherently provides 2D projection images, whereas the physical world is three-dimensional. For plasmonic nanoparticles, this limitation is particularly critical because their optical response is extremely sensitive to subtle geometric variations. Even small errors in structural parameters can lead to incorrect interpretations of plasmonic coupling and damping. Therefore, a technique capable of resolving the full 3D morphology is essential. Electron tomography (ET) overcomes this limitation by reconstructing the three-dimensional structure from a tilt series of TEM or STEM images [53, 54]. By acquiring projections from multiple angles and combining them with mathematical algorithms, ET provides an accurate representation of the 3D nanoparticle morphology. Every image must satisfy the projection requirement, meaning that the contrast is a monotonic function of thickness. For crystalline material where diffraction contrast cannot be neglected, ET has to be performed in HAADF-STEM to fulfill the projection requirement [53, 55]. Despite its potential, electron tomography suffers from some intrinsic limitations. The limited space between the pole piece and the sample holder prevents acquisition over the complete $\pm 90^\circ$ tilt range, resulting in the so-called missing wedge artifact. This leads to elongation and blurring in the reconstruction. Iterative reconstruction algorithms such as the: *Simultaneous Iterative Reconstruction Technique (SIRT),Expectation–Maximization (EM)*, *Total Variation Minimization (TVM)* help mitigate these limitations and improve reconstruction quality.

Energy-dispersive X-ray spectroscopy

Energy-dispersive X-ray spectroscopy (EDX) is an analytical technique used to determine the elemental composition of a sample by detecting the X-rays generated during its interaction with an electron beam. When an inner-shell electron is removed by the incident beam, a vacancy in its electronic structure is created. Subsequently, this vacancy is filled by an electron from a higher-energy shell, and the energy difference between the two states is released in the form of a characteristic X-ray. Because each element emits X-rays at well-defined energies, analyzing the energy distribution of the emitted radiation enables both qualitative and quantitative elemental characterization and mapping.

In situ optically-coupled TEM

Very recently, integrating laser excitation into a TEM has become a powerful way to study light–matter interactions in plasmonic nanoparticles with nanometer resolution and in real time [56]. There are two main approaches to in-couple light in a TEM: either through a fiber-based in situ holder, or directly into the microscope column in free space. In this thesis, we use the second approach, illustrated in Figure 1.4b. In

this configuration, the optical excitation is independent of the sample holder. The main advantage is the possibility to combine it with different specialized holders, such as tomography, gas, or heating holders. The laser is guided through an optical fiber to an in-coupling unit, where it is converted into a free-space beam and directed onto the sample via a mirror inside the column. The in-coupling unit allows alignment corrections per wavelength, enabling tunability across the visible and near-infrared range. The disadvantage of this configuration is that the laser spot cannot be highly focused into a diffraction limited spot on the sample. Overall, this setup is quite flexible: different types of laser sources can be used, from continuous-wave to pulsed systems, and the excitation wavelength can be tuned to match the plasmon resonance of the nanoparticle. In addition, synchronizing the laser pulses with the electron beam and/or the detector enables time-resolved measurements, allowing us to access ultrafast light-induced dynamics at the single-particle level.

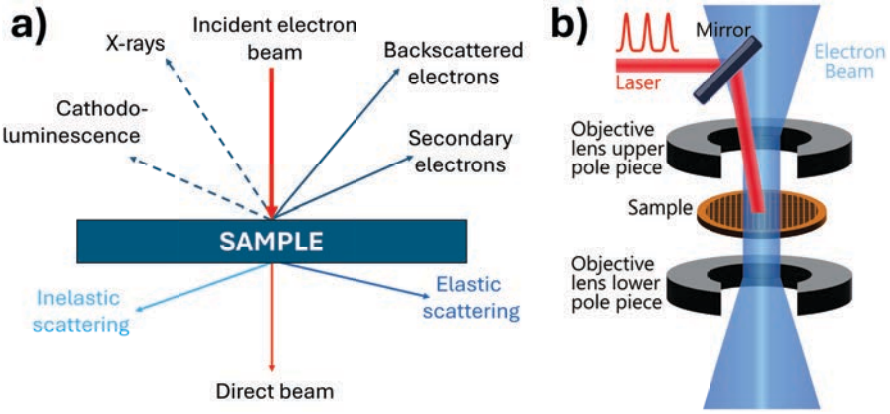

Figure 1.4: *a) Schematic illustration of the different signals generated by electron–sample interactions. b) Modified Transmission Electron Microscope with a light in-coupling unit and a mirror placed at the upper pole pieces of the objective lens allowing real-time observation of in situ optical excitation.*

Diffraction and 4D-STEM

When the electron beam interacts with the crystal planes of a crystalline material, it is elastically scattered. The sample behaves like a diffraction grating, generating a diffraction pattern in the back focal plane of the objective lens. This pattern can be measured in an electron diffraction experiment. A TEM equipped with scan coils can perform 4D-STEM when paired with a direct or pixelated detector. In this technique, a 2D diffraction pattern is acquired at each probe position, resulting in a four-dimensional dataset (two spatial dimensions × two reciprocal-space dimensions), hence the name *4D-STEM* [57]. The electron beam can be converged in different ways

depending on the desired spatial and diffraction resolution. In the *Convergent Beam Electron Diffraction* (CBED) configuration, the electron beam is highly converged, as in regular STEM mode. The resulting diffraction pattern consists of large disks, instead of distinct spots. This configuration enables very high spatial resolution, but very low diffraction resolution. The size and overlap of the diffraction disks in the CBED configuration can be adjusted by varying the convergence angle of the probe [58]. When the convergence semi-angle of the probe is larger than the Bragg angle, CBED diffraction disks begin to overlap. On the other end, by using a quasi-parallel beam the diffraction pattern becomes much sharper, consisting of spots rather than disks. While the real-space resolution decreases significantly, the diffraction resolution becomes very high. This configuration is often referred to as *parallel nano-beam diffraction* (NBD).

1.2.4 Other e-beam techniques and electron beam damage

Through inelastic interactions with the electron beam, the optical response of metal nanoparticles can also be probed using electron-based spectroscopies such as electron energy-loss spectroscopy (EELS) and cathodoluminescence (CL). Performed directly inside the electron microscope, these techniques enable a direct correlation between nanoparticle structure and optoelectronic behavior. Because they allow visualization of the electromagnetic near-field distribution, EELS and CL have become powerful tools for mapping the spatial position and extent of plasmonic modes in nanostructures with complex geometries [59] or sub-nanometer gaps [60], as well as for studying energy-transfer processes in plasmonic systems [61, 62]. Despite their strengths, electron-based spectroscopy techniques present several limitations. Compared to optical techniques, they typically offer lower energy and temporal resolution. These methods are also challenging to perform under ambient conditions and rely on broadband excitation imposed by the exciting electron beam with limited control over polarization. Furthermore, the prolonged electron-beam exposure required for high-quality measurements can lead to sample damage.

Because of this damage, the interaction of the electron beam with metal nanostructures has been shown to modify their plasmon resonances [63]. For isolated metal nanoparticles, a modest red-shift and broadening of the resonance peak are often observed after electron beam exposure. These changes are mainly attributed to the deposition of carbonaceous contaminants and transformation of ligands into amorphous carbon. Carbon has a higher refractive index ($n = 2.42$) than the surrounding vacuum environment, leading to a red-shift of the LSPR. Furthermore, the carbon layer introduces additional optical losses, contributing to broadening of the resonance peak. As the electron dose increases, the contamination layer becomes thicker, leading to progressively larger red-shifts. These changes were shown to be irreversible [64,

65]. Electron-beam damage can be reduced by using a lower-energy electron beam and by minimizing the exposure time.

Coupled metal nanoparticles are highly sensitive to changes in the environment, coupling strength, and gap morphology, making the influence of beam exposure more dramatic [65]. The electron beam destroys bridging molecules and can displace the nanoparticles, changing the interparticle distances. Figure 1.5 demonstrates this effect on the gold dimers coupled by BDT molecules studied in *Chapter 2 and 3*. The dark-field scattering spectra acquired for the same dimer before (solid line), after scanning electron microscopy (SEM) imaging (dashed line), and after TEM imaging (dotted line) are shown in Figure 1.5a. SEM imaging induced a small redshift of the bonding mode while leaving the single particle mode unchanged, already indicating that structural modifications occur even at the lower electron energies typical of SEM. As expected, the effect was more pronounced after TEM imaging: the single sphere mode showed a slight redshift and broadening consistent with carbon deposition, while the bonding mode was nearly completely suppressed. Figure 1.5b shows scattering spectra before and after TEM imaging for multiple individual dimers, confirming that these alterations are not isolated but a systematic consequence of electron beam exposure. These effects are irreversible and are shown to significantly alter the optical response. This demonstrates that optical characterization must precede electron microscopy in any correlative single-particle study and underlines the importance of the correlative approach developed in this thesis.

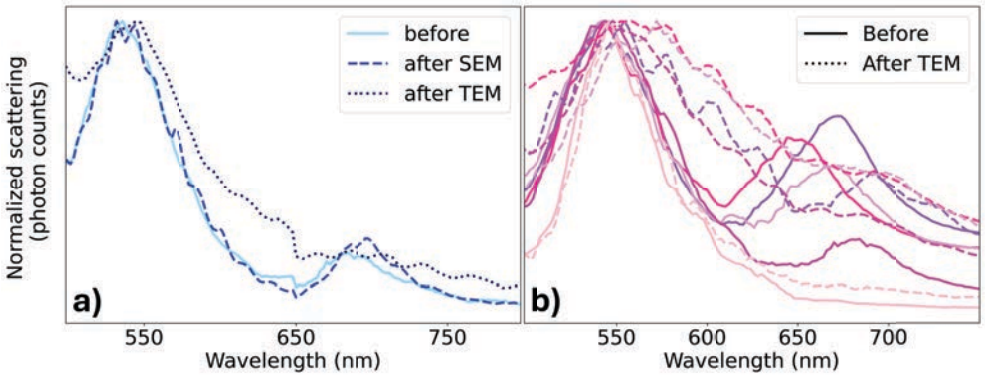

Figure 1.5: *Effect of the electron beam on the optical properties. a) Dark-field scattering spectra of the same dimer consisting of two gold spheres separated by a molecular bridge of 1,4-benzenedithiol molecules, measured before, after SEM imaging, and after TEM imaging. SEM images were acquired at 5 kV while TEM images at 300 kV. b) Dark-field scattering spectra of four dimers measured before and after TEM imaging.*

1.3 This thesis: Motivation and outline

This thesis investigates how the morphology and interface structure of hybrid plasmonic nanosystems can be characterized and manipulated and how they influence their optical response at the single-particle level. To achieve that, single-particle dark-field scattering spectroscopy is used to probe the optical properties, while electron microscopy provides detailed structural information. By using these experimentally determined morphology as direct input for optical simulations, comparison with measured spectra allows the extraction of physical properties. Pulsed laser excitation integrated into the TEM is used to induce and monitor morphological and compositional changes in real time. This approach provides a pathway toward controlled modification of hybrid plasmonic nanosystems at the atomic scale. In this work, electron microscopy is therefore used both as a characterization tool for simulations and as a platform for in situ manipulation. This correlative approach is applied to two hybrid nanosystems: gold nanosphere dimers bridged by molecular junctions, and gold nanorods coated with a titania shell. This thesis is structured as follows.

Chapter 2 describes the synthesis of gold nanosphere dimers coupled with BDT molecules and the characterization of their optical response using single-particle dark-field scattering spectroscopy. The optical properties are correlated with two-dimensional STEM images. The limitations of extracting morphologies, and particularly interparticle gap sizes, from 2D HAADF-STEM are discussed, including projection effects, segmentation variability, and beam-induced modifications. The gap sizes are then compared with values obtained from optical data, showing that this extraction is not unique, as similar spectra can result from different combinations of gap size, dielectric environment, and junction model. Overall, this chapter demonstrates that neither electron microscopy nor optical spectroscopy alone provides a reliable determination of the gap, complicating quantitative morphology–optics correlations and identification of the transport regime.

Chapter 3 introduces a more accurate approach to investigate dimer morphology by using electron tomography, which provides full three-dimensional structural information. Using the ET reconstructions, a method is developed to reliably extract the sub-nanometer gap size by fitting the reconstruction intensity profile along the gap with a convolution between a Gaussian function and a step function. The proposed fitting approach enables consistent and robust gap determination, reaching pixel-level accuracy. This improved morphological information allows the extracted structures to be translated into accurate surface meshes for electromagnetic simulations. Finally, the 3D reconstructions are used as a reference to assess and improve gap estimation from 2D imaging.

Chapter 4 addresses the metal–semiconductor interface in $Au@TiO_2$ nanorods. In plasmonic–semiconductor hybrid systems, interface quality and TiO_2 crystallinity

are among the key factors governing injection efficiency in the semiconductor and the transport efficiency of the injected carriers. This chapter focuses on the effect of precursor and ligand choice on the morphology, defect density of the TiO_2, and interface quality. The chapter outlines how the initially amorphous shell can be crystallized while minimizing Au core deformation via two approaches: conventional low-temperature solution-based crystallization and laser-induced crystallization performed directly inside the TEM. The latter enables real-time monitoring of structural evolution, revealing how crystalline domains form in the TiO_2 shell and how the Au core responds to pulsed optical excitation. This represents a novel in situ approach to controlled interface engineering.

Chapter 5 demonstrates real-time and reversible control over the composition of individual $AuCu$ alloy nanorods coated with TiO_2 using pulsed laser excitation inside the TEM. By tuning the laser fluence, the copper content of the gold nanorod can be continuously varied, from pure gold through increasingly copper-rich alloy compositions. The process can be reversed by evaporating copper at higher fluences and restoring the original gold structure. The rate of copper incorporation and evaporation is followed quantitatively by time-resolved diffraction, providing direct insight into the kinetics of laser-driven alloying at the single-particle level. This demonstrates that light can be used not only to probe but also to actively modify nanoparticle composition at the single-particle level, opening a route toward dynamic control of plasmonic and catalytic properties.

Together, the results of this thesis highlight that the optical response of plasmonic nanoparticles is highly sensitive to morphology and interface structure at the nanometer and sub-nanometer scale. Reliable interpretation therefore requires equally precise structural characterization. Electron microscopy provides the structural precision needed, while the correlative single-particle approach developed here enables structure and optical function to be directly linked. This work demonstrates the importance of accurate three-dimensional morphological characterization, particularly for sub-nanometer features such as molecular junction gaps and metal–semiconductor interfaces. In addition, this thesis shows that in situ laser excitation inside the TEM enables controlled modification and real-time observation of structural and compositional changes at the single-particle level. Pulsed optical excitation provides a route toward dynamic control of nanoscale systems, allowing processes such as crystallization, alloying, and structural evolution to be directly observed. This combined approach allows structure and functionality to be directly linked and dynamically tuned at the single-particle level. Together, these advances establish light not only as a probe but also as an active tool for controlling nanoscale material properties, and motivate future research into the quantitative relationship between interface structure and efficiency in hybrid plasmonic nanosystems.

2 Dimer synthesis in solution and correlation of dark-field scattering and 2D morphology

Keywords: *conductive coupling, bonding dipolar mode, tunneling transport, molecular junctions, dimer assembly, dark-field scattering, TEM–optical correlation*

Plasmonic nanoparticle dimers provide a powerful platform for exploring light–matter interactions at sub-nanometer scales. They confine light to ultrasmall volumes and enable charge transfer across sub-nm or conductive gaps. In this regime, the optical response is extremely sensitive to the interparticle gap, making its accurate determination critical not only to tune the optical properties, but also to properly understand the transport mechanisms. In this work, we synthesize gold nanosphere dimers linked by 1,4-benzenedithiol (BDT) and investigate their optical properties using correlated dark-field scattering and electron microscopy at the single-particle level. We show that the gap sizes extracted from two-dimensional STEM images are highly unreliable. Projection effects, variations from segmentation, and beam-induced modifications influence strongly the measured gap. This prevents a direct correlation between morphology and optical response. We then show that extracting the gap from optical spectra is also not unique. Similar scattering responses can be reproduced with different combinations of gap size, dielectric environment, and the physical model used to describe the junction. Taken together, these results show that neither 2D imaging nor optical spectroscopy alone can provide a reliable measure of the interparticle gap. This highlights the challenges in establishing quantitative morphology–optics correlations and to unambiguously identify the transport regime governing the coupling in plasmonic dimers separated by molecular junctions.

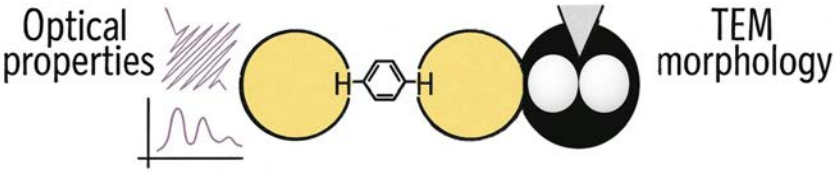

2.1 Introduction

Plasmonic nanoparticles (NPs) illuminated by light support collective electron oscillations, known as localized surface plasmon resonances (LSPR). When two metallic nanoparticles are brought into close proximity, their individual plasmon modes hybridize into bonding and antibonding configurations [66]. The bonding dipolar plasmon (BDP) is the bright, radiative mode that dominates the optical response in the classical regime [67]. It is excited when the incident light is polarized along the dimer axis, giving rise to a strongly enhanced longitudinal mode, while transverse excitations largely retain the character of the individual particles [68]. This hybridization leads to strong localization and enhancement of the electromagnetic field in the gap region, exceeding that of single nanoparticles. Because of this field enhancement, plasmonic dimers provide a powerful platform for studying light–matter interactions at very small length scales. They have applications in ultrasensitive sensing and photocatalysis, but are also of strong fundamental interest.

As the gap between two metallic nanoparticles approaches the sub-nanometer regime, the coupling mechanism transitions from purely capacitive to partially or fully conductive. This can occur through quantum tunneling across bare gaps, or through conductive bridging materials such as molecular junctions or metallic filaments. In this conductive regime an additional plasmon mode arises: the charge transfer plasmon (CTP) mode [69–75]. Charge transfer also affects the capacitive BDP mode, resulting in a blue-shift of the resonance compared to electromagnetic simulations [60], also referred to as screened BDP.[69, 74] Such blue-shifts have also been observed in non-touching dimers with sub-nanometer gaps [67, 76]. The onset of tunneling, where electrons cross the gap without physical contact, is therefore often associated with the spectral signature of a blue-shifted BDP. Plasmonic gaps can probe molecular electronic properties by converting the AC transport response of the junction into a measurable far-field signal, providing access to information beyond standard DC transport measurements.

Despite extensive theoretical predictions and experimental indications, direct observation of the CTP mode in tunneling plasmonics remains limited [77]. A CTP resonance has been reported in specific systems, such as silver nanocubes bridged by molecular junctions [78], though its interpretation remains debated [79]. Most claims of tunneling rely on indirect signatures such as BDP blue-shifts, rather than clear observation of a CTP mode. Recent quantum electrodynamics studies challenge the tunneling interpretation. Surface-enhanced Landau damping, a quantum effect unrelated to charge transfer, can produce similar blue-shifts [80]. It therefore remains unclear whether tunneling at optical frequencies occurs in these systems or whether the response is dominated by quantum-corrected surface effects.

The optical response of plasmonic dimers with sub-nanometer gaps is governed by two closely linked factors: the interparticle gap size and the charge transport properties of the junction. Although the transport properties are determined by the physical nature of the gap, modeling the optical response requires assumptions about charge transport parameters such as conductivity or tunneling decay, which are not well established at optical frequencies for molecular junctions. As a result, different model choices can lead to different predicted BDP and CTP peak positions and intensities, even for the same geometry. Since both gap size and charge transport influence the spectral response in similar ways, they cannot be reliably disentangled without independent knowledge of one of the two. This fundamental ambiguity is rarely addressed explicitly, although it represents a major limitation in interpreting optical measurements in this regime.

To explore this entanglement, in the following two chapters we focus on dimers of gold nanospheres separated by 1,4-benzenedithiol (BDT) molecular junctions. The molecular structure of BDT is shown in Figure 2.1b. BDT is particularly suitable for this purpose due to its strong chemical affinity for gold, arising from the thiol end groups, which bind to gold surfaces via sulfur atoms. Furthermore, hybridization between the molecular orbitals of BDT and the electronic states of gold can enable charge transport through Au–BDT–Au junctions [81, 82]. Such transport has been extensively studied under DC bias conditions. In this work we investigate whether similar mechanisms can contribute to electron transport at optical frequencies.

For an isolated BDT molecule, the highest occupied molecular orbital (HOMO) and lowest unoccupied molecular orbital (LUMO) are delocalized over the benzene ring through π orbitals, with additional states closer to the gap contributed by the sulfur atoms [81, 83]. BDT exhibits a large HOMO–LUMO gap in the gas phase of approximately 9 eV [84]. BDT binds to gold via sulfur atoms after removal of the hydrogen atoms. The resulting thiolate groups exhibit electron-withdrawing character, strengthening the bonding to gold and enhancing electronic coupling at the metal–molecule interface [85]. The molecular orbitals hybridize with the Au 6s and 5d bands, which broadens and shifts their energies relative to the Fermi level [81, 82, 85, 86]. As a result, charge transport is not governed by the full HOMO–LUMO gap, but by the smaller energy offset between the molecular orbitals and the Fermi level [86, 87]. In Au–BDT–Au junctions, this effective energy offset is typically on the order of 0.3–2 eV, depending on the junction geometry and bonding configuration [86, 88, 89]. Electrostatic screening by the metal can further reduce this barrier [82].

In this chapter, we show the entanglement between gap geometry and charge transport. We first investigate the limitations and uncertainties associated with correlating dark-field scattering with 2D morphological characterization of individual gold nanosphere dimers with sub-nanometer gaps. Using single-particle correlative measurements that combine dark-field spectroscopy with 2D electron microscopy, we

directly link the optical response to the dimer morphology and assess how reliably the interparticle gap size can be extracted. We show that 2D STEM images are strongly affected by projection effects and segmentation ambiguity. We then illustrate that extracting the gap size from optical data also suffers from fundamental limitations, arising from parameter degeneracy. Different combinations of gap size, dielectric environment, and transport model can reproduce indistinguishable spectral responses. Taken together, these results highlight what correlated structural and optical measurements can and cannot reveal about sub-nanometer gaps, and motivate the need for more reliable approaches, such as full three-dimensional morphological reconstruction, which will be introduced and discussed in the next chapter.

2.2 Methodology

2.2.1 Self-assembly of gold nanoparticles

Chemicals

All starting materials were used without further purification. Cetyltrimethylammonium bromide (CTAB, 96%), benzene 1,4-dithiol (BDT), and ethanol were purchased from Sigma-Aldrich. Milli-Q grade water (resistivity 18.2 MΩ cm at 25° C) was used in all experiments.

The 50 nm in diameter gold nanoparticles were first synthesized according to a recently reported method [90]. A dimers solution was then prepared by introducing BDT into a solution of CTAB-capped gold nanoparticles. Due to the stronger binding affinity of BDT than CTAB to gold surfaces, the native ligands were replaced by BDT, leading to the self-assembly of nanoparticles into dimers (Au-BDT-Au dimers) with a yield close to 30% . The gold nanoparticles were colloidally self-assembled using a modified protocol by *Goppert et al.* [91]. The concept behind the reaction is illustrated in Figure 2.1. Initially, the CTAB ligands surrounding the gold nanoparticles are exchanged for BDT. This ligand exchange is thermodynamically favorable given the different nature of the binding interactions. CTAB binds to gold through electrostatic interactions, while for BDT sulfur atoms strongly covalently bind to gold. Following ligand exchange, BDT-capped nanospheres assemble due to the high affinity of sulfur atoms for gold. A monolayer (c.1) or a bilayer (c.2) of BDT can be present in the gap.

1.3e^{-8} M of CTAB capped gold nanoparticles, 50 nm in diameter, were used as a stock solution. 139 μl of stock solution was diluted by adding 5 mM CTAB solution to 10 ml fresh Milli-Q water. Subsequently, 425 μl of the diluted gold nanoparticle solution was transferred to a PMMA cuvette, and an initial absorption spectrum was acquired. All UV–Vis measurements in this work were carried out using a Lambda750 spectrometer (PerkinElmer) with PMMA cuvettes of 10 mm optical path

length. Then, 750 μl of Milli-Q water was added to the cuvette, followed by 10 μl of a 5 mM CTAB solution to stabilize the NPs and 340 μl of 10 mM BDT in ethanol. Additional ethanol was finally added to destabilize the CTAB capping layer and promote ligand exchange. Furthermore, the addition of ethanol was essential to fully dissolve the BDT, which has low solubility in water. Incompletely dissolved BDT emulsifies in water settling at the liquid-air interface, causing the solution to turn from transparent to cloudy. Due to the higher affinity of the sulfur atoms in BDT for gold, the CTAB ligands are readily replaced by BDT.

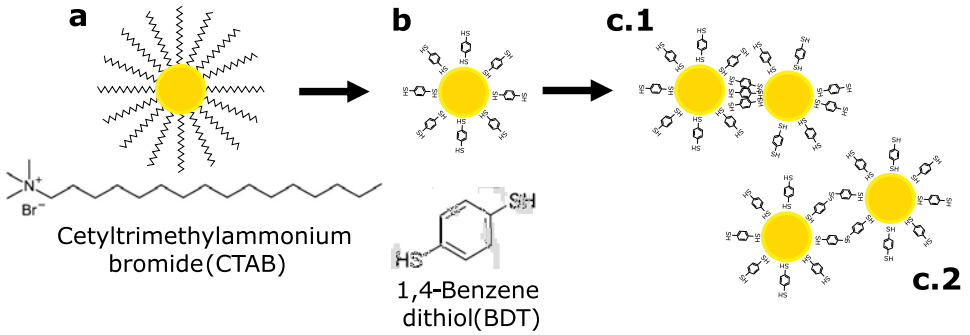

Figure 2.1: *Ligand exchange schematic: a) Gold nanosphere capped with CTAB ligands. The CTAB ligands are replaced by BDT through ligand exchange b). BDT-capped gold nanospheres subsequently assemble to form dimers c).*

2.2.2 Quasi-dark-field scattering setup

Scattering spectra of individual dimers were measured using a custom-built confocal dark-field spectroscopy setup. A simplified sketch is shown in Figure 2.2. The excitation source is a picosecond supercontinuum laser (1), combined with a laser line tunable filter (LLTF) (2). The filter enables excitation wavelengths between 400–1100 nm with a $\approx$ 2.5 nm bandwidth. The beam is first spatially cleaned and circularly polarized using a Glan-Thompson polarizer(4), a 1/4 wave plate (5), and a 1/2 wave plate (6). The laser is then focused onto the sample through an inverted microscope (9) using a high-NA (1.45) objective. The objective is an immersion oil objective with a refractive index $n = 1.518$. A custom made holder was developed to mount the TEM grid directly onto the objective (18). The sample is mounted on a motorized piezo stage, which allows for nanometers-precision movements. Back-scattered light is collected by the same objective and redirected into the collection path through a 20/80 beam splitter (10). In the collection path, a home made partial beam block with a diameter of 2 mm (11) is placed. The beam block stops the direct laser light, only allowing light scattered at higher angles to pass. This configuration

results in a quasi–dark-field detection scheme based on angular filtering. Finally, in order to filter out any stray light under high angles a 10 μm pinhole is placed in front of the detector at a Fourier-conjugate plane (14). The remaining scattered light is detected by an avalanche photodiode, APD (15). The APD records the photon counts corresponding to the scattered intensity collected within the selected angular range as a function of the incident wavelength. This configuration is well suited for measuring the LSPR of plasmonic nanoparticles, which exhibit strong scattering into high-angle components.

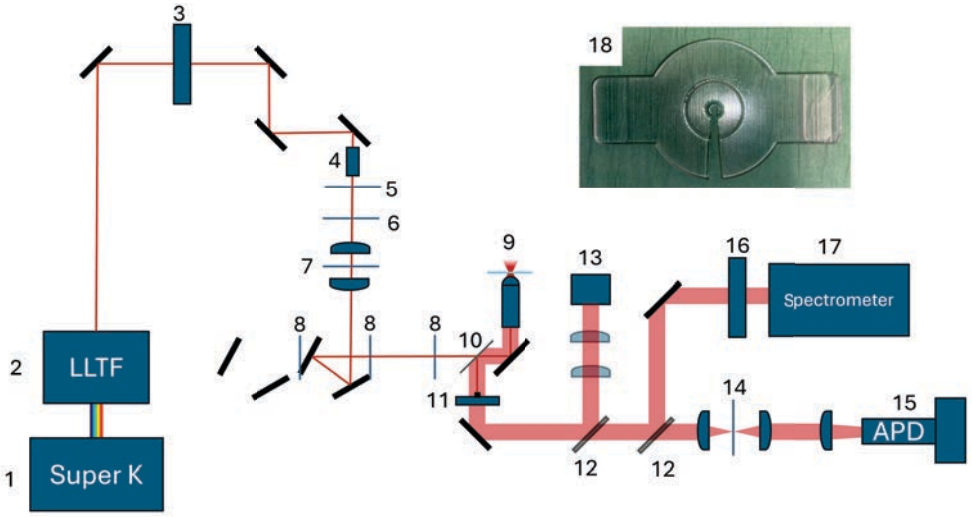

1. Laser
2. Filter
3. OD filter wheel
4. Glan-Thompson polarizer
5. ¼ wave plate
6. ½ wave plate
7. 100 µm pinhole
8. Iris
9. NA 1.45 oil objective
10. 20:80 beam splitter
11. Partial beam block
12. Flip mirror
13. Basler RGB Camera
14. 10 µm pinhole
15. APD
16. Filter wheel
17. Spectrometer
18. Sample holder

Figure 2.2: *dark-field scattering set-up scheme. In 18 the sample holder for TEM grids is shown. A TEM grid is mounted in the center circular hole.*

2.2.3 Correlation procedure

Each experiment was performed following the same protocol. dark-field scattering measurements were acquired using an immersion oil objective. The TEM grid was mounted on the TEM holder attached to a piezo-controlled stage. The stage was moved to locate a window on the grid. First, a map of the entire window was recorded with a step size of 0.5 μm, as shown in Figure 2.3a. Each bright dot in the map

corresponds to the scattering signal from a scatter. The size of the scattering spot is related to the scattering cross-section and can therefore be used to discriminate between big agglomerates and smaller ones or single particles. In our setup, for a single nanoparticle the point-spread function is expected to be approximately $1 \times 1\,\mu m^2$. Subsequently, smaller selected areas were scanned to better identify individual nanoparticles using a step size of $0.2\,\mu m$, Figure 2.3b. The scan was repeated at 532 nm, Figures2.3b.1, and at 680 nm, 2.3b.2. With the first wavelength, all Au nanospheres can be identified, while with the second wavelength only dimers (and occasionally trimers or bigger agglomerates) produce a detectable scattering signal corresponding to the BDP. This is why fewer bright spots appear in Figure 2.3b.2.

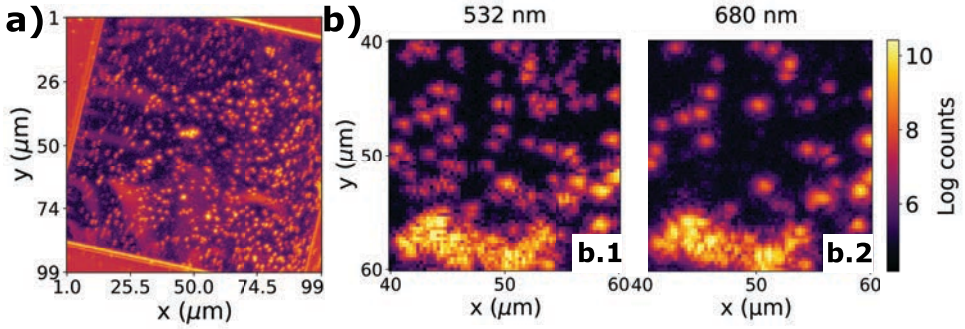

Figure 2.3: *Identification of dimers in scattering. a) Scattering map of an entire window of a SiO_2 TEM grid acquired at 532 nm. The intensity is presented on a logarithmic scale. Each bright spot corresponds to the scattering from a single scatterer. The pixel size is 0.5 μm. b) Scattering map acquired from a zoom-in of the entire window. The pixel size is 0.2 μm. b.1) The map is acquired at 532 nm to excite all nanoparticles, while in b.2) the excitation wavelength is 680 nm to selectively excite the bonding mode.*

For each bright spot, the laser was first focused. Finally, a spectrum was acquired by scanning the excitation wavelength from 500 to 850 nm and recording the signal on the APD at each wavelength. The spectra were acquired using an integration time of 20 ms and a wavelength step size of 2 nm. A filter switch at 650 nm introduced a discontinuity in the excitation intensity, which manifests as a jump in the measured signal. The spectra acquired were therefore corrected for this intensity step, but are otherwise raw data. In order to extract the peak position and line width, each spectrum was fitted with a double Lorentzian in the energy scale.

Once the optical measurements were completed, the grid was removed from the holder and thoroughly rinsed with toluene. The next step was the correlation of each scattering spectrum with its corresponding morphology. The grid was therefore

brought to the TEM and a STEM image of each of the optically measured particle was acquired.

2.2.4 Optical simulations

All simulations of the optical properties of the plasmonic dimers were performed using the Boundary Element Method (BEM), as implemented in the MATLAB MNPBEM (Metal NanoParticle Boundary Element Method) toolbox. All simulations were carried out in the fully retarded regime to account for radiation damping and phase retardation. The dimers were excited with a plane wave with circularly polarized light propagating in the z-direction. The dielectric function of gold was taken from McPeak et al.[92]. Further details on the method are provided in *Section 1.2.2* of the *Introduction*.

2.2.5 Electron microscopy

The first measurements reported were performed in an aberration-corrected NeoARM (S)TEM with Cold Field Emission Gun operated at 200 kV. The electron tomography images at different angles were instead acquired using an aberration-corrected Thermo Fisher Scientific Titan microscope, operated at 300 kV.

2.3 Results and discussion

2.3.1 Dimers yield optimization

Given the need for reliable single-particle correlation, and the fact that optical measurements must be performed before electron microscopy to avoid beam-induced damage, we first optimized the dimer yield. For this optimization, we monitored the rate of nanoparticle agglomeration in real time by UV–Vis spectroscopy, in which dimer formation appears as a second peak at higher wavelengths corresponding to the BDP mode.

Two parameters were optimized: the volume of ethanol added and the reaction time. The first is not only crucial to dissolve BDT, which is not soluble in water, but also for destabilizing the CTAB layer around the nanoparticles. Too much ethanol leads to uncontrolled agglomeration, while too little does not allow ligand exchange to occur. The reaction time is critical for controlling the agglomeration rate. If the reaction is left for too long, uncontrolled agglomeration occurs, leading to larger aggregates. The ethanol volume was varied between 100 μl and 400 μl. Figure 2.4a shows the UV–Vis spectra acquired for the solution after the addition of different amounts of ethanol. For ethanol additions of 100 μl and 250 μl, the spectra were

acquired after a waiting time of one hour. They do not show any peak appearing at higher wavelengths but only the single particle LSPR at 532 nm, meaning that no dimer formation or agglomeration happened. For an ethanol volume of 350 μl, the spectrum was acquired after 8 minutes and a clear peak at 650 nm appeared. Finally, for 400 μl of ethanol the spectrum was acquired after 2 minutes and a larger shoulder around 750 nm started to appear, which indicates the formation of larger aggregates.

An ethanol volume of 350 μl was identified as optimal, as it sufficiently destabilizes the CTAB layer to allow ligand exchange without inducing uncontrolled agglomeration. Using this ethanol volume, time-dependent absorption spectra were acquired to determine the optimal reaction time. These spectra are shown in Figure 2.4b. An immediate redshift can be observed for the single-sphere absorption peak at 530 nm after the addition of ethanol and BDT. This is attributed to the increase of the dielectric constant of the environment when going from pure water to a solution of water, ethanol, and BDT. According to simulations, going from a refractive index of $n = 1.333$ for water to $n = 1.361$ for pure ethanol should only result in a shift of about 2 nm. The larger observed shift may be attributed to the formation of a BDT layer around the nanoparticles. The refractive index of BDT lies in the range of $n = 1.5$–1.7, as reported in chemical property databases, which exceeds that of CTAB ($n = 1.43$)[93]. As the reaction proceeds, the single-particle resonance decreases in intensity and exhibits a slight blue-shift. This mode corresponds to the transverse mode of the dimer. The observed blue-shift arises from weak coupling between the two spheres. The interaction is predominantly repulsive, which increases the energy of the transverse mode [94]. At the same time, a new peak emerges at longer wavelengths. This new peak, centered around 650 nm, corresponds to the BDP mode of a nanoparticle dimer system, and its intensity keeps increasing over time as the density of dimers increases. At later stages, additional shoulders and peaks appear at higher wavelengths due to the formation of larger agglomerates. Furthermore, the normalized spectra shown in Figure 2.4c reveal a broadening of the absorbance peak at 530 nm, suggesting a polydispersity in the gap size and formation of trimers, and therefore in the blue shift of the peak. Peaks at slightly different positions are superimposed, resulting in a broader peak. Additionally, the broadening can be enhanced by plasmon damping induced by the presence of BDT molecules.

The highest dimer yield occurred at 10 minutes reaction time. At this moment, the BDP peak at 650 nm has a high intensity while remaining relatively narrow. At this reaction time, 20 µL aliquot of the solution was drop-cast onto a TEM grid consisting of nine windows of 100 μm × 100 μm made of 50 nm SiO_2 membranes from SimPore for the subsequent optical characterization. Consistent with the UV–Vis results, the TEM image of that sample in Figure 2.5a shows a mixture of monomers, dimers, trimers, and larger agglomerates. From the TEM images a dimers percentage of 35% was found.

The reaction was quenched by adding 1 mL of a 5 mM CTAB solution. CTAB restabilizes the nanoparticle surfaces and suppresses further agglomeration by restoring electrostatic repulsion between particles. However, as shown in Figure 2.4d, over time the BDP peak at 650 nm continues to broaden until it becomes a shoulder after approximately 18 hours (cyan curve). The sample was therefore not stable on long timescales in solution, likely because excess free BDT remained present and continued to drive slow agglomeration. While CTAB increased the kinetic barrier for particle approach, it did not fully suppress the thermodynamically favorable binding between BDT and gold. Nevertheless, the presence of CTAB clearly slowed down further agglomeration compared to Figure 2.4b.

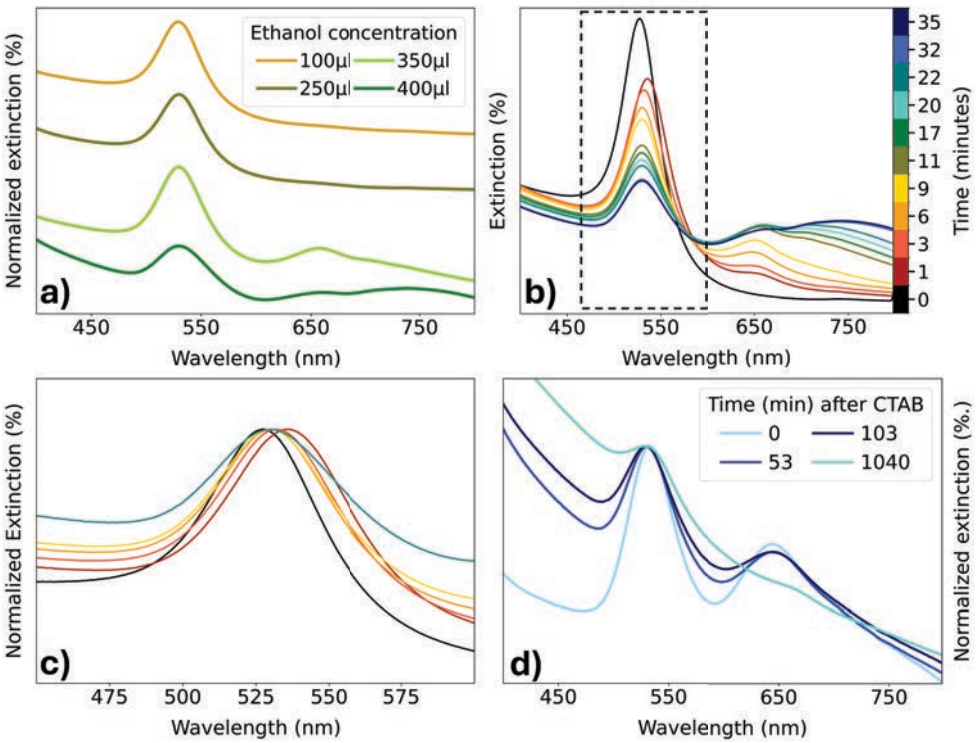

Figure 2.4: *a) Extinction spectra of the solution during dimers formation for different ethanol concentrations. b) Time-resolved extinction spectra during ligand exchange. The black spectrum corresponds to the initial nanoparticles before ethanol and BDT addition. c) Zoom in of the highlighted region in b) corresponding to the single particle/transverse dimer mode. For better visualization only normalized representative spectra are shown. d) Extinction spectra over time after quenching the reaction by adding 1000µl of 5 mM CTAB solution.*

Having established the optimal synthesis conditions, we next characterized the gap size distribution of the resulting dimers. Representative STEM images are shown in Figure 2.5b. From each individual dimer the gap size was extracted. First the images were binarized using a fraction of the Otsu's thresholding algorithm. Details on the choice of this fraction will be given at the end of *Chapter 3*, *Section* 3.3.4. The gap was determined as the smallest distance between non-zero pixels using the Exact Euclidean Distance Transform (EEDT). For each pixel in the segmented background, this function computes the shortest distance to the foreground segmentation. The smallest possible distance is then selected as the estimate of the gap size. The gap size distribution is shown in Figure 2.5c. A relatively wide range of gap sizes was measured, from 0.5 nm up to 2.25 nm. Density functional theory (DFT) calculations were used to estimate the expected gap size for different configurations of BDT bridging two gold atoms. All the possible sites for BDT to bind to gold were considered as well as the BDT molecule orientation transitioning from perfectly flat to vertical. The simulated gap sized calculated and normalized by the number of possible configurations are overlaid on the experimental values in Figure 2.5c. Calculated gap sizes range from 0.4 nm to 1.2 nm, consistent with the experimentally measured gap sizes. The larger experimentally observed gap values are likely due either to the presence of more than a monolayer of molecules within the junction, or to individual nanoparticles coated with a BDT monolayer that are randomly positioned in close proximity on the substrate after drop casting. To illustrate the consequences on the optical properties of this gap size distribution, we simulated scattering spectra using the MNPBEM toolbox for two perfect spheres with a radius of 22 nm and the gap sizes extracted from the STEM images and summarized in Figure 2.5c. The resulting spectra in Figure 2.5d show a large spread in BDP resonance position arising from gap size variation alone, without any morphological variation of the spheres. However, as can be clearly seen from Figure 2.5b, the nanospheres also differ in size and facet structure. We therefore expect an additional distribution in the optical properties of the dimers. This highlights the necessity of establishing a direct correlation between the measured optical response and the morphology extracted from (S-)TEM images.

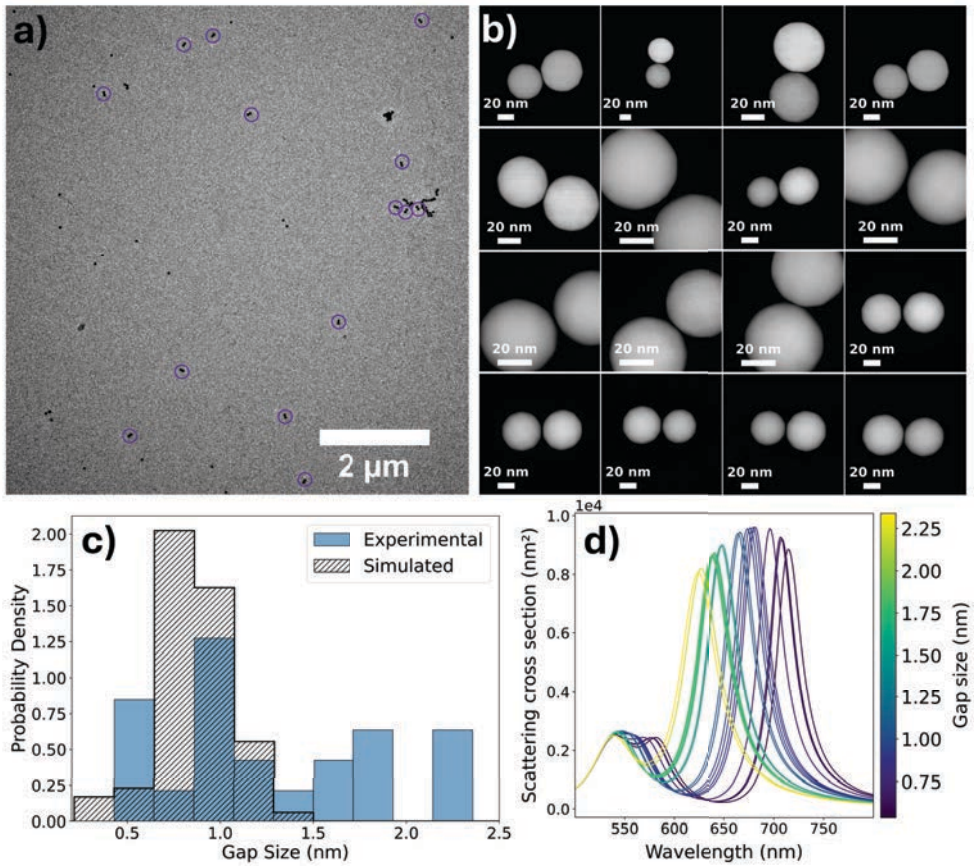

Figure 2.5: *a) Representative low-magnification TEM image of the solution at optimized dimers yield conditions, drop-cast onto a TEM grid. b) Representative STEM images of individual dimers. c) Gap size distribution of experimental (blue) and simulated dimers (black). The experimental values were extracted from 28 different dimers imaged in STEM mode, while the simulated ones from 2556 different configurations. d) Simulated scattering spectra for two perfect spheres of 22 nm in diameter for each of the experimental gaps extracted in c). The splitting of the single-particle peak visible at smaller gap sizes is a numerical artifact of the BEM mesh due to artificial charge built-up and has no physical meaning.*

2.3.2 2D-correlation

To disentangle the respective contributions of gap size and particle morphology on the optical response, we performed single-particle correlative measurements on individual dimers. Dark-field scattering spectra were acquired for six individual dimers on a

SiO_2 grid using circularly polarized light. The spectra are shown in Figure 2.6a and the corresponding STEM images of each optically measured particle in Figure 2.6b. STEM imaging of the SiO_2 was initially not possible due to charging effects. To mitigate this, the backside of the grid was coated with a conductive carbon layer. The small white spots visible in the STEM images in Figure 2.6a originate from this coating, which was not perfectly uniform.

The six measured spectra show substantial variation in BDP peak position, intensity, and linewidth with each dimer producing a distinct optical fingerprint. One of the most prominent effects is the influence of size asymmetry between the two nanospheres in a dimer. For dimers with unequal particle sizes (P1, P2, P3), the BDP resonance shows both an increase in intensity and a red-shift. We attribute both effects to size asymmetry breaking the symmetry of the charge distribution. The bonding mode is pulled toward the lower resonance energy of the larger particle, and the normally dark antibonding mode acquires a finite dipole moment, potentially contributing additional spectral weight near the BDP. This behavior is well reproduced by numerical simulations (Figure S2.1a). Using MNPBEM, we calculated the scattering spectra of two nanospheres separated by a 0.8 nm gap for symmetric and asymmetric dimers. The simulations confirmed that size asymmetry increases the BDP intensity and red-shifts its resonance position. However, even within each group of similarly sized dimers in Figure 2.6, clear spectral differences in peak position, linewidth, and intensity remain.

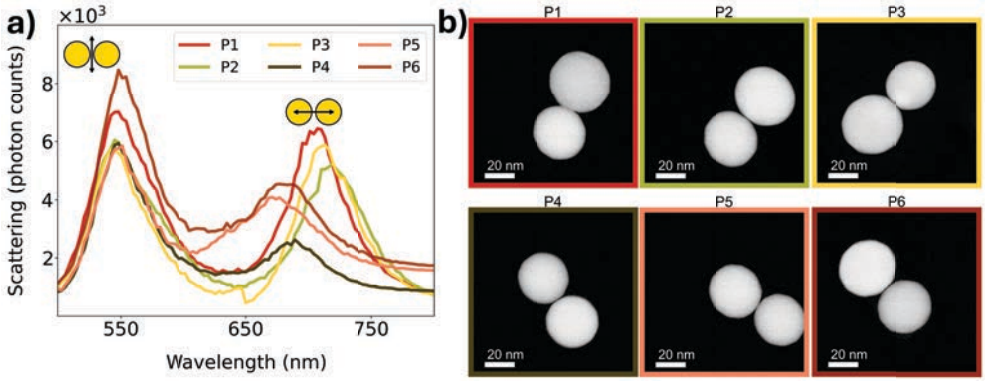

Figure 2.6: *a) Measured dark-field scattering spectra of six dimers whose STEM images are shown in b).*

2.3.3 The gap size from 2D STEM images

As a first attempt to understand whether the spectral differences between dimers can be attributed to sub-nanometer variations in gap size, we extracted particle and gap

dimensions directly from the 2D STEM images in Figure 2.6b.
The particle outlines were extracted after smoothing and binarization using Otsu thresholding, a standard binarization approach for electron microscopy images. Connected component labeling was used to identify individual nanoparticles in the resulting binary images. For each component, a circle of equal area was fitted to extract the radius. The interparticle gap was then extracted using the EEDT. However, this approach only succeeded for three of the six dimers. Only one component was found for P1, P3, and P5, indicating that the two spheres could not be separated into distinct components, likely due to high background intensity, beam-induced deformation, or very small gaps. For the remaining dimers, gaps of 0.74 nm (P2) and 0.94 nm (P4 and P6) were obtained.

These extracted geometrical parameters were then used as input for numerical simulations to test whether the observed spectral differences could be reproduced. MNPBEM simulations require defining the dielectric environment in addition to the particle morphology. We estimated the refractive index using a simplified one-parameter effective medium approximation, resulting in $n = 1.56$, as discussed in the *Appendix 2.5* in Figure S2.1b and Equation 2.1. Using the geometries extracted from the STEM images and the fitted dielectric constant as input, MNPBEM simulations were run. The results in Figure S2.2 show that the overall ordering of the BDP peak positions was reproduced. The model correctly identified which dimers scatter at higher, intermediate, and lower energies. However, it failed to capture the absolute peak positions and the exact size of the spectral shifts between dimers. This discrepancy can arise either from the approximation in treating the environment as an effective medium or from the gap sizes obtained from the 2D analysis not fully representing the true interparticle separations. If the latter is the case, it remains unclear whether this originates from limitations in the segmentation procedure or from the inherent constraints of interpreting a three-dimensional structure through two-dimensional projection imaging.

Since a STEM image is a two-dimensional projection of a three-dimensional object, the apparent gap size is expected to depend strongly on the viewing direction, in particular for the faceted particles studied here. To test this hypothesis and quantify the magnitude of projection-induced uncertainty, tilt-series measurements are needed. However, the SiO_2 grids used for the correlative measurements, which is required due to refractive index matching with the immersion oil objective, were not well suited for this purpose. Tomography was not possible on this grid due to bending of the window, resulting in shadowing from the support bars at tilt angles above 40°. Furthermore, higher-resolution imaging was not achievable. Even at very low beam currents, gold atoms became mobile, reducing the gap size and in some cases forming gold bridges.

We therefore drop-casted dimers synthesized through the same protocol onto Quantifoil copper grids, which support stable imaging at higher resolution and al-

low tilting up to ±75°. For one dimer on the Quantifoil grid, HAADF-STEM images were acquired at tilt angles from -66° to +66° in steps of 2°. The angle-dependent acquisition was repeated twice to test the stability of the dimer under the electron beam. Figure 2.7a shows two representative projections of the same dimer at -66° and 0°. In the two projections the gap morphology appears different: the first image at -66° shows a narrow and pointed gap, whereas the image at 0° reveals a broad and flat interface. Both reflect the true three-dimensional geometry of the faceted particles from different viewing angles. This immediately illustrates the fundamental limitation of 2D imaging: a single projection provides only a partial snapshot of the three-dimensional structure, and the apparent gap size is an intrinsic function of the viewing direction rather than a unique physical property of the dimer.

In addition, we found that the segmentation process adds uncertainty to the gap determination as well. To quantify both effects, gap sizes were extracted from each projection using a conventional segmentation approach based on global thresholding, in which a single intensity threshold is applied to the pixel intensity histogram to separate foreground (particles) from background. Since the threshold value depends on the chosen algorithm, we compared three widely used methods to simultaneously assess this additional source of uncertainty: the Minimum,[95] Mean,[95] and Otsu [96] methods. The latter is defined as the value that maximizes the inter-class variance in the intensity histogram. The Mean method uses the mean intensity as a threshold value, whereas the Minimum method selects the threshold value corresponding to the minimum between the peaks in the intensity histogram. An example of a pixel intensity histogram and threshold position for the three methods is shown in Figure 2.7b for the HAADF-STEM image of the gold dimer at 0°. In Figure 2.7a, the results of the three segmentation methods are overlaid on the projection STEM images. This comparison already shows that the extracted particle outlines strongly depend on the chosen method. For Otsu and Mean thresholding, the particles appear smaller than in the STEM image, whereas for the Minimum threshold they appear larger. Figure 2.7c shows the impact on the gap size quantitatively for all projection angles (from -66° to 66° in steps of 2°) and for all thresholding methods. For the same dimer, the resulting gap values extracted form the segmented images with the EEDT method explained above, vary widely, ranging from 0.5 nm to 3.5 nm.

This large spread arises because the thickness-dependent HAADF-STEM signal produces a skewed intensity distribution without a clear separation between foreground and background, making the choice of threshold inherently ambiguous as illustrated in Figure 2.7b. Additional effects such as detector shadowing and carbon contamination further modify the background, contributing to the variation between methods and between consecutive acquisitions. To illustrate the optical consequences of this uncertainty, Figure 2.7d shows simulated scattering spectra for gap sizes extracted from three representative tilt angles and the different thresholding methods.

The predicted BDP peak positions shift by over 100 nm across this range. This discrepancy exceeds the spectral differences observed between dimers in Figure 2.6a. We therefore conclude that 2D STEM images are not suitable for reliably determining the interparticle gap in these systems: both the projection geometry and the segmentation ambiguity contribute uncertainties that are too large to support quantitative morphology–optics correlations at the sub-nanometer scale. The gap extracted from 2D projections is not a physical property of the dimer, but a projection-dependent quantity.

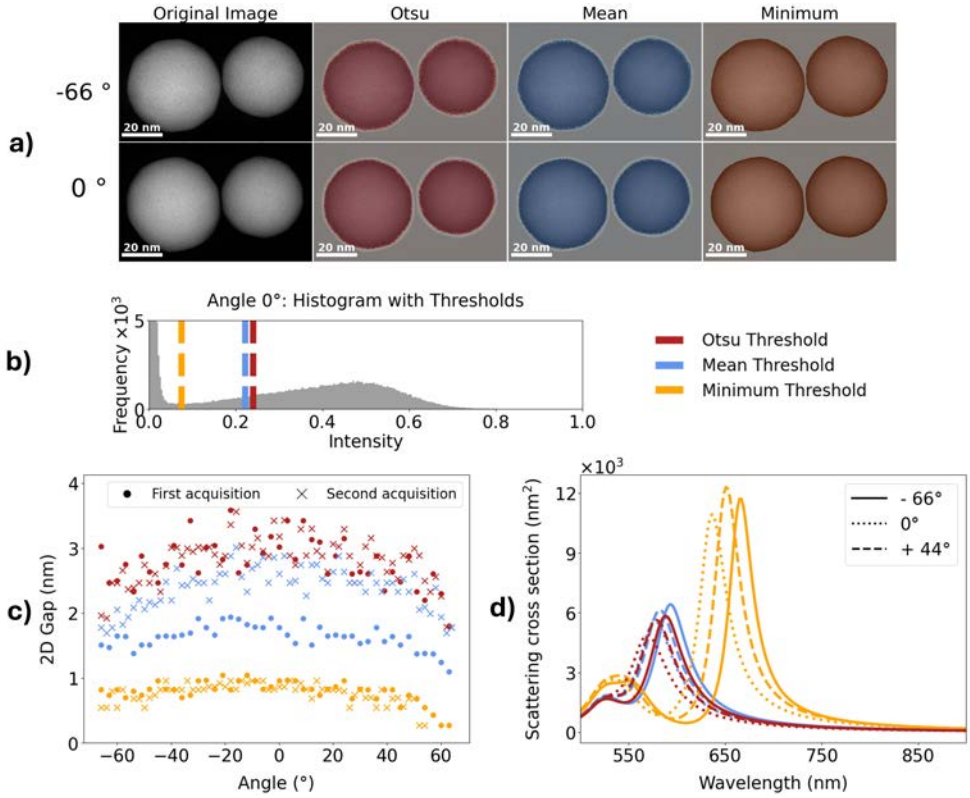

Figure 2.7: *Analysis of STEM images of two consecutive experimental tomography series of the same gold spheres dimer at tilt angles between ±66°. a) STEM images at two tilt angles, along with the corresponding binarized images overlaid: Otsu (red), Mean (blue), Minimum (yellow). b) Histogram of the STEM image at 0°, showing the threshold positions for the different binarization algorithms c) Extracted gap sizes from the binarized images for the three different threshold methods and two consecutive data acquisitions. d) Simulated scattering spectra for the 3D shapes obtained from three representative angles and the different binarization algorithms.*

2.3.4 The gap size from optical measurements

In the previous section, we highlighted the limitations of extracting gap sizes from two-dimensional STEM images. We now explore whether the gap size can be extracted from the optical spectra themselves. The goal was to determine the gap size that best reproduces the experimental spectra. Because the optical response is highly sensitive to interparticle separation, comparing simulated and measured spectra for each dimer should allow identification of the most accurate gap size.

To test this, we performed MNPBEM simulations for dimers P2, P4, and P6. The gap size was varied within ± 0.5 nm in steps of 0.05 nm around the values extracted from the STEM images in Figure 2.6b. Using the previously determined refractive index $n = 1.56$ (Figure S2.1b) and the particle morphologies extracted from the STEM images, the scattering cross-section was simulated as a function of the size of the gap in MNPBEM. Figure 2.8a shows the simulated BDP peak positions as a function gap size for the three dimers ($\triangle$). The experimentally measured peak positions, obtained by fitting a double Lorentzian, are shown as horizontal dashed lines. The corresponding gap values that best reproduce the experimental data are indicated by vertical solid lines. The shaded regions represent the interparticle gap extracted from STEM images, with uncertainties determined by the pixel size (± 0.137 nm). Each dimer is represented by a different color. Figure 2.8a shows that the best-fit values differ for each dimer and deviate from those obtained from 2D STEM approach described in the previous section. For P2, the gap decreased from 0.74 nm (STEM) to 0.54 nm (optical). For P4, it decreased from 0.94 nm to 0.74 nm. For P6, the gap decreased from 0.94 nm to 0.89 nm.

The best-fit gap values remained within the expected range of BDT junction lengths (Figure 2.5c). Since the result depends on the assumed dielectric environment of the gap medium, we next examine the sensitivity of the extracted gap size to this assumption. The simulations were thus repeated by varying the refractive index in the range $n = 1.52$ to $n = 1.60$. Figure 2.8b shows the BDP peak position as a function of gap size for dimer P4 at different refractive indices. Each refractive index is represented by a different symbol. As shown in Figure 2.8b, the extracted gap spans a wide range between 0.57 and 0.85 nm.

These results show that the extracted gap depends strongly on the assumed refractive index. Even small variations in n lead to significant shifts in the inferred gap size, demonstrating that optical gap extraction is not unique. In the previous simulations, the surrounding medium was approximated as an effective mixture of immersion oil and BDT molecules, with a refractive index estimated by matching the experimental single-particle resonance to the simulated one. However, this value is not uniquely defined and represents only an approximation of the local dielectric environment. In addition, the result depends on how the junction itself is modeled.

Treating the BDT gap as a homogeneous medium neglects its conductivity, molecular nature and possible charge transport effects such as tunneling. Different model assumptions can therefore produce similar spectra for different physical gap sizes, a problem that we explore systematically in the next section. Optical fitting thus suffers from parameter degeneracy, where comparable spectra can be obtained from different combinations of gap size, refractive index, and gap model.

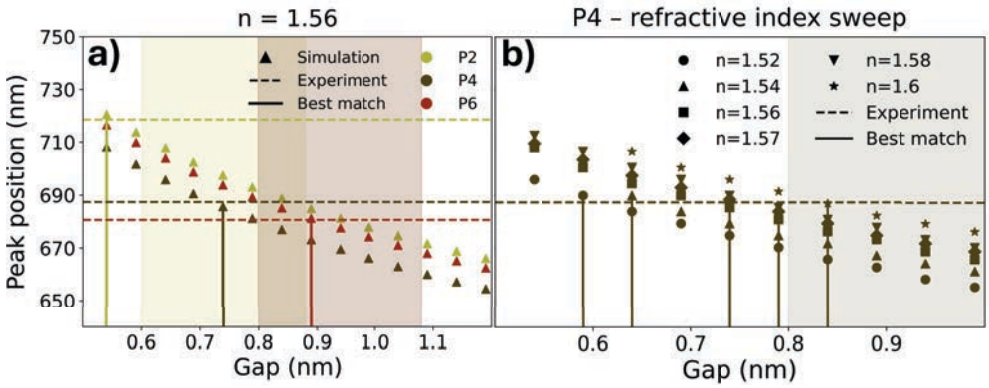

Figure 2.8: *a) BDP peak position as a function of gap size for three dimers (P2, P4, and P6) at a refractive index of* $n = 1.56$. $\triangle$ *markers represent the simulated peak positions obtained for different gap sizes. Horizontal dashed lines indicate the experimentally measured peak positions for each dimer, obtained by fitting a double Lorentzian function. The vertical lines highlight the corresponding gap value that best matches the experimental peak for each dataset. Shaded regions indicate the interparticle gap extracted from STEM images, with uncertainty determined by the pixel size* (± 0.137 *nm). The 2D STEM gap values for P4 and P6 are identical within this resolution and therefore overlap in the plot. b) Simulated BDP peak position as a function of gap size for dimer P4, shown for different refractive indices. The dashed line indicates the experimental peak position, vertical lines mark the best match gaps, and the shaded region represents the gap size extracted from the STEM image.*

2.3.5 Electromagnetic models for plasmonic nanogaps: the dielectric environment uncertainty

As discussed in the introduction of this chapter, the transport mechanism in BDT at optical frequencies remains an open question. To model the optical response of the gap region, five physical descriptions were therefore considered, ranging from a purely dielectric approximation to models incorporating charge transport and quantum effects: (a) classical dielectric, (b) quantum-corrected (QCM), (c) transport (d) conductance, and (e) conductivity. In the classical dielectric model, the gap is treated as a

non-conductive medium characterized by an effective refractive index. The quantum-corrected model (QCM) accounts for tunneling-induced screening originating from the metallic spheres. The transport model describes charge transfer through molecular tunneling across the junction, where the conductance is calculated from the molecular tunneling barrier, characterized by either the decay constant β or the barrier height ϕ. The conductance model takes a similar approach but uses a fixed conductance value $G = \alpha G$ taken directly from experimentally measured single-molecule conductance values obtained from break junction measurements. The conductivity model introduces a bulk-like finite conductivity, enabling classical current flow across the junction, the limit of highly conductive junctions where transport is no longer governed by discrete molecular channels but approaches classical ohmic behavior. For all models, the parameters are chosen consistently with the literature values for BDT molecules. Details on each model and on the parameters used to describe the BDT molecular junction are provided in the *Appendix 2.5.1.*

Electromagnetic simulations of gold nanoparticle dimers were performed using the MNPBEM toolbox [47]. The dimer geometry consisted of two gold nanospheres separated by a nanogap, modeled as a homogeneous cylinder as shown in Figure S2.3. The ribbon size is fixed by requiring that the local surface separation remains below the maximum molecular length of a BDT molecule of 1.2 nm, as inferred from the simulated data in Figure 2.5c. In reality the gap region exhibits three-dimensional spatial variation and could be more accurately described by a multilayer geometry, sometimes referred to as an 'onion-like' structure. Such an approach would also allow one to account for configurations where multiple molecular layers are present. In that case, the effective conductivity of the junction would be modified: for example, a bilayer of BDT molecules would introduce an additional tunneling barrier, resulting in a lower conductance compared to a single-molecule bridge, but still significantly higher than in the absence of molecules. However, implementing such a structure within the MNPBEM framework is not straightforward and computationally heavy. Since the goal of these simulations is to compare the qualitative spectral signatures of different junction models rather than to obtain fully quantitative predictions, approximating the gap as a homogeneous cylinder is acceptable. All models share the same effective refractive index for the surrounding medium of $n = 1.56$. In this case the spectral response is less sensitive to this value than in the purely classical case, as the junction properties dominate the optical response.

Figure 2.9 compares the simulated scattering spectra obtained using the different models for a representative dimer compared to its measured spectrum (P2 in Figure 2.6). The particle size and gap dimensions (0.74 nm) were taken from the STEM analysis in *Section 2.3.3.* For each model, the relevant parameters were systematically swept within the ranges reported in the literature for similar systems, as shown in Figure S2.4. As these parameters are not uniquely defined for molecular junctions

at optical frequencies, each model produces a range of spectral responses rather than a single prediction. The spectra shown in Figure 2.9 correspond to the best agreement between simulations and experimental data for each model, using physically reasonable parameter values for a BDT molecular junction.

Significant differences between the different models are observed, particularly in the BDP peak position, in the linewidth, and in the intensity ratio relative to the transverse mode. For the peak position, the transport, conductance, and conductivity models all provide better agreement with the experimental spectrum than both the classical dielectric model and the QCM, the latter predicting an even larger blue shift of the BDP due to tunneling-induced screening. The transport-based models tend to predict a reduced BDP intensity compared to purely dielectric descriptions. As shown in Figure S2.4 c-d, this intensity keeps decreasing as the conductance gets higher, either by increasing the value of α or by reducing the tunneling decay β. This trend appears consistent with the experimental observations, where the BDP intensity is lower than the transverse mode of isolated particles. In contrast, the classical simulations show an opposite behavior, with a very intense BDP mode. Part of the reduced intensity at longer wavelengths in the measured spectra may also be a consequence of experimental limitations. The detection efficiency of the APD is lower at higher wavelengths and the intensity calibration at the time of the measurements was not optimized. Nevertheless, similar trends were observed in complementary cathodoluminescence (CL) measurements on the same dimer systems (not shown here), indicating that the reduced BDP intensity is not only an instrumental artifact, but a real feature. The BDP linewidth also differs between models. Compared to the classical approach, all transport and conductivity based descriptions exhibit broader peaks, in closer agreement with the experimental spectra (Figure 2.9). This broadening originates from the imaginary part of the gap permittivity. In the classical model, the gap is purely dielectric and does not introduce additional dissipation to the intrinsic losses in gold. In contrast, when the gap is described by a finite conductivity, an additional imaginary component is introduced in the dielectric function. This term adds ohmic dissipation beyond the intrinsic losses in gold and results in a broader plasmon resonance.

While a quantitative determination of the transport mechanism remains out of reach due to the parameter degeneracy discussed above, the comparison between models and experiment provides qualitative insight into the nature of charge transport through the BDT junction. The failure of the classical dielectric model indicates that the molecular junction actively contributes to the optical response beyond simply filling the gap with a passive dielectric medium. The QCM compares worst to the experiment, consistent with its design for bare vacuum tunneling gaps rather than chemically bonded molecular junctions. This suggests that pure vacuum-like tunneling is not the dominant transport mechanism in Au-BDT-Au junctions at optical

frequencies. The transport and conductivity models provide the best overall agreement. ϕ and α are defined in the literature for single molecules. The number of contributing molecules N enters the total junction conductance $G_{total} = NG_{molecule}$ and it is difficult to determine unambiguously. It is likely that different but physically reasonable values could reproduce the spectra equally well.

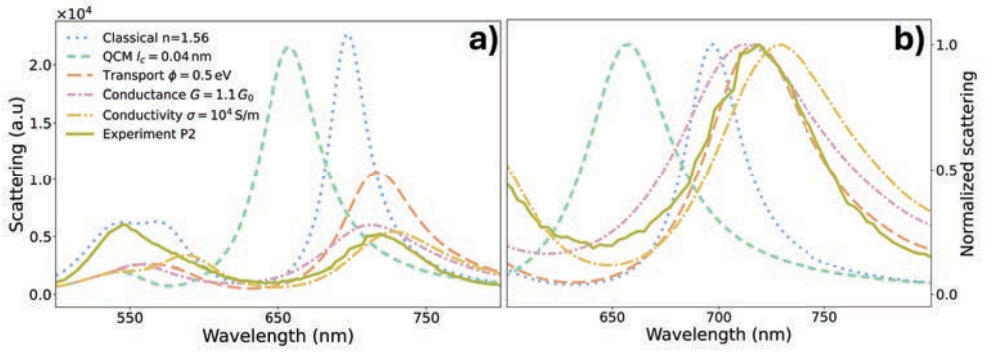

Figure 2.9: *a) Comparison between experimental and simulated scattering spectra of particle P2 for different models. The experimental spectrum (solid olive line) is compared with different modeling approaches, including the classical dielectric description (blue dotted line), quantum-corrected model (QCM, green dashed line), the transport model (orange long dashed line), the conductance model (pink dash/dot line), and the conductivity model (yellow dash/dot line). b) Normalized scattering spectra focusing on the BDP plasmon resonance region. All curves are normalized to the BDP peak above 600 nm to facilitate direct comparison.*

Taken together, the results consistently indicate that BDT mediates a finite conductance across the gap. Nevertheless, all models are capable of reproducing the general spectral shape within certain parameter ranges, as illustrated in Figure S2.4. This highlights a fundamental limitation: the optical response depends not only on the gap size, but also on the chosen physical model and the assumed parameters. Even when structural and optical measurements are performed on the same single particle, agreement between experiment and simulation does not uniquely determine either the gap size or the transport mechanism. Multiple combinations of geometry, dielectric environment, and junction model can produce indistinguishable spectra. This parameter degeneracy motivates the need for independent and more reliable structural characterization, which is addressed in the next chapter.

2.4 Conclusion

In this chapter, we performed single-particle correlative measurements combining dark-field scattering spectroscopy with 2D electron microscopy on gold nanosphere dimers linked by BDT molecular junctions. Even dimers that appeared similar in STEM images showed clear differences in their optical response, highlighting the strong sensitivity of the plasmonic behavior to sub-nanometer structural details. In particular, size asymmetry between the particles led to a red-shifted and more intense BDP mode compared to symmetric dimers, consistent with symmetry breaking in the hybridized plasmon modes. We then examined how well the interparticle gap size could be determined from two independent routes. Two-dimensional STEM images were not reliable for this purpose. Projection effects and segmentation ambiguities prevented accurate gap size determination. While a simple 2D analysis reproduced the ordering of BDP peak positions across dimers, it could not predict absolute peak positions or spectral shifts accurately. Extracting the gap size from optical spectra suffered from a related but distinct limitation. The inferred gap depended strongly on the assumed dielectric constant of the environment and model of the junction, such that different combinations of gap size, environment, and transport description produced indistinguishable spectra. Gap determination from either route is therefore fundamentally non-unique. Despite this degeneracy, the comparison between models and experiment provides qualitative insight into the nature of charge transport through the BDT junction. Models incorporating finite conductance, best reproduced both the BDP peak position and the relative intensity ratio, suggesting that BDT supports finite conductance at optical frequencies and that the junction operates in an intermediate regime between purely capacitive coupling and fully conductive behavior. The exact physical picture cannot be uniquely determined from the optical spectra alone.

Overall, these results showed that correlative measurements can reveal asymmetry, trends in optical response, and signatures of molecular transport. At the same time, they demonstrated that reliable structure–property correlations require independent and accurate determination of the gap geometry. In the next chapter, this is addressed using electron tomography, which provides direct access to the full three-dimensional structure of the nanogap and allows a more reliable determination of the gap size.

2.5 Appendix

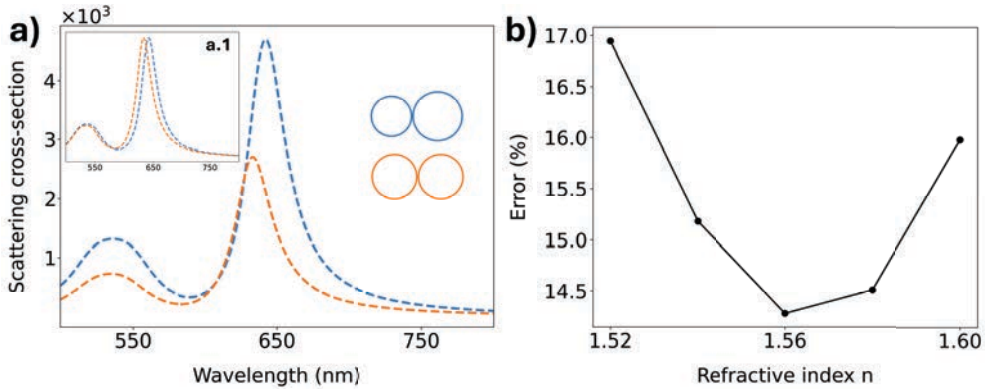

Figure S2.1: *a) Simulated scattering spectra for symmetric (orange) and asymmetric (blue) Au NS dimers. Inset a.1: normalized spectra. b) Spectral error as a function of the refractive index n. The error is calculated for the single-particle resonance between the experimental spectra in Figure 2.6 and the simulated spectra. The simulated spectra use as input the thresholded geometry from the STEM correlation in Figure S2.2b, while varying the refractive index from 1.52 to 1.6. The best-fit value of* $n = 1.56$ *is physically reasonable, consistent with an effective dielectric environment that includes contributions from both the surrounding oil medium* ($n = 1.518$) *and the BDT molecules on the nanoparticle surface* ($n = 1.5$–1.7).

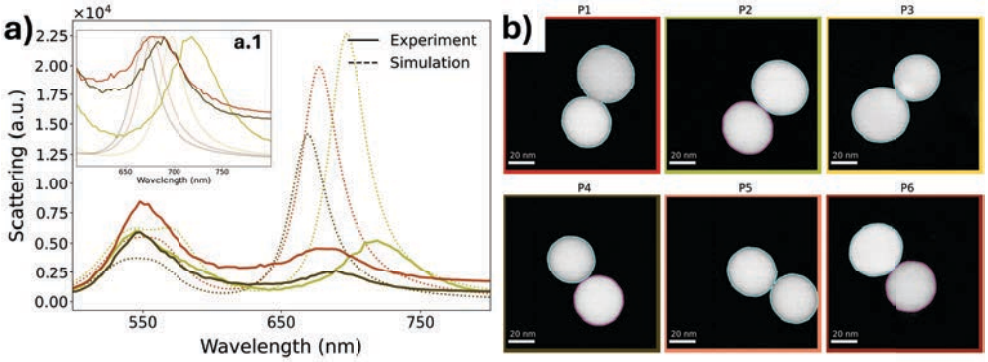

Figure S2.2: *a) Experimental (solid line) and simulated (dotted line) scattering spectra for three dimers, for which the segmentation process succeeded (P2, P4 and P6). b) Respective STEM images of each dimer. The outline of the STEM images after thresholding in shown in blue and purple overlaid on the original images.*

2.5.1 Junction models for plasmonic nanogaps

The dimer geometry used in all simulations is shown in Figure S2.3, consisting of two gold nanospheres separated by a cylindrical gap ribbon. The optical response of the gap region was modeled using five different physical descriptions, ranging from a purely dielectric approximation to models incorporating quantum effects and charge transport, as detailed below. Together these models span the range from weak tunneling, where the molecule acts as an insulating barrier, to quasi-ohmic behavior, where metallic-molecular hybridization enables efficient charge transport across the junction.

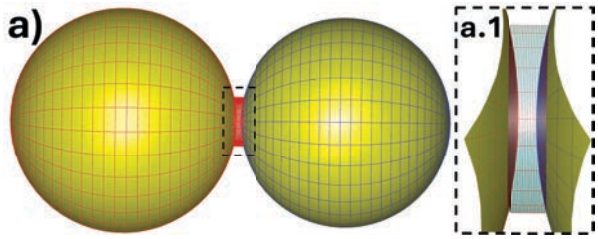

Figure S2.3: *Dimer geometry used in the MNPBEM simulations. a) Full dimer mesh. a.1) Zoom-in of the nanogap region defined as a cylinder.*

a. Classical framework with effective medium In the classical model, the system is fully described by the particle geometry and the dielectric environment. The surrounding medium is approximated by an effective refractive index, which accounts for the presence of oil, BDT, and the SiO_2 substrate. Spectra were simulated for refractive indices ranging from 1.518 (pure immersion oil) to 1.6 (pure BDT) and compared to the experimental data. The single-particle mode was used for this estimation, as it is less sensitive to morphology than the dimer mode. By minimizing the spectral error within the 500–600 nm range, the best agreement between simulation and experiment was obtained for $n = 1.56$, as shown in Figure S2.1b. This value is higher than the refractive index of the immersion oil, indicating that the local dielectric environment is modified by the presence of BDT molecules. This effective refractive index is introduced through a simple mixing model of the corresponding refractive indexes:

$$n = \sqrt{n_{\text{oil}}^2 \cdot f + n_{\text{BDT}}^2 \cdot (1 - f)} \tag{2.1}$$

where f represents the volume fraction of the surrounding medium.

b. Quantum-Corrected Model (QCM) To account for quantum-mechanical screening in sub-nanometer gaps, we employ the quantum-corrected model (QCM)

introduced by Esteban *et al.* and further developed by Hohenester *et al.* [47, 75]. The gap is described by a Drude-like dielectric function:

$$\varepsilon_{\text{gap}}(\omega) = \varepsilon_\infty - \frac{\omega_p^2}{\omega\left(\omega + i\gamma_{\text{eff}}\right)} \tag{2.2}$$

where $\varepsilon_\infty = 1$, ω_p is the gold plasma frequency, and γ_{eff} accounts for tunneling-induced damping.
The effective damping is given by:

$$\gamma_{\text{eff}} = \gamma_p \exp\left(\frac{l_{\text{eff}}}{\ell_c}\right) \tag{2.3}$$

with γ_p the bulk damping, $l_{\text{eff}} = d_{gap}/2$ the effective tunneling distance for a given gap (d_{gap}), and ℓ_c the characteristic tunneling length ($\ell_c \approx 0.04$ nm for gold). This value is defined in vacuum and may change in the presence of a medium such as oil or molecular layers. This model captures electron tunneling-induced screening. Results for varying the gap size are shown in Figure S2.4a. As expected, the onset of charge transfer emerges for gap sizes below ~ 0.5 nm where the tunneling probability is not zero.

c. Molecular transport In the presence of molecules in the gap, charge transport across the molecular junction occurs via coherent transmission through the molecular orbitals. It can be approximated by an exponentially decaying conductance G analogous to tunneling through an effective barrier. The electrons tunnel through molecular orbitals by surpassing an energy barrier defined by the molecular junctions [78, 87, 97]. Within the Simmons tunneling model [98], the single-molecule conductance is approximated as:

$$G_{molecule} = G_0 \exp(-\beta d_{gap}) \tag{2.4}$$

where $G_0 = 2e^2/h$ is the conductance quantum, and β the decay constant. A key characteristic of this transport is its exponential decay with separation distance, making it valid only at very short distances [87]. This expression describes the conductance of a single BDT molecule. In a molecular junction, however, multiple molecules can bridge the gap and act as parallel transport channels, so that the total conductance scales linearly with their number $N_{molecules}$. Due to the curvature of the nanoparticles, only molecules located near the center of the junction can bridge the gap. This region is defined by the condition that the local separation does not exceed the maximum molecular length (1.2 nm for BDT), and can be characterized by a lateral radius $\rho_{\max}$. The corresponding area, $A = \pi\rho_{\max}^2$, defines the active region for charge transport. Assuming a molecular footprint of approximately 0.25 nm^2, this leads to an estimated number of contributing molecules of $N \sim 10^2$, depending on the exact geometry.

The decay constant β can be expressed in terms of effective barrier height ϕ, using the Wentzel–Kramers–Brillouin (WKB) approximation:

$$\beta = \sqrt{\frac{2m\phi}{\hbar^2}} \tag{2.5}$$

ϕ is the energy offset between the molecular orbitals and the Fermi level of the gold electrodes in the approximation of a rectangular potential barrier. For the MNPBEM simulations, the tunneling conductance is finally converted into an effective optical conductivity:

$$\sigma_{\text{eff}} = \frac{N_{molecule} G_{molecule}\, r_{\text{eff}}}{A} \tag{2.6}$$

where r_{eff} represents the effective gap thickness of the ribbon and A its cross-sectional area. Equation 2.6 leads to the dielectric function of the cylindrical gap region defined as:

$$\varepsilon_{\text{gap}}(\omega) = \varepsilon_{\text{bg}} + \frac{i\sigma_{\text{eff}}}{\varepsilon_0 \omega} \tag{2.7}$$

This model explicitly incorporates molecular properties through β or ϕ. In Figure S2.4b, the simulated dimer scattering cross-section as a function of β and ϕ is reported. β describes how easily electrons can travel through a molecule via quantum tunneling. A decrease in the tunneling decay constant β enhances interparticle coupling, leading to a redshift of the bonding plasmon mode. Furthermore, it enhances charge delocalization across the junction, reducing charge accumulation at the gap and lowering the intensity of the bonding dipolar plasmon mode. In the highly conductive limit, where the junction approaches metallic behavior, the BDP blueshifts as charge screening across the gap increases. Typical values are $\beta \approx 0.1$–0.3 Å^{-1} for unsaturated molecules and $\beta \approx 2.9$ Å^{-1} for vacuum tunneling [73, 78, 87]. Therefore for BDT we can assume a β around $0.3\,$Å^{-1}, as used in Figure 2.9.

d. Effective conductance Alternatively, the conductance can be obtained directly from experimental measurements of single-molecule junctions. In this case, the junction can be approximated by a fixed molecular conductance within the Landauer formalism:

$$G_{molecule} = \alpha G_0 \tag{2.8}$$

This expression can be interpreted as a simplified description of the tunneling model, where α is the transmission probability. The dependence on molecular length and barrier properties is absorbed into an experimentally measured effective parameter α. The conductance of a single BDT molecule in a Au–Au junction, measured using STM break junction techniques, is typically on the order of $4 \times 10^{-4}\, G_0$ (at an applied bias of 1 V) up to $1.1 \times 10^{-2}\, G_0$ [99–101]. It depends strongly on experimental conditions, on the sulfur–gold binding configuration and the molecular orientation. A

commonly used representative value is $0.01\,G_0$ for low bias [99–101]. This corresponds to a transmission probability of approximately 0.01, meaning that only about 1% of electrons are transmitted through the junction. Assuming ~ 100 molecules contribute in parallel and a single-molecule conductance of $G_{\mathrm{BDT}} \sim 0.01\,G_0$, the total junction conductance is therefore on the order of $G \sim 1\,G_0$. However, this does not imply that the junction behaves as a fully metallic bridge. The conductance is distributed over a finite cross-sectional area, and the resulting effective conductivity remains well below that of bulk gold. As a consequence, the system does not exhibit a clear transition to a charge-transfer plasmon regime but remains in an intermediate regime where capacitive coupling still dominates and tunneling-induced screening becomes relevant. As shown in Figure S2.4c, the bonding dipolar plasmon is red-shifted and broadened with increasing in conductance, while its intensity is moderately reduced. With increasing conductance, the BDP becomes progressively screened, resulting in a blue shift. However, the conductance is not sufficient to induce a full transition to charge-transfer plasmons, and no distinct new mode appears.

e. Ohmic conductivity In the Ohmic model, the gap is described by a frequency-dependent Drude-type permittivity:

$$\varepsilon_{\mathrm{gap}}(\omega) = \varepsilon_{\mathrm{bg}} + \frac{i\sigma}{\varepsilon_0 \omega} \tag{2.9}$$

where $\varepsilon_{\mathrm{bg}}$ is the background permittivity of the gap medium ($n = 1.56$), and σ is the DC conductivity of the junction. This dielectric function is mathematically identical to that of the transport and conductance model (Equation 2.9), and the two models are therefore equivalent in their electromagnetic description, differing only in whether σ is derived from molecular parameters or treated as a free fitting parameter. This gives the conductivity model greater flexibility in reproducing experimental spectra, independently of the physical assumptions about molecular transport. The conductivity was varied from $\sigma = 10^2\,\mathrm{S\,m^{-1}}$ to $\sigma = 4.52 \times 10^7\,\mathrm{S\,m^{-1}}$, spanning the range from insulating molecular junctions to conductivities approaching bulk gold. The resulting plasmonic response is shown in Figure S2.4d. Using the estimated conductance $G \sim G_0$ determined in the Conductance model, the effective conductivity of the junction is $\sigma_{\mathrm{eff}} \approx 3 \times 10^3\,\mathrm{S/m}$, which is approximately four orders of magnitude lower than the conductivity of bulk gold ($\sim 10^7\,\mathrm{S/m}$). This places the junction well within the insulating-to-intermediate regime of the conductivity range explored in Figure S2.4d. As shown there, in this regime the BDP redshifts and broadens with increasing σ, while its intensity decreases, consistent with the trends observed in the transport and conductance models. The junction does not behave as a fully metallic bridge and therefore does not support a charge-transfer plasmon, confirming that the system remains in an intermediate regime between purely capacitive coupling and fully conductive behavior throughout the physically relevant parameter range.

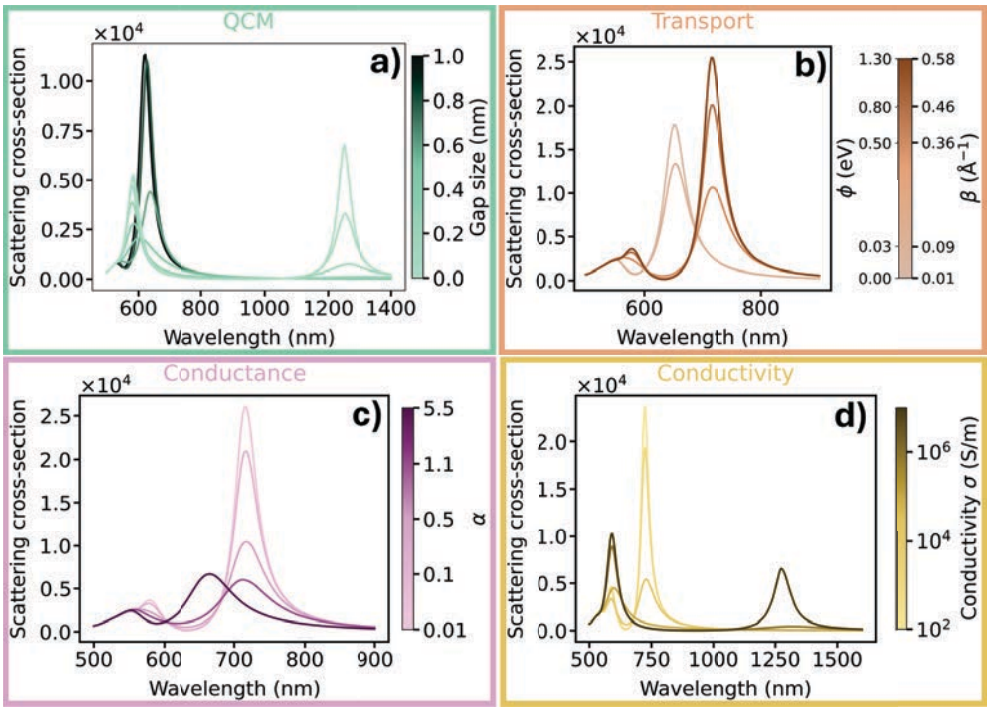

Figure S2.4: *a) Simulated scattering spectra using the QCM as a function of gap size. b) Simulated scattering spectra using the transport model as a function of the tunneling decay constant β and energy barrier ϕ. c) Simulated scattering spectra using the conductance model as a function of the transmission probability α. d) Simulated scattering spectra using the conductivity model as a function of the effective conductivity σ.*

3 Reliable determination of sub-nanometer gaps in plasmonic gold dimers

Keywords: *Tomography, nanogap size, convolution fitting, step function, plasmonic dimers*

Accurately characterizing sub-nanometer gaps in plasmonic nanoparticle dimers is essential for understanding their optical properties, particularly in the transition from classical to quantum plasmonic behavior. While two-dimensional (S)TEM imaging provides high spatial resolution, it lacks the three-dimensional morphological information needed to reliably extract gap sizes. In this work, we combine electron tomography with a robust data analysis workflow to quantify interparticle gaps in gold nanosphere dimers with sub-nanometer precision. We show that gap size estimates are highly sensitive to reconstruction algorithms, segmentation thresholds, and meshing parameters. To overcome this, we introduce a model-fitting approach based on convolving a step function with a Gaussian function, enabling consistent and accurate gap measurements even in the absence of a known ground truth. Validation on simulated datasets confirms pixel-level accuracy, and application to experimental data demonstrates the method's robustness and general applicability. The resulting 3D reconstructions are directly integrated into electromagnetic simulations, allowing reliable interpretation of the dimer's optical response. Finally, we show that the 3D reconstruction can be used as ground truth to improve gap estimation from 2D imaging. This workflow offers a broadly applicable strategy for correlating morphology and optical function in plasmonic systems and provides a crucial step toward resolving quantum effects in nanoscale light–matter interactions.

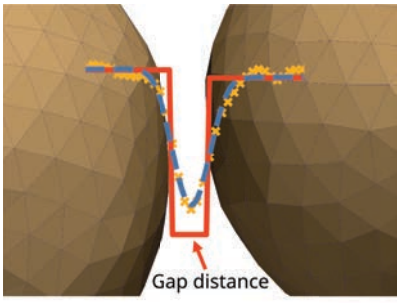

3.1 Introduction

Plasmonic nanoparticle dimers bridged by molecular junctions are powerful platforms for studying molecular electronic properties and quantum plasmonic phenomena at optical frequencies. As demonstrated in the previous chapter, the optical response encodes information about the molecular junction and the interparticle gap. However, extracting quantitative information is fundamentally limited by parameter degeneracy. Different combinations of gap size, dielectric environment, and transport model produce indistinguishable spectral responses. Independent and accurate knowledge of the gap geometry is therefore essential to disentangle these contributions. Two-dimensional high-angle annular dark-field scanning transmission electron microscopy (HAADF-STEM) imaging is an intuitive first approach to gap size determination. However, it is fundamentally limited for sub-nanometer gaps, as demonstrated in *Chapter 2*. As a projection technique, 2D STEM collapses the full three-dimensional gap geometry onto a single image, making the measured gap strongly dependent on the projection angle and the orientation of the dimer on the substrate. Moreover, because HAADF-STEM signal scales with the projected sample thickness, spherical nanoparticles produce a gradual intensity gradient toward their edges rather than a sharp boundary, causing a smooth overlap between the particle and background distributions in the intensity histogram. As recently shown for metallic nanostructures [48], this makes global thresholding systematically unreliable for accurate morphology extraction. This is particularly critical for sub-nanometer gaps where the gap signal overlaps with the tails of both particle intensity distributions. As a result, while 2D imaging can reveal trends, it cannot provide the absolute gap values required for quantitative structure–property correlations.

To overcome these intrinsic limitations of 2D projection imaging, we turn to electron tomography (ET). In ET, a tilt series of HAADF-STEM images is acquired by rotating the sample over a range of angles. The full 3D volume is reconstructed from these projections, providing direct access to the three-dimensional morphology of the dimer. However, while ET resolves the missing depth information of 2D imaging, it introduces a new set of challenges that are particularly critical for sub-nanometer gaps. First, the limited tilt range achievable in a TEM, typically less than $\pm 80°$ due to mechanical constraints, leaves an angular region unsampled, known as the missing wedge. This introduces elongation and blurring artifacts in the reconstruction direction perpendicular to the sample support plane. Second, the reconstruction quality depends strongly on the chosen algorithm and regularization parameters. Third, segmentation of the reconstructed volume remains sensitive to noise and data processing steps such as smoothing. Finally, converting the segmented volume into a surface mesh for electromagnetic simulations can further distort the gap region with mesh simplification being a critical step in the process. Because the optical response of

plasmonic dimers is highly sensitive to gap size differences of 0.1 nm or less, all of these uncertainties become critical and must be carefully understood and quantified to enable quantitative structure–property correlations.

In this chapter, we address these issues by developing a robust strategy for accurately determining interparticle gap sizes from 3D ET reconstructions. We introduce a model based on the convolution of a step function with a Gaussian blur kernel along the gap. This approach allows the gap size to be extracted with pixel-level accuracy from the step function, independently of the reconstruction algorithm or smoothing parameters. We first validate the method using simulated HAADF-STEM tilt series with known ground truth, and then we apply it to experimental Au–BDT–Au dimers. We show how the extracted gap size can be used to adjust the segmentation threshold and surface meshing, ensuring that the 3D geometry supplied to electromagnetic simulations faithfully represents the physical system. Finally, we transfer the 3D insights to 2D images. By using the gap size from tomography as ground truth, we determine the Otsu threshold fraction that reproduces the same gap in the 2D image. This workflow enables reliable structure–property correlations for plasmonic dimers with sub-nanometer gaps and provides a critical step toward distinguishing classical, quantum-corrected, and charge-transfer regimes in their optical response.

3.2 Methodology

3.2.1 Nanodimers colloidal assembly

The dimers were synthesized following the optimized protocol from *Chapter 2*, *Section 2.3.1*

3.2.2 Electron tomography

High Angle Annular Dark Field Scanning Transmission Electron Microscopy (HAADF-STEM) and Electron Tomography were performed using an aberration-corrected Thermo Fisher Scientific Titan microscope, operated at 300 kV with a screen current of 42 pA. Images were acquired with a Fischione M3000 HAADF detector using a convergence semi-angle of 19.4 mrad and collection angles ranging from approximately 83 to 200 mrad. A camera length of 115 mm, magnification of 640000 x and pixel size of 137 pm were used. Images were acquired with a dwell time of 3 µs and a frame time of 4 s. For the electron tomography experiments, images were acquired with alpha tilts from ±75° with 2° steps. The electron beam was blanked in between successive acquisitions. The acquisition time for a full tomographic tilt series was approximately 30 minutes. Subsequently, another tilt series (from ±75 ° with 2° steps) for the same particle was acquired to investigate the stability over time and

upon illumination by the electron beam. HAADF-STEM images before and after the acquisition of the tilt series were compared to evaluate possible damage caused by the electron beam [102, 103].

3.2.3 Reconstruction of tomography data

As previously introduced, the 2D projections serve as input for reconstruction algorithms to retrieve the 3D shape. The acquired 2D projection images were first aligned using a cross-correlation-based algorithm. After alignment the background was removed by subtracting the median of the intensity histogram, followed by detector shadowing and cupping artifact correction. The cupping correction utilizes an algorithm based on *Van Den Broek et al.* [104]. The corrected projections then serve as input for the reconstruction algorithms. In this work, two reconstruction algorithms were investigated: Total Variation Minimization (TVM) and Expectation Maximization (EM) algorithm. EM reconstructions were based on the implementation included in the Astra Toolbox [105] and we used 15 iterations to avoid overfitting to noise [48]. TVM reconstructions were performed using the Chambolle-Pock algorithm with isotropic TV regularization, a non-negativity constraint and L2 data-error norm [106]. The algorithm was implemented based on GPU-accelerated primitives from Astra Toolbox [105] and PyTorch [107]. For these TVM reconstructions, the number of iterations was set to 1000, and the TV regularization weight was set to 3e-4. These parameters were optimized based on simulated reconstructions.

3.2.4 Simulation of STEM projections

To test our gap determination workflow, we simulated 2D HAADF-STEM projection images of a gold dimer system with a known gap size. To ensure that our simulated images closely resembled experimental STEM data, we accounted for inherent noise and imaging artifacts commonly present in electron microscopy. Key sources of artifacts include Gaussian blurring caused by de-focus and astigmatism, as well as Poisson noise, which arises due to the discrete nature of electron detection. Additionally, background signal contributions from the sample support were incorporated to create realistic STEM image simulations. The simulation flow is summarized in the scheme in Figure S3.1a. The simulated STEM images were generated by forward projecting (a.2) a voxelized model of two gold nanoparticles (a.1), each with a diameter of 50 nm and varying the gap distances, using the ASTRA toolbox (version 2.1.0) [105]. Gaussian blurring was applied to each projection using a Gaussian filter. Background signal levels were estimated from experimental data by analyzing the mean intensity of the sample support in HAADF-STEM images. This background was then added to the simulated projections. Finally, Poisson noise was introduced. The variance of the noise was manually optimized to match the noise level of experimental images. To

validate the accuracy of the noise modeling in our simulated data, we compared line profiles from both simulated and experimental projections. As illustrated in Figure S3.1b, both line profiles show strong qualitative agreement, confirming the fidelity of the simulations. The small deviation arises because the simulation does not include the cupping artifacts present in the 2D experimental images. However, these artifacts are corrected during reconstruction, therefore they do not represent a problem. Similarly, the histograms of the 3D reconstruction, shown in Figure S3.1c, display the same distribution. The differences in intensity are merely a matter of normalization.

In this manner, we simulated HAADF-STEM projection images of different dimer configurations: 1) using perfect spheres with a radius of 23 nm and gap varying between 1.09 nm and 0.55 nm; 2) a dimer with one sphere of 23 nm and the other of 30 nm in radius and a gap size of 0.82 nm; 3) a dimer based on the voxelized experimental structure to account for asymmetric and not perfectly spherical particles with a gap of 0.68 nm. The somewhat arbitrary gap values chosen above resulted from the finite pixel size, for which we chose the same value as in the experiment (0.14 nm).

In this study, advanced TEM simulation methods, such as the multislice approach, were not employed as our focus was not on atomic resolution imaging or quantitative image intensities.

3.2.5 Surface meshing of tomography data

We followed the workflow of *Dieperink et al.* to generate a surface mesh from experimental and simulated ET data [48]. Before segmentation, a Gaussian filter was applied to smooth the reconstruction. The degree of smoothing in terms of pixels, denoted by σ_{sm}, is provided throughout the text and varied from $\sigma_{sm} = 0$ (no smoothing) to $\sigma_{sm} = 4$. The smoothed reconstructions were then segmented using either Otsu's method or a fraction of the Otsu threshold value. Afterwards, the voxelized structure was converted into a surface mesh using the Marching Cubes algorithm implemented in the scikit-image library [108, 109]. Then, to ensure a realistic computing time for electromagnetic simulations, the mesh needed to be simplified. We realized that the method used for mesh simplification made a critical difference for the reliability of the BEM simulations. For the dimers with sub-nm gaps, we found that the Approximate Centroidal Voronoi Diagram (ACVD) algorithm performed best for mesh simplification. This method performs re-meshing via Voronoi clustering, producing a more uniform distribution of triangles across the surface compared to other methods, such as the Fast Simplification algorithm, at the expense of potentially smoothing surface features. We applied this algorithm via the pyacvd module based on the work by *S. Valette et al.* [110]. We believe that this method works particularly well for the dimer case, as it favors uniform meshing. This is important to prevent numerical artifacts arising from elongated mesh elements, which are common in boundary

and finite-element method simulations. This is particularly important for the gap region, where only a few mesh elements significantly contribute to the overall optical response.

To demonstrate the difference in mesh simplification, we compare the quality of the meshes obtained using ACVD and the fast simplification algorithm for a simulated dimer in Figure S3.2a-b, where the gap size after meshing as a function of segmentation threshold is shown. The meshing procedure was tested on the voxelized structure used as input for the STEM simulation as explained in the previous paragraph and on an experimental data. It can be noticed that the gap size after meshing as a function of segmentation threshold changed more smoothly for the ACVD method compared to the Fast Simplification method, both for the simulated (Figure S3.2a) and experimental data (Figure S3.2b). This suggests that the fast simplification method introduces numerical inaccuracies due to a less homogeneous mesh. Therefore, we believe that the ACVD mesh simplification is a more reliable method for the gold dimers and for the rest of this work we consistently use ACVD for mesh re-sampling. The target number of faces was set to 6000.

3.2.6 BEM optical simulations

The MATLAB MNPBEM toolbox was used to simulate the optical properties of gold dimers [47]. This method solves Maxwell's equations for objects with homogeneous and isotropic dielectric properties separated by sharp interfaces. In this method, only surfaces of the objects need to be discretized, which leads to comparatively high convergence with low computational cost [48]. The inputs required for these simulations include the dielectric environment and the object's exact morphology in the form of a surface mesh. Here the key parameters are the size and shape of the gold nanoparticles and the gap size between them. The dielectric constant of gold was taken from McPeak [92]. For the surrounding medium a constant refractive index of 1.334 was set, corresponding to water immersion oil. The dimers were excited with a plane wave with circularly polarized light propagating in the z-direction. All scattering plots shown are the average of the scattering from left- and right-circular polarization. A full (retarded) Maxwell's equations solver was used.

3.2.7 Convolution fit

To retrieve the gap size from the reconstructed data set, we fitted a convolution of a Gaussian function and a step function to the extracted line profile. Physically, this model assumes that the true gap has a sharp boundary, which can be described by a step function, while imaging and reconstruction effects introduce a Gaussian-like blurring. Equation 3.1 and Equation 3.2 describe the Gaussian function and the step function, respectively, while Equation 3.3 represents their convolution. In Eq. 3.1, A

is the peak height of the Gaussian function, μ is the mean or center of the Gaussian distribution, representing the location of the peak. σ_{fit} is the standard deviation of the Gaussian function, controlling its width. A larger σ_{fit} corresponds to a wider Gaussian, which in our case is related to both the applied smoothing σ_{sm} and the experimental noise. Naturally, $\sigma_{fit} > \sigma_{sm}$ as shown in Figure S3.3a . In the step function equation, Eq. 3.2, the parameters are the following. I_{HL} is the intensity on the left side of the gap before the step position. I_L is the intensity between the step positions, in the gap area. I_{HR} is the intensity on the right side of the gap, after the step position. x_L^0 and x_R^0 are the positions where the step changes from one intensity to another and, therefore, the difference between them represents the gap size. Finally, the result of the convolution at position x represents the combined effect of the step and Gaussian functions.

The Gaussian was centered on the step function to ensure symmetric convolution around the transition point and avoid skewing from zero-padding. To improve fit quality, the experimental data were interpolated and resampled to match the number of points in the Gaussian. The fitting process was then carried out using linear least squares minimization for σ, I_{HL}, I_{HR}, I_L. The positions of the left and right steps were optimized using grid search, where the step function was shifted pixel by pixel across the data and for each shift a fit was performed. The fit with the lowest error was selected. To improve convergence, initial parameters estimates were obtained by independently fitting two logistic functions to either side of the gap, as shown in Figure S3.4c. The inflection points of these logistic functions provided an estimate of the gap's position, while the maximum and minimum on each side were used to estimate I_{HL}, I_{HR}, andI_L. A logistic function was chosen, as it is a sigmoid function with a qualitative behavior similar to the convolution of a Gaussian and a step function. This similarity allows it to provide a good initial guess for the subsequent fitting step. Details of the initial parameters, together with the constraints on their lower and upper boundaries used for the convolution fitting, are summarized in Table S3.1 of the *Appendix 3.5*.

$$G(x) = A \cdot \frac{1}{\sqrt{2\pi} \cdot \sigma_{\text{fit}}} \cdot e^{-\frac{(x-\mu)^2}{2\sigma_{\text{fit}}^2}} \tag{3.1}$$

$$S(x) = \begin{cases} I_{HL} & \text{if } x \leq x_L^0 \\ I_L & \text{if } x_L^0 < x < x_R^0 \\ I_{HR} & \text{if } x \geq x_R^0 \end{cases} \tag{3.2}$$

$$(S * G)(x) = \int_{-\infty}^{\infty} S(t) \cdot G(x-t)\, dt \tag{3.3}$$

3.3 Results and discussion

In the following, we first analyze the experimental 3D reconstructions using conventional segmentation methods based on Otsu thresholding, highlighting the associated limitations and uncertainties in gap size determination. We then develop and validate a convolution-based fitting approach using simulated datasets with known ground truth. Finally, we apply this method to the experimental data to extract reliable gap sizes and use these results to correlate the dimer morphology with its optical response.

3.3.1 3D experimental data

The aim of this chapter is to establish a workflow for determining the size of a sub-nanometer gap between two (plasmonic) nanoparticles with high accuracy, ideally on the order of the chosen pixel size, to be able to simulate the optical properties of this dimer as precisely as possible. To this end, we use the tilt series presented in Figure 2.7 to reconstruct the three-dimensional morphology of the dimer. In *Chapter 2*, this dataset was used to demonstrate the strong dependence of the apparent gap size on segmentation method and projection angle. Here, we instead perform a full electron tomography reconstruction, providing direct access to the true 3D gap geometry. As a first outcome of this reconstruction, the separation between foreground and background voxels is significantly improved compered to the 2D case (Figure S3.1c). A voxel represents the three-dimensional equivalent of a pixel. Additionally, we confirmed that the Au nanoparticles did not change or move relative to each other under electron beam illumination by acquiring two consecutive tilt series per dimer (Figure S3.5).

Although tomography improves the segmentation process, extracting an accurate dimer gap size from the 3D dataset remains non-trivial. A key factor in this process is the choice of reconstruction method. We have recently shown that for the reconstruction of metal nanoparticles [48], Total Variation Minimization (TVM) outperformed other common methods, such as the Expectation Maximization (EM) algorithm. TVM performs well for isolated nanoparticles because it incorporates prior knowledge about object smoothness. In contrast, EM does not rely on prior knowledge of the object, but instead models the noise statistics, making it particularly suitable for Poisson-distributed data such as STEM images. We compared both reconstruction algorithms for the present dimer system (*Section 3.2.3*). Slices through the reconstructions are shown in Figure 3.1a, with corresponding 3D visualizations in Figure 3.1b. As expected, TVM better preserves particle shape along the missing wedge direction. However, it also tends to partially fill the gap region. In contrast,

EM preserves the gap, but is more strongly affected by missing-wedge artifacts. This difference is clearly visible in the line profiles shown in Figure 3.1a.3 and a.4.

To extract the size of the gap from these reconstructions, they were segmented using the Otsu threshold method, which we found to be the most robust for ET reconstructions [48]. We anticipated that the gap size is significantly influenced by the noise in the reconstruction, which propagates into the segmentation. Given that the pixel size in the HAADF-STEM images, and consequently the voxel size in the reconstruction, was 0.14 nm, a 1 pixel difference due to noise artificially alters the gap size. Therefore, the data were smoothed using a Gaussian filter after reconstruction to reduce the local noise. Gap sizes were extracted from the segmented reconstructions by applying the Exact Euclidean Distance Transform (EEDT), as described in *Chapter 2*, but extended to three dimensions. The results are presented in Figure 3.1c, showing the gap size as a function of the standard deviation applied for the Gaussian filter (σ_{sm}). When no data point is displayed for a particular σ_{sm}, it indicates that the segmentation resulted in the connection of the two spheres, and no gap could be identified.

In Figure 3.1c, the spread in gap size is reduced compared to 2D analysis, but the extracted values still depend on the degree of smoothing. For TVM reconstructions (purple), the gap size decreases with increasing smoothing. This is expected, as TVM produces elevated voxel intensities in the gap region, enhancing the apparent connection between the particles. Additional smoothing further reduces the gap. In contrast, the EM reconstructions exhibit a non-monotonic ("volcano") behavior. Without smoothing, the gap size is underestimated due to noise and misclassified voxels. Moderate smoothing reduces this effect, leading to an increase in the measured gap. However, for stronger smoothing, blurring dominates and the gap decreases again.

Ultimately, to link a specific geometry of the dimer system to optical measurements, electromagnetic simulations of the optical properties need to be performed. The BEM method requires a surface mesh of the 3D system as an input. This can be done in two manners: 1) approximation through a model system using perfect spheres and 2) direct surface mesh generation from the input tomography data. The first approach involves using the extracted gap size (Figure 3.1c) and the radius obtained by fitting two spheres to the voxelized data. Although it is simpler and computationally efficient, this method does not capture deviations in particle morphology. The nanoparticles are rarely perfect spheres and, in our case, surface facets can indeed be seen (Figure 3.1a). The non-spherical geometry also led to artifacts when approximating the sphere diameter and sometimes to overlapping spheres for small gap sizes. Therefore, we recommend the second approach, which involves creating a surface mesh directly from the 3D tomographic reconstruction. Although it is significantly more challenging, this approach is more accurate, as it incorporates the actual morphology

of the investigated nanoparticles. We followed the workflow of *Dieperink et al.* [48]. First, we smoothed the reconstruction. Related to the discussion surrounding Figure 3.1c, we compared $\sigma_{sm} = 1$ and $\sigma_{sm} = 2$. Then we segmented itusing the Otsu method for thresholding. The segmented data were then transformed into a surface mesh with a low enough number of faces to actually be able to perform the BEM simulations in a reasonable time. To achieve this, a combination of the marching cube and ACVD mesh simplification algorithm was used as detailed in *Section 3.2.5* [48].

In Figure 3.1d, simulated scattering spectra are shown using as input the mesh structures obtained from EM and TVM reconstructions after applying Gaussian smoothing with $\sigma_{sm} = 1$ and $\sigma_{sm} = 2$. Although the spread is reduced compared to the 2D case, noticeable differences between the spectra obtained from different reconstruction methods and smoothing conditions remain. We attribute these variations to three main factors: (1) differences in the extracted gap size after segmentation, (2) modifications introduced during mesh simplification, and (3) deviations in the reconstructed particle morphology. For $\sigma_{sm} = 1$, the gap size differs by approximately 0.3 nm between the TVM and EM reconstructions (Figure 3.1c). Since an increasing gap size leads to a blue-shift, as expected the spectrum obtained from the TVM reconstruction is blue-shifted compared to EM. However, the magnitude of this shift is smaller than expected for such a gap difference, indicating that factors (2) and (3) also play a role. For $\sigma_{sm} = 2$, this becomes even more evident: although the gap sizes after segmentation are identical, the simulated spectra still differ. This demonstrates that mesh simplification and morphological differences significantly affect the optical response.

It is important to note that mesh simplification unavoidably introduced small deviations in the morphology of the dimer. Since the scattering response of dimers is highly sensitive to sub-nanometer variations in the gap size, these morphological differences can significantly impact the final results. To better understand the influence of mesh simplification, we extracted the gap sizes at the two different stages of the pipeline: after segmentation (in voxel space) and after mesh simplification (Figure S3.6a). We observed that mesh simplification led to a slightly smaller gap for the TVM reconstructions, whereas the gap for the EM reconstructions increased. This effect reduced the difference in apparent gap size for $\sigma_{sm} = 1$, explaining the unexpectedly small spectral difference in Figure 3.1d. For $\sigma_{sm} = 2$, meshing resulted in a smaller gap of the TVM reconstruction, supporting the observed redshift compared to the EM reconstruction. It is important to note that the quality of the mesh after mesh simplification played a critical role in achieving reliable electromagnetic simulations as detailed in the *Section 3.2.5*. Due to the small features in the gap region that dominate the optical response for these dimers, it is important to avoid distortions and significant size differences in the mesh faces.

Next to differences in gap size, changes in morphology can also contribute to the observed differences in the simulated scattering spectra (factor 3). Electron tomography is well known to suffer from the so-called missing wedge artifact. This artifact stems from the physical constraint in the pole piece gap of an objective lens, which limits the tilt range of holders. For an ideal reconstruction, a tilt range of ±90° would be required, which is not achievable in practice. The missing angular information results in blurring and lemon-shaped artifacts perpendicular to the sample support plane. This can be clearly seen in the xz-slices through the reconstruction shown in Figure 3.1a. The effect is more drastic for the EM reconstruction because the prior knowledge used in TVM helps to suppress these artifacts effectively. The overlay of both reconstructions after meshing in Figure 3.1b clearly shows a pronounced elongation in the z direction for the EM reconstruction (salmon). This also resulted in a slightly larger volume of the EM reconstructions compared to the TVM ones (Figure S3.6b). Finally, to investigate how the elongation caused by the missing wedge influences the simulated optical properties, scattering spectra were simulated for different gap sizes and varying ellipticities of the particles (Figure S3.6c). We observed that the missing wedge effect, manifesting itself as an elongation along the z direction, would lead to a small red-shift of the gap plasmon resonance. These results suggest that factor 3) influenced the simulated scattering spectra the least compared to factors 1) and 2).

Together, all three factors explain the differences in the simulated scattering spectra. Figure 3.1, therefore, demonstrates that only a good combination of smoothing and segmentation results in the correct size of the gap and accurate simulated scattering spectra. However, for experimental data, these parameters are unknown. Rather than relying on a specific combination of smoothing and segmentation parameters, it is desirable to apply a method that can determine the gap size independently of these processing choices. If the gap can be reliably determined, then the segmentation and meshing can be adjusted to ensure the determined gap size is preserved. In the following, we propose a procedure to precisely determine the interparticle gap, allowing us to minimize these uncertainties for the experimental data.

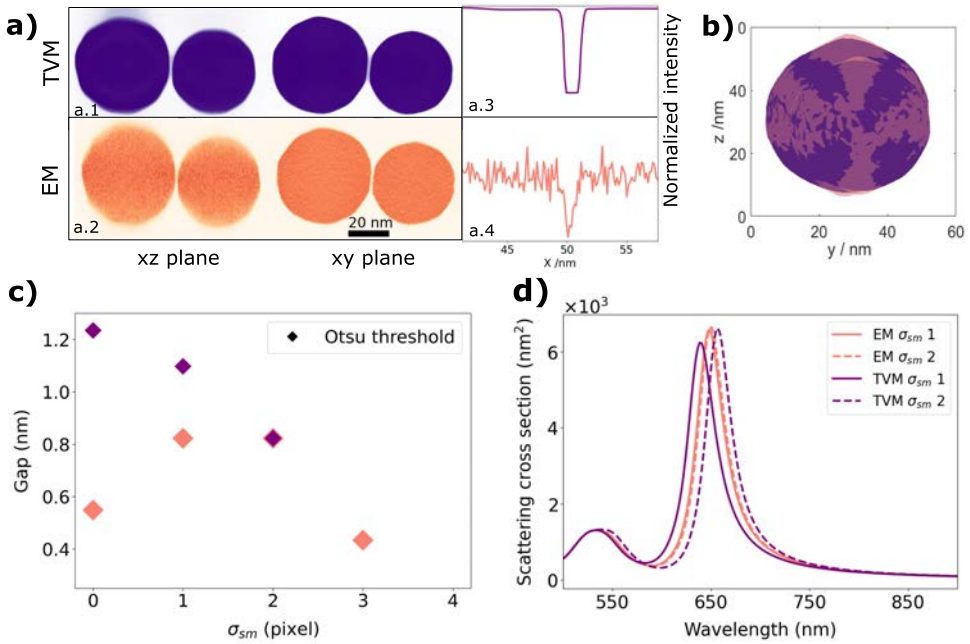

Figure 3.1: *Analysis of experimental electron tomography data obtained from the same gold dimer as shown in Figure 2.7. a) Slices along the xz plane and xy plane of 3D reconstructions obtained by TVM (purple) (a.1) and EM (salmon) (a.2) algorithms. Corresponding line profiles along the gap in the x direction are shown for the TVM and EM reconstructions in a.3 and a.4, respectively. b) The BEM mesh input is visualized across the yz plane, with meshes obtained from the EM (salmon) and TVM (purple) reconstructions overlaid in a semi-transparent manner. c) The extracted gap from each reconstruction is shown. The gap is defined as the smallest Euclidean distance between the two particles after binarizing the data using Otsu's thresholding method. The reconstructions were smoothed with different values of σ_{sm} before segmentation. d) Simulated scattering spectra using as input the mesh obtained from EM and TVM reconstruction smoothed with $\sigma_{sm} = 1$ and $\sigma_{sm} = 2$.*

3.3.2 Simulated data and convolution method

The challenge in evaluating the experimental data presented in Figure 2.7 and Figure 3.1 is that the exact size of the gap is unknown. To address this issue, we simulated electron tomography data for dimers of gold nanoparticles with known varying interparticle gap sizes. Details about the procedure of these simulations are given in *Section 3.2.4*. The same workflow as for the experimental series was used to reconstruct the 3D morphology from the simulated tilt series. In the previous section, it

became evident that the choice of data processing pipeline strongly affects the final gap size estimation, even when using electron tomography. To overcome this limitation, we developed a robust model to retrieve the gap size through fitting of the ET data. Fitting provides an effective way to extract quantitative information, as it incorporates knowledge about the physical system.

In our approach, line profiles were extracted along the gap direction from the central slice of the reconstruction. We then fitted the line profiles on the basis of the following assumptions. In a 3D reconstruction, the intensity is not a function of thickness, in contrast to 2D HAADF-STEM images. Therefore, in the ideal case without noise or imaging artifacts, the gap would appear as a perfect step function. In practice, however, 3D reconstructions are affected by microscope aberrations and image misalignment, whose combined effect can be approximated by a Gaussian-shaped point spread function [111]. Based on this, we fit the line profile along the gap using a convolution of a step function and a Gaussian blur kernel, allowing the gap size to be extracted from the step function component. The underlying workflow is described in the following.

The first step in the workflow was to find the center slice through the reconstruction, which was done for the binarized data and then applied to the non-binarized data (before segmentation). Thereby, we ensured that the fitting was performed along the smallest gap distance. The position of the line profile was identified using the EEDT applied to the binarized data, which determines the z- and y-coordinates of the closest pixels. From these positions, line profiles were extracted along the x-direction of the reconstruction before segmentation. The x-direction corresponds to the gap direction. To account for local variations in the gap region, the position of the line profile was shifted within a range of ± 3 pixels in each direction around the smallest distance between the two closest pixels (Figure S3.4a). We note that this approach may lead to inaccuracies if the gap is not aligned along a principal axis, for example in systems with strong asymmetry or uneven substrates. However, for the systems studied here, the gap direction was consistently aligned along the x-axis, and the method can be extended to arbitrary orientations if needed. In the next step, the averaged line profile (Figure S3.4b) was fitted with the convolution model. To account for noise-induced asymmetries, the step function was allowed to have different intensity levels on either side of the gap. To improve convergence, initial parameters were estimated by independently fitting two logistic functions to the left and right sides of the gap (Figure S3.4c). The fitting itself was performed using least-squares minimization; details are provided in *Section 3.2.7*.

Tilt series of HAADF-STEM data were simulated for different dimer configurations including realistic experimental noise to test this workflow. The first system consisted of two perfect spheres (Figure S3.7), each with a radius of 23 nm, and a gap size varying between 1.09 nm (a.1) and 0.55 nm (a.3). The second configuration was

a dimer with one sphere of 23 nm radius and the other of 30 nm radius, separated by a gap of 0.82 nm (a.2). These initial tests demonstrated that our fitting procedure could reliably reproduce the size of the gap with one pixel accuracy, regardless of the smoothing strength of the reconstructions or whether they were equally and non-equally-sized particles (Figure S3.7). The fit results clearly produced more accurate estimates than the classic Otsu segmentation, which completely failed for very small gap sizes (Figure S3.7c.3) as well as for $\sigma_{sm} = 0$ and $\sigma_{sm} > 3$.

Since experimental systems are rarely perfectly spherical, we further tested the method on a more realistic geometry. For this, we used the segmented 3D structure based on experimental results as the ground truth and simulated an HAADF-STEM tilt series. The initially segmented gap size of the voxelized structure, which was 0.68 nm for this specific reconstruction, served as the reference. We already know that this is not the accurate gap size of the experimental data, but only serves here as a known ground truth to test our fitting approach on a more realistic structure. Similarly to Figure 3.1, we applied different reconstruction algorithms and smoothing strengths σ_{sm} to the reconstructed data set before fitting. In Figure 3.2a, the averaged line profile through the closest pixel of the EM reconstruction for this generated ground truth is shown, along with the fitted function for σ_{sm}=0 (no additional smoothing). The fit results for σ_{sm}=1 for the TVM and EM reconstructions are displayed in Figure 3.2b and 3.2c, respectively. Figure 3.2d shows the extracted gap size from each fit. Unlike the results obtained without fitting (Figure 3.1), the fitted gap size is insensitive to additional data pre-processing. Moreover, for every σ_{sm} we could extract the expected gap size (straight blue line) within the accuracy of $\pm$ 1 pixel ($\pm$ 0.14 nm, light blue box). The error was dominated by the pixel size and error propagation from the fit barely increased it. Therefore, our fitting approach offers a simple and reliable method to extract the gap size that is independent of the data processing pipeline before fitting. Furthermore, it can be applied to any particle geometry as it does not require prior knowledge of the particle shape, as shown in Figure 3.2. It should be noted that this works particularly well if the gap is not located along the direction of the missing wedge. Thus, an optimal alignment of the dimer system before acquiring a tomography series is essential for achieving the most reliable results.

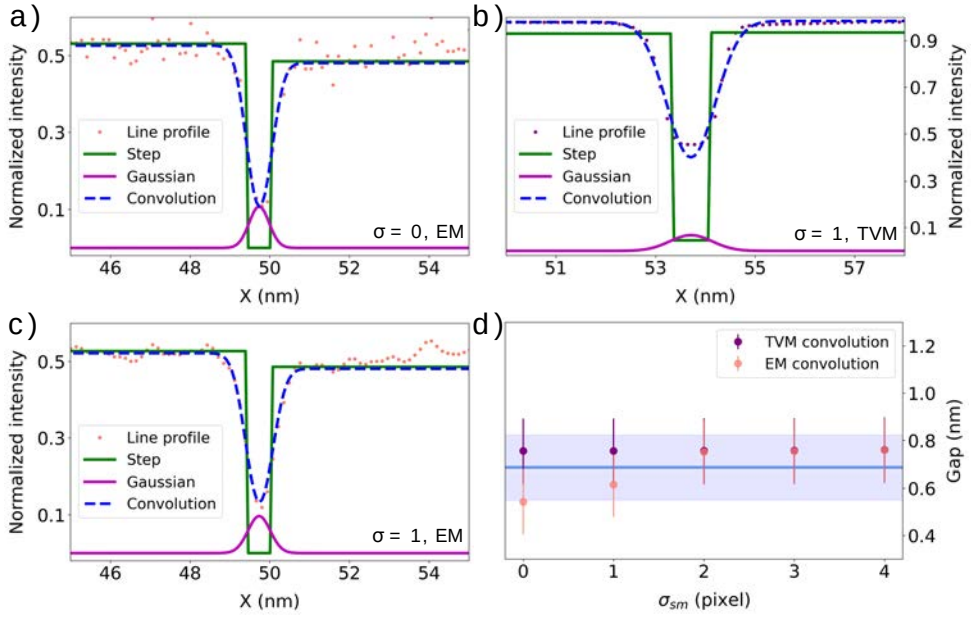

Figure 3.2: *Convolution fit applied to the simulated series of a dimer, reconstructed using the EM (salmon) and TVM (purple) algorithms. A representative convolution fit is illustrated for the EM reconstruction with applied smoothing of* $\sigma_{sm} = 0$ *in a) and* $\sigma_{sm} = 1$ *in c). In b), a representative convolution fit is shown for the TVM reconstruction with applied smoothing* $\sigma_{sm} = 1$*. In d) the extracted gap from each fit is plotted in salmon (EM reconstruction) and purple (TVM reconstruction) after applying different levels of smoothing. The ground truth for the simulated known gap (0.68 nm) is represented by the blue line. The light blue region indicates the tolerance corresponding to the pixel size* ± 1*.*

3.3.3 Convolution on experimental data

Once the model was successfully validated on simulated data, we applied it to the experimental reconstructions from Figure 3.1. As shown in Figure 3.3, the model performed well on experimental data, both for the TVM (Figure 3.3a and b) and the EM reconstructions (Figure 3.3c). Independent of the pre-processing, i.e. the reconstruction algorithm or applied smoothing parameter σ_{sm}, we extracted a very similar gap size as shown in Figure 3.3d. Excluding the gap size extracted from TVM for $\sigma_{sm} = 0$, the maximum difference in gap sizes from the different fits was found to be 0.074 nm, which is only half of the pixel size. Small discrepancies in gap size arose for $\sigma_{sm} = 0$ and large Gaussian blurring values ($\sigma_{sm} = 4$) for similar reasons as discussed in Figure 3.1. For $\sigma_{sm} = 0$, single voxel protrusions due to the non-

smoothed noise likely also caused the larger fitting error for the extracted gap size for EM. For TVM, the cause of the larger deviation for $\sigma_{sm} = 0$ was the intensity plateau in the gap region due to the nature of the algorithm, which caused a mismatch with our model as seen in Figure 3.3a. As shown in Figure 3.3b, this problem did not occur for larger non-zero σ_{sm}. It is therefore advisable to use slight smoothing of the reconstruction to avoid the different effects for the different reconstructions. Nonetheless, for all the different processing parameters we extracted a gap size within the pixel error. By averaging the gap values from the TVM and EM reconstructions for $\sigma_{sm} = 1$, $\sigma_{sm} = 2$, and $\sigma_{sm} = 3$, an average gap size of 0.87 nm was obtained. This result is in excellent agreement with computational work on calculating the length of the BDT molecules in between gold atoms, which resulted in 0.84-0.85 nm [88, 112].

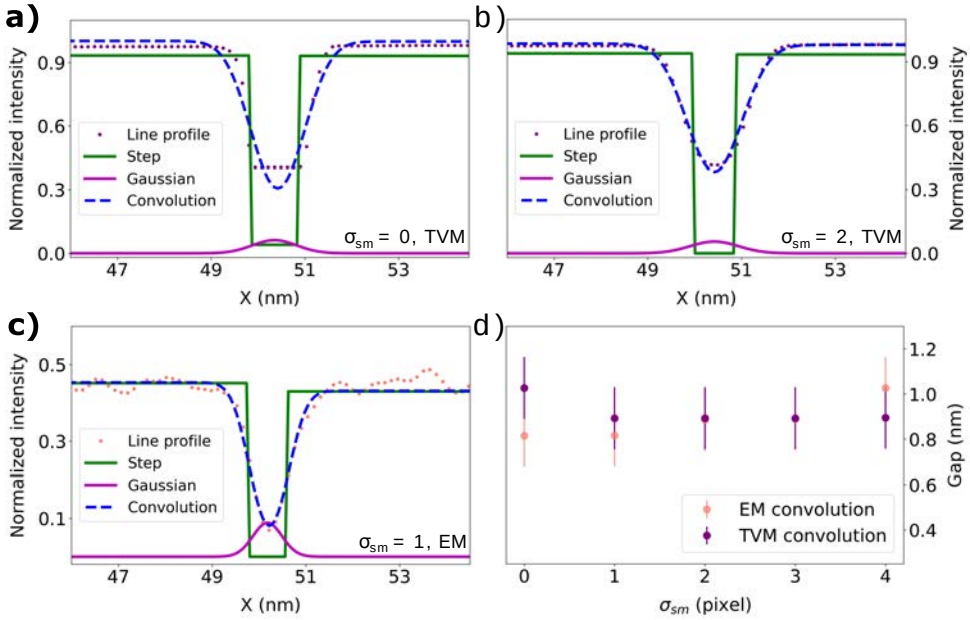

Figure 3.3: *Convolution fit applied to the experimental series reconstructed using EM (salmon) and TVM (purple) algorithms. A representative convolution fit is illustrated for the TVM reconstruction with applied smoothing $\sigma_{sm} = 0$ in a) and $\sigma_{sm} = 2$ in b). In c), a representative convolution fit is shown for the EM reconstruction with applied smoothing $\sigma_{sm} = 1$. The extracted gap sizes for each fit are summarized in Figure d).*

As discussed previously, a surface mesh is required as input for BEM simulations. In Figure 3.1, the mesh determination was highly uncertain due to ambiguities in the extracted gap size. Based on the robustness of the convolution fit, we now use the averaged fitted gap value (0.87 nm) as a reference and adjust the surface mesh

accordingly. To achieve this, the reconstruction was first segmented using a threshold derived from the convolution fit. Specifically, the threshold was estimated from the intersection between the convolution curve and the step function, which we define as a threshold fraction $\theta_t = 1$. A representative example of the identification of θ_t is shown in Figure S3.4d. However, mesh simplification introduces small but unavoidable deviations in the morphology. Since the optical response is highly sensitive to sub-nanometer gap variations, it is essential that the gap size after meshing remains consistent with the fitted value. Therefore, we compare the gap size before and after meshing. Figure 3.4a shows the gap sizes extracted before and after meshing, calculated by applying the EEDT, for different fractions of the threshold θ_t. As expected, the gap size changes during meshing, with deviations of up to 0.2 nm. For EM reconstructions, the gap size systematically increases after meshing, whereas for TVM reconstructions it decreases or remains nearly constant. These changes cannot be fully avoided without using a very large number of mesh faces, which would make the simulations computationally unfeasible. To evaluate this effect, we varied the number of faces in the mesh (Figure S3.8a). Significant deviations were only observed for very coarse meshes (1000 faces), while no noticeable differences were found between 6000 and 10000 faces.

To avoid these issues, we propose an alternative solution: the segmentation threshold is fine-tuned such that the gap size after meshing and mesh simplification matches the value obtained from the fit, which is now taken as the ground truth. As described earlier, the fitted gap size was determined to be 0.87 nm. In Figure 3.4a, the different lines correspond to variations in the threshold value relative to the initial value θ_t obtained from the fit. For the studied dimer, the fitted gap size after meshing is recovered for threshold values of $0.88\,\theta_t$ and $0.84\,\theta_t$ for the EM and TVM reconstructions, respectively. The corresponding simulated scattering spectra are shown in Figure 3.4b. The strong overlap between the spectra indicates that this approach yields a consistent mesh representation of the morphology and provides a robust method for calculating the optical response, independent of the specific pre-processing parameters. Due to the missing wedge effect, the EM reconstruction exhibits a slightly larger volume than the TVM reconstruction, a trend that is observed for all values of θ_t (Figure S3.9a). As expected for near-spherical particles, this volume difference does not significantly affect the scattering response, which is instead dominated by the gap size. Finally, the same behavior is observed for the simulated data. When the gap size after re-meshing is matched to the gap obtained from the fitting, the spectra obtained from EM and TVM reconstructions overlap with the ground truth spectrum (Figure S3.8c). This provides additional confirmation that the proposed workflow enables accurate electromagnetic simulations without ambiguity in the structural input. In turn, this allows for reliable comparisons with experimental spectra and opens the possibility to unambiguously identify quantum effects in these systems.

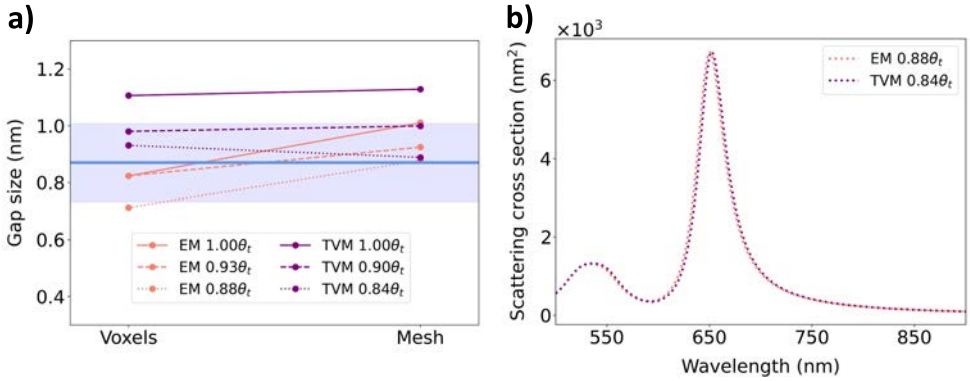

Figure 3.4: *a) Comparison of the gap extracted using the EEDT applied to the voxelized data before (Voxels) and after meshing for different fraction of θ_t, where θ_t=1 is the threshold obtained from the fit. b) Comparison of simulated scattering spectra for the meshed EM and TVM reconstructions for the same gap size after meshing.*

3

3.3.4 Transferring 3D morphological insights to 2D STEM images

While electron tomography provides the most reliable determination of the interparticle gap, it is not always experimentally feasible. As discussed in *Chapter 2*, optical measurements require SiO_2 membrane grids, which are incompatible with tomography due to bending and shadowing effects under tilting. Therefore, for the optically characterized dimers only 2D STEM images are available. Rather than abandoning quantitative gap extraction in these cases, the 3D ground truth established here can be used to calibrate the 2D thresholding procedure. This approach follows the same principle as recently demonstrated for simpler nanoparticle shapes [48], where a fixed fraction of the Otsu threshold was shown to provide reliable size extraction from 2D STEM images. Here we extend this to the more challenging case of sub-nanometer gaps in plasmonic dimers, using the convolution fit result as a physically meaningful reference to identify the optimal threshold fraction. We can now consider the gap extracted from the convolution fit (0.87 nm) as the ground truth and use it to benchmark gap sizes obtained from 2D STEM images. To this end, we applied different fractions of the Otsu threshold to the STEM image acquired at $-66°$ for the same dimer analyzed by electron tomography in this chapter. Figure 3.5 shows the extracted gap size as a function of the Otsu threshold fraction. By comparing these values with the ground-truth gap of 0.87 nm, we find that a threshold fraction between 0.2 and 0.4 provides the best agreement.

Having established this calibration, we then applied a fixed fraction of 0.3 of

the Otsu threshold to a separate batch of dimers, for which only 2D STEM images and dark-field scattering spectra are available. The STEM data were acquired under the same instrument settings and experimental conditions as those used for the tomography-based analysis, ensuring consistency between the two datasets. This dataset differs from the correlation presented in *Chapter 2*. In that case, the presence of background carbon and the use of a different instrument prevented the application of the threshold fraction estimated here. Figure S3.10 shows the correlated dark-field scattering spectra and the corresponding 2D STEM images. The scattering spectra are noisier than those shown in Figure 2.6, as the measurement setup was not yet fully optimized at the time of acquisition and a water immersion objective was used instead of an oil immersion objective. The optical spectra were then simulated for each dimer using the classical effective medium approach described in *Chapter 2*. The morphological parameters used as input (sphere size and gap size) were extracted from the 2D STEM images binarized using both the full Otsu threshold and the calibrated fraction of $0.3 \times$ Otsu. As shown in Figure 3.5, the calibrated threshold yields a smaller, more physically realistic gap size, which results in a redshifted BDP resonance in better agreement with the experimental spectra. For the dimer with the yellow spectrum, applying $0.3 \times$ Otsu caused the two spheres to merge during binarization, and no simulated spectrum is therefore shown.

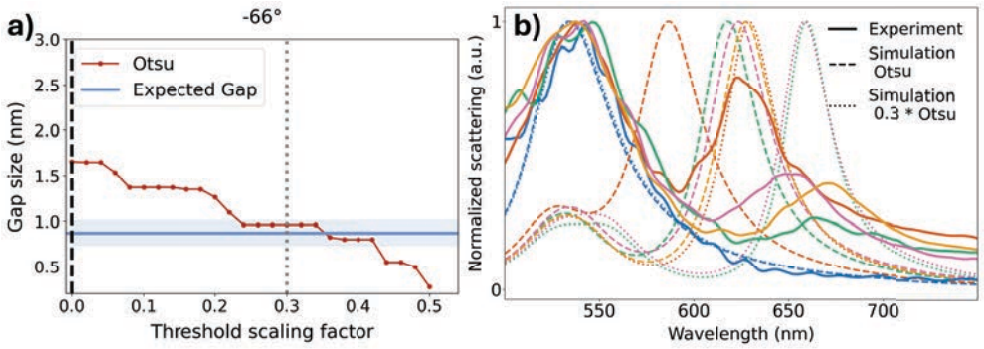

Figure 3.5: *a) Extracted gap size as EEDT from the STEM image taken at* $-66°$ *shown in Figure 2.7 as a function of fraction of the Otsu threshold. The blue horizontal line indicates the expected ground-truth gap obtained from the convolution fit of the 3D reconstruction. The light-blue band represents the experimental pixel-size uncertainty of* ± 0.14 *nm. b) Comparison of normalized scattering spectra for individual particles, showing experimental measurements (solid lines) and simulations using different thresholding parameters. Simulated spectra are presented for Otsu thresholding (dashed lines) and scaled Otsu thresholding (0.3 × Otsu, dotted lines). Each color corresponds to a specific dimer, enabling comparison between experiment and simulation.*

Overall, this comparison shows that a calibrated 2D thresholding method can provide consistent estimates of the gap size. However, 3D reconstruction remains more accurate, as it captures the full particle morphology. This highlights the importance of 3D approaches, while also showing that calibrated 2D methods remain useful when tomography is not available. The classical effective medium model used here for the optical simulations represents only one of the junction descriptions explored in *Chapter 2*. Ideally, the full multi-model comparison developed there would be applied to dimers for which the 3D morphology is also known, allowing the parameter degeneracy identified in *Chapter 2* to be broken. This requires correlative measurements combining dark-field spectroscopy, electron tomography, and optical modeling on the same single particle. Developing TEM grids that are compatible with both optical measurements and electron tomography therefore represents an important direction for future work.

3.4 Conclusion

In this chapter, we demonstrated that electron tomography significantly improves segmentation accuracy compared to the 2D analysis from *Chapter 2*. However, it also introduces uncertainties related to data processing, as the extracted gap size depends on the chosen reconstruction algorithm and the degree of smoothing applied. To address these challenges, we developed an optimal workflow for extracting sub-nanometer gaps and converting the 3D data into a reliable surface mesh. We found that fitting a convolution of a step function and a Gaussian function to line profiles from tomography reconstructions produces consistent gap size measurements. This method was validated using simulated data, where the known ground truth gap sizes were successfully retrieved with an accuracy on the order of the pixel size (0.14 nm in our case). The remaining uncertainty is therefore limited by the voxel size of the reconstruction. Once the gap size is accurately estimated from the fitting procedure, the segmentation threshold in the tomography reconstruction can be adjusted to preserve the gap size during meshing and mesh simplification. The resulting surface mesh is then used for electromagnetic simulations of the gold dimer's optical response. We believe that this approach is broadly applicable to a range of gap sizes and material systems. Furthermore, reducing the pixel size in experiments can further minimize the error in gap size estimation. Finally, we showed that insights from the 3D analysis can be used to improve gap estimation from 2D STEM images by selecting an appropriate threshold. This approach also makes the analysis more scalable. Electron tomography cannot be applied to large numbers of dimers, but it can be done on a few to establish a calibration, which can then be applied to a much larger set of 2D STEM measurements. However, due to projection effects fundamental limitations remain that only full 3D characterization can overcome. Combining on the same

single particle such 3D morphological characterization with the multi-model optical analysis of *Chapter 2* remains an important goal for future work. Overall, this work provides a robust and general framework for accurately determining sub-nanometer gaps in plasmonic systems. This enables a more reliable interpretation of their optical response and supports the study of classical-to-quantum transitions in nanoscale light–matter interactions.

3.5 Appendix

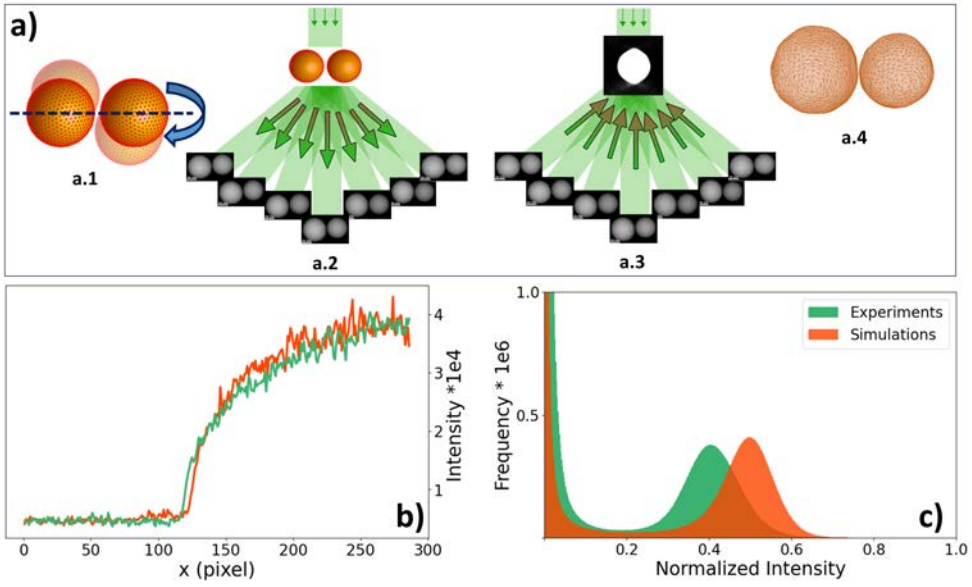

Figure S3.1: *Simulation of electron tomography data. a) Workflow for creating simulated STEM images and for subsequent reconstruction and surface meshing: (a.1) Voxelized model of the dimer; (a.2) Forward-projection of the 3D structure to create 2D images, with noise added to each projection; (a.3) The noisy 2D images are back-projected to reconstruct the 3D object; (a.4) The reconstruction is thresholded, meshed, and simplified to create a 3D mesh structure. b) Representative line profiles from 2D projection images. c) Histogram of the 3D reconstruction performed using the EM algorithm with 15 iterations for the experimental (green) and simulated dataset.*

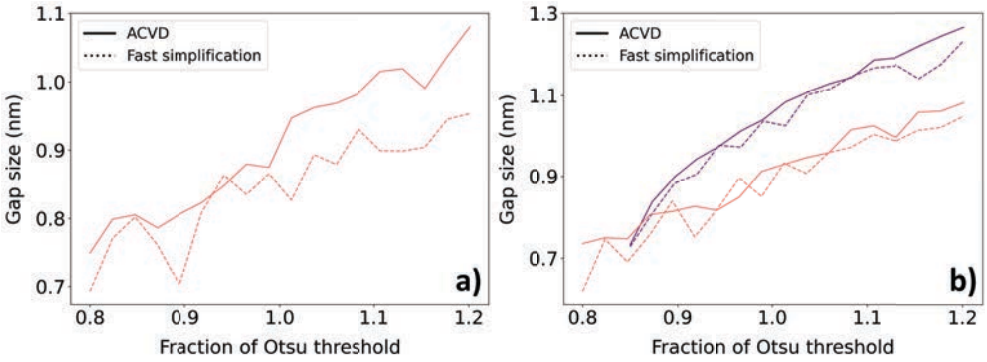

Figure S3.2: *a) Gap size as a function of Otsu threshold fraction for simplified meshes generated using ACVD and Fast Simplification, applied to both EM (salmon) and TVM (purple) reconstructions. a) Results for the simulated dimer. b) Results for the experimental dimer (as in Figure 4).*

Parameters	Initial value	Lower bound	High bound
High intensity Right	Max_{right}	-5% of initial value	+5% of initial value
High intensity Left	Max_{left}	-5% of initial value	+5% of initial value
Low intensity	Minimum	0	Initial value
Amplitude	10	0	100
Gaussian Position	(Step right+ Step left)/2	Initial value	Initial value
Gaussian smoothing	σ_{sm}	0	10
Step right	Inflection right	initial value -10 pixel	initial value +10 pixel
Step left	Inflection left	initial value -10 pixel	initial value +10 pixel

Table S3.1: *Initial parameters for the convolution fit obtained by fitting two logistic functions to the right and left side of the gap. Max_{right} corresponds to the highest intensity of the right logistic function, while Max_{left} of the left logistic function. The minimum, i.e. the initial value for the gap intensity, is the average of the lowest value of the right and left logistic functions. Finally, the inflection points of these logistic functions provide an estimate of the gap's position. The position of the Gaussian is kept centered in the middle of the gap. See Figure S3.4 for more details.*

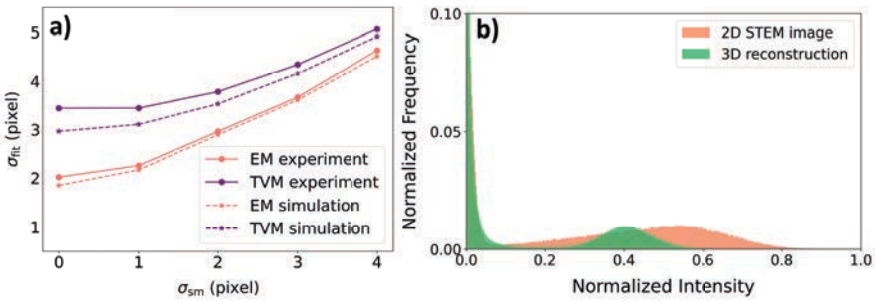

Figure S3.3: *a) Comparison between sigma values used for smoothing of the reconstruction (σ_{sm}) and extracted from the convolution fit (σ_{fit}) both for experimental and simulated data. b) Normalized histograms of the voxel intensities of the 3D experimental reconstruction of a dimer and a 2D STEM image of the same system.*

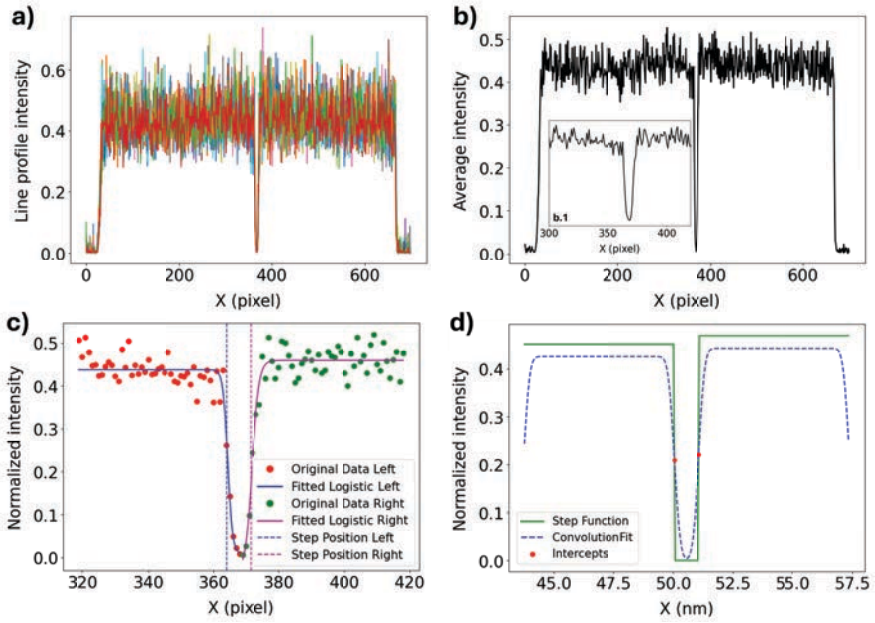

Figure S3.4: *Fitting procedure. a) Line profiles along the gap in the xy and xz directions over 12 neighboring pixel positions. b) Averaged line profile for which the convolution fit is performed. The inset b.1 shows a zoomed-in view around the gap. c) A logistic function is fitted to the left and right sides of the step to determine the starting parameters, which serve as input for the it (see Table S3.1). (d) Threshold values are extracted from the intersection points between the original data and the fit.*

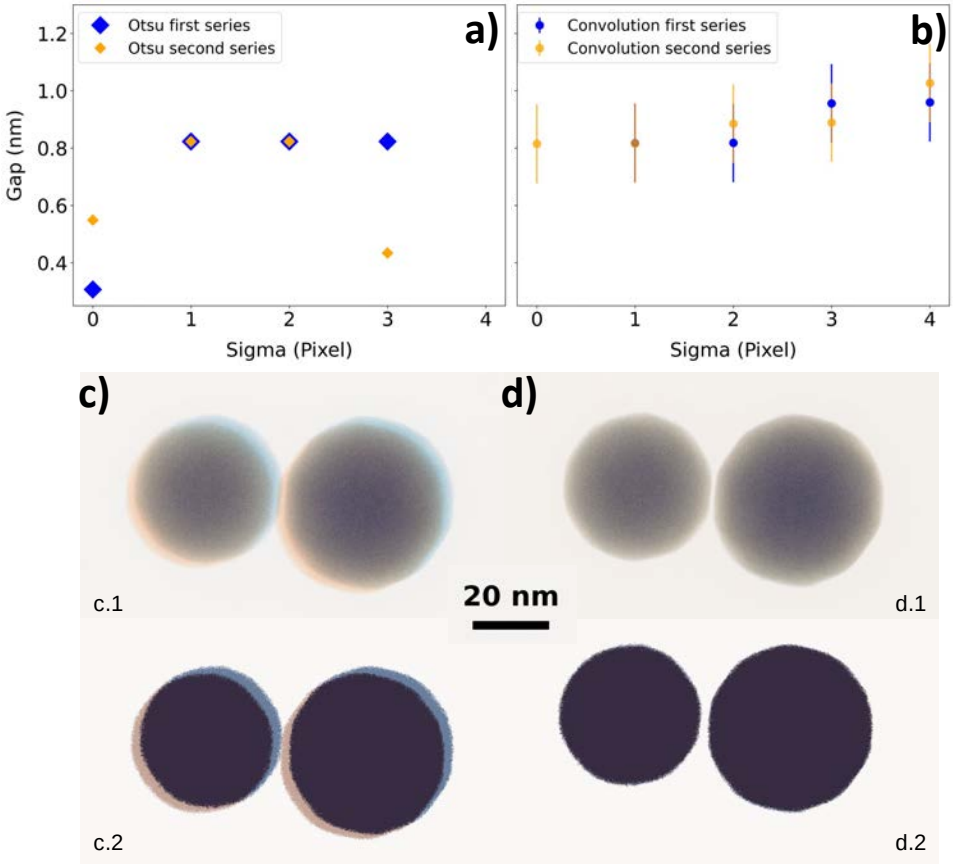

Figure S3.5: *a) Gap size extracted by applying the EEDT to the Otsu-thresholded EM reconstructions obtained from the first (blue) and second (orange) tilt series of the same dimer. b) Gap size extracted from the same two reconstructions using the fitting model. c) Overlay of the 2D STEM images at 0° taken before acquisition of the first tilt series (blue) and after the second tilt series, shown for the original images (c.1) and after binarization (c.2). d) Overlay of the same images after applying a cross-correlation algorithm to correct for rotation under the electron beam and positional shifts. (d.1) displays the raw 2D STEM images, while (d.2) shows the images after applying Otsu thresholding.*

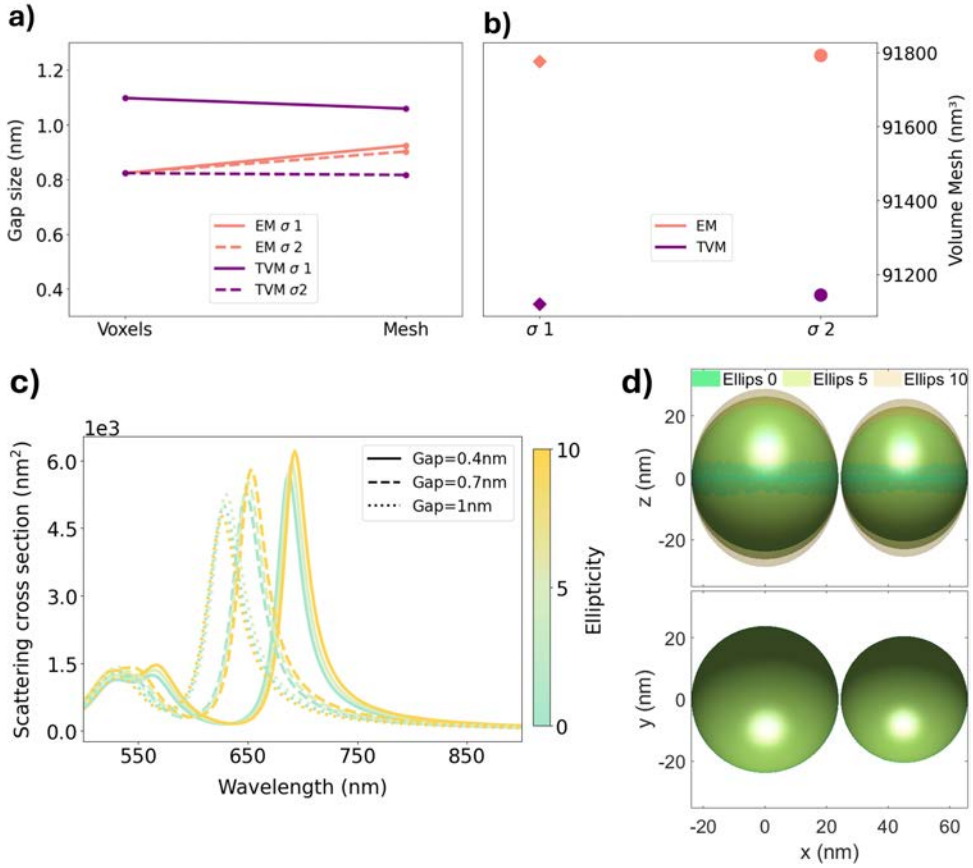

Figure S3.6: *Comparison of gap sizes before and after meshing for different σ_{sm} b) Volume of the mesh obtained from EM (salmon) and TVM (purple) reconstructions. The slightly larger volume obtained with EM compared to TVM is attributed to the stronger influence of the missing wedge in the EM reconstruction.c) Simulated scattering spectra for increasing ellipticity. Scattering spectra were simulated for two spheres with radii of 23 nm and 20 nm, separated by varying gap distances. Increasing ellipticity along the z-direction was introduced to simulate the missing wedge artifacts commonly associated with ET reconstructions. d) 3D input morphology for the simulations.*

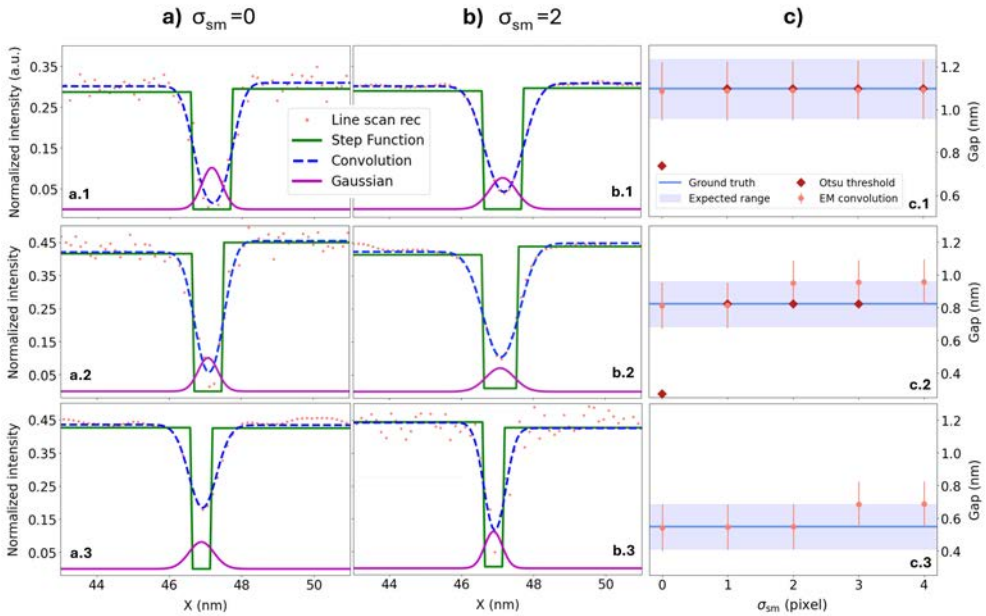

Figure S3.7: *Convolution fit tested on simulated tomography data. c) Gap sizes obtained from the 3D EM reconstruction of three simulated dimers: Two dimers with spheres of 23 nm in radius and gap sizes of 1 nm (c.1) and 0.55 nm (c.3). A dimer with one sphere of 23 nm in radius and the second of 30 nm in radius, with a gap size of 0.81 nm (c.2). The gap sizes extracted from the fitting are shown in salmon, while those obtained by applying the EEDT to the Otsu-thresholded EM reconstructions are shown in red. When no data point is displayed for a particular σ_{sm}, the segmentation failed and resulted in the connection of the two spheres. For each gap size the corresponding fits are displayed for $\sigma_{sm} = 0$ in a) and $\sigma_{sm} = 2$ in b*

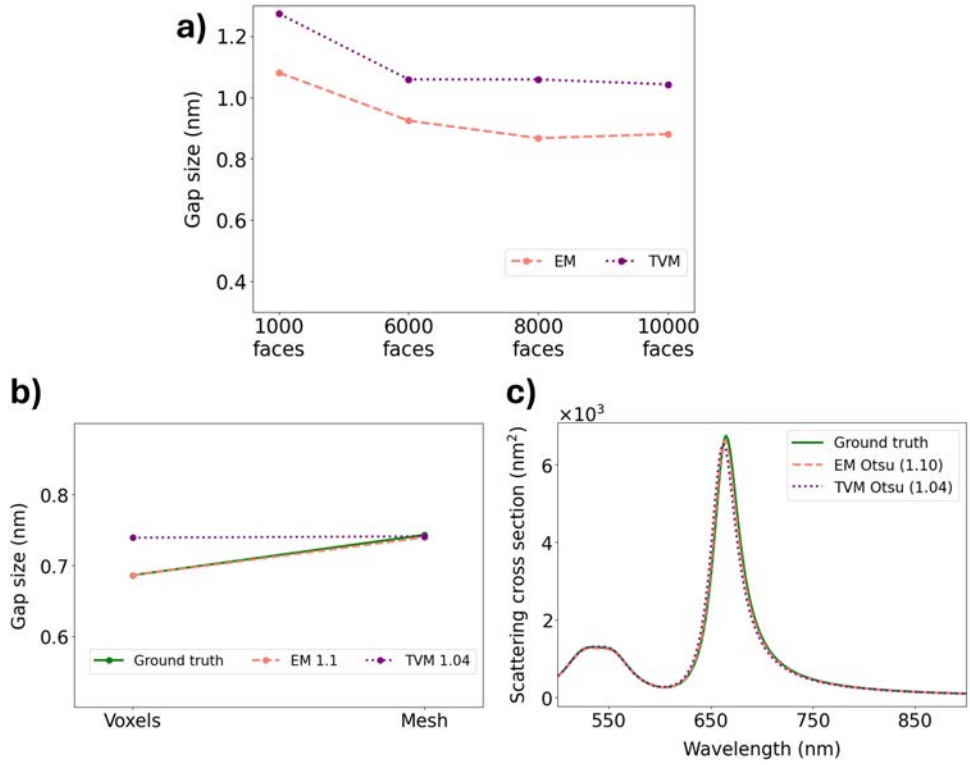

Figure S3.8: *a) Comparison of gap size extracted as Euclidian distance for EM and TVM reconstruction after smoothing with $\sigma_{sm} = 1$ and ACVD mesh simplification to different target faces (1000, 6000, 8000 and 10000). b) Gap size as Euclidean distance before (voxels) and after meshing. A fraction of the Otsu threshold was selected to match the EM and TVM reconstruction gap sizes with the ground truth gap size after meshing. c) The corresponding scattering spectra show perfect agreement. The simulated dimer was a voxelized structure derived from experimental data, as in Figure 3.2 Therefore, the "ground truth" refers to the voxelized model used as input for the STEM simulations. To compute its optical properties, the ground truth structure was first converted into a mesh using the same procedure as for the EM and TVM reconstructions: the marching cubes algorithm followed by ACVD remeshing to 6000 faces.*

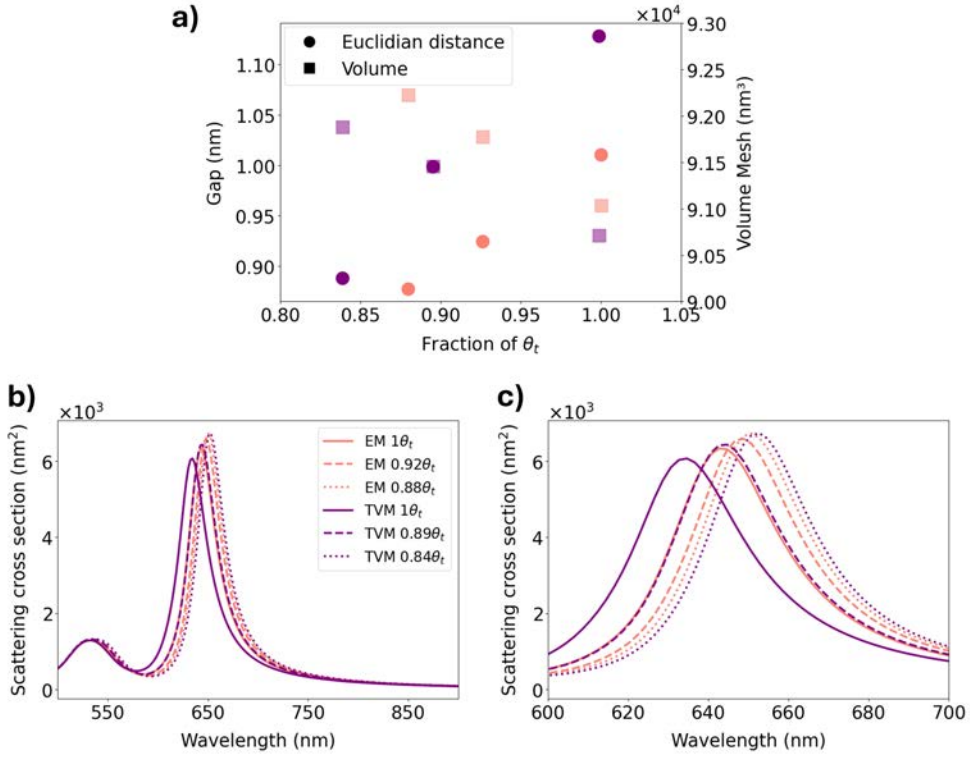

Figure S3.9: *a)Gap size as Euclidean distance (circle) and volume (square) of the mesh for EM (salmon) and TVM (purple) reconstructions for different θ_t. b) Corresponding scattering spectra simulated with BEM and c) Zoom in of the scattering peaks.*

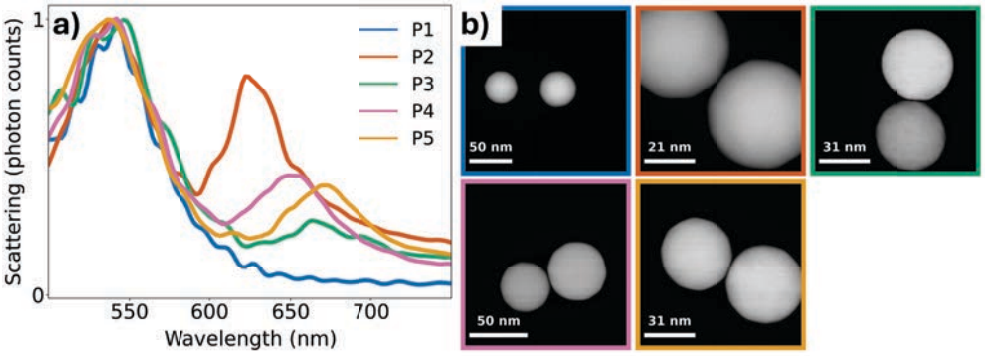

Figure S3.10: *a) Normalized measured dark field scattering spectra of six dimers whose STEM images are shown in b).*

4 Synthesis and crystallization pathways of $Au@TiO_2$ NRs

Keywords: core-shell, crystallization, hydrothermal treatment, in situ TEM laser modification, interface quality, charge transfer

The efficiency of plasmonic $Au@TiO_2$ photocatalysts depends on hot-electron injection across the metal-semiconductor interface and on the subsequent carrier dynamics within the TiO_2 shell, including trapping at defect states, back-transfer to the Au core, and transport to the reactive surface. Optimizing these processes requires precise control over interface quality and TiO_2 crystallinity. Achieving such control in colloidal core-shell nanostructures remains challenging. Here, we investigate how precursor chemistry, ligand choice, and crystallization route govern shell morphology, defect density, phase selection, and interface quality in $Au@TiO_2$ nanorods. A chloride-based precursor ($TiCl_3$) enables controlled shell growth, while ligand-dependent impurity incorporation strongly influences TiO_2 phase selection during crystallization. Low-temperature hydrothermal treatment and laser-induced crystallization inside the TEM are explored as alternatives to conventional high-temperature annealing. Hydrothermal treatment yields predominantly anatase but disrupts the shell morphology, whereas laser-induced crystallization enables localized crystallization with limited Au core reshaping, directly confirmed by real-time structural observation. Overall, these results provide a foundation for the rational design of $Au@TiO_2$ systems with improved charge injection and carrier transport.

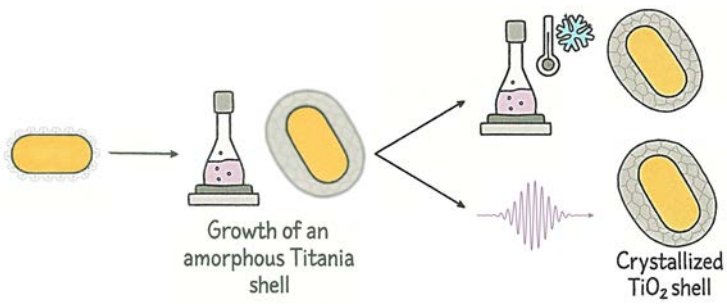

4.1 Introduction

Photocatalysis is a green technology that uses photons to drive chemical reactions in the presence of a photocatalyst [113]. It enables processes ranging from pollutant degradation to the production of value-added chemicals by converting light into chemical energy [11, 114–116]. Semiconductors are widely used as photocatalysts due to their band structure. When illuminated with photons above the band gap, electron–hole pairs are generated that can participate in redox reactions [117, 118]. Among these, TiO_2 is one of the most extensively studied systems [114], with photocatalytic activity first demonstrated in 1972 [119].

However, the wide band gap of TiO_2 limits absorption to the UV range, corresponding to less than 5% of the solar spectrum [115]. Coupling TiO_2 with plasmonic metals is a widely explored strategy to extend activity into the visible range [120]. In particular, Au nanoparticles are attractive due to their stability, tunable optical response, and strong localized surface plasmon resonance (LSPR), combined with favorable band alignment with TiO_2 [9, 120–122]. The performance of Au/TiO_2 photocatalytic systems is governed by two key processes: the efficiency of hot-electron injection across the interface, and the subsequent transport and dynamics of the injected carriers within the TiO_2.

Under resonant illumination, localized surface plasmon resonance (LSPR) excitation produces energetic hot carriers that relax on ultrashort timescales. These carriers can be injected into the coupled semiconductor through different mechanisms, as discussed in *Chapter 1*. Among these, direct plasmon-induced charge transfer is particularly efficient but depends strongly on the atomic-scale structure of the metal–semiconductor interface. To investigate these processes experimentally, a well-defined model system is required. Au nanorods were studied here because their longitudinal LSPR can be tuned across the visible range via the aspect ratio and it is highly sensitive to structural and environmental changes [123]. Moreover, their longitudinal mode does not overlap with interband transitions, enabling quantitative analysis of plasmon damping via linewidth broadening due to chemical interface damping (CID) in single-particle measurements [124]. This makes them well suited to probe plasmon damping and charge transfer as a function of structure, interface, and crystallinity. Recent studies have shown that, under ideal conditions, hot electron transfer across Au/TiO_2 interfaces can be highly efficient[16, 24]. Total injection efficiencies of up to ∼50% have been experimentally reported for small Au nanoparticles, with values decreasing for larger particles due to reduced interband absorption [16].

Although hot-electron injection at Au/TiO_2 interfaces can be highly efficient, the experimentally measured photocatalytic performance remains low due to rapid recombination and inefficient charge transport within the semiconductor. Only electrons that reach the surface of the TiO_2 can participate in catalytic reactions. How-

ever, many carriers become trapped in defect states within the material or undergo back-transfer to the Au core, where they recombine with holes. Time-resolved measurements by Ostovar et al. revealed that the injected electron population decays on ultrafast timescales, with characteristic components ranging from ∼1 ps to ∼100 ps [24]. The fast components are attributed to interfacial back-transfer of electrons to the Au core before they escape the interface, while slower components are assigned to trapping or recombination processes within the TiO_2 [24, 25]. Suppressing back-transfer and extending carrier lifetimes requires precise control over both the interface quality and the structural properties of the TiO_2 shell.

Achieving a well-controlled Au/TiO_2 interface remains challenging. Core–shell structures are typically synthesized using colloidal methods, where surface ligands are required to stabilize the Au nanoparticles. On the one hand, increasing the contact area between the metal and semiconductor provides more pathways for interfacial charge transfer, enhancing the injection efficiency. This makes core–shell architectures particularly attractive [125, 126]. On the other hand, the large lattice mismatch inherent to these core–shell architectures hinders the formation of well-defined, low-defect interfaces. In addition, surface ligands such as sodium dodecyl sulfate (SDS) or citrate, required for the colloidal stability of the Au NPs, can remain at the interface during shell growth, introducing defects and an interfacial gap. As mentioned above, interfacial defects can act as recombination centers or promote electron back-transfer [24, 25, 124, 127, 128]. The thickness and chemical nature of this gap is expected to depend on ligand length and binding strength. Long or strongly bound ligands can act as insulating spacers, while shorter or more weakly bound ligands may allow more intimate contact. Ligand choice can therefore strongly influence interface quality and even affect impurity incorporation during shell formation.

Beyond the interface, the structural properties of the TiO_2 shell strongly affect performance. A higher degree of crystallinity reduces defect-assisted carrier trapping and scattering, improving charge transport. Furthermore, different polymorphs (anatase, rutile, brookite) exhibit distinct electronic and catalytic properties (Table 4.1). While anatase is often considered the most photocatalytically active phase due to its longer carrier lifetimes and diffusion length [129], mixtures of anatase and rutile can show enhanced performance through a synergistic effect in which the phase boundary promotes charge separation [129, 130]. However, in Au/TiO_2 systems under plasmonic excitation, holes remain in the metal and only electrons are injected into the semiconductor, making electron transport the key limiting factor and pure anatase the favored phase. Phase formation is influenced by synthesis conditions, grain size, heating rate, impurities, and defect density [131]. In particular, oxygen vacancies lower the activation energy for rutile formation and therefore play a central role in phase selection. In core–shell systems, where TiO_2 forms via heterogeneous nucleation, these effects remain poorly understood.

An additional challenge is that colloidally grown TiO_2 shells are typically amorphous and require annealing above 400°C to crystallize. At these temperatures, Au nanorods become unstable, undergoing a reduction in aspect ratio and an increase in surface roughness. Changes in aspect ratio shift the LSPR position, while surface roughness [132, 133] and defects [134, 135] enhance plasmon damping through increased electron scattering. This introduces an additional contribution to linewidth broadening that is independent of charge transfer, complicating its quantitative interpretation. Moreover, increased surface scattering may compete with interfacial charge transfer as a decay pathway, reducing its efficiency. Preserving nanorod morphology during crystallization is therefore essential for maintaining injection efficiency and enabling reliable single-particle linewidth measurements. To address this, different crystallization strategies have been explored: low-temperature hydrothermal treatment and laser-induced crystallization. Hydrothermal treatment below 100 °C has been shown to induce crystallization of amorphous titania into anatase [136]. The underlying mechanism relies on water hydrating the amorphous TiO_2 network, which increases the mobility of Ti species and facilitates the structural rearrangement required for crystallization, at temperatures far below those needed for conventional dry annealing [136]. Pulsed laser heating offers an alternative to induce TiO_2 crystallization, providing rapid and localized temperature spikes followed by fast cooling. This may enable crystallization while limiting Au diffusion and potentially freezing the system in a non-equilibrium structural configuration. Pulsed laser heating has been demonstrated for TiO_2 thin films and nanotubes [137–139]. Noel et al. showed that collective plasmon-mediated heating of Au nanoparticles can generate sufficiently high local temperatures to crystallize TiO_2 sol-gel films under ambient conditions [140]. However, the application of laser-induced crystallization to $Au@TiO_2$ core–shell nanostructures remains largely unexplored, where both metal core stability and interface quality must be preserved.

In this chapter, we investigate how precursor chemistry, ligand choice, and crystallization route determine shell morphology, defect density, interface quality, and TiO_2 phase selection in $Au@TiO_2$ nanorods. Two precursors, an alkoxide and a chloride-based, are used to synthesize amorphous TiO_2 shells with distinct morphologies and defect densities. In addition, two gold surface ligands with different molecular lengths and binding strengths are compared to evaluate their effect on interfacial structure and impurity incorporation. To induce crystallization while minimizing Au core deformation, two approaches are explored: low-temperature hydrothermal treatment and laser-induced crystallization. The latter is the primary focus, as pulsed laser excitation is performed directly inside the TEM, enabling localized heating and in situ observation of structural evolution in both TiO_2 and Au. Together, these results provide insight into how synthesis and crystallization conditions govern the structural and interfacial properties of $Au@TiO_2$ nanorods, forming a basis for future studies

linking crystallinity and interface quality to plasmonic charge-transfer efficiency.

Property	Anatase	Rutile	Brookite	Amorphous
Crystal structure	Tetragonal	Tetragonal	Orthorhombic	
Atoms per unit cell	4	2	8	-
Unit cell dimensions (Å)	a=b=3.78, c=9.51	a=b=4.59, c=2.95	a=5.46,b=9.18, c=5.14	-
Density (g cm^{-3})	3.9	4.25	4.11	3.0-3.2
Band gap (eV)	3.26	3.05	3.14	-
Band gap type	indirect	direct	direct	-
Hardness (Mo)	hard, 5.5-6	very hard, 6-7	hard, 5.5-6	not very hard
Refractive index	2.57	2.95	2.81	2.4

Table 4.1: *Properties of amorphous TiO_2 and its different polymorphs. Values are taken from different sources [141–144].*

4.2 Methodology

4.2.1 Chemicals

All starting materials were used without further purification. The following chemicals were purchased from Sigma-Aldrich: a Titanium chloride(III) ($TiCl_3$) solution about 15% in about 10% hydrochloric acid for synthesis, a sodium bicarbonate ACS reagent 99.7%, Titanium isopropoxide (IV) (TTIP) 97%, glacial acetic acid 99.8%, and 2-Propanol (IPA) 99.8% . 25x75 nm citrate capped NRs and SDS capped NRs were purchased from Nanopartz. Milli-Q grade water (resistivity 18.2 MΩ cm at 25°C) was used in all experiments. Quantifoil R 1.2/20 200-mesh copper TEM grids were purchased from Quantifoil and 20 nm SiO_2 membranes with 50×50 μm windows were purchased from SimPore.

4.2.2 Electron Microscopy

The experiments reported were performed in an aberration-corrected NeoARM (S)TEM with Cold Field Emission Gun operated at 200 kV.

Light in-coupling

The microscope is equipped with a JEOL–IDES Luminary laser in-coupling unit composed of a fiber-coupled laser, an inlet port, and a compact optical delivery system

with a mirror to adjust the position of the laser spot and a collimator to focus the beam onto the sample. Laser alignment was performed using the JEOL–IDES fluorescent (PLAH) holder, which enables direct visualization of the laser spot and alignment with the electron beam. For the measurements reported here, we used a wavelength of 700 nm with 10 nm bandwidth and a repetition rate of 26 MHz, corresponding to 38.5 ns in between pulses. At this wavelength the peak length is around ~ 22 ps. The laser was focused onto the sample with a spot size of $\sim 40\,\mu$m FWHM (full width at half maximum) and $64\,\mu\mathrm{m}/e^2$, as determined from a 2D Gaussian fit of the laser spot as shown in Figure S5.1a.

Energy-dispersive X-ray spectroscopy (EDX) analysis

Energy Dispersive X-ray (EDX) data were acquired on the JEOL DrySD100GV EDX detector ($100\,mm^2$, windowless, 133 eV@Mnka resolution). The EDX spectra were processed using the standard two-window background subtraction procedure as implemented in HyperSpy [145]. In this chapter elemental maps were generated from background-corrected data, while the spectra are the uncorrected raw counts summed over all pixels. For visualization purposes only, elemental maps were smoothed using a Gaussian filter and the contrast was enhanced by normalization and gamma correction.

Electron diffraction analysis

Selective aperture electron diffraction (SAED) patterns were acquired with a selective aperture of $20\,\mu$m and a camera length between 40 cm and 150 cm. Diffraction patterns were analyzed using the CrystBox ringGUI tool [146]. After background subtraction, diffraction ring positions were determined from azimuthally averaged intensity profiles. SAED allows obtaining information about the reciprocal space of an area restricted by the selective aperture. This area is typically on the order of hundreds of nanometers.

Information about the reciprocal space can also be obtained from real-space TEM images by calculating their Fast Fourier Transform (FFT), with much higher spatial resolution. The FFT of small areas within a TEM image can in fact be calculated. It is therefore possible to select individual crystalline patches and analyze their crystallinity. The FFT converts a real-space image into the frequency domain. For this analysis, individual crystalline patches were first identified in the TEM images, and FFTs were computed for each of these regions. In the resulting FFT patterns, Bragg (bright) spots correspond to different periodic lattice spacings in the real-space image. The brightest spots were detected, and a 2D Gaussian function was fitted to each spot to identify its center with sub-pixel accuracy. Lattice spacings (d-spacings) were then calculated as $d = 1/g$, where g is half the distance between opposite Friedel pairs in reciprocal space. To account for residual astigmatism and anisotropic dis-

tortions, multiple d-spacing measurements obtained from the same crystalline patch were averaged within a relative tolerance. Finally, each crystalline patch was assigned to a specific TiO_2 polymorph based on comparison with literature d-spacing values setting a tolerance of 6%. It should be noted that the pixel size in the FFT depends on the magnification used to acquire the TEM images and the size of the area used to calculate the FFT. For the experimental settings in this work the pixel size of the FFT varied between 0.1 and 0.01 nm^{-1}, which translates into an uncertainty between 0.0005 and 0.01 nm^1 on the d-spacing. Therefore we allowed a 6% tolerance when identifying a polymorph.

In this chapter, diffraction and FFT analysis are applied to TiO_2, which appears in three different polymorphs (anatase, rutile, and brookite). These phases can be distinguished by their characteristic diffraction peaks: anatase shows a prominent (011) reflection at 0.352 nm and a (004) reflection at 0.238 nm; rutile is identified by its main (110) reflection at 0.325 nm and a (011) reflection at 0.249 nm; while brookite is characterized by the (120) reflection at 0.290 nm and a (111) reflection at 0.345 nm.

4.3 Results and discussion

This section addresses the three main challenges identified in the *Introduction*: controlling the Au/TiO_2 interface through ligand and precursor choice, achieving TiO_2 crystallization without compromising Au nanorod morphology, and understanding the factors determining the resulting crystal phase. While TiO_2 nanoparticle synthesis is well established, the interplay of these effects is more complex in core–shell systems such as $Au@TiO_2$, where TiO_2 forms predominantly via heterogeneous nucleation on the metal, mediated by surface ligands.

4.3.1 Design of the initial $Au@TiO_2$ interface and morphology: role of ligand and precursor chemistry

As discussed in the *Introduction*, surface ligands and precursor chemistry strongly influence both the morphology of the TiO_2 shell and the quality of the Au/TiO_2 interface. In this work, AuNRs capped with two different molecules were compared: SDS and citrate. For SDS-capped AuNRs, previous studies report successful TiO_2 shell growth followed by high-temperature annealing using $TiCl_3$. In contrast, to the best of our knowledge, the combination of citrate-capped AuNRs with $TiCl_3$ has not been previously reported, and is explored in this work.

The molecular structures of the ligands are shown in Figure 4.1. Although both carry a negative charge, their interfacial behavior differs significantly [147]. SDS is 1.5–2 nm long and forms dynamic surfactant layers that stabilize nanorods through steric and electrostatic interactions. These layers can act as soft templates for shell

growth, but may also introduce an organic spacer between the Au core and the TiO_2 shell, limiting direct hot-carrier transfer. In contrast, citrate is much shorter ($\sim$0.4 nm) and binds more directly to the Au surface through its carboxylate groups, forming a relatively thin and accessible interfacial layer. It can also be readily displaced by competing species [148], and its binding weakens under acidic conditions, reducing nanoparticle stability [149]. This behavior in acidic conditions can be understood from its acid–base properties: citrate contains three carboxyl groups with pKa values of approximately 3.1, 4.8, and 6.4, and is therefore progressively protonated at lower pH. As the pH decreases, the loss of negative charge weakens both electrostatic stabilization and binding affinity to the Au surface. In contrast, the sulfate headgroup of SDS is a much stronger acid (pKa $\lesssim$ 0) and remains deprotonated and negatively charged even under strongly acidic conditions, allowing the surfactant layer to remain stable. As a result, under the acidic conditions typical of TiO_2 shell growth, citrate progressively loses its binding affinity to the Au surface, whereas SDS remains intact. This difference in acid stability directly affects how accessible the Au surface is during shell formation: citrate-capped particles are therefore expected to enable more intimate $Au@TiO_2$ contact and a smaller interfacial gap compared to SDS.

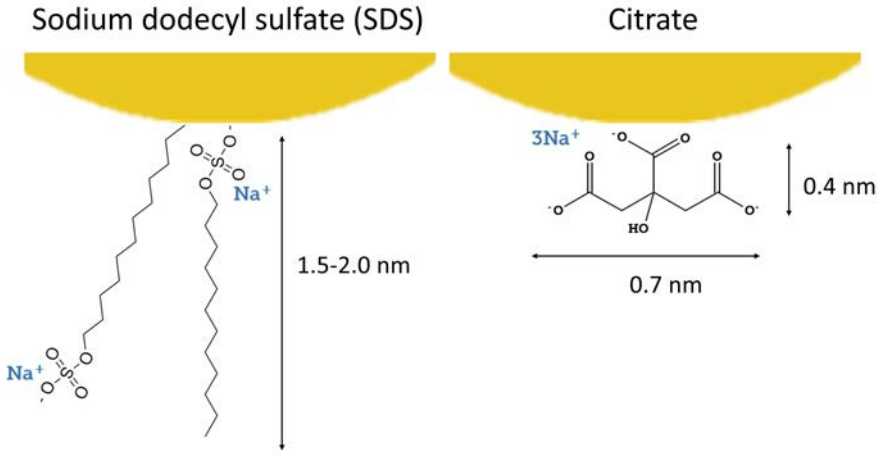

Figure 4.1: *Molecular structure and length of SDS and citrate ligands on a gold surface*

Beyond controlling the interface spacing, ligands also influence the nucleation of TiO_2 during shell growth. They can provide sites for heterogeneous nucleation that compete with homogeneous nucleation in the bulk solution [150]. In addition, they affect interparticle interactions during sol–gel processes. Amphiphilic surfactants such as SDS can promote aggregation of TiO_2 species in solution through hydrophobic interactions [151], whereas small hydrophilic ligands such as citrate mainly provide

electrostatic stabilization. As a result, differences in shell morphology and thickness are expected depending on the ligand, as shown in the following section.

In addition to the effects of ligand choice, the titanium precursor plays a key role in determining shell formation. TTIP and $TiCl_3$ were used to synthesize amorphous TiO_2 shells with different structural properties and suspected defect densities, which are expected to influence both growth behavior and subsequent crystallization. Alkoxide precursors such as TTIP undergo hydrolysis and condensation reactions that can yield homogeneous and dense TiO_2 when the reaction kinetics are carefully controlled [152, 153]. However, excess water or elevated pH leads to rapid precursor decomposition, resulting in uncontrolled precipitation and non-uniform growth [152, 154]. In contrast, chloride-based precursors such as $TiCl_3$ react rapidly in acidic and ionic media, generating reactive species (e.g. H^+, Cl^-) that promote both nucleation and defect formation [150, 155]. The resulting defect density plays a central role in determining both crystallization pathways and charge-carrier dynamics. At moderate concentrations, oxygen vacancies and Ti^{3+} states introduce shallow trap states that can slow carrier recombination [156, 157], but act as efficient recombination centers when present in excess [158].

These precursor-specific hydrolysis behaviors also depend on the surface ligands present on the Au nanorod. In TTIP-based systems, nucleation is largely governed by ligand coordination chemistry [159, 160]. Chelating ligands such as citrate can form stable complexes with Ti(IV), slowing hydrolysis and promoting surface-directed growth. As a result, citrate is expected to have a stronger influence on directing TiO_2 formation at the nanoparticle interface than non-chelating ligands such as SDS [160]. In contrast, in $TiCl_3$ systems, hydrolysis produces protonated Ti–OH_x species that electrostatically interact with negatively charged ligand layers on Au. This can promote heterogeneous nucleation for both SDS- and citrate-capped nanorods [150]. In citrate-capped systems, partial ligand displacement at low pH induced by the acid $TiCl_3$ may expose the Au surface, enabling more direct interactions between Ti species and Au, consistent with reported Au–OH interactions at hydroxylated interfaces [161].

Overall, ligand and precursor choice define the initial interface structure and the properties of the amorphous TiO_2 shell. In the following section, these parameters are systematically varied to establish controlled starting systems for subsequent crystallization studies.

4.3.2 Controlled synthesis of amorphous $Au@TiO_2$ nanorods

Having established how precursor chemistry and ligand choice are expected to govern shell morphology, defect density, and interface quality, we now discuss the amorphous TiO_2 shells synthesized using TTIP and $TiCl_3$. The structural differences observed before crystallization provide the basis to explain the different crystallization behav-

iors discussed in the next sections.

a. Titanium (IV) isopropoxide precursor

The colloidal growth of an amorphous TiO_2 shell around citrate capped AuNRs using TTIP, was carried out following a protocol adapted from Atta et.al. [162], as detailed in the *Appendix 4.4.1a*. Citrate capped AuNRs in water with a 25 nm diameter and an LSPR at 600 nm were used. SDS capped AuNRs were not attempted, as SDS is not expected to provide the chelation required to control TTIP hydrolysis, as discussed earlier [160].

Figures 4.2a–c show STEM images and EDX net counts maps, confirming the formation of a thin but non-uniform TiO_2 shell around the AuNRs. The EDX sum spectrum (Figure 4.2c) reveals the presence of sodium (Na) impurities, likely originating from residual citrate ligands. Complete washing of the original AuNRs solution was not possible due to the instability of the specific batch of the citrate-stabilized nanorods used here under more aggressive washing conditions, resulting in residual Na^+ and water. More extensive washing may reduce these impurities in future studies for a different batch. Figure 4.2d shows UV–Vis spectra for varying TTIP concentrations. The blue curve shows to bare AuNRs redispersed in IPA. The orange and green curves refer to TTIP concentrations of 0.26 mM and 2.6 mM, respectively. The former correspond to the sample shown in Figure 4.2a, while the latter corresponds to the one in Figure S4.1. For the lower concentration (orange), the longitudinal mode at 600 nm shows only a small redshift compared to the bare NRs, confirming shell formation resulting in an increase in the local refractive index. In contrast, at higher concentration (green), the plasmon peak is no longer clearly visible, while the TiO_2 peak around 300 nm becomes more prominent. This suggests that higher TTIP concentration leads to uncontrolled titania formation and Au nanoparticles are embedded in large amorphous networks, as confirmed by the STEM images in Figure S4.1.

In conclusion, the use of TTIP as a precursor did not allow for controlled TiO_2 shell growth around Au nanorods. Uniform shell thickness could not be achieved, and increasing precursor concentration led to the formation of large amorphous titania networks rather than well defined core–shell nanostructures. This behavior is consistent with the high reactivity of TTIP previously discussed. The residual water in the nanoparticle dispersion increased the water-to-titanium ratio and promoted rapid hydrolysis and condensation [154]. Under these conditions, homogeneous nucleation in solution competed with heterogeneous nucleation on the Au surface. At low precursor concentrations this resulted in non-uniform shell growth, while at higher concentrations the balance shifts further toward homogeneous nucleation, leading to extended amorphous networks in which the Au nanoparticles become embedded in-

stead of forming distinct core–shell structures.

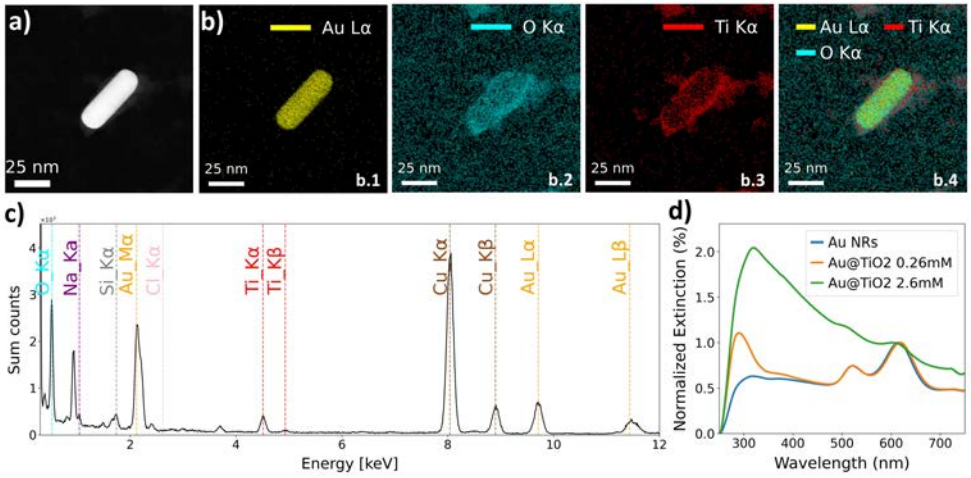

Figure 4.2: *TTIP-based amorphous TiO_2 shell growth a) STEM image of AuNRs after growth of a TiO_2 shell for 0.26 mM TTIP b) EDX net counts map for selected elements: Au, Ti, and O. c) Uncorrected sum EDX signal d) UV-vis spectra of the bare AuNR solution (blue) and after the growth of a titania shell at different TTIP concentrations, 0.26 mM in orange and 2.6 mM in green.*

b. Titanium (III) chloride precursor

The colloidal growth of an amorphous TiO_2 shell around both citrate and SDS capped AuNRs using $TiCl_3$ as precursor was carried out following a protocol adapted from Wu et. al. [163] and Fang et. al. [126]. $TiCl_3$ is stabilized in strongly acidic conditions (initial pH $\sim$ 1.4). The pH is then gradually increased to approximately 2.5–3 by controlled addition of $NaHCO_3$, which induces partial hydrolysis of the Ti precursor and enables controlled shell growth. Details on the synthesis are provided in the *Appendix 4.4.1b.*

First, the results for citrate-capped NRs are discussed. In Figure 4.3a, a representative STEM image after TiO_2 shell growth shows the formation of a relatively uniform TiO_2 shell around the Au NR. The corresponding EDX maps (Figure 4.3b) and spectrum (Figure 4.3c) show no significant impurities. Figure 4.3d presents the UV–Vis spectra before (blue curve) and after (green curve) shell growth, where a redshift of approximately 80 nm of the longitudinal LSPR is observed, consistent with an increased local refractive index. The plasmon peak remains well defined, indicating that aggregation is minimal and that the sample consists mainly of isolated particles, as confirmed by overview TEM images shown in S4.2a. However, the shell thickness

could not be increased beyond ∼10 nm, even at higher precursor concentration or faster $NaHCO_3$ addition. This limited shell growth is likely due to the presence of the hydrophilic citrate, which stabilizes Ti species in solution and prevents aggregation, limiting further deposition onto the particle surface. To quantify the shell density of citrate capped $AuNR@TiO_2$, we measured the dark-field scattering (DFS) spectra of 10 particles and correlated each with the morphology form TEM measurements. By combining the shell thickness measured from TEM with the magnitude of the LSPR redshift from scattering, the effective refractive index of the shell can be estimated through optical simulations. Using effective medium theory, the shell was modeled as a porous mixture of TiO_2 and immersion oil used for the DFS measurements. As shown in Figure S4.3, by matching optical simulations with the measured scattering we estimated a TiO_2 volume fraction of approximately 0.3. Details are given in the *Appendix 4.4.1.A*.

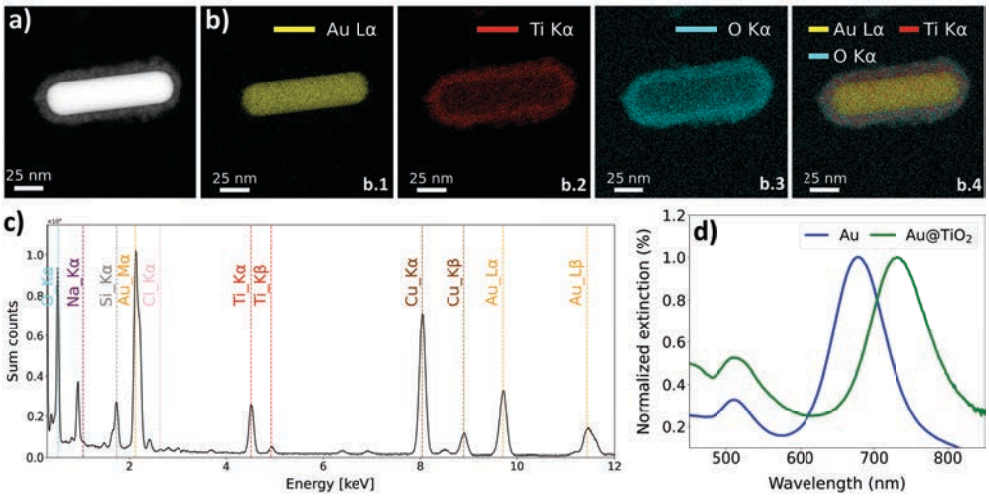

Figure 4.3: *$TiCl_3$ amorphous shell grown around citrate-stabilized $Au@TiO_2$ nanorods a) STEM image b) EDX net counts map for selected elements: Au, Ti, and O. c) Uncorrected sum EDX signal. d) UV-vis spectra of the bare AuNR solution (blue) and after the growth of a titania shell (green)*

The same synthesis procedure was repeated for SDS-capped AuNRs. Figure 4.4a shows the UV–Vis spectra for the SDS capped NRs before (blue curve) and after growth of amorphous TiO_2 shells at varying addition rates of $NaHCO_3$. Increasing the $NaHCO_3$ addition rate, and therefore the hydrolysis rate, induced a progressive red-shift of the longitudinal plasmon peak due to the thicker TiO_2 shell. Slower, truly dropwise addition produced thinner and more uniform shells (green curve), while faster addition promoted earlier hydrolysis in solution, leading to thicker shells

(pink and purple curves). This is confirmed by the corresponding TEM images shown in Figure 4.4b, which revealed an increasing TiO_2 shell thickness from 6 to 40 nm. As in the citrate case, the particles remain as individual nanorods, as demonstrated by the well-defined UV–Vis plasmon peak and the overview TEM image shown in Figure S4.2b.

By combining the shell thickness measured from TEM with the magnitude of the LSPR redshift from UV–Vis, the effective refractive index of the shell can be estimated through optical simulations. As for the scattering case, the shell was modeled as a porous mixture of TiO_2 and water using effective medium theory. A TiO_2 volume fraction of 0.2 was obtained for all shell thicknesses (see *Appendix 4.4.1.A*). This indicates that the amorphous shell is highly porous. Comparing this result with the higher TiO_2 volume fraction of 0.3 obtained for citrate-capped systems suggests that SDS results in a more porous shell. This is consistent with the larger molecular size of SDS and its tendency to form micelle-like aggregates, which can act as soft templates during TiO_2 shell growth. In addition, the higher stability of SDS under acidic conditions may allow the surfactant layer to remain present during the early stages of nucleation, promoting the formation of a more open and less dense shell.

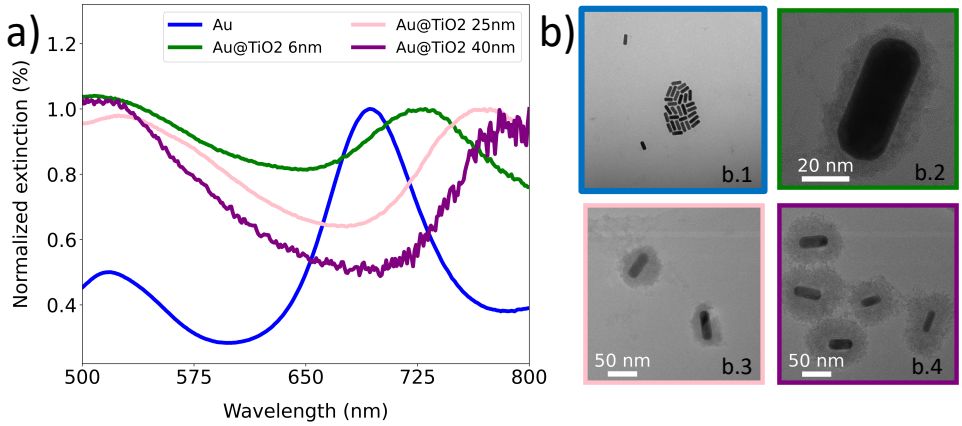

Figure 4.4: *$TiCl_3$-based amorphous TiO_2 shell grown around SDS-stabilized $Au@TiO_2$ nanorods a) UV-vis spectra for bare Au-SDS capped NRs (blue) and for different TiO_2 shell thicknesses between 6 nm and 40 nm. b) Corresponding representative TEM images.*

The EDX map of the thickest shell (Figure 4.5) reveals a clearly detectable Na and Cl signal (Figure 4.5b.4), significantly higher than in citrate-based systems. The same impurities were found in the thinner shell in Figure S4.5. Since both Na and Cl species are introduced during the synthesis through $NaHCO_3$ and $TiCl_3$, their

presence would be expected in all samples. However, in citrate-based systems almost no Na signal and only a very weak Cl signal are detected. This suggests that the impurities do not originate primarily from the precursors themselves, but from how they interact with the ligand environment. In SDS-based systems, the interaction between the sodium head groups and the porous TiO_2 network may promote trapping of Na and Cl species within the shell, leading to their higher concentration compared to citrate-based samples.

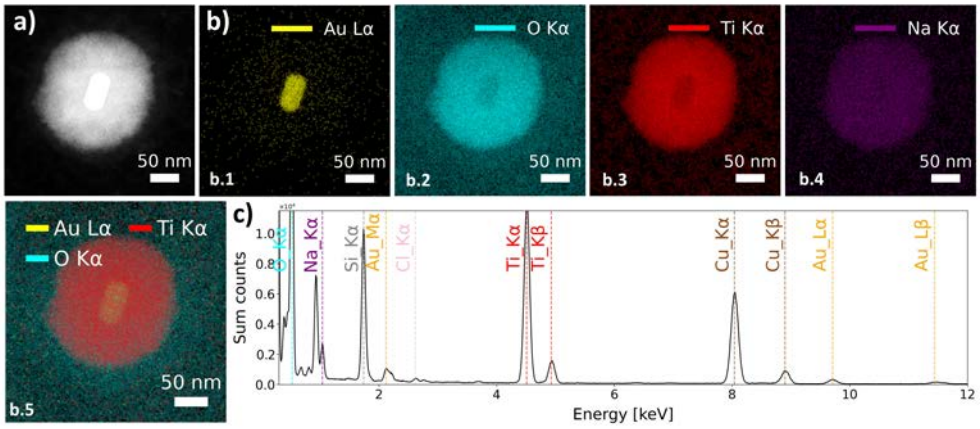

Figure 4.5: *$TiCl_3$ amorphous shell grown around SDS-stabilized $Au@TiO_2$ nanorods a) STEM image b) EDX net counts map for different element: Au, O, Ti, Na. c) Uncorrected sum EDX signal.*

Together, these results demonstrate that controlled amorphous TiO_2 shell growth around AuNRs requires careful matching of precursor chemistry and ligand choice. TTIP-based synthesis did not yield uniform shells under the conditions explored, with higher precursor concentrations leading to uncontrolled network formation rather than conformal coating. In contrast, $TiCl_3$ enabled more controlled growth, despite the expected rapid hydrolysis behavior. All syntheses were performed in excess of titania precursor, resulting in free TiO_2 in solution, which was removed during washing. Shell thickness was therefore primarily governed by the $NaHCO_3$ addition rate. Only for SDS system control over the shell thickness was achieved. Ligand choice strongly determined the final structure. Citrate-capped AuNRs produced relatively pure shells with a self-limiting thickness of ∼10 nm, while SDS-capped systems allowed much thicker shells (up to 40 nm) at the cost of high porosity and significant sodium and chloride incorporation. The observed differences in shell density, porosity, and impurity incorporation are expected to strongly influence mass transport, nucleation processes, and crystalline phase upon crystallization.

Preliminary single-particle structure–property correlation

Having established the structural differences between TTIP- and $TiCl_3$-based amorphous shells, we now investigate whether these differences are reflected in the optical response of the nanorods through preliminary single-particle dark-field scattering measurements. As introduced earlier, charge transfer at the Au/TiO_2 interface can be probed via linewidth broadening arising from chemical interface damping (CID). This provides information on the rate of electron injection across the interface, but does not directly capture the subsequent carrier dynamics within the TiO_2. Transport to the surface, as well as competition with back-transfer and defect trapping, are governed by the crystallinity and defect density of the TiO_2. Single-particle linewidth analysis therefore represents one important component, but must ultimately be combined with complementary techniques such as transient absorption spectroscopy to disentangle injection efficiency from carrier dynamics in the semiconductor. While linewidth broadening reflects injection efficiency, transient absorption probes the population of free carriers in the TiO_2 conduction band and their decay dynamics, enabling a more complete picture of charge transfer and transport processes.

In this work, single-particle scattering spectra of bare Au nanorods and $Au@TiO_2$ nanorods were measured for citrate-based samples synthesized using both TTIP and $TiCl_3$ precursors. Importantly, the shells are still amorphous at this stage, such that no influence of crystallinity is expected. Each particle was subsequently imaged by TEM to determine its exact morphology, allowing direct comparison with boundary element method (BEM) simulations performed on the experimentally determined geometries. The simulations for the $TiCl_3$ based samples were carried out using an effective shell refractive index of $n = 1.85$, consistent with the TiO_2 volume fraction of ~ 0.32 (see *Appendix 4.4.1.A*). For the TTIP based ones an average refractive index of $n = 1.9$ was used. As shown in Figure 4.6, this results in good overall agreement between simulated and experimental peak positions for most particles. The $TiCl_3$-based samples (Figure 4.6b) exhibit a clearer and more reproducible redshift upon shell growth, consistent with the formation of a more uniform and conformal shell. In contrast, TTIP-based samples (Figure 4.6a) show increased scatter in peak position, reflecting a less controlled shell morphology. The experimental linewidth was extracted by fitting a Lorentzian profile convolved with a Gaussian function (FWHM = 2.5 nm in wavelength) to account for the finite bandwidth of the LTTF filter. When plotted as a function of peak position in Figure 4.6c-d, the bare Au nanorods show the expected increase in linewidth toward higher energies due to the dielectric response of gold. Upon coating with TiO_2, an additional broadening is observed for both precursor systems, consistent with increased damping introduced by the shell. Although some spread remains due to uncertainties in fitting, particle morphology, and refractive index assumptions, the overall trends consistently indicate enhanced damping

in $Au@TiO_2$ nanorods compared to bare Au nanorods when comparing particles of similar volume and resonance energy. No systematic dependence on particle volume is observed, which is not unexpected given the relatively limited volume differences among NRs.

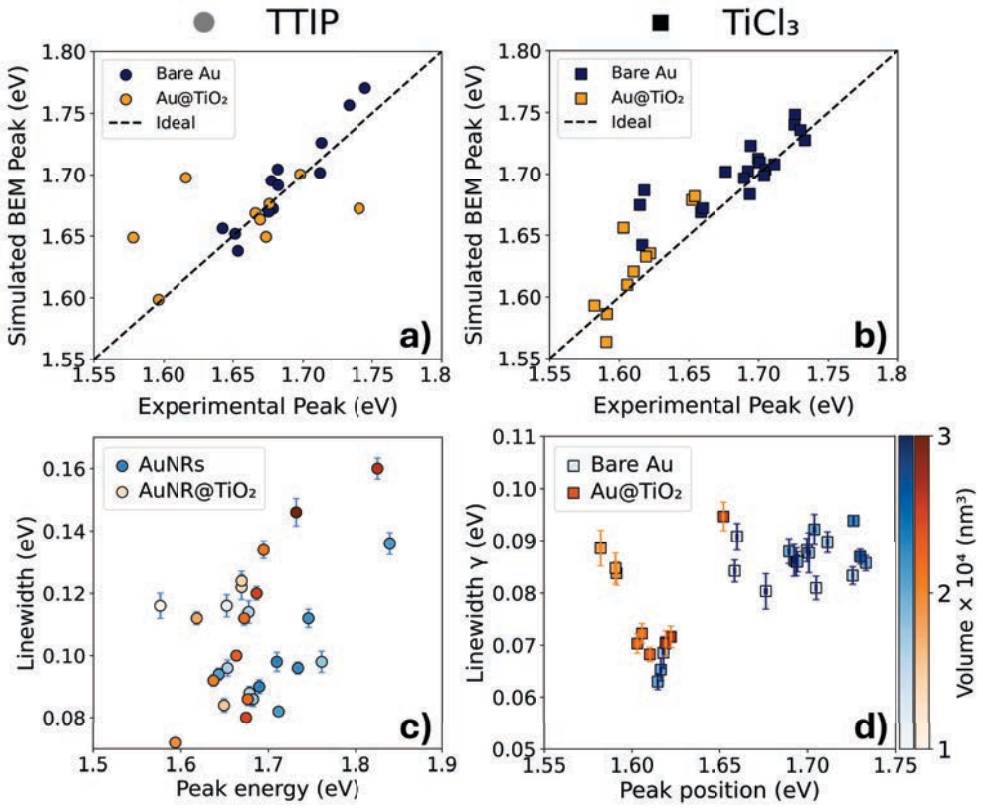

Figure 4.6: *Comparison of plasmon peak position and linewidth for bare Au nanorods (blue) and TiO_2-coated Au nanorods (orange) synthesized using two different precursors: TTIP (○) and $TiCl_3$ (□). a,b) Simulated BEM peak energies plotted against experimental values, with the dashed line indicating ideal one-to-one correspondence. c,d) Linewidth as a function of peak position, showing the distribution and variability of plasmon damping. Marker color represents particle volume ($\times 10^4$ nm^3). Error bars correspond to uncertainties obtained from Lorentzian fit.*

However, a key limitation of the present dataset is the strong dependence of the measured linewidth on laser intensity. The correction applied here was not sufficient to fully account for this effect, preventing a quantitative interpretation of the observed broadening in terms of CID efficiency. In addition, the measurements remain

incomplete, as only citrate-based samples were characterized and insufficient time remained to extend the study to SDS-based systems after further optimization of the experimental setup.

Despite these limitations, the results demonstrate that TiO_2 shell formation induces measurable changes in both peak position and linewidth, highlighting the sensitivity of the optical response to interfacial and structural properties. These findings motivate future systematic studies combining DFS and transient absorption spectroscopy at the single-particle level. Such an approach will enable simultaneous access to injection efficiency and carrier dynamics, allowing a more complete understanding of how synthesis, morphology, and interface quality influence charge transfer pathways. Ultimately, these insights can be correlated with photocatalytic performance to assess whether improved control over the TiO_2 structure can overcome the typically low efficiencies of plasmonic systems.

4.3.3 Crystallization strategies

A standard method to crystallize amorphous TiO_2 is thermal heating at temperatures above 400°C. However, at these temperatures Au atoms become mobile, leading to nanoparticle deformation and additional surface roughness and defects. Such morphological changes broaden the LSPR linewidth through increased (surface) scattering, complicating quantitative interpretation of linewidth changes in terms of charge-transfer efficiency. Furthermore, they potentially reduce injection efficiency in the TiO_2 by introducing a competing plasmon decay channel as discussed in the *Introduction*. To overcome these limitations, we explore alternative crystallization routes that may reduce Au reshaping while enabling TiO_2 crystallization. Two approaches are considered: low-temperature hydrothermal crystallization and laser-induced crystallization. These differ in both heating mechanism and timescale, and are therefore expected to lead to different structural and interfacial outcomes.

As discussed in the *Introduction*, both the crystalline phase and the degree of crystallinity of the TiO_2 shell are expected to strongly influence carrier transport and photocatalytic efficiency, making control over phase selection a key objective. Amorphous TiO_2 crystallizes as anatase at lower temperatures, while rutile is the thermodynamically stable phase above 600–800 °C [131, 164]. However, the crystallization behavior depends also on the structural properties of the amorphous material, determined by precursor and ligand choice [131]. In particular, oxygen vacancies can promote rutile formation well below this threshold temperature by lowering the activation energy for lattice rearrangement [131, 165]. Chemical conditions such as pH further influence phase selection. Strongly acidic conditions (pH $\leq$ 1) promote rutile formation at lower temperatures [166], but are incompatible with the colloidal stability of citrate- and SDS-capped nanorods [167, 168].Additionally, crystallization is

kinetically controlled. Slower heating rates allow the anatase-to-rutile transformation to initiate and complete at lower temperatures, whereas faster heating suppresses this conversion, shifting it to higher temperatures where the thermodynamic driving force is larger [131]. These constraints mean that phase outcome in $Au@TiO_2$ systems is determined by the interplay between shell defect density, reaction conditions, and the limits imposed by the nanoparticles stability.

4.3.3.A Low temperature hydrothermal crystallization

Hydrothermal crystallization transforms amorphous materials into crystalline phases in aqueous media. Already in 1998, Yanagisawa and co-workers showed that water can accelerate the crystallization of amorphous titania into anatase [136]. Water incorporates into the amorphous TiO_2 network, increasing the mobility of Ti species and lowering the activation energy for structural rearrangement, enabling crystallization at temperatures far below those required for conventional dry annealing. [136].

For the TTIP-based system (Figure 4.2), crystallization was observed only in thinner titania regions, while most of the shell remained amorphous. This is likely a consequence of the low defect density of TTIP-derived TiO_2, resulting in a higher activation energy for lattice reorganization. Combined with the lack of controlled shell growth, this led us to focus on the $TiCl_3$-based system, where the amorphous network is more porous and favorable for rearrangement.

a. Titanium (III) chloride precursor Based on the amorphous shell properties discussed in *Section 4.3.2*, we expect the hydrothermal crystallization behavior to depend strongly on the defect density and impurity content of the amorphous TiO_2 shell. For citrate-based shells, the lower Na incorporation compared to SDS-based shells results in fewer impurities and oxygen vacancies, which is expected to favor anatase as the dominant crystallization product under mild conditions. To test this, the amorphous $Au@TiO_2$ NRs solutions were heated in an oil bath at 100 °C for two hours. This temperature was identified as optimal: no crystallization occurred at 80 °C, while 150 °C led to poor reproducibility due to solvent evaporation and aggregation.

First, the results using the citrate amorphous $Au@TiO_2$ NRs from Figure 4.3 after heating are discussed. Representative STEM–EDX and TEM and diffraction images of the resulting structures are shown in Figure S4.6 and Figure 4.7, respectively. The initially uniform TiO_2 shell reorganized into a porous and discontinuous network (Figure S4.6). In some cases, a better-preserved shell was partially retained for reasons that remain unclear. This restructuring suggests dissolution–reprecipitation processes under hydrothermal conditions, driven by increased mobility of Ti species. The release or redistribution of Cl^- and Na^+ ions initially trapped in the

shell may further contribute to this restructuring. Given the low impurity content of citrate-based shells, this effect is expected to be minor. Consistent with this, UV–Vis spectra show a blue-shift of the longitudinal plasmon peak after hydrothermal treatment (Figure S4.6d), indicating a reduced effective refractive index due to increased porosity.

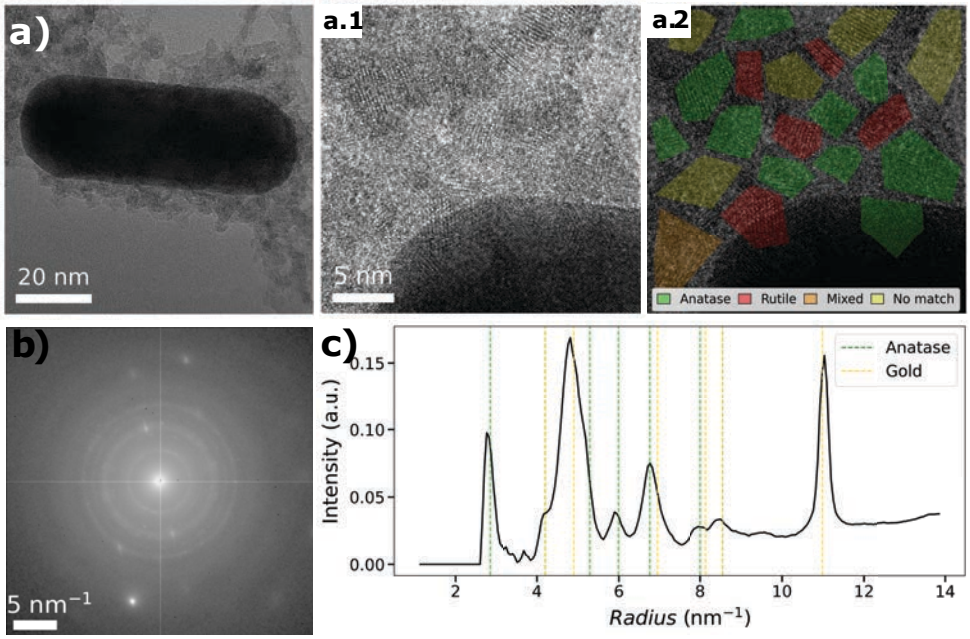

Figure 4.7: *Citrate-stabilized $Au@TiO_2$ after low temperature crystallization in solution a) TEM image of a NR with a crystalline titania around. a.1) Zoom-in to highlight the interface and the crystallinity of the titania shell. In a.2 individual crystalline patches are identified and color-coded according to the TiO_2 polymorph determined from FFT d-spacings: anatase (green), rutile (red), mixed anatase/rutile (orange), and regions where no TiO_2 reflection could be assigned within 6% tolerance (yellow). b) Diffraction profile of the same NR as in a). c) Azimuthally averaged radial intensity profile of the diffraction pattern in (b), with expected peak positions from the literature indicated by dashed lines: Au in yellow, and TiO_2 anatase in green.*

Despite the discontinuous morphology, TEM and diffraction reveal the presence of many crystalline patches. A representative high-resolution TEM image is shown in Figure 4.7a. Individual crystalline patches were identified and assigned to TiO_2 polymorphs based on FFT-derived d-spacings, as described in *Section 4.2.2*. FFT analysis of 20 patches shows 50% anatase, and 25% rutile, whereas 25% could not be unambiguously assigned within the applied tolerance. These results indicate that anatase is the predominant phase under these conditions. The violin plot in Figure S4.7a provides the full distribution of extracted d-spacings. It is worth noting that a fraction of the measured d-spacings exceed the bulk anatase value of 0.352 nm, indicating lattice distortion likely induced by residual defects within the shell [169, 170]. The average crystalline domain area, quantified from Figure 4.7a.2 is $\sim$18 nm^2, as summarized in Figure S4.7b. Selected-area electron diffraction (SAED) in Figure 4.7b-c confirms the predominance of the anatase phase.

The $Au@TiO_2$ samples prepared from SDS-capped Au NRs were subjected to the same hydrothermal treatment at 100 °C. First, results from the thin SDS sample (green curve in Figure 4.4a) are discussed. A representative STEM image and the corresponding EDX elemental maps of a heat-treated TiO_2-coated NR are shown in Figure S4.8a and b, respectively. Figure 4.8a shows a TEM image of another nanorod from the same batch, together with zoom-in views of the interface (a.1 and a.2). After hydrothermal treatment, the shell develops some discontinuities.

The high-resolution TEM images in Figure 4.8a reveal the presence of crystalline patches within the shell. However, phase analysis of the thin SDS shell was more challenging than for the citrate sample, mainly because the characteristic d-spacings of anatase and brookite are very similar and difficult to distinguish at the FFT resolution of the TEM images used here ($0.01\,nm^{-1}$). As for the citrate case, individual crystalline patches were identified, and for each patch the FFT was calculated and the corresponding d-spacing extracted. Figure 4.8b shows the resulting phase map, while the distribution of extracted d-spacing values is summarized in the violin plot in Figure 4.8c. Overall, the data confirm that the TiO_2 shell crystallized upon hydrothermal treatment. An unambiguous distinction between anatase and brookite cannot be made from these measurements alone, and higher-resolution imaging would be required. Interestingly, the average crystalline domain area was $\sim$39 nm^2, larger than the 18 nm^2 observed for the citrate sample. This may indicate the presence of rutile, which is known to form larger crystallites than anatase and would be consistent with the higher impurity content of SDS-derived shells promoting rutile formation through defect-assisted crystallization.[131].

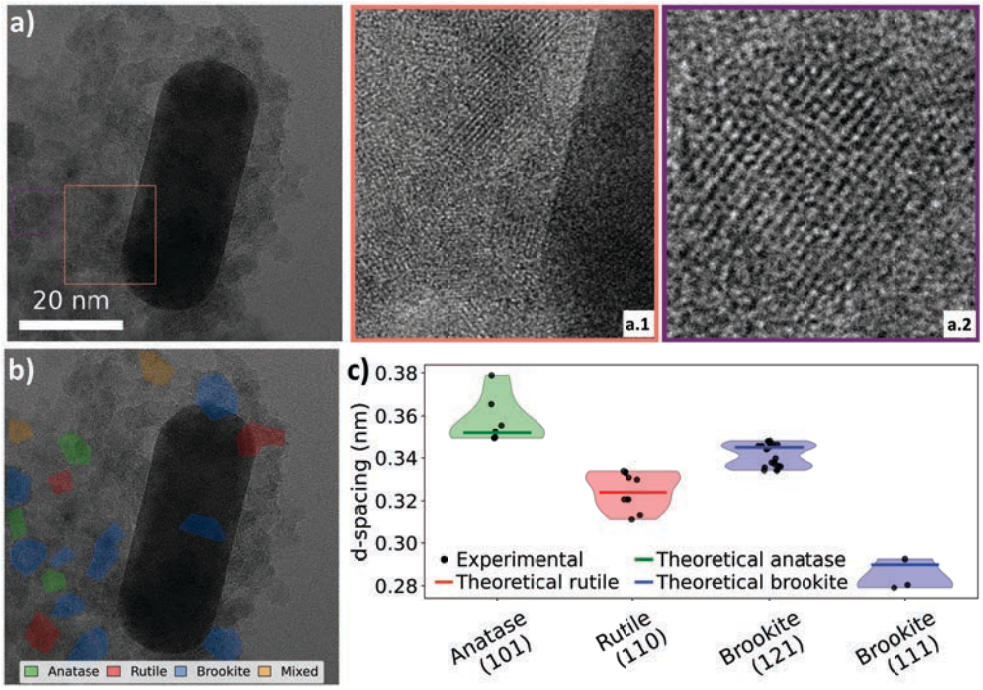

Figure 4.8: *Thin-shell SDS-stabilized $Au@TiO_2$ nanorods after low-temperature crystallization in solution. a) TEM image of a representative $Au@TiO_2$ nanorod. Insets (a.1 and a.2) show magnified views of the regions highlighted in (a). b) Phase map of the crystalline patches identified in (a), with domains color-coded according to the assigned TiO_2 polymorph based on FFT-derived d-spacings: anatase (green), rutile (red), brookite (blue), mixed anatase/rutile (orange), and unassigned regions (yellow). Phase attribution was performed using a relative tolerance of 6%. c) Violin plot showing the distribution of d-spacings measured for the crystalline domains in (b).*

The thicker SDS sample (pink curve in Figure 4.4a, corresponding to a shell thickness of approximately 25 nm) was subjected to the same hydrothermal treatment at 100 °C. As shown in the TEM image in Figure 4.9a, an increase in shell thickness from 25 nm to 35 nm is observed after heat treatment. This increase in apparent shell thickness likely reflects swelling of the amorphous network under hydrothermal conditions, as water molecules are incorporated into the TiO_2 structure in the form of Ti-OH groups. The overall shell morphology is substantially better preserved compared to both the citrate and thin SDS samples, with the shell remaining largely continuous around the nanorod. Crystallographic analysis is more limited, as the thick shell hinders atomic-resolution imaging. Only a few crystalline patches could be clearly identified (Figure 4.9a.1). The available data suggest predominantly anatase crystal-

lization although a statistically robust phase assignment is not possible. The relatively low overall degree of crystallinity and preserved morphology may be attributed to limited water penetration. Since hydrothermal crystallization relies on hydration of the amorphous network, crystallization likely occurs mainly in the outer regions, while inner regions remain amorphous. The electron diffraction pattern shown in Figure 4.9b, provides ensemble-level crystallographic information. The corresponding azimuthally averaged radial intensity profile in Figure 4.9c shows diffraction peak positions consistent with the main reflections of anatase TiO_2, although the peaks are weaker and less pronounced than those observed for the thinner shells, consistent with the limited water penetration and lower degree of crystallinity of the thick shell discussed above.

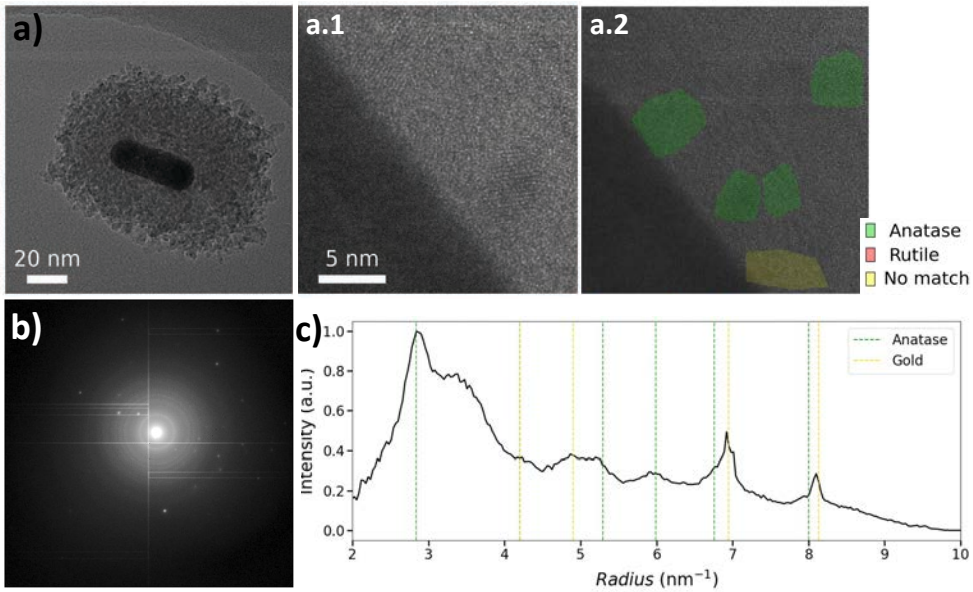

Figure 4.9: *Thick shell SDS-stabilized $Au@TiO_2$ nanorods after low-temperature hydrothermal crystallization. a) TEM image of a NR with a crystalline titania around. a.1) Zoom-in to highlight the interface and the crystallinity of the titania shell. a.2) Phase map of individual crystalline patches identified in (a.1), color-coded according to the TiO_2 polymorph assigned from the d-spacings obtained from the FFT. b) Electron diffraction pattern acquired from the nanorod shown in (a). Horizontal straight lines are just an artifact of the detector. c) Azimuthally averaged radial intensity profile of the diffraction pattern in b), with expected peak positions from the literature marked as dashed lines: Au in yellow, and anatase TiO_2 in green*

Hydrothermal treatment at 100 °C induced crystallization in $TiCl_3$-based shells, although further optimization is required to reduce shell porosity and preserve the

initial core–shell morphology. Morphologically, citrate-based shells exhibited porous and discontinuous structures, whereas SDS-based shells were better preserved. This is consistent with a templating effect of the surfactant layer. SDS is known to undergo sulfate ester hydrolysis in water at 100 °C on the timescale of hours [171]. The TiO_2 shell undergoes condensation and partial crystallization sufficient to preserve the mesoscale structure before the surfactant hydrolyzes and its products diffuse out of the matrix, leaving a well-preserved but porous core-shell architecture. In the citrate case, the absence of such a templating layer allows uncontrolled dissolution-recrystallization, ultimately disrupting the shell morphology. In terms of crystallinity, anatase dominated in the citrate system, while phase identification in SDS samples remained uncertain due to limited resolution and patch statistics. The possible influence of the higher defect density in SDS-derived shells on rutile formation could not be resolved under these mild conditions, which is consistent with the strongly temperature-dependent nature of defect-assisted phase selection: at 100 °C, the thermodynamic driving force for anatase formation may simply dominate regardless of defect density, and the activation energy for rutile nucleation remains too high to be overcome by oxygen vacancies alone. The possible influence of the higher defect density in SDS-derived shells can become more relevant at higher temperatures, where defect-assisted phase transformation is expected to dominate. In addition, hydrolysis of SDS during treatment may generate local acidity (via formation of bisulfate species [171]), which could influence condensation and phase selection. While strongly acidic conditions are known to promote rutile formation [166], the extent of acidification under the present conditions is likely insufficient to overcome the kinetic barriers to rutile nucleation at 100 °C.

4.3.3.B Laser induced crystallization

Laser-induced heating in the TEM provides an alternative pathway to crystallization that differs fundamentally from conventional thermal annealing in both timescale and peak temperature. The rapid optically driven heating and cooling generate short thermal spikes that can reach much higher peak temperatures than conventional annealing. It can therefore provide enough local energy for TiO_2 crystallization while limiting long-range atomic diffusion in the Au core due to rapid heat dissipation. This is expected to better preserve nanorod morphology compared to conventional annealing, where prolonged heating at high temperatures leads to significant Au atom mobility and nanorod reshaping. It should be noted that the TEM operates under high vacuum conditions, where the extremely low oxygen partial pressure thermodynamically favors oxygen loss from the TiO_2 lattice, promoting the formation of oxygen vacancies. This contributes to the defect landscape governing phase selection alongside impurity content, a factor that must be considered when interpreting the crystallization outcomes below. An additional advantage is that crystallization can

be carried out directly inside the TEM, allowing real-time observation of structural changes.

After synthesis and washing, the solutions were drop-cast onto Quantifoil TEM grids consisting of a copper mesh supporting a thin carbon film. The grids contain 200 square windows (100 μm × 100 μm) formed by a 20 nm carbon film. Inside the TEM, the $Au@TiO_2$ nanostructures were illuminated with high laser fluence (6–18 $\mu J/cm^2$) at their resonance wavelength. Although $Au@TiO_2$ nanostructures absorb light via their LSPR, COMSOL Multiphysics simulations in *Chapter 5* showed that photothermal heating of the carbon support dominates under these conditions. For example, at a fluence of 6 $\mu J/cm^2$, the carbon film reached temperatures of ∼1000 K at the center, decreasing to 700 K within 25 μm (Figure S5.2). Control experiments on SiO_2 grids, which do not absorb efficiently, showed no crystallization or reshaping of the Au even at the highest fluence, confirming that under the present experimental conditions laser-induced crystallization is primarily driven by substrate-mediated heating.

a. Titanium (IV) isopropoxide precursor

We first investigate laser-induced crystallization for the TTIP-based system. Although hydrothermal treatment was not carried out for this sample due to the uncontrolled network morphology, it provides a useful reference case for laser-induced crystallization. Like the $TiCl_3$/citrate sample, it uses citrate as a ligand, but unlike that sample it contains a measurable amount of Na contamination from incomplete washing (Figure 4.2c). It therefore represents an intermediate case in terms of impurity content, between the clean $TiCl_3$/citrate system and the Na-rich $TiCl_3$/SDS system. This allows us to assess how Na-related oxygen vacancies influence phase selection across the three cases.

Laser-induced crystallization was performed on the sample with a relatively thick TiO_2 network (green spectrum in Figure 4.2d and STEM image in Figure S4.1). The particles were irradiated using the laser in-coupling module integrated into the TEM for 15 s, with picosecond laser pulses at 600±5 nm and a fluence of 8 $\mu J/cm^2$. At the repetition rate used in the experiment (78 MHz), the time between pulses was 12.8 ns, while the pulse duration at this wavelength was ∼ 30 ps. Figure 4.10 shows a representative nanorod before (a) and after (b) laser exposure. The magnified images in b.1 and b.2 reveal the formation of crystalline domains within the TiO_2 shell following laser irradiation. In Figure 4.10c individual crystalline patches identified in panel (b) are overlaid and color-coded according to the TiO_2 polymorph assigned from FFT-derived d-spacings. A clear predominance of the rutile phase is observed. The violin plot in Figure S4.9a provides the full distribution of the extracted d-spacings. This is confirmed by SAED in Figure 4.10d–e, where diffraction peaks are consistent with those of rutile.

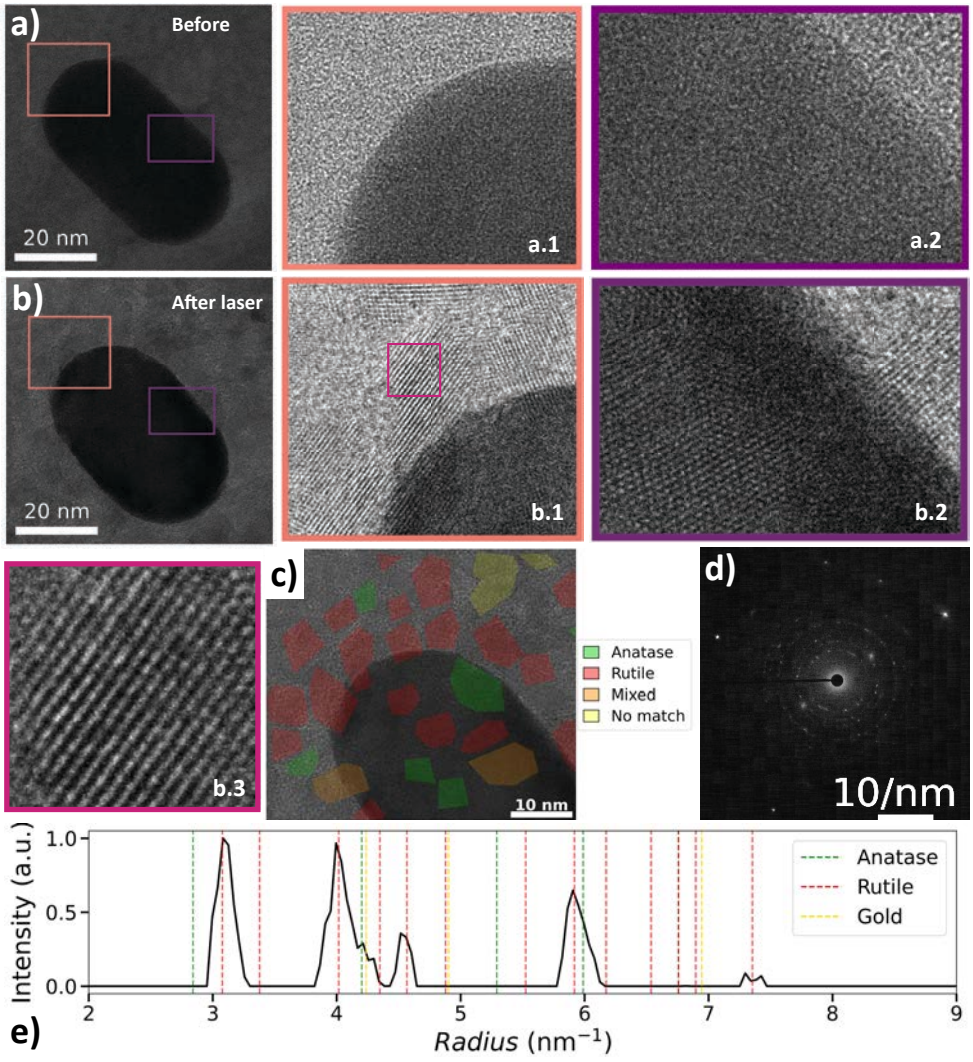

Figure 4.10: *Laser induced crystallization of a TTIP citrate-stabilized $Au@TiO_2$NR. a) TEM image of a AuNR coated with a titania shell, with magnified views of the $Au@TiO_2$ interface shown in panels a.1 and a.2. b) The same NR after 30 seconds of laser exposure at $600 \pm 10\,nm$ with a fluence of $8\,\mu J/cm^2$ inside the TEM. Panels b.1 and b.2 show zoomed-in regions of the interface highlighting the crystalline nature of the titania upon laser illumination. b.3) Shows the zoom-in of the highlighted area in b.1. c) Assignment based on the FFT of each patch to the different TiO_2 polymorphs. d) Diffraction pattern of the same NR shown in (b). e) Azimuthally averaged radial intensity profile of the diffraction pattern in (c), with expected peak positions from the literature marked as dashed lines.*

As discussed in *Section* 4.3.3, rutile formation is favored by a high defect density, in particular oxygen vacancies. The observed preference for rutile in this sample is therefore consistent with the sodium impurities detected in the EDX map of the amorphous TiO_2 shell (Figure 4.2). Because Na^+ has a lower valence than Ti^{4+}, its incorporation into the TiO_2 network creates oxygen vacancies to maintain charge neutrality, lowering the activation energy for rutile formation [131, 165]. In addition, the low oxygen partial pressure in vacuum favors oxygen loss from the TiO_2 lattice, leading to the formation of oxygen vacancies. However, the dominant contribution to oxygen vacancy formation, and thus to rutile crystallization, is attributed to the presence of sodium, as will become apparent from the $TiCl_3$/citrate samples discussed below, where a lower defect density correlates with preferential anatase formation. The average crystalline domain area was $35\,nm^2$. The relatively larger crystalline domains observed here are consistent with the tendency for rutile to form coarser grains [131].

A key motivation for laser-induced crystallization was to limit Au nanorod reshaping compared to conventional thermal annealing. The results support this: as shown in Figure S4.10, the aspect ratio decreases consistently but mildly upon pulsed laser illumination across four particles, by approximately 0.2, with one particle showing no measurable change. Furthermore, the Au cores after illumination do not appear significantly roughened. This suggests that surface scattering remains limited, and therefore would not introduce a significant additional contribution to LSPR linewidth broadening. As a result, reliable single-particle linewidth measurements can still be performed.

As an attempt to assess the effect of TiO_2 crystallization on the optical properties, the evolution of the single-particle scattering response under laser illumination was followed using the home-built dark-field scattering setup described in *Chapter 2* and Figure 2.2. The $Au@TiO_2$ sample was drop-cast on a SiO_2 grid and measured using a immersion oil objective. The grid is therefore immersed in immersion oil of refractive index 1.518 and thermal conductivity of $\sim 0.13 - 0.17$ W/(mK) compared to the $\sim$0.026 W/(mK) for air, approaching zero for vacuum. First, a spectrum of the $Au@TiO_2$ NR was acquired. Then the laser was set to the wavelength peak of the measured LSPR, and focused, at 100% power and a 78 MHz repetition rate. The fluence of the laser at the sample plane was $\sim 800\,\mu J/cm^2$). The single $Au@TiO_2$NR was illuminated for one minute at this power. The spectra before and after high power laser illumination together with the TEM image after lase exposure are shown for 2 different particles in Figure 4.11. In all cases a blueshift and an increase in FWHM are observed, indicating that the particles reshaped under these conditions due to the high fluence used. A broadening potentially attributable to TiO_2 crystallization cannot be unambiguously identified without a pre-exposure TEM image to establish the initial shell structure. These results highlight two key challenges in

translating the TEM crystallization conditions to the optical setup. First, the much higher thermal conductivity of the immersion oil compared to vacuum means that the same laser fluence produces substantially less heating in the optical experiment. Second, the SiO substrate used here does not absorb as efficiently as the carbon support used in the TEM, further altering the heating conditions. Together, these differences make it difficult to directly apply the fluence parameters optimized in the TEM to the optical setup, and the absence of real-time structural monitoring makes iterative optimization challenging. Nevertheless, these measurements demonstrate that with optimized intermediate fluences, sufficient for shell crystallization but below the reshaping threshold, this approach has the potential to become a valuable tool for directly correlating TiO_2 crystallization with changes in plasmonic damping at the single-particle level.

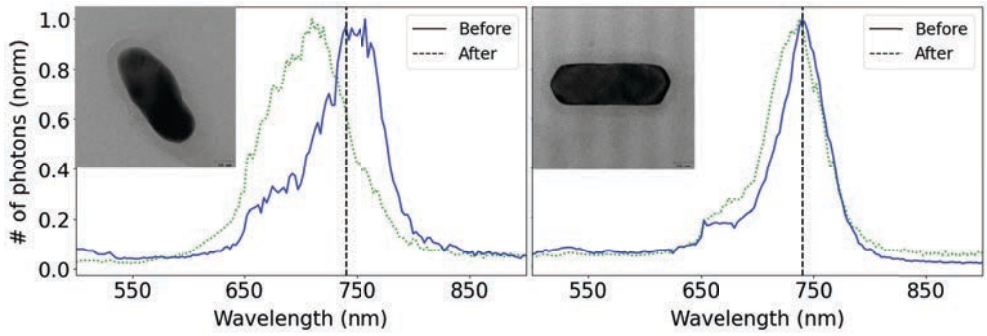

Figure 4.11: *Single-particle dark-field scattering spectra of two $AuNR@TiO_2$ nanoparticles before (blue solid line) and after (green dashed line) laser illumination at higher power. Each particle was illuminated for 1 minute at 78 MHz with a measured power of 1.1 mW. The excitation wavelength was chosen individually to match the longitudinal surface plasmon resonance (LSPR) of each $AuNR@TiO_2$ and is indicated by the vertical black dashed line*

b. Titanium (III) chloride precursor

To assess the influence of impurity content and oxygen vacancy density on phase selection, laser-induced crystallization was also performed on $TiCl_3$-based samples. The particles were irradiated for 60 s at 700 ± 5 nm with a fluence of $5\,\mu J\,cm^{-2}$. The longer wavelength compared to the TTIP experiments (600 ± 5 nm) was chosen to match the LSPR of the $Au@TiO_2$. However, as discussed we later found that crystallization is mainly driven by photothermal heating of the carbon support film, which absorbs over a broad wavelength range. Therefore, the excitation wavelength has little effect on the heating conditions.

First, representative results for citrate-capped NRs are shown in Figure 4.12. A well-defined and mainly crystalline TiO_2 shell is formed upon laser irradiation, as shown in Figure 4.12b. High-resolution TEM images of another particle from the same batch after laser-induced crystallization in Figure 4.12c (c.1-3) confirm the formation of crystalline domains inside the TiO_2 shell. Each crystalline patch is identified and its FFT is calculated and used to identify the phase in which TiO_2 crystallized.

A shown in Figure 4.12c.3, where the crystalline patches are colored according to the assigned phase, it predominantly crystallized into anatase. This is confirmed by SAED (Figure 4.12d), where peak positions match anatase reflections. The average crystalline domain size is $\sim 24\,nm^2$, slightly larger than the $18\,nm^2$ obtained by hydrothermal treatment. This likely stem from the higher peak temperatures reached during laser heating, which provide more energy for grain growth and may result in improved carrier transport within the crystallized shell. Furthermore, the shell underwent $\sim$ 23% shrinkage upon laser irradiation. This is attributed to densification of the initially amorphous TiO_2 during crystallization and the removal of residual organic species, reducing the porosity.

Regarding nanorod morphology, one key observation should be highlighted. From Figure 4.12a and b, the aspect ratio decreases from 2.9 to 2 while the nanorod length remains constant, indicating that the diameter increased rather than the rod having globally reshaped. As will be discussed in *Chapter 5*, copper contamination can migrate into Au nanorods under laser irradiation, leading to an increase in diameter. We believe that, without the copper contamination, the actual reshaping of the Au core is relatively limited in terms of aspect ratio change. Some surface roughening is visible and is more pronounced than in the TTIP case. This may reflect the confining effect of the thin but conformal $TiCl_3$/citrate shell. Confinement suppresses long-range Au atom migration, while promoting local surface rearrangement, as atoms cannot migrate freely to minimize surface energy. This effect has also been observed in other confined core-shell systems such as $Au@SiO_2$ [172]. In contrast, the more open TTIP network confines the Au core less rigidly, allowing atoms to migrate more freely along the surface and resulting in a smoother interface.

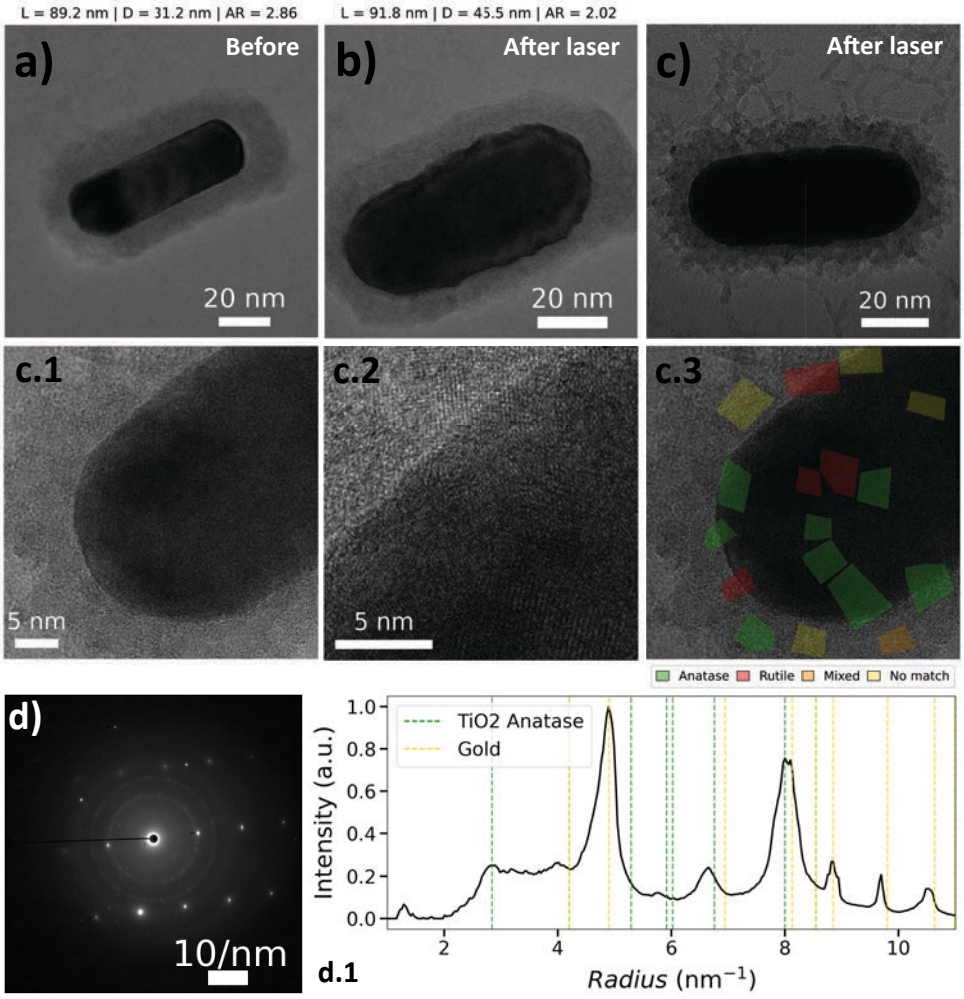

Figure 4.12: *Laser induced crystallization of a $TiCl_3$ citrate-stabilized $Au@TiO_2$NR. TEM image of a NR before (a) and after (b) laser irradiation. c) Another particle after laser irradiation. c.1) and c.2) zoom-ins of the particle in c) to better see the interface and the crystalline TiO_2. In c.3) individual crystalline patches in (c.1) are identified and color-coded according to the TiO_2 polymorph determined from FFT-derived d-spacings: anatase (green), rutile (red), mixed anatase/rutile (orange), and regions where no TiO_2 reflection could be assigned within 6% tolerance (yellow). d) Diffraction pattern of the same particle in c). d.1) Azimuthally averaged radial intensity profile of the diffraction pattern in (d) with expected peak positions from the literature marked as dashed lines: Au in yellow, and titania anatase in green.*

To avoid copper contamination from the copper of the Quantifoil grids migrating into the Au nanorods under laser irradiation, a SiO_2 grid coated with a thin carbon film was used for the SDS-capped sample. This maintains carbon-mediated heating while eliminating the copper source. The same laser irradiation conditions were then applied to the sample with a thicker shell grown on SDS-capped NRs. As shown in Figure 4.13b.1 and b.2, crystalline domains form in the TiO_2 shell after laser exposure. FFT-based phase mapping of the crystalline regions in Figure 4.13c reveals a predominance of rutile TiO_2, with an average crystalline domain area of $31\,nm^2$. The corresponding violin plot of extracted d-spacings (Figure 4.13d) further confirms that the measured lattice spacings cluster around the characteristic rutile reflection at 0.325 nm. As mentioned before, rutile formation is favored by a high density of oxygen vacancies, consistent with the sodium impurities detected in the EDX map of the amorphous TiO_2 shells grown on SDS-capped NRs (Figure 4.5), together with the vacuum annealing conditions. The resulting TiO_2 shell appears less dense compared to the citrate-based sample, and the Au core exhibits higher mobility under laser exposure. While SDS provides structural templating during slow hydrothermal treatment, it also introduces an interfacial spacer that weakens the coupling between the Au core and the shell, reducing stability under rapid laser heating. For the nanorod shown in Figure 4.13a–b, the aspect ratio decreases from 2.7 to 2.4 after laser exposure. However, this change is not the dominant effect. Instead, from the changes in contrast, a significant loss of gold is inferred, indicating material redistribution or partial evaporation under laser irradiation. This remains an observation, as it is based on two-dimensional projections, and because TEM intensity is not a monotonic function of thickness. STEM imaging and electron tomography should be performed to confirm this. This behavior suggests that the thick but porous shell provides limited confinement of the Au core at high temperatures, allowing Au atoms to diffuse and escape. Consistent with this, the shell shrinkage is relatively small (approximately 3%), indicating limited densification during crystallization. This reduced shrinkage can be attributed to the combination of a highly porous structure and the rapid heating–cooling cycles induced by laser irradiation. While local rearrangement of the TiO_2 network occurs, the short timescales restrict long-range diffusion and prevent full densification of the shell. In contrast, citrate-derived shells are more compact and continuous, enabling more effective densification during crystallization and resulting in larger volume contraction of the TiO_2 shell. Their denser structure also provides stronger confinement of the Au core, which suppresses gold loss despite similar thermal conditions. These observations highlight that, in addition to defect chemistry, both the structural density of the shell and the timescale of the heating process play a key role in determining crystallization behavior and metal core stability under laser excitation.

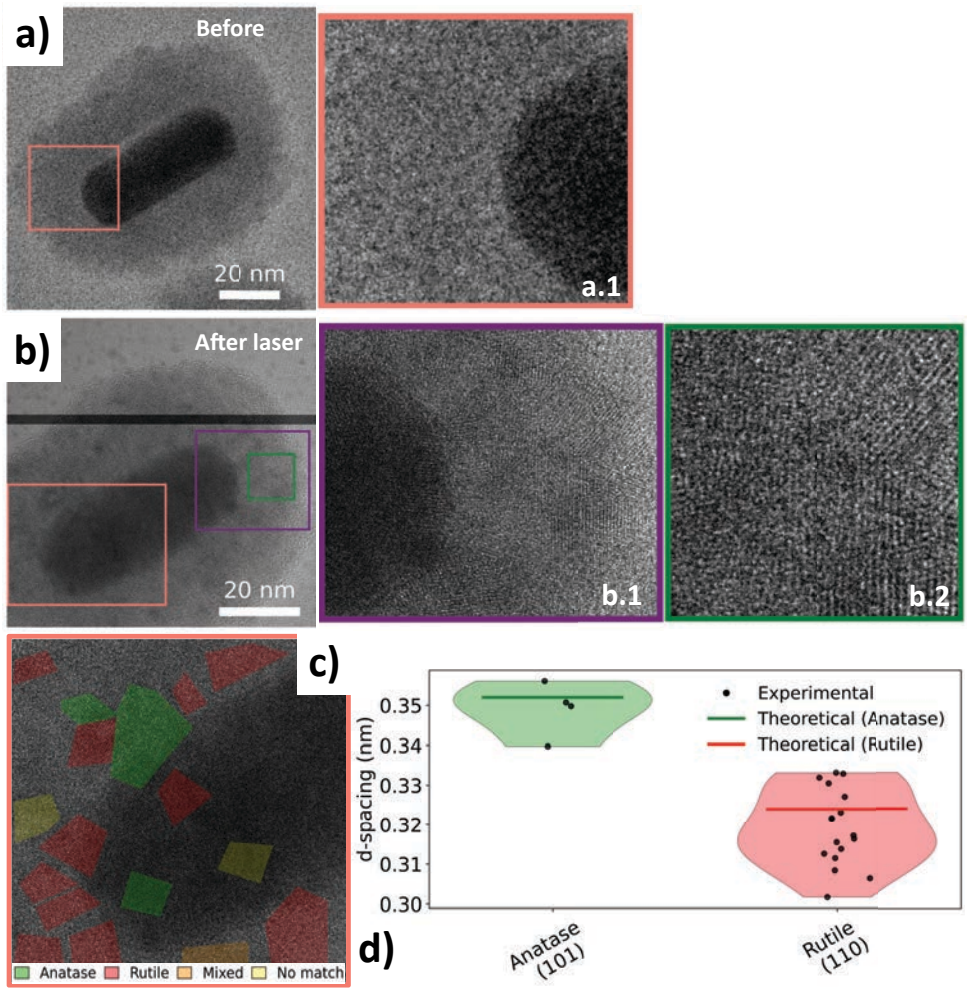

Figure 4.13: *TEM image of a SDS-stabilized Au@TiO_2NR before (a) and after (b) laser exposure. a.1) shows a zoom of the highlighted region in a), revealing the absence of crystallinity in the shell before laser exposure. b.1) and b.2) show zoom-ins of the shell after laser illumination, corresponding to the color-coded highlighted regions in b), where crystalline domains are observed. c) Phase map of the salmon-highlighted region in b), in which individual crystalline patches are assigned to different TiO_2 phases based on the d-spacing extracted from the FFT and overlaid with different colors on the TEM image. d) Violin plot summarizing the d-spacing values measured for each crystalline patch shown in c).*

In this section we demonstrated that laser-induced crystallization is a promising route for crystallizing TiO_2 shells around Au nanorods with limited reshaping, which could be directly assessed thanks to the in situ nature of the technique. Across all three systems, the results consistently confirmed the role of impurity content in determining the crystallization pathway. The $TiCl_3$/citrate sample, with the lowest Na and Cl content, crystallized predominantly into anatase. In contrast, both the TTIP/citrate sample, which contained measurable Na contamination from incomplete washing, and the Na- and Cl-rich $TiCl_3$/SDS sample crystallized preferentially into rutile. This confirms that impurity-induced oxygen vacancies are the dominant factor governing phase selection under laser-induced crystallization conditions, with precursor and ligand choice determining the defect landscape of the amorphous shell prior to crystallization. Furthermore, a key advantage of this approach is that parameters optimized in situ in the TEM can in principle be transferred to an optical setup, enabling direct comparison of single-particle optical properties before and after crystallization, though as shown above, differences in substrate and thermal environment must be carefully accounted for.

4.3.4 Conclusion and Outlook

This chapter investigated how precursor chemistry, ligand choice, and crystallization strategy govern shell morphology, defect density, phase selection, and interface quality in $Au@TiO_2$ nanorods, with the aim of establishing synthesis conditions that support efficient hot-carrier injection and transport.

TTIP-based sol–gel growth resulted in non-uniform and poorly controlled amorphous TiO_2 shells due to uncontrolled hydrolysis driven by residual water under the experimental conditions explored. Higher precursor concentrations led to extended TiO_2 networks rather than conformal coatings. In contrast, synthesis based on $TiCl_3$ allowed more homogeneous and controlled shell growth, with shell thickness governed primarily by the addition rate of $NaHCO_3$. Within the $TiCl_3$ system, ligand choice determined impurity incorporation and interfacial purity. Citrate-capped nanorods produced thin, uniform shells with minimal Na and Cl contamination, while SDS-capped systems allowed much thicker but highly porous shells containing trapped sodium and chloride species.

Crystallization behavior depended strongly on shell structure, defect content, and the crystallization approach. Low-temperature hydrothermal treatment successfully induced crystallization in $TiCl_3$-based shells while preserving the Au nanorod morphology. However, the resulting shell morphology differed significantly between ligand systems. Citrate-based shells underwent extensive dissolution–reprecipitation, leading to porous and partially discontinuous structures, whereas SDS-based shells were better preserved, likely due to the templating effect of the surfactant layer. Anatase

was consistently observed in the citrate system, while phase assignment for SDS-based samples remained uncertain due to limited resolution and statistics. The expected trend of higher impurity content favoring rutile was not clearly observed, possibly because anatase is thermodynamically favored at 100 °C. Further work is required to understand how temperature, reaction time, and water content influence both crystallinity and morphology.

Laser-induced crystallization inside the TEM provided an alternative and new route for crystallizing TiO_2 shells around Au nanorods, combining localized heating with real-time structural monitoring at the single-particle level. Although a direct quantitative comparison with conventional annealing was not performed, only mild and localized changes in aspect ratio were observed, particularly for the $TiCl_3$/citrate system. This is consistent with the expected advantage of rapid heating–cooling cycles in limiting long-range Au atom diffusion. Some surface roughening was observed, particularly for the conformal $TiCl_3$-based shells, consistent with the confining effect of the shell limiting long-range Au atom diffusion during rapid heating. Even in this case, the crystalline phase formed was closely linked to impurity content. The $TiCl_3$/citrate sample, with the lowest Na and Cl content, crystallized into anatase, whereas both the TTIP/citrate sample and the Na- and Cl-rich $TiCl_3$/SDS sample preferentially formed rutile. This indicates that impurity-induced oxygen vacancies govern phase selection, with precursor and ligand choice determining the defect landscape prior to crystallization. Although a fully quantitative phase analysis was limited by TEM resolution, consistent trends were observed across all systems.

Overall, these results show that precursor chemistry, ligand choice, and crystallization strategy together determine the final shell morphology, phase, and interface quality in $Au@TiO_2$ nanorods. The ability to perform crystallization directly inside the TEM while monitoring structural evolution in real time provides a powerful platform for future studies.

However, further work is required to address the limitations of the present study. In particular, achieving direct atomic-resolution imaging of the Au/TiO_2 interface will be essential to better understand the structure–property relationships governing charge transfer. In addition, independent quantification of defect density using spectroscopic techniques such as XPS or EELS would provide a more complete picture of the role of oxygen vacancies in phase selection. A key next step will be to extend single-particle linewidth measurements to crystallized $Au@TiO_2$ samples with improved laser calibration, enabling quantitative assessment of CID efficiency as a function of TiO_2 phase, crystallinity, and interface quality. Combined with transient absorption spectroscopy to probe carrier populations and decay dynamics, this will provide a more complete picture of how structural properties govern charge transfer and carrier transport in these systems.

4.4 Appendix

4.4.1 Details on synthesis

a) TTIP precursor

Briefly, 1 ml of 25 nm × 65 nm citrate capped NRs with LSPR at 600 nm in water, was centrifuged for 5 minutes at 6000 rpm. The supernatant was removed, leaving a 20 μL concentrated nanoparticles pellet in water at the bottom. This solution was redispersed in 0.6 mL of isopropanol (IPA) and sonicated for 5 minutes to ensure monodispersity. The solution obtained was then transferred to a 4 ml vial containing a magnetic stirring bar and placed on a stirring plate. A mixed precursor solution was prepared by combining a 1.7 M acetic acid solution in IPA and a 33 mM TTIP in IPA in a 2:3 volume ratio. Next, 50 μl of this pre-mixed solution were added to the redispersed nanoparticles while stirring. After half an hour, 30 μl of water diluted 100 times with IPA was added to the solution to trigger a controlled hydrolysis reaction 4.1, followed by condensation 4.2.

$$\mathrm{Ti(OR)_4 + 4H_2O \rightarrow Ti(OH)_4 + 4ROH} \tag{4.1}$$

$$\mathrm{Ti(OH)_4 \rightarrow TiO_2 + 2H_2O} \tag{4.2}$$

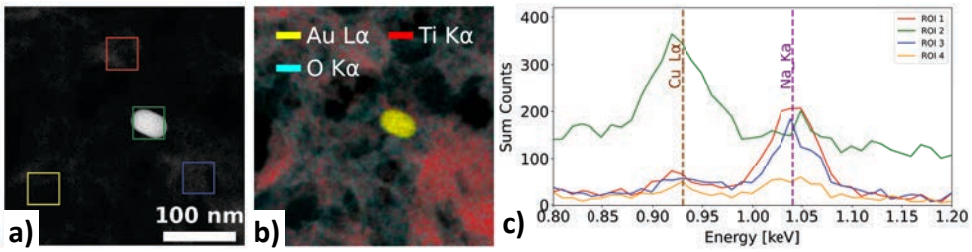

Figure S4.1: *TTIP amorphous shell around citrate-stabilized $Au@TiO_2$NR synthesized with 2.6 mM of TTIP (green line in Figure 4.2d. a) STEM image of a gold nanorod surrounded by a titania network, with the different regions analyzed highlighted). b) Map with the overlaid gold, titanium and oxygen signals. c)EDX spectra summed over each of the regions highlighted in a). Each colored area in a) corresponds to the EDX spectrum shown in the same color in c).*

b) Titanium (III) chloride precursor

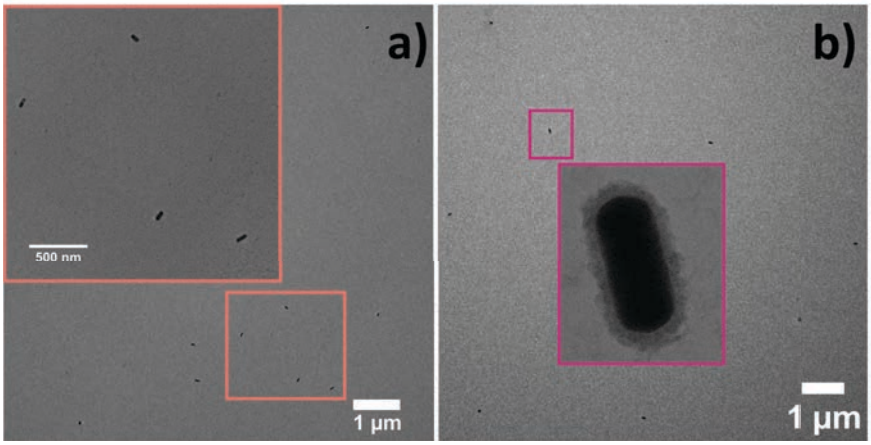

Figure S4.2: *Zoom-out images highlighting the presence of isolated particles for the shells grown from $TiCl_3$ for both a) the citrate sample and b) the SDS sample. Zoomed-in images are included to highlight this single-particle character.*

The colloidal growth of an amorphous TiO_2 shell around both citrate and SDS capped AuNRs was carried out following a protocol adapted from Wu et. al. [163] and Fang et. al. [126] using $TiCl_3$ as precursor. $TiCl_3$ dissociates to Ti^{3+} in acidic solution.

$$TiCl_3 \rightarrow Ti^{3+} + 3Cl^- \tag{4.3}$$

Upon controlled addition of $NaHCO_3$, partial hydrolysis of Ti^3 occurs, generating reactive $TiOH^+$ species.

$$Ti^{3+} + xH_2O \rightarrow Ti(OH)_x^{(3-x)+} + xH^+ \tag{4.4}$$

These hydrolyzed species preferentially adsorb onto negatively charged surfaces, where heterogeneous nucleation and condensation lead to formation of a Ti-based shell, which subsequently oxidizes to TiO_2.

$$TiOH + TiOH \rightarrow TiOTi + H_2O \rightarrow \mathrm{TiO_2} + 3\mathrm{H^+} \tag{4.5}$$

The precursor Ti^{3+} solution was prepared by adding 100 µL of 12% $TiCl_3$ to 4 mL of Milli-Q water under vigorous stirring to ensure complete mixing. The pH of the resulting reddish solution was measured to be 1.4 using a pH meter. Under maximum stirring, 460 µL of 1 M $NaHCO_3$ solution was added dropwise. Slow addition was essential to avoid rapid hydrolysis and precipitation of TiO_2 in solution. After approximately 400 µL, the solution turned transparent, and the pH was measured to be 2.43. A few seconds were allowed to pass before adding the remaining 60 µL. After this addition, the solution immediately turned blue, with a measured pH of 2.9,

indicating the formation of partially hydrolyzed $Ti^{3+}OH_x$ complexes. Immediately afterward, 500 μL of the citrate or SDS capped AuNRs, previously washed twice to remove loosely bound ligands and re-dispersed in water, were added while keeping vigorous stirring. The negative surface charge of the ligand layers attract the positively charged $TiOH^+$ cations resulting in growth of a shell around the NRs [173]. After seven minutes the solution was placed in eppendorf tubes and centrifuged at 6000 rpm for 5 minutes. The supernatant was removed and the pallet on the bottom redispersed in Milli-Q water. This washing procedure was repeated three times.

4.4.1.A TiO_2 volume fraction estimation

To quantify the shell density of citrate-capped $AuNR@TiO_2$, scattering spectra using an immersion oil objective were measured for 10 individual particles. Each spectrum was correlated with the corresponding geometry (nanorod size and shell thickness) obtained from TEM imaging. The scattering response of each particle was then simulated using its experimentally determined geometry, while sweeping the effective refractive index of the shell from pure oil ($n = 1.518$) to pure amorphous TiO_2 ($n = 2.4$). From the best match between experimental and simulated spectra across all particles, an effective refractive index of $n = 1.85$ was obtained (Figure S4.3). The shell was then described using a simplified one-parameter effective-medium approximation, $n = \sqrt{n_{\mathrm{TiO_2}}^2(1-f) + n_{\mathrm{oil}}^2 f}$, modeling the shell as a homogeneous mixture of amorphous TiO_2 and oil. Solving the equation for $n = 1.85$ yielded a TiO_2 volume fraction of approximately 0.32.

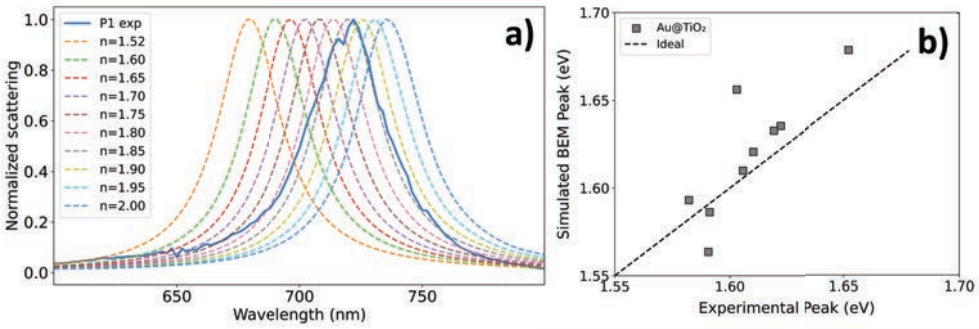

Figure S4.3: *a) Simulated scattering spectra for a $Au@TiO_2NR$ with an amorphous shell ($TiCl_3$ precursor, citrate-stabilized) as the shell refractive index is varied between 1.518 and 2.0. The morphology for the simulations is taken form the correlated TEM measurements. The solid line represents the experimental spectrum measured. b) Peak position of all simulated scattering spectra for a shell refractive index of $n = 1.85$ as a function of the experimental peak position.*

For SDS-capped $AuNR@TiO_2$, the shell density was estimated using simulated absorption spectra for different shell thicknesses (6, 25, and 40 nm). The same effective-medium approximation was used, modeling the shell as a mixture of amorphous TiO_2 ($n = 2.4$) and water, with water as the surrounding medium. The water volume fraction (f) was varied between 0 (fully dense TiO_2) and 1 (pure water) to match the experimental spectra. As shown in Figure S4.4, the best agreement corresponds to a porosity of 0.8, corresponding to a TiO_2 volume fraction of 0.2, indicating highly porous shells. The observed increase in shell thickness in SDS-based systems is consistent with the role of surfactants in modifying nanoparticle aggregation during sol–gel growth. Hydrophobic interactions between SDS molecules promote the formation of larger, more porous structures [151].

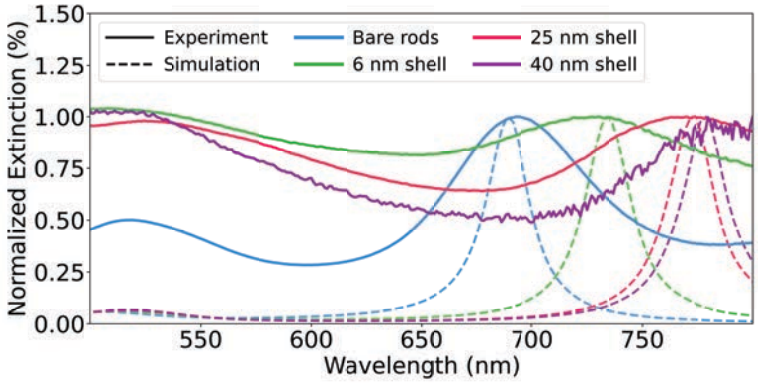

Figure S4.4: *Normalized absorption spectra of Au nanorods with varying TiO_2 shell thicknesses, comparing experimental data (solid lines) with simulations (dashed lines). The simulations assume an effective TiO_2 refractive index corresponding to a porous shell (volume fraction of 0.2).*

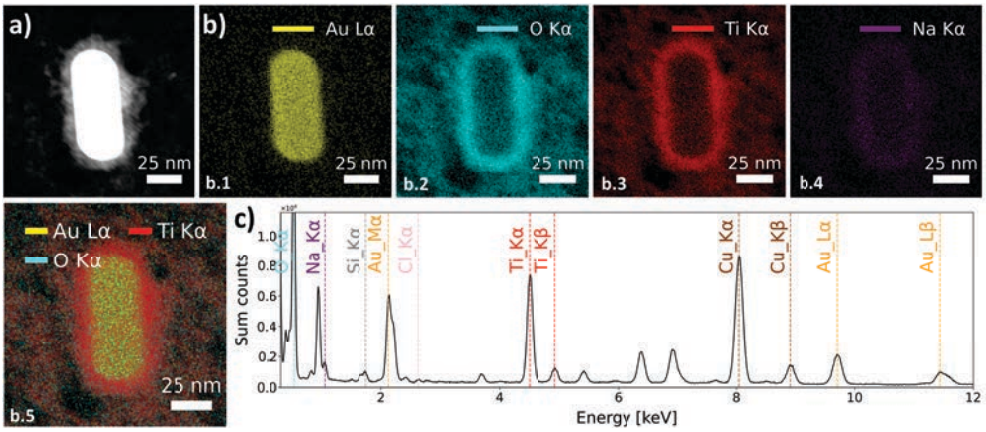

Figure S4.5: *$TiCl_3$ thin amorphous shell around SDS-stabilized $Au@TiO_2NR$. a) STEM image b) EDX net counts map for different element: Au, O, Ti, Na. c) Uncorrected sum EDX signal.*

4.4.2 Further analysis on hydrothermal crystallization

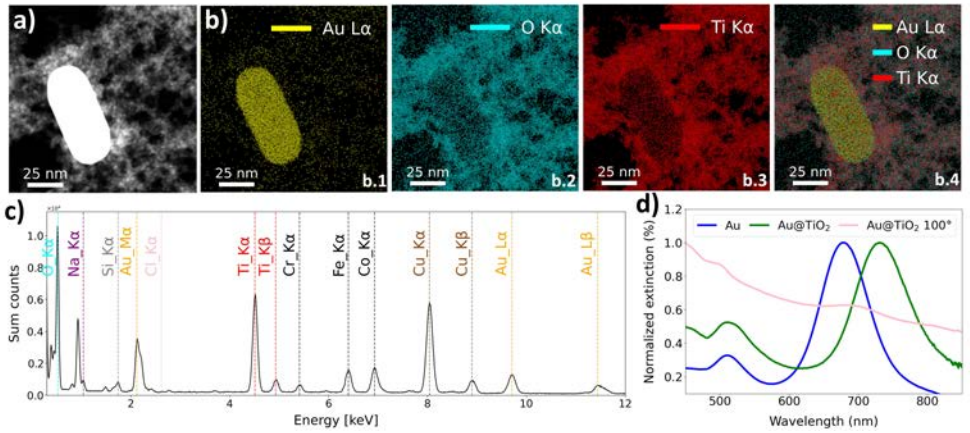

Figure S4.6: *Citrate-stabilized $Au@TiO_2$ after hydrothermal crystallization. a) STEM image of a AuNRs after growth of a TiO_2 shell b) EDX net counts map for selected elements. c) Uncorrected sum EDX signal d) UV-vis spectra of the bare rods and the $Au@TiO_2$ sample before (green) and after (pink) thermal treatment.*

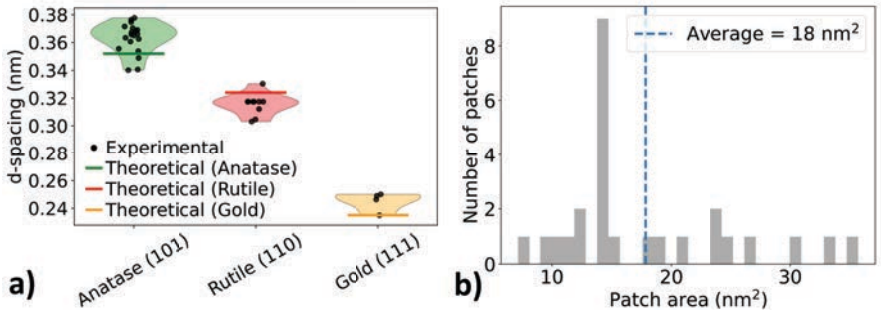

Figure S4.7: *Citrate-stabilized $Au@TiO_2$ after low temperature crystallization in solution a) Violin plot showing the distribution of d-spacings measured for the crystalline domains in Figure 4.7a.2. b) Size distribution of the identified grains.*

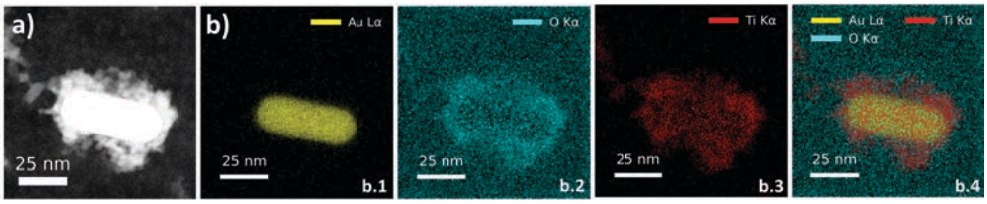

Figure S4.8: *Thin-shell SDS-stabilized $Au@TiO_2$ after hydrothermal crystallization. a) STEM image b) EDX net counts map for selected elements.*

4

4.4.3 Details on laser induced crystallization

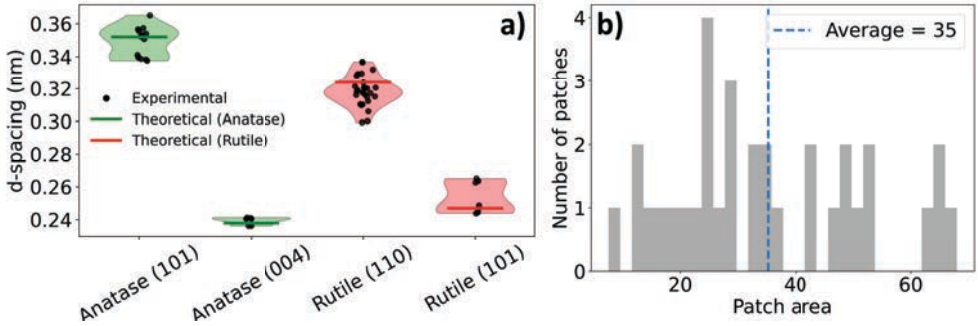

Figure S4.9: *$Au@TiO_2$ grown from TTIP after laser induced crystallization a) Violin plot showing the distribution of d-spacings measured for the crystalline domains in Figure 4.10c. b) Size distribution of the identified grains.*

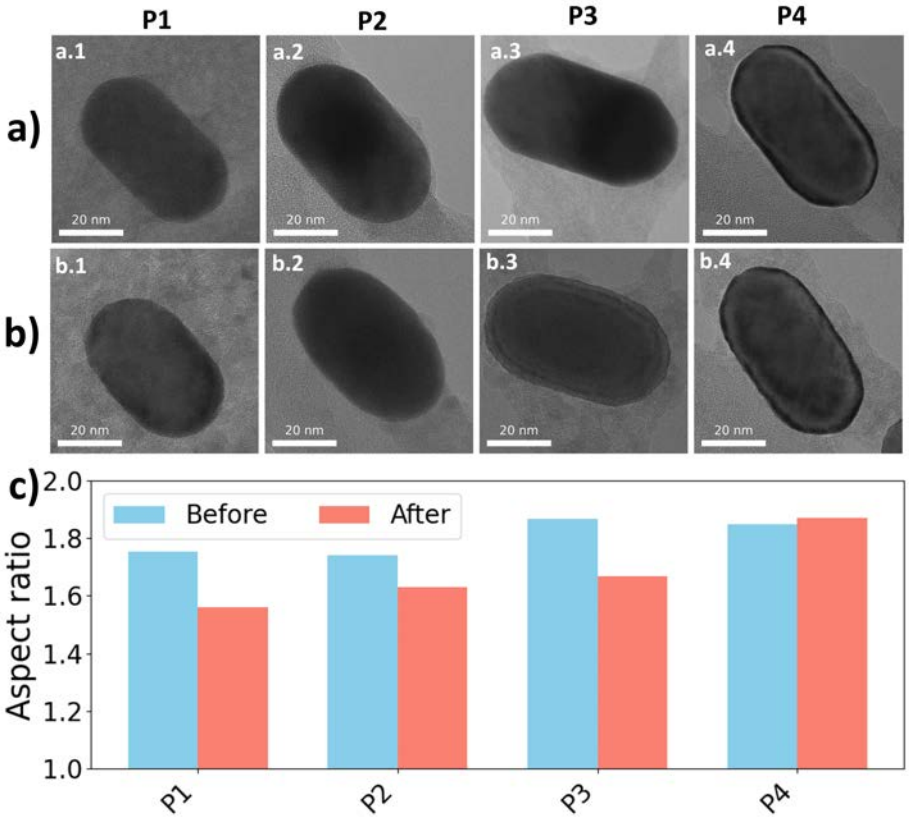

Figure S4.10: *TEM images of four TTIP-based $Au@TiO_2$ NRs (citrate ligand) a) before b) and after b) laser illumination at 600±5 nm and 8 $\mu J/cm^2$, showing limited overall reshaping of the Au core. c) Aspect ratio of each nanorod, calculated as the ratio of length to diameter, before (blue) and after (salmon) laser illumination, confirming a consistent but mild decrease of approximately 0.2 across particles, with one particle showing no measurable change.*

5 Optically driven AuCu alloying in single nanoparticles revealed by in situ TEM

Keywords: *In situ TEM, photothermal alloying, bimetallic nanoparticles, composition control*

AuCu alloys are versatile materials whose physical and optical properties can be finely tuned through composition, making precise control over the Au/Cu ratio highly desirable. Here, we demonstrate that pulsed laser excitation provides a promising route to dynamically drive and control alloy formation in single nanoparticles. We track the structural and compositional evolution of individual $Au@TiO_2$ core–shell nanorods under optical excitation in situ using transmission electron microscopy (TEM) combined with picosecond pulsed laser illumination. Laser irradiation mobilizes copper-containing species from the carbon support, which migrate to the nanorod surface and alloy with gold to form a homogeneous AuCu alloy. The copper fraction can be tuned with laser fluence, reaching values above 80%, before the local temperature exceeds the threshold for copper sublimation and a gold-rich structure is partially restored. Time-resolved diffraction shows that the process is reversible but kinetically asymmetric: incorporation is rapid, while the slower evaporative removal allows the copper fraction to be tuned more finely on the return path. These results demonstrate that, under pulsed laser excitation, nanoparticle composition can be actively driven, observed, and frozen on demand at the single-particle level through control of laser fluence and illumination time

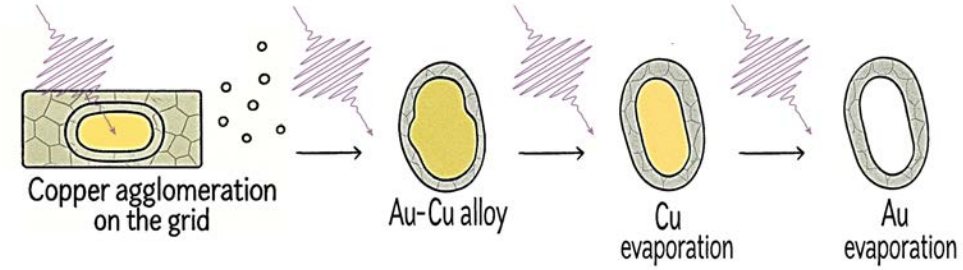

5.1 Introduction

Bimetallic nanoparticles offer a versatile platform for tuning functionality through compositional design. This tunability ultimately depends on atomic-scale structure. In such systems, catalytic, optical, and electronic properties are dictated not only by the overall composition, but also by the local distribution of elements, their degree of ordering, and the particle morphology [174–177]. Au-Cu nanoparticles represent a particularly interesting model system in this regard [178–180]. Across their phase diagram, they span ordered intermetallic compounds (Au_3Cu, $AuCu$, $AuCu_3$) and disordered solid solutions. Their properties change sensitively with composition and atomic arrangement [181, 182]. At the same time, Au-Cu is practically relevant. Au stabilizes Cu against oxidation, while Cu introduces chemical reactivity and modifies the electronic and plasmonic response of pure Au. The functionality of plasmonic Au-Cu alloys depends strongly on local composition and ordering. For example, tuning the relative Au/Cu content modifies the balance between interband and intraband excitations, thereby altering the distribution of hot carriers and the dominant chemical reaction pathways [183]. Changes in composition can therefore switch the system between distinct catalytic regimes, highlighting the potential for composition to act as an active control parameter.

However, achieving controlled and homogeneous alloying in Au-Cu nanoparticles remains a fundamental challenge. Chemical synthesis provides control over the average Au-Cu composition via precursor ratios and reaction conditions. However, the reduction potentials of Au^{3+} and Cu^{2+} are substantially different. Synchronizing their reduction potentials requires careful tuning of ligands, precursors and stoichiometry, and reproducibility remains sensitive to small variations in reactions conditions [178]. Particle-to-particle variability in composition is also pronounced at the single-particle level. Prunier et al. showed that nanoparticles synthesized with widely different target compositions exhibited nearly identical compositions [184]. In particular all synthesis led to strongly Au-rich nanoparticles, because gold nucleates preferentially regardless of the precursor ratio [184]. Furthermore, Au–Cu nanoparticles already synthesized exhibit a post-synthesis tendency toward Au surface segregation due to the lower surface energy of Au [181, 184]. Post-synthesis thermal annealing can drive further mixing and ordering [185]. All conventional approaches, such as chemical synthesis, physical deposition, and thermal annealing, set the composition at the moment of preparation and provide no route to continuously and reversibly adjust it during operation or characterization.

In this context, pulsed optical excitation presents a unique route to access and dynamically control alloy states that are difficult or impossible to reach through conventional methods [186]. The rapid heating during a laser pulse, followed by ultrafast quenching in the surrounding medium, can kinetically trap transient compositional

states before long-range diffusion and segregation processes fully develop [186–188]. This capability has been exploited extensively in *ex situ* approaches. Pulsed laser ablation in liquids and laser excitation of pre-synthesized colloidal heterostructures have been explored to produce solid-solution alloys spanning from binary systems to high-entropy alloys of five or more elements, including combinations such as Au–Cu that are difficult to mix homogeneously by wet-chemical routes [184, 186]. Beyond kinetic trapping, pulsed laser offers unmatched temporal control. It can be switched on and off with electronic precision down to the single-pulse level, much faster than the thermal inertia of any resistive heater. This means that compositional changes can be initiated, modulated, and paused with a precision and speed that no thermal approach can match. Once the laser is switched off, the composition is kinetically stable at room temperature indefinitely, since diffusion coefficients at ambient conditions are negligibly small [185].

Despite the demonstrated power of pulsed laser-assisted alloying, dynamic insight into how the process unfolds at the single-particle level remains difficult to obtain. Closing this gap requires following the process in real time, with simultaneous structural and compositional information at the level of individual nanoparticles. In situ TEM has emerged as a powerful platform for this kind of study under external stimuli. in situ thermal heating has been used to follow alloying and atomic redistribution in bimetallic core-shell nanoparticles and nanowires, revealing how interdiffusion proceeds, how composition and ordering evolve over time, and how surface segregation and intermediate phases shape the final structure [185, 189]. Access to the real-time evolution of alloying at the single particle level allows one to reach a mechanistically understanding of the process. Laser-driven alloying is mechanistically distinct from thermal annealing, since it proceeds through rapid heating and quenching cycles under strongly non-equilibrium conditions. Extending these dynamic insights to pulsed laser excitation is therefore essential. Such studies have only recently become possible with the development of in situ optical TEM [56].

In this chapter, we exploit a TEM equipped with a picosecond pulsed laser light in-coupling unit to follow in real time the structural and compositional evolution of $AuNR@TiO_2$ core-shell nanorods under picosecond optical excitation at megahertz repetition rates. We show that laser illumination drives the migration of copper-containing species from the carbon support film onto the nanorod surface, where they alloy with gold to form a homogeneous AuCu solid solution. The Cu fraction in the resulting alloy is quantified and tracked through lattice parameter shifts measured by electron diffraction. We show that the copper content can be tuned continuously by adjusting laser fluence. Above 80% Cu incorporation can be reached before copper sublimes at higher fluences, restoring the original gold structure. This approach demonstrates that the composition of an individual nanoparticle can be actively tuned and modified under optical excitation. Moreover, it provides direct access to inter-

mediate, non-equilibrium alloy states that are not readily achievable through conventional synthesis routes. More broadly, these results establish a pathway toward a light-driven dynamic control of nanoparticle composition at the single-particle level. Functionality may be adjusted in situ through optical excitation.

5.2 Methodology

The experiments reported were performed in an aberration-corrected NeoARM (S)TEM with Cold Field Emission Gun (CFEG, 0.3,eV FWHM energy spread), operated at 200 kV. The BF-TEM images were acquired on a TVIPS XF416 R(ES) bottom mounted camera. Scanning transmission electron microscopy (STEM) images were acquired with an annular bright field (ABF) or an annular dark field (ADF) detector.

5.2.1 Light in-coupling

The microscope is equipped with a JEOL–IDES Luminary laser in-coupling unit composed of a fiber-coupled laser, an inlet port, and a compact optical delivery system with a mirror to adjust the position of the laser spot and a collimator to focus the beam onto the sample. Laser alignment was performed using the JEOL–IDES fluorescent (PLAH) holder, which enables direct visualization of the laser spot and alignment with the electron beam. A typical experiment consisted of acquiring consecutive TEM images under pulsed laser illumination while varying the fluence by adjusting the peak laser power between 40% and 80% of the maximum power. For the measurements reported here, we used a wavelength of 700 nm with 10 nm bandwidth and a repetition rate of 26 MHz, corresponding to 38.5 ns in between pulses. At this wavelength the peak length is around $\sim$ 22 ps. The laser was focused onto the sample with a spot size of $\sim 40\mu$m FWHM and 64 μm/e^2, as determined from a 2D Gaussian fit of the laser spot as shown in Figure S5.1a.

The power measured at the fiber output before entering the TEM was used to calculate the fluence in μJ/cm^2, assuming a Gaussian beam, values are reported in Figure S5.1b. The average laser output power was measured with a power meter at discrete percentage of the peak power, between 30% and 100% in steps of 10%. Assuming constant pulse energy at different repetition rates, the average power corresponding to each repetition rate was estimated. Finally, fluence values at intermediate power-percentage settings were obtained by linear interpolation between adjacent measured data points. This interpolation provides an approximation, as the relationship between power percentage and average output power is not strictly linear. Since the power cannot be measured inside the column, the actual fluence at the sample is expected to be slightly lower due to optical losses in the IDES unit. During illumination, images were recorded every few seconds over hundreds of seconds; at

26 MHz, which corresponds to 2.6×10^7 pulses per second.

The exact fluence for the same laser settings varied slightly from experiment to experiment, however, we note that even with these slight variations, the same qualitative trends are seen every time. Reasons for these small variations are the following. First, changes in laser alignment on the order of several μm may occur. As seen in Figure S5.1b, a laser spot increasing from 64 to 100 μm leads to a dramatic change in fluence. Furthermore, the exact position within the window of the NR under examination plays an important role. Although all studied $AuNRs@TiO_2$ were located near the center of the window, the exact distance from the copper bar strongly affects heat dissipation. Since copper acts as a heat sink, the closer the particle is to the bar the faster the Quantifoil substrate cools down, and the less the sample heats up. Therefore, a unique quantification of reshaping as a function of fluence and temperature is not straightforward. Nevertheless, all experiments showed consistent qualitative trends, with only minor variations in the exact peak power required to induce reshaping.

5.2.2 Diffraction and 4D-STEM data analysis

The diffraction data acquired on the TimePix detector were treated in the following manner. First, the center of mass (COM) of each diffraction pattern was calculated and then used to align every image to each other to account for any shift of the direct beam in between measurements. The main diffraction peaks of each image were then detected. A Gaussian was fitted in a window of 7x7 pixels around the pixel with the highest intensity to detect the center of each diffraction spot. The corresponding reflections from different data sets were then clustered together across every illumination step. Finally, the distance from the COM to the fitted peaks was calculated.

5.2.3 Heat simulations

Heat simulations were conducted with COMSOL v5.5. The geometry simulated is displayed in Figure S5.2a. Briefly, we simulated a 100 μm wide carbon thin film surrounded by copper grid bars (35 μm). The thickness of the carbon film was 12 nm and a gold nanorod was placed in the center of the TEM window. The amorphous carbon was experimentally observed to turn into disorder graphite under laser exposure. Therefore, we defined the center of the window as disordered graphite to match this experimental observations. The temperature increase was computed with the module for the heat transfer in solids. We defined two heat sources, one for the nanoparticle and one for the carbon substrate. For the nanoparticle, it was defined as the product of its absorption cross section with the laser fluence. For the carbon, we calculated the absorbed power with the Beer-Lambert law assuming an absorption coefficient

of 2919 $cm^{-}1$. The heat source for the thin film was a 2D gaussian. Finally, the temperature was computed with a steady-state simulation.

The solution of the steady-state study was further used as initial temperature condition for the time-dependent study displayed in Figure S5.2b. We observed that it takes about 2 ms for the system to cool down to room temperature. This shows that the cooling time is much longer than the time in between the pulses (38.5 ns).

5.3 Results and discussion

5.3.1 Copper incorporation under laser illumination

To investigate laser-induced alloying of gold nanoparticles with copper, we used the citrate capped Au nanorods coated with an amorphous titania shell grown from $TiCl_3$ precursor ($AuNR@TiO_2$) synthesized as described extensively in *Chapter 4*. The TiO_2 shell has a dual purpose. First, it is a widely used support material in heterogeneous catalysis, making $AuNR@TiO_2$ a practically relevant catalyst architecture. Second, its porous amorphous structure allows atomic species to diffuse through it and reach the gold core while mechanically constraining the core during transformation. The particle solution was drop-cast onto Quantifoil R 1.2/20 200-mesh copper TEM grids with a 12 nm carbon support film. Experiments were performed in a modified JEOL NeoARM equipped with a cold field emission gun and a pulsed laser light in-coupling unit, as described in *Section 5.2.1*. The laser (700 nm, 26 MHz repetition rate) was focused onto the sample over a $\sim$64 μm spot, significantly larger than an individual nanoparticle (Figure S5.1). Under these conditions, the carbon film, which was present across the entire grid window, was the dominant photothermal absorber. The gold nanorods are themselves efficient photothermal heaters. Their nanoscale volume results in a negligible contribution to the overall thermal budget of the window compared to the absorption from the carbon film at this large spot size. At a repetition rate of 26 MHz, the inter-pulse interval is only 38.5 ns. Because the 12 nm carbon film is thermally thin, it cannot dissipate the deposited heat between pulses. It reaches instead a quasi-steady-state elevated temperature, effectively behaving as a continuous-wave heat source despite the pulsed excitation (Figure S5.2b). COMSOL finite element heat simulations confirmed this picture. At the laser powers used, the carbon film reached temperature increases of approximately $\approx$ 650 K at the center of the illuminated window, decaying to 500 K within 25 μm (Figure S5.2a). At these high temperatures, we observed that the amorphous carbon actually partially turned into disordered graphite, which we took into account in our heat simulations. The temperature increase of 650 K corresponds to a specific reference fluence at 50% laser power and serves to indicate the order of magnitude of heating reached in these experiments; the actual temperature varies between individual experiments as the laser

fluence is adjusted stepwise throughout each acquisition.

Early in situ heating experiments conducted on carbon-supported TEM grids before MEMS heating holders became standard, established that copper-containing species can form and migrate on carbon films at elevated temperatures. For example, Jernigan *et al.* and Zhang *et al.* reported copper migration and agglomeration on carbon supports at 600–700 °C [190, 191]. We hypothesize that under laser-induced heating, atomic and sub-nanometer copper species can be mobilized from the grid and diffuse through the porous TiO_2 shell and incorporate directly into the gold lattice. The near-uniform heating across the window shown in Figure S5.2a, means that copper-containing species can become thermally activated simultaneously across a large area. To confirm that our laser conditions are sufficient to mobilize copper from the Quantifoil substrate, we performed control experiments on empty grids in the absence of nanoparticles (Figure S5.3). Using the identical illumination geometry explained above, sparse dark dots appeared on the carbon film after illumination at $3.0\,\mu J/cm^2$ (Figure S5.3b). Increasing the power to $3.8\,\mu J/cm^2$ caused these dots to grow and agglomerate into larger clusters (Figure S5.3c-d). Figure S5.4 shows that the *d*-spacings of the larger clusters is consistent with Cu_2O rather than metallic Cu. At the highest laser fluence ($18\,\mu J/cm^2$) the clusters disappeared from the center of the window and appeared near the cooler edges of the window closer to the bar (Figure S5.3e), consistent with the temperature gradient over the grid window (Figure S5.2a). In this case, the center region had reached the sublimation temperature of the copper clusters and the colder outer regions had reached temperatures high enough to form clusters. This demonstrates that the spatial extent of available copper is self-limiting as a result of the temperature gradient across the window.

With this physical picture established, we turn to the behavior of $AuNR@TiO_2$ deposited on the same carbon TEM grids under laser illumination. In this experiment, the laser fluence was increased stepwise throughout each acquisition, allowing morphological changes of individual particles to be followed at different fluences. Each fluence step was maintained until morphological changes stopped, indicating that the particle had reached a stable configuration at that excitation level. Then the fluence was further increased. Representative results are shown in Figure 5.1a, with the applied laser fluence profile, plotted in Figure 5.1b. Initially, the laser was applied at a fluence of $4.5\,\mu J/cm^2$ for 40 s, switched off, and then turned back on at the same fluence for another 370 s. The fluence was subsequently increased to $4.8\,\mu J/cm^2$ for 187 s and finally to $5.1\,\mu J/cm^2$ for 88 s. A TEM image of the $AuNR@TiO_2$ before laser illumination is shown in Figure 5.1a.1. Under laser exposure, the particle underwent a pronounced morphological transformation. The nanoparticle progressively grew, leading to deformation and noticeable expansion of the surrounding TiO_2 shell. This is an indication that material from outside the nanorod entered through the porous shell and accumulated inside (Figure 5.1a.2-a.4). The TiO_2 shell itself de-

formed but remained intact, consistent with its high vaporization temperature (above 2000 °C), which makes it robust under the conditions used here. At higher laser fluence (5.1 μJ/cm^2), the particle partially returned toward its original shape (Figure 5.1a.5). This indicates that part of the incorporated material began to sublime and leave the particle. This expansion and contraction sequence was reproducible across multiple grid windows and different nanorods, Figure S5.5. Only minor adjustments in laser power were required between experiments due to small variations in laser spot size, nanorod position relative to the laser spot and proximity to the grid bars, which affects the temperature reached and local heat dissipation. For comparison at each illumination step, the corresponding TEM image was thresholded and the particle outline extracted and smoothed with a Gaussian filter. The resulting outlines as a function of time are shown in Figure 5.1c: the nanorod (blue) clearly expanded to a maximum projected area (orange) before shrinking back toward its original dimensions (yellow) at higher fluence.

Two control experiments were performed. First, to test if this is indeed copper entering the Au nanorod, we applied directly a fluence that was above the observed sublimation threshold of the copper-containing clusters on the empty grid in Figure S5.3e. As shown in Figure S5.6, when directly applying a high laser fluence of 8.5 μJ/cm^2, the original particle completely disappeared, indicating that the sublimation temperature of gold was reached. It is also interesting to observe that the shape of the TiO_2 shell remained preserved even after complete sublimation of the gold core, and no noticeable nanorod reshaping or increase in the projected area was detected. This suggests that under higher laser power, the surrounding material on the grid sublimates before it can diffuse into the $AuNR@TiO_2$, and that it is likely indeed copper that causes the nanoparticle changes. Second, the influence of the electron beam was tested by repeating the same experiments with the beam switched off during laser irradiation, acquiring images only before and after exposure. The particle underwent the same transformation as in experiments performed with the beam on, confirming that laser illumination alone is sufficient to drive copper incorporation and alloying. However, the rate of copper incorporation was generally lower in the absence of the beam, suggesting that the electron beam accelerates the process. One possible explanation is that the negative charge of the electron beam attracts positively charged copper ions toward the illuminated region, adding a directional bias to the otherwise random thermal diffusion of copper species toward the gold particle. Although the absolute kinetics of incorporation may be influenced by the beam, the general findings are independent of beam-induced effects and represent intrinsic behavior of the laser-driven system.

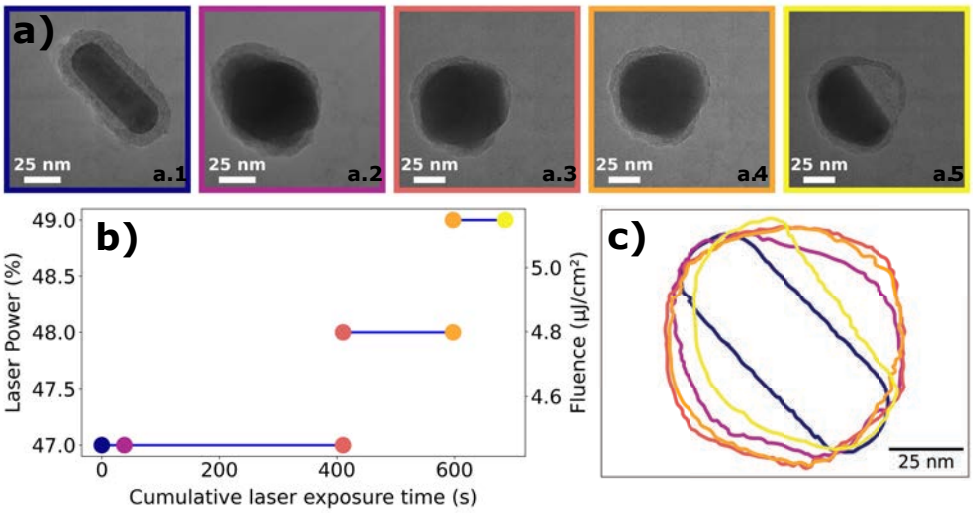

Figure 5.1: *a) TEM images of a $AuNR@TiO_2$ under laser exposure: before laser exposure(a.1), after the first laser exposure at $4.5\,\mu J/cm^2$, after the second laser exposure at the same fluence (a.3), after the third laser exposure at $4.8\,\mu J/cm^2$ (a.4), and after the last laser exposure at $5.1\,\mu J/cm^2$. b) Applied laser power and corresponding calculated fluence (for a laser spot of $64\,\mu m$ at $26\,MHz$) as a function of time. The horizontal segments indicate the time intervals during which each laser power was applied. c) Extracted outline smoothed with Gaussian filter of the Au nanorod at successive times under laser illumination as in a).*

5.3.2 Volume evolution and spatial distribution

The TEM observations in *Section 5.3.1* suggested that material entered the $AuNR@TiO_2$ under laser illumination, deforming the gold core and expanding the TiO_2 shell. If indeed copper was incorporated into the gold nanorod, as hypothesized, an increase in particle volume should be measured. To test this, we performed electron tomography on the same particle shown in Figure 5.1, acquiring tilt series before illumination and after the first (a.2) and last (a.5) stages of laser exposure. Each tomography series consisted of ADF-STEM 2D projections acquired from $-65\,^\circ$ to $+65\,^\circ$ in steps of $3\,^\circ$. Representative ADF-STEM images at $0\,^\circ$ and $\pm 65\,^\circ$ are shown in Figure 5.2a before (blue a.1), after illumination over 40 s at a fluence of $4.5\,\mu J/cm^2$ (purple a.2) and after the final exposure at $5.1\,\mu J/cm^2$ over 88 s (yellow a.3). After the first exposure, the material visibly spread onto the TEM substrate, resulting in a noticeably flatter interface between the nanorod and the grid at high tilt angles (purple arrows, in Figure 5.2a.2). Importantly, the TiO_2 shell also clearly deformed

outward, indicating that the newly incorporated material was growing inside the shell rather than simply depositing on its surface. At higher fluence (Figure 5.2a.3), the additional material largely disappeared and the nanorod partially recovered its original shape, consistent with the TEM results in *Section 5.3.1.* The same particle imaged with the bright-field detector (a.4) makes the shell deformation particularly clear, as the lower Z contrast of TiO_2 is better captured under these detector settings. The tilt series were aligned by cross-correlation and reconstructed using an expectation-maximization algorithm. After segmentation with the Otsu threshold, the particle volume was calculated at each stage. The results are shown in Figure 5.2b: the volume increased approximately fourfold after the first illumination stage, then decreased to roughly twice the original volume after higher-fluence exposure. This confirms that substantial new material entered the nanorod during laser illumination, far more than could be accounted for by thermal expansion alone. At higher fluences it was partially removed, consistent with suspected sublimation of the incorporated copper, which has a lower sublimation point than gold at the operating pressure of the TEM.

To gain more time-resolved insight into how material is incorporated during illumination, we turn to the ADF-STEM image series in Figure 5.2c, acquired on a different particle under laser illumination at stepwise increasing fluence. In ADF-STEM, image contrast scales monotonically with both specimen thickness and atomic number Z. A higher signal indicates therefore either more material (a thicker nanoparticle) or heavier atoms. Under laser illumination, a region of increased contrast appeared at the center of the nanorod and grew progressively until it extended beyond the original TiO_2 shell boundaries (Figures 5.2 c.3–c.7). This high-contrast region most likely reflects growth in the third dimension. Copper entered through a weak point in the TiO_2 shell and accumulated preferentially along the path of least resistance, causing the particle to thicken out of plane rather than expanding uniformly in the image plane. This is directly visible in the line profiles extracted along the center of the nanorod shown in Figure 5.2d. For the blue line 3, a sharp and localized increase in intensity appeared in the middle of the rod while the intensity along the rest of the rod decreased. The increase in intensity corresponds to the protrusion and is therefore due to an increase in thickness. The decrease in intensity instead is due to the mixing of gold ($Z = 79$) with copper, which as a lower atomic number ($Z = 29$), while the thickness can be assumed to remain constant. This interpretation is further supported by observations of other particles where the protrusion was clearly anisotropic and visible predominantly in one direction in 2D projection (Figure S5.5). The line profiles in Figure 5.2d confirm that this contrast reduction is spatially uniform across the in-plane rod from the start of the illumination sequence. This indicates that copper was incorporated homogeneously throughout the nanorod volume rather than accumulating as a segregated surface layer. At higher laser power (Figures 5.2c.8–c.12), both effects reversed: the sharp intensity peak in the line profile

corresponding to the out-of-plane protrusion disappeared and the in-plane contrast of the gold core recovered toward its original level, consistent with sublimation of the incorporated copper, which has a substantially lower vapor pressure than gold at the operating pressure of the TEM.

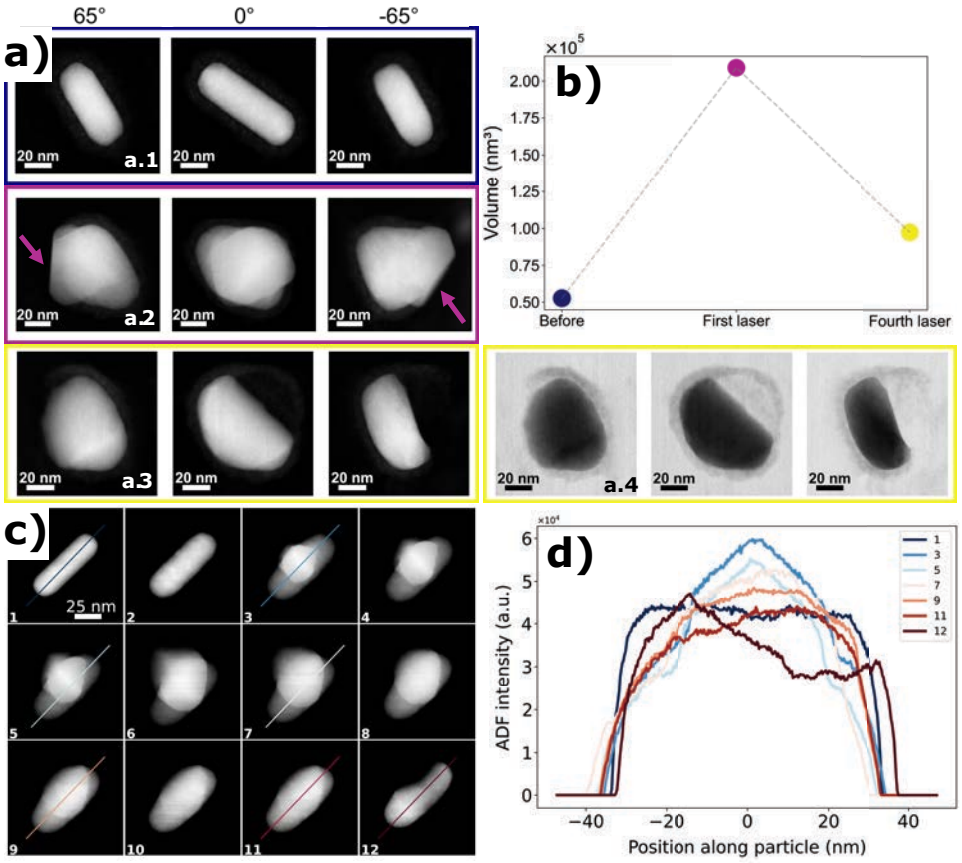

Figure 5.2: *a) ADF-STEM images taken tilting the holder at* 0 °, +65 °, −65 ° *(a.1) before, (a.2) after 700 nm and 26 MHz laser illumination at* 4.5 $\mu J/cm^2$ *for 40 seconds and (a.3) after illumination at* 5.1 $\mu J/cm^2$ *for 88 seconds. In (a.4) are the same images as in (a.3) but acquired with the bright field detector. b) Volume of the three 3D reconstructions after binarization. c) STEM images of another particle before (1), under 700 nm and 26 MHz laser illumination at* 5.8 $\mu J/cm^2$ *(2-6) and at* 7.0 $\mu J/cm^2$ *(6-12). d) Line profile of the intensity extracted along the same coded color line in c)*

Together, the tomography and STEM series established that laser illumination drives a substantial and reversible volumetric change in the $AuNR@TiO_2$. Further-

more, the incorporated material is distributed homogeneously through the particle. Based on the control experiments in *Section 5.3.1*, we attribute this material to copper migrating from the substrate. To directly confirm this assignment, EDX maps were acquired on a different particle before and after successive illumination stages at increasing laser fluence (Figure 5.3). The corresponding STEM images are shown in Figure 5.3a. Each map was acquired using the exact same parameters and magnification over 8 minutes. The fluence was increased stepwise between acquisitions: the first EDX map was acquired before any laser exposure, the second two were acquired after illuminating the sample with $3.7\,\mu J/cm^2$, the fourth with $4.8\,\mu J/cm^2$ and the last with $5.1\,\mu J/cm^2$.

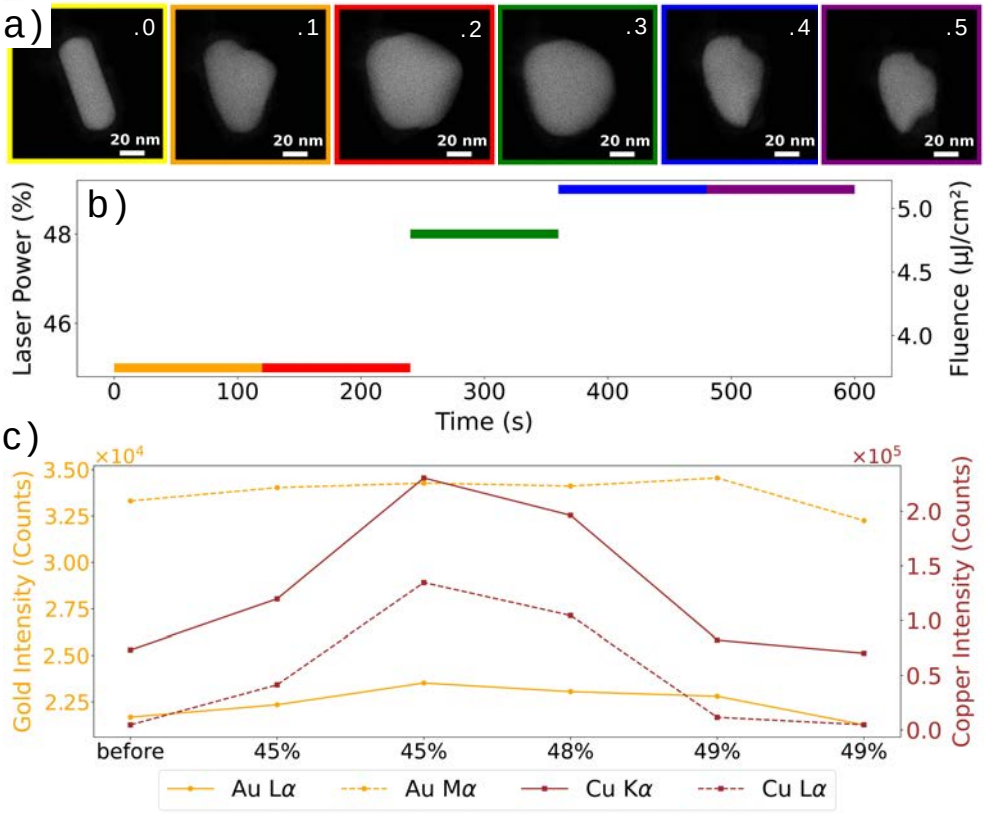

Figure 5.3: *a) STEM images of a NR at different stages of laser illumination. b) The laser power and corresponding fluence applied over time. c) Peak intensities of Au and Cu are shown for the same spectra after background removal and Gaussian fitting.*

Figure 5.3c shows the intensity of the characteristic X-ray lines for Au and Cu (AuL_α, AuM_α, CuK_α, CuL_α) obtained by quantitative fitting. The gold signal remained constant throughout the series despite the particle growing in size, while the copper signal increased substantially during the first two exposures and subsequently decreased at higher fluence. Since EDX signal scales with the amount of material present, the constant gold signal rules out gold redistribution as the source of the volume increase, and the rising copper signal directly confirms that the incorporated material is copper. Control experiments on the contribution of the copper signal from the grid bar and from the column due to secondary electrons were performed, ruling out that the increase in copper signal was just an artifact of the measurement.

5.3.3 Composition control and alloy homogeneity

Having established that copper is incorporated into the $AuNR@TiO_2$ under laser illumination, the key remaining question is whether it forms a spatially homogeneous alloy with gold or remains segregated, for instance accumulating preferentially in the region of the protrusion. To address this at the spatial resolution accessible by EDX, summed X-ray counts were extracted from several distinct regions across a single nanoparticle that developed a large protrusion after laser-induced alloying (Figure S5.7a). As shown in Figure Figure S5.7b, the ratio of the gold and copper signals remained uniform across all sampled regions, indicating that copper was distributed evenly throughout the particle at this length scale rather than concentrated in any particular zone. This points toward homogeneous alloying rather than core-shell segregation or surface decoration.

To further probe local compositional homogeneity, we performed 4D-STEM experiments in quasi-parallel nano-beam diffraction mode. This technique provides a diffraction pattern at each probe position and allows comparison of local lattice parameters across the particle. TEM images of the chosen $AuNR@TiO_2$ before (Figure 5.4a.1) and after (Figure 5.4a.2) laser illumination show that a large protrusion developed during illumination, extending well beyond the original TiO_2 shell boundary. This outward growth indicates that gold atoms redistributed beyond their original morphology to participate in forming the alloy, a finding consistent with the strongly negative mixing enthalpy of AuCu at the nanoscale, which makes Au-Cu bond formation energetically favorable over maintaining a pure gold core adjacent to a copper-rich region[192]. The virtual dark-field image reconstructed from the 4D-STEM dataset is shown in Figure 5.4b, confirming the spatial extent of the crystalline material after illumination.

Diffraction patterns extracted from two distinct regions, the original nanorod interior (green, Figure 5.4c.1) and the newly grown material outside the original shell (magenta, Figure 5.4c.2), are compared in Figure 5.4c.3, where they are additively

overlaid. In this representation, green indicates signal unique to the original rod position, magenta indicates signal unique to the grown region, and white indicates full overlap. The two patterns overlap almost completely, with the only deviation occurring at small radial distances, where TiO_2 diffraction originating from the shell was present exclusively in the original rod region. The near-perfect overlap of the diffraction patterns from both regions demonstrates that the original nanorod and the newly grown material share the same lattice parameter. They are crystallographically indistinguishable and form a single homogeneous AuCu solid solution. To quantify this, diffraction spot positions in both patterns were determined by 2D Gaussian fitting and the radial displacement Δr between corresponding reflections in the two regions was calculated in Figure 5.4d. All reflections show Δr values close to zero, with no systematic trend, confirming that there is no measurable lattice parameter difference between the original rod location and the grown material and that copper is homogeneously distributed throughout the particle at the length scale accessible by this measurement.

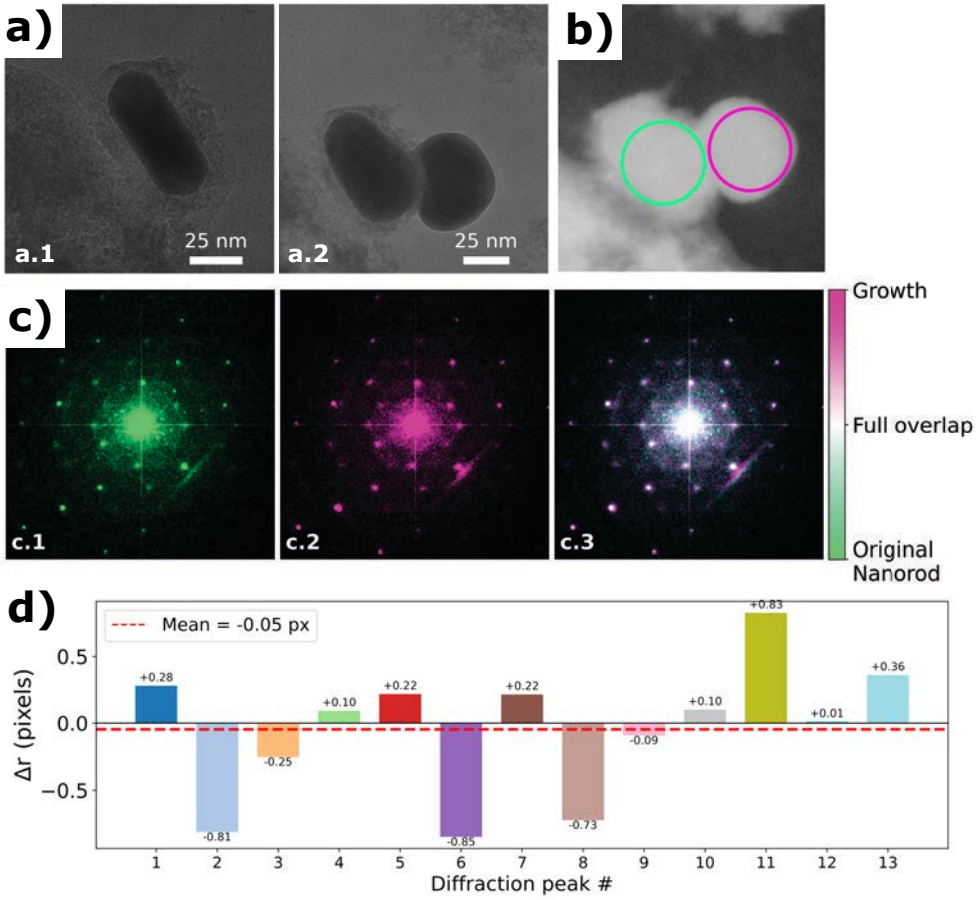

Figure 5.4: *a) HR−TEM image of a $AuNR@TiO_2$ before laser illumination (a.1) and after after irradiation at $5.5\,\mu J/cm^2$ of the maximum laser power (a.2) and b) Real space image of the same $AuNR@TiO_2$ in a.2 c) Diffraction pattern from the corresponding area inside the circle in b from the area inside the green circle, while from the area inside the pink circle in c.2 after logarithmic normalization and percentile contrast enhancement. In c.3 the two diffraction patterns are overlaid to highlight differences, with green indicating signal unique to c.1, magenta unique to c.2, and white indicating full overlap between the two patterns. d)Radial displacement of the diffraction spots between c.1 and c.2. Each bar shows the change in distance Δr of one diffraction reflection fitted with a Gaussian from the direct beam center between the two regions. Positive values indicate expansion, negative values contraction. The red dashed line indicates the mean displacement across all reflections*

5.3.4 Diffraction-based analysis of composition dynamics and kinetics

We then turned to electron diffraction, which allows rapid acquisition during laser illumination and provides access to the evolution of the lattice parameter on millisecond timescales. In the present experiment, each diffraction pattern was acquired over 1 s to improve signal-to-noise, although shorter acquisition times can be achieved by increasing the beam convergence. In this way, diffraction provides a time-resolved probe of alloy composition at the single-particle level. Diffraction is sensitive to the lattice parameter of the alloy and can therefore quantify the copper fraction through Vegard's law [193]. The Vegard's law states that in a solid solution of two components, the lattice parameter is roughly the composition-weighted mean of the lattice parameters of the constituent elements at the same temperature [193]. Therefore, for an Au–Cu alloy with Cu fraction x the lattice parameter is approximately:

$$a_{\mathrm{AuCu}} = (1 - x)a_{\mathrm{Au}} + xa_{\mathrm{Cu}} \tag{5.1}$$

Both gold and copper crystallize in the FCC structure with well-separated lattice parameters. Gold has an atomic radius of 134 pm and a lattice parameter a=407.82 pm, whereas copper has an atomic radius of 117 pm and a lattice parameter a=361.49 pm, corresponding to (111) d-spacings of 0.235 nm and 0.208 nm, respectively. As a result, copper incorporation into the gold lattice produces a measurable contraction of the lattice parameter that can be tracked in real time through the positions of diffraction spots. To measure diffraction spacings, consecutive electron diffraction patterns were acquired using the TimePix3 pixelated detector on a single $AuNR@TiO_2$ while the laser was on, with a stepwise laser fluence increase from 5.5 μJ/cm^2 to 13.5 μJ/cm^2. It is worth noting that these are slightly higher fluences compared to the experiments in Figures 5.1 and 5.2. These higher fluences were required to achieve the same particle modifications as observed before, likely be due to a slight misalignment in the laser on the day of the experiments. The larger laser spot resulted in a lower fluence as shown in Figure S5.1b. Between each fluence increment, a TEM image of the particle was acquired to monitor morphological changes; representative images at selected illumination stages are shown in Figure 5.5a, confirming the same expansion-then-contraction reshaping sequence described in *Section 5.3.1.* The laser power profile and corresponding fluence are shown in Figure 5.5b. A representative diffraction pattern is shown in Figure 5.5c. The sharp diffraction spots arising from the crystalline nanorod are superimposed on two broad amorphous rings from the carbon substrate, which were observed to sharpen progressively under laser heating as amorphous carbon partially graphitized.

The positions of individual diffraction spots were tracked across all illumination steps by fitting a 2D Gaussian to each spot and computing its radial distance from the center of mass (COM) of the diffraction pattern (Figure 5.5c, colored overlays). All

tracked reflections show the same trend: a progressive outward radial shift up to the fourth illumination step, followed by a gradual return toward the initial positions at higher fluence. Since an outward shift corresponds to a smaller d-spacing by Bragg's law, this directly reports lattice contraction consistent with copper incorporation. The d-spacing for the two reflections closest to the COM is plotted as a function of illumination time in Figure 5.5d: it decreases from 0.235 nm, consistent with pure gold, to a minimum of approximately 0.215 nm, before recovering toward the initial value at higher fluence. Applying Vegard's law to the minimum d-spacing of 0.215 nm yields a copper fraction of approximately 75%. It should be noted that the same trend is followed by all the diffraction reflections tracked in the patterns.

Since these diffraction patterns were recorded while the laser was on, thermal expansion of the lattice partially counteracted the contraction following copper incorporation, causing the copper fraction to be underestimated. To decouple these effects, additional diffraction patterns were acquired with the laser switched off after some illumination steps, allowing the substrate to return to room temperature between measurements. The laser-off series in Figure S5.8 shows the same trend: initial d-spacing decrease followed by recovery. It should be noted that laser-off diffraction data were only available after specific laser exposure steps. When comparing the laser-on and laser-off measurements after the second laser exposure step, the estimated copper fraction increased from approximately 70% under laser illumination to approximately 80% once the laser was switched off, highlighting the significant influence of thermal expansion during irradiation. Since the laser-on data reached a minimum d-spacing at the end of the third laser exposure step, where no corresponding laser-off diffraction pattern was acquired, it is reasonable to expect an even higher copper content when thermal contributions are removed. Based on the observed trend, the copper fraction at this stage is therefore estimated to approach 85% under laser-off conditions. This fraction is consistent in order of magnitude with the fourfold volume increase measured by tomography in *Section 5.3.2*. Assuming a similar atomic volumes for Au and Cu, a fourfold volume increase implies a composition of approximately $Au_{0.25}Cu_{0.75}$, in good agreement with the diffraction result. We note that the absolute copper fraction will vary between particles depending on the amount of copper locally available from the surrounding substrate, while the comparison between tomography and diffraction involves different particles measured under slightly different conditions. Nevertheless, the quantitative consistency across these independent measurements strengthens the conclusion that a high copper fraction, on the order of 75–85%,can be achieved under laser illumination.

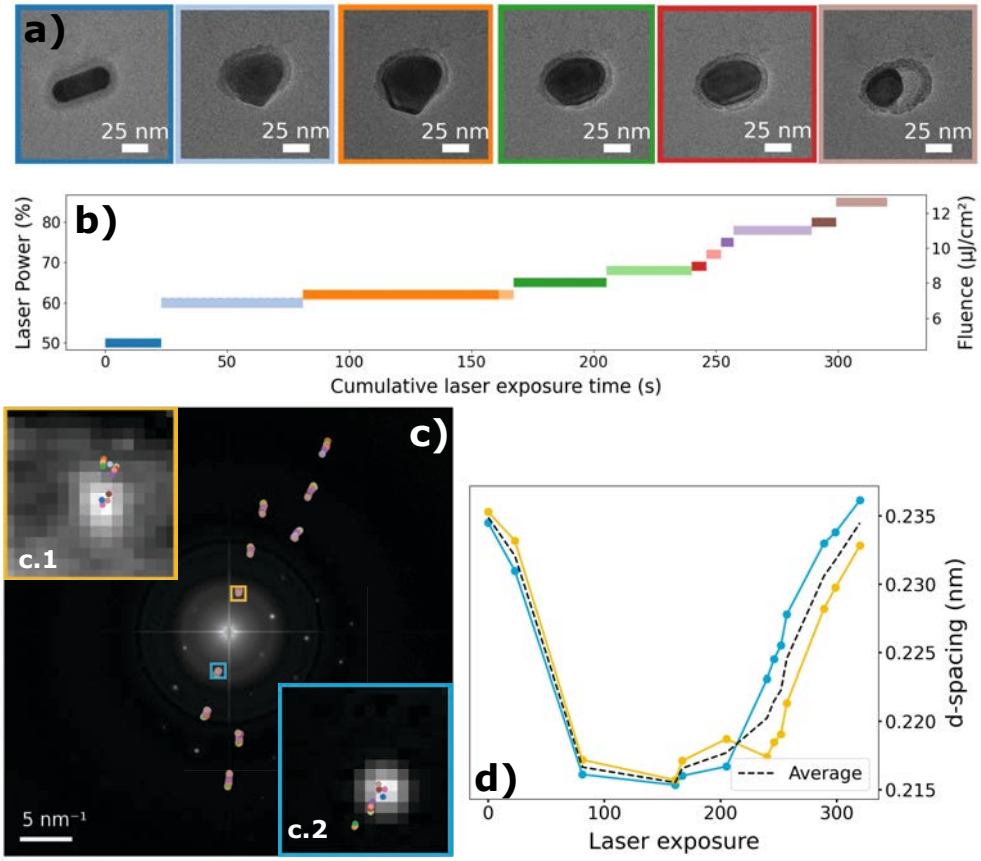

Figure 5.5: *Diffraction under laser illumination a) TEM images of the NR at different stages of laser illumination b) Exposure time for each laser step. On the y axis the respective laser power and fluence are shown while the x-axis represents the cumulative illumination time for each laser exposure step. c) Positions of diffraction spots tracked from the last diffraction pattern acquired in each laser exposure step shown in b), overlaid on the diffraction spectra acquired before laser exposure. The colors of the tracked diffraction spots correspond to the laser exposure step colors shown in b), with bright pink indicating the dataset acquired prior to any laser illumination. In c.1 and c.2 a zoom in on the two diffraction spots closest to the COM is shown, highlighting the change in position of the diffraction dots as function of laser exposure. d) d-spacing as a function of laser illumination time for the two diffraction dots in c) is shown. The dotted line represents the average of the two diffraction spacings to account for sub-pixel errors.*

Furthermore, from the difference in d-spacing measured under laser-on and laser-off conditions, we were able to estimate the temperature reached during laser irradiation. Thermal expansion leads to a lattice change according to:

$$\frac{\Delta d}{d} = \alpha \, \Delta T \tag{5.2}$$

where α is the linear thermal expansion coefficient. Using the measured difference in d-spacing between laser-on and laser-off conditions yields an estimated temperature reached under laser of approximately $T \approx 800\text{K}$. This value is of the same order of magnitude as the temperatures predicted by the heat simulations shown in Figure S5.2b–c. The remaining difference can be attributed to partial heat dissipation between laser pulses, such that the experimentally measured temperature represents an average value that is lower than the peak temperature reached in the simulations.

Having established the extent of alloying, we now examine the kinetics of copper incorporation and removal. A clear asymmetry between these two processes is evident in Figure 5.5d. During the initial heating steps, the diffraction peaks shift rapidly toward Cu-rich compositions, whereas at higher fluences the return toward pure Au proceeds much more gradually. These data were extracted from diffraction patterns acquired at the end of each illumination step and therefore do not capture the continuous evolution of the composition during laser exposure. To access this continuous evolution, we analyze diffraction patterns acquired throughout individual laser exposure steps (Figure 5.6). These measurements reveal that copper incorporation occurs on a much shorter timescale than copper removal, producing a pronounced kinetic asymmetry.

The rapid incorporation reflects a coupled sequence of processes: thermal activation and partial melting of nearby copper-containing clusters, transport of copper species to the Au nanorod surface, and fast interdiffusion leading to alloy formation throughout the particle. As shown in Figure 5.6b.1, incorporation largely completes within $\sim$10 s. At the temperatures reached during illumination ($\sim$850 K), the interdiffusion coefficient of Cu in Au is on the order of $10^{-16}\,\text{m}^2\,\text{s}^{-1}$ [185], corresponding to diffusion times of only a few seconds across a 25 nm nanorod. Internal diffusion is therefore not rate-limiting; instead, incorporation rates depend on the supply of copper from the local environment and are thus sensitive to particle geometry and proximity to copper sources.

In contrast, copper removal proceeds much more slowly and is governed by surface evaporation rather than bulk diffusion. At the temperatures required for sublimation, internal diffusion remains fast and maintains compositional equilibrium across the particle, continuously replenishing surface copper from the interior. The rate-limiting step is therefore the escape of copper atoms from the particle surface.

Copper evaporation in vacuum can be described by the Hertz–Knudsen equation:

$$\frac{dN}{A\,dt} = \frac{\alpha\,(p_{\mathrm{Cu}} - p_{\mathrm{env}})}{\sqrt{2\pi m k_{\mathrm{B}} T}} \tag{5.3}$$

where A is the surface area available for evaporation, α the evaporation coefficient, p_{Cu} the equilibrium copper vapor pressure, p_{env} the environmental pressure, m the atomic mass of copper, and T the temperature.

Using the evaporative flux obtained from Eq. 5.3, the characteristic time required to remove the incorporated copper can be estimated as

$$t = \frac{V_{\mathrm{Cu}}\,\rho_{\mathrm{Cu}}}{\Phi\,A_{\mathrm{rod}}} \tag{5.4}$$

where V_{Cu} is the incorporated copper volume, ρ_{Cu} the copper density, Φ the evaporation flux, and A_{rod} the available surface area. V_{Cu} and A_{rod} are estimated from tomography at 47% Cu content (Figure 5.2b).

Assuming $T = 850\,\mathrm{K}$, $\alpha = 1$, $p_{\mathrm{Cu}} = 1.33 \times 10^{-3}\,\mathrm{Pa}$, $p_{\mathrm{env}} = 2.2 \times 10^{-5}\,\mathrm{Pa}$, and $\rho_{\mathrm{Cu}} = 8960\,\mathrm{kg\,m^{-3}}$, the model predicts complete copper removal after approximately 60 s for a typical nanorod geometry.

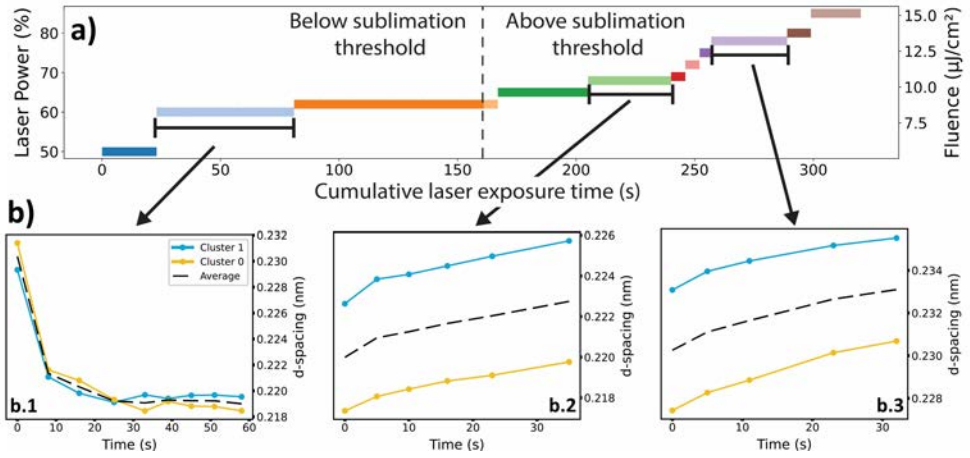

Figure 5.6: *a) Fluence as a function of time for each laser exposure as in Figure 5.5b. b) d-spacing of the two reflections closest to the COM tracked during three representative laser illuminations. The dotted line represents the average of the two diffraction spacings to account for sub-pixel errors. b.1) d-spacing tracked during the second laser exposure over 58 seconds. b.2) d-spacing tracked during the sixth laser exposure over 38 seconds. b.3) d-spacing tracked during the ninth laser exposure over 32 seconds.*

This estimate represents a lower bound, as the calculation assumes that the entire particle surface is available for evaporation. In reality, the TiO_2 shell restricts the effective escape area, which substantially slows down copper removal. The experimentally observed removal times of several hundred seconds in Figures 5.6b.2 and b.3, are therefore consistent with surface-limited evaporation moderated by shell geometry. These results confirm that copper removal is controlled by evaporative flux from the particle surface rather than by any diffusive process within the alloy.

Taken together, these observations reveal two complementary and independently tunable handles on alloy composition. Laser fluence sets the thermodynamic window, determining whether the system sits in a regime where incorporation dominates or where evaporative loss becomes significant. Illumination time controls how far the composition evolves within that window. Because evaporation requires substantially higher fluences and longer times than incorporation, the alloy composition is kinetically robust against small perturbations in laser power once formed, and can be driven back toward pure Au only by deliberate escalation of fluence. Switching the laser off at any point kinetically traps the current composition indefinitely, providing a practical and flexible route to targeting a desired Cu fraction at the single-particle level.

5.4 Conclusion

This work demonstrates that pulsed optical excitation enables dynamic, reversible control over the composition of individual bimetallic nanoparticles, as directly visualized in situ by transmission electron microscopy. Specifically, we show that Au nanorods encapsulated in a TiO_2 shell can incorporate copper from the surrounding substrate under laser illumination, forming a homogeneous AuCu solid solution with tunable composition. Through a combination of TEM imaging, electron tomography, EDX, and diffraction analysis, we established that laser-induced heating drove substantial and reversible structural and compositional changes. Copper incorporation led to pronounced volumetric expansion and lattice contraction consistent with alloy formation, reaching Cu fractions up to about 75–85%. At higher laser fluences, partial removal of copper via sublimation restored the system toward its initial Au-rich state. Importantly, 4D-STEM and diffraction measurements confirmed that the resulting alloy was spatially homogeneous across the particle, rather than phase-segregated. The maximum Cu fractions achieved are likely not an intrinsic limit of the alloying process, but are instead constrained by the finite availability of copper in the local region of the TEM window, which acts as the material reservoir.

The alloying process was governed by asymmetric kinetics: rapid incorporation of copper at moderate fluence, followed by slower removal at higher fluence. This asymmetry provides two independent control parameters, laser fluence and illumina-

tion time, enabling precise tuning of composition. Once the laser is switched off, the alloy state is kinetically trapped at room temperature, allowing intermediate, non-equilibrium compositions to be stabilized on demand. Beyond demonstrating a novel route to achieve high Cu incorporation in Au nanoparticles, this study demonstrates the potential of optical excitation as a tool for actively controlling material composition at the single-particle level. The ability to reversibly drive and freeze alloy states opens new opportunities for tailoring catalytic, plasmonic, and electronic properties in situ.

5.5 Appendix

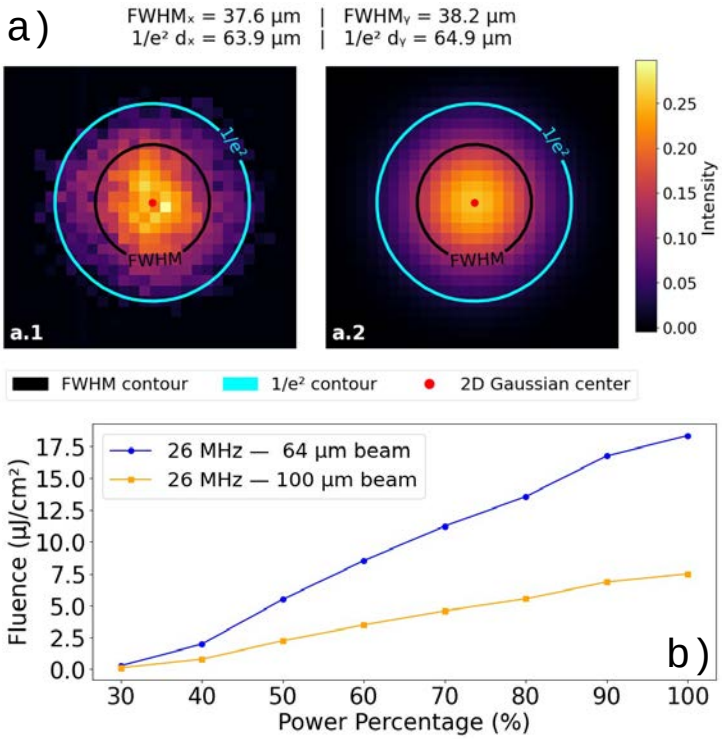

Figure S5.1: Characterization of the laser spot size and fluence. a) Visualization of the laser beam on a photoluminescent alignment TEM holder. (a.1) Experimental laser spot image and (a.2) fitted two-dimensional Gaussian model. The 1/e2 is shown in cyan and the FWHM contour in black. b) Fluence as a function of power percentage output of the picosecond laser measured at 700 nm and 26 MHz for beam diameters ($1/e^2$) of 64 μm (blue) and 100 μm (orange)

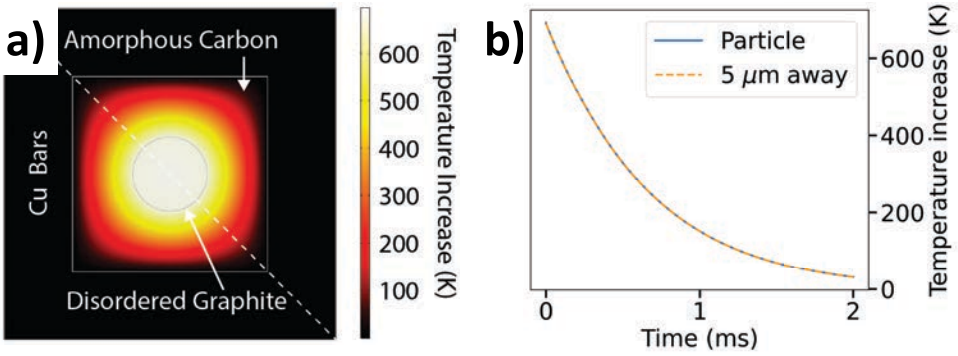

Figure S5.2: *a) COMSOL heat simulation at maximum temperature exhibiting the temperature gradient of a single grid square of a Quantifoil copper grid . b)Simulated temperature decay in time after the laser was turned off at time zero for the used TEM grid geometry and laser excitation conditions. The temperature was extracted in the center, where the Au nanoparticles was located (blue line) and 5 μm away (orange dotted line).*

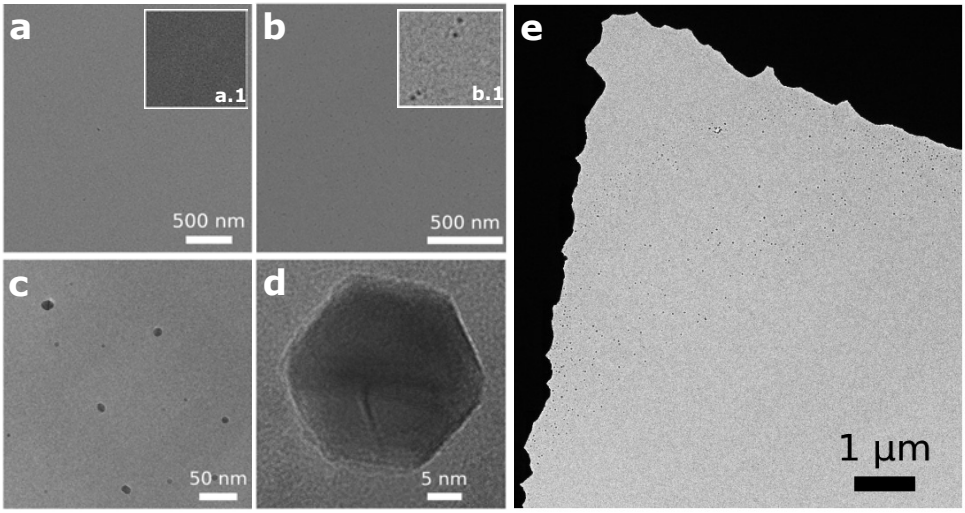

Figure S5.3: *Empty Quantifoil grid under laser illumination before (a) and after (b) laser exposure at*$3.0\,\mu J/cm^2$*, with corresponding zoom-ins in a.1 and b.1. c) Larger clusters formed when the laser power was increased to* $3.8\,\mu J/cm^2$*. d) Zoom-in of one of the agglomerates in c). e) Appearance of clusters near the copper bars after laser exposure at full power (*$18.3\,\mu J/cm^2$*).*

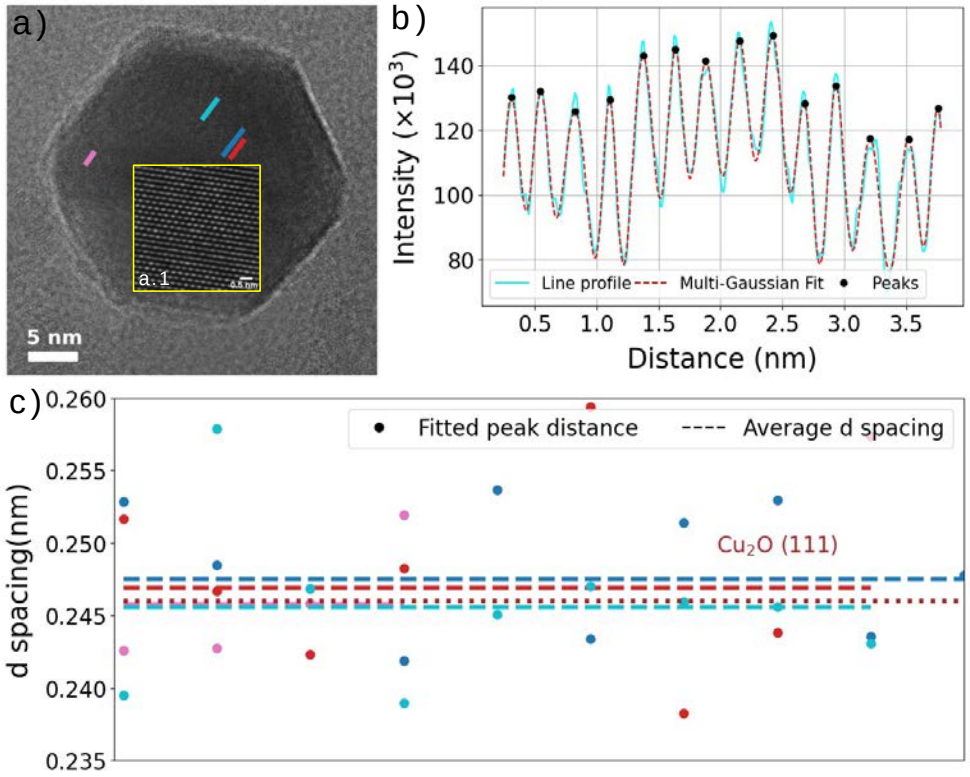

Figure S5.4: *a) TEM image of a large cluster formed on a Quantifoil grid after laser exposure at* $7.1\,\mu J/cm^2$*. In a.1 a zoom-in is shown, where individual atomic columns are visible. b) Example of line profile extracted along the cyan line in a). c) Profile analyses along each colored line in a). The dotted brown line represents the theoretical d-spacing for the (111)* Cu_2O*.*

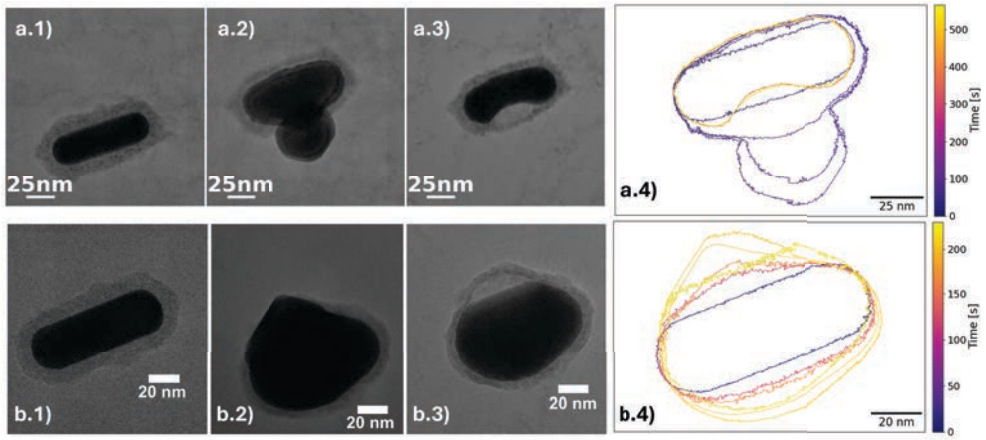

Figure S5.5: *TEM images of other AuNRs@TiO2 under laser exposure. a) Images of a single particle before laser exposure (a.1), immediately after switching on the laser at* $4.8\,\mu J/cm^2$ *(a.2), and after several seconds of illumination (a.3). The corresponding particle outline under laser illumination is shown in (a.4). b) Images of another particle before exposure (b.1), after* $4.8\,\mu J/cm^2$ *(b.2), and after* $8.5\,\mu J/cm^2$ *(b.3). The outline of this particle at successive times under laser illumination is shown in (b.4)*

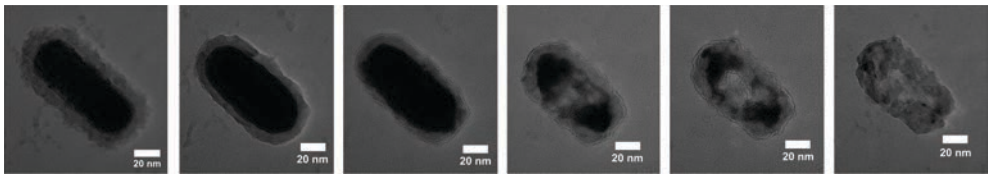

Figure S5.6: *$AuNR@TiO_2$ before and under continuous laser illumination at 8.5 $\mu J/cm^2$. Images at successive times during laser exposure are shown.*

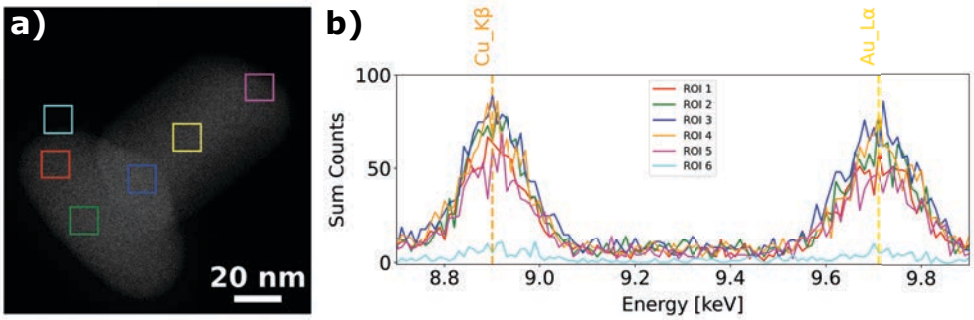

Figure S5.7: *Gold nanorod after laser illumination, with the different regions analyzed highlighted. b) EDX spectra summed over each of the regions highlighted in a). Each colored area in a) corresponds to the EDX spectrum shown in the same color in b)*

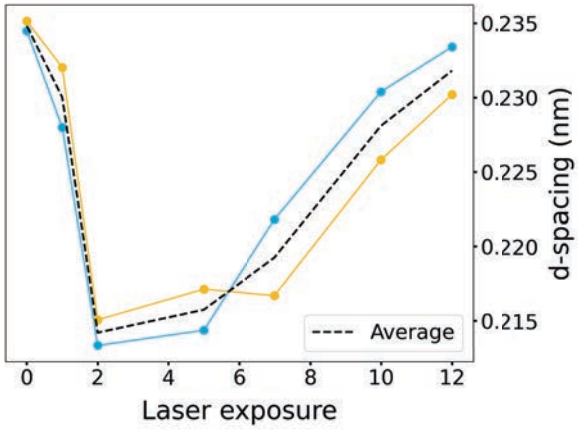

Figure S5.8: *Same as Figure 5.5d but with laser OFF. d-spacing extracted for the two diffraction reflections closer to the COM after different stages of laser exposure at room temperature*

Bibliography

[1] ourworldindata, *Ourworldindata*, (2025) `https://ourworldindata.org/grapher/global-energy-substitution?time=1950..latest` (visited on 05/24/2026).

[2] H.-H. Kuo, T.-G. Vo, and Y.-J. Hsu, "From sunlight to valuable molecules: a journey through photocatalytic and photoelectrochemical glycerol oxidation towards valuable chemical products", Journal of Photochemistry and Photobiology C: Photochemistry Reviews **58**, 100649 (2024).

[3] E. Hutter and J. H. Fendler, "Exploitation of localized surface plasmon resonance", Advanced materials **16**, 1685–1706 (2004).

[4] K. L. Kelly, E. Coronado, L. L. Zhao, and G. C. Schatz, "The optical properties of metal nanoparticles: the influence of size, shape, and dielectric environment", The Journal of Physical Chemistry B **107**, 668–677 (2003).

[5] T. W. Odom and G. C. Schatz, *Introduction to plasmonics*, 2011.

[6] X. Cui, Q. Ruan, X. Zhuo, X. Xia, J. Hu, R. Fu, Y. Li, J. Wang, and H. Xu, "Photothermal nanomaterials: a powerful light-to-heat converter", Chemical Reviews **123**, 6891–6952 (2023).

[7] G. Mie, "Beiträge zur optik trüber medien, speziell kolloidaler metallösungen", Annalen der physik **330**, 377–445 (1908).

[8] R. Verma, G. Sharma, and V. Polshettiwar, "The paradox of thermal vs. non-thermal effects in plasmonic photocatalysis", Nature Communications **15**, 7974 (2024).

[9] C. Clavero, "Plasmon-induced hot-electron generation at nanoparticle/metal-oxide interfaces for photovoltaic and photocatalytic devices", Nature Photonics **8**, 95–103 (2014).

[10] U. Kreibig and M. Vollmer, *Optical properties of metal clusters*, Vol. 25 (Springer Science & Business Media, 2013).

[11] F. Tong, X. Liang, X. Bao, and Z. Zheng, "Photocatalysis on hybrid plasmonic nanomaterials: from catalytic mechanism study at single-particle level to materials design", ACS Catalysis **14**, 11425–11446 (2024).

[12] A. Stefancu, N. J. Halas, P. Nordlander, and E. Cortes, "Electronic excitations at the plasmon–molecule interface", Nature Physics **20**, 1065–1077 (2024).

[13] S. Y. Lee, P. V. Tsalu, G. W. Kim, M. J. Seo, J. W. Hong, and J. W. Ha, "Tuning chemical interface damping: interfacial electronic effects of adsorbate molecules and sharp tips of single gold bipyramids", Nano letters **19**, 2568–2574 (2019).

[14] G. Rubloff, "Metal-semiconductor interfaces and schottky barriers", in *Dynamical phenomena at surfaces, interfaces and superlattices* (Springer, 1985), pp. 220–243.

[15] P. J. Schuck, "Hot electrons go through the barrier", Nature nanotechnology **8**, 799–800 (2013).

[16] N. Ghorai, Z. Yang, S. T. Gebre, S. Wu, F. Zhao, I. N. Ivanov, and T. Lian, "Efficient size-dependent hot electron transfer from au to tio2 nanoparticles", Nano Letters **25**, 3253–3258 (2025).

[17] T. Yang, B. Lu, Y. Zuo, and J. Huang, "Configuration engineering of plasmonic-metal/semiconductor nanohybrids for solar fuel production", Chemistry of Materials **37**, 1685–1715 (2025).

[18] H. Oh, S. Chatterjee, Z. Jia, E. Gomez, S. A. Lee, J. Lin, O. Verma, S. Link, and C. F. Landes, "Plasmonic pathway to hybrid nanomaterials through energy transfer", Science Advances **11**, eady7016 (2025).

[19] G. Liu, Y. Lou, Y. Zhao, and C. Burda, "Directional damping of plasmons at metal–semiconductor interfaces", Accounts of Chemical Research **55**, 1845–1856 (2022).

[20] S. K. Cushing, J. Li, J. Bright, B. T. Yost, P. Zheng, A. D. Bristow, and N. Wu, "Controlling plasmon-induced resonance energy transfer and hot electron injection processes in metal@tio2 core–shell nanoparticles", The Journal of Physical Chemistry C **119**, 16239–16244 (2015).

[21] K. Wu, J. Chen, J. R. McBride, and T. Lian, "Efficient hot-electron transfer by a plasmon-induced interfacial charge-transfer transition", Science **349**, 628–632 (2015).

[22] J. Ma and S. Gao, "Plasmon-induced electron–hole separation at the ag/tio2(110) interface", ACS Nano **13**, PMID: 31393703, 13658–13667 (2019).

[23] D. C. Ratchford, A. D. Dunkelberger, I. Vurgaftman, J. C. Owrutsky, and P. E. Pehrsson, "Quantification of efficient plasmonic hot-electron injection in gold nanoparticle–tio2 films", Nano letters **17**, 6047–6055 (2017).

[24] B. Ostovar, S. A. Lee, A. Mehmood, K. Farrell, E. K. Searles, B. Bourgeois, W.-Y. Chiang, A. Misiura, N. Gross, A. Al-Zubeidi, et al., "The role of the plasmon in interfacial charge transfer", Science Advances **10**, eadp3353 (2024).

[25] R. Long and O. V. Prezhdo, "Instantaneous generation of charge-separated state on tio2 surface sensitized with plasmonic nanoparticles", Journal of the American Chemical Society **136**, 4343–4354 (2014).

[26] M. L. Brongersma, N. J. Halas, and P. Nordlander, "Plasmon-induced hot carrier science and technology", Nature nanotechnology **10**, 25–34 (2015).

[27] R. Jiang, B. Li, C. Fang, and J. Wang, "Metal/semiconductor hybrid nanostructures for plasmon-enhanced applications", Advanced materials **26**, 5274–5309 (2014).

[28] D. M. Foster, T. Pavloudis, J. Kioseoglou, and R. E. Palmer, "Atomic-resolution imaging of surface and core melting in individual size-selected au nanoclusters on carbon", Nature communications **10**, 2583 (2019).

[29] W. Albrecht, E. Bladt, H. Vanrompay, J. D. Smith, S. E. Skrabalak, and S. Bals, "Thermal stability of gold/palladium octopods studied in situ in 3d: understanding design rules for thermally stable metal nanoparticles", ACS nano **13**, 6522–6530 (2019).

[30] G. González-Rubio, J. González-Izquierdo, L. Bañares, G. Tardajos, A. Rivera, T. Altantzis, S. Bals, O. Peña-Rodríguez, A. Guerrero-Martínez, and L. M. Liz-Marzán, "Femtosecond laser-controlled tip-to-tip assembly and welding of gold nanorods", Nano letters **15**, 8282–8288 (2015).

[31] M. Nazemi, S. R. Panikkanvalappil, C.-K. Liao, M. A. Mahmoud, and M. A. El-Sayed, "Role of femtosecond pulsed laser-induced atomic redistribution in bimetallic au–pd nanorods on optoelectronic and catalytic properties", ACS nano **15**, 10241–10252 (2021).

[32] J. Yan, D. Zhu, J. Xie, Y. Shao, and W. Xiao, "Light tailoring of internal atomic structure of gold nanorods", Small **16**, 2001101 (2020).

[33] S. Link, Z. L. Wang, and M. A. El-Sayed, "Alloy formation of gold−silver nanoparticles and the dependence of the plasmon absorption on their composition", The Journal of Physical Chemistry B **103**, 3529–3533 (1999).

[34] T. Milagres de Oliveira, W. Albrecht, G. Gonzalez-Rubio, T. Altantzis, I. P. Lobato Hoyos, A. Beche, S. Van Aert, A. Guerrero-Martinez, L. M. Liz-Marzan, and S. Bals, "3d characterization and plasmon mapping of gold nanorods welded by femtosecond laser irradiation", ACS nano **14**, 12558–12570 (2020).

[35] L. Wang, M. Hasanzadeh Kafshgari, and M. Meunier, "Optical properties and applications of plasmonic-metal nanoparticles", Advanced Functional Materials **30**, 2005400 (2020).

[36] D. Astruc, "Introduction: nanoparticles in catalysis", Chemical Reviews **120**, 461–463 (2020).

[37] C. Novo, D. Gomez, J. Perez-Juste, Z. Zhang, H. Petrova, M. Reismann, P. Mulvaney, and G. V. Hartland, "Contributions from radiation damping and surface scattering to the linewidth of the longitudinal plasmon band of gold nanorods: a single particle study", Physical Chemistry Chemical Physics **8**, 3540–3546 (2006).

[38] S. Schultz, D. R. Smith, J. J. Mock, and D. A. Schultz, "Single-target molecule detection with nonbleaching multicolor optical immunolabels", Proceedings of the National Academy of Sciences **97**, 996–1001 (2000).

[39] J. Olson, S. Dominguez-Medina, A. Hoggard, L.-Y. Wang, W.-S. Chang, and S. Link, "Optical characterization of single plasmonic nanoparticles", Chemical Society Reviews **44**, 40–57 (2015).

[40] W.-S. Chang, J. W. Ha, L. S. Slaughter, and S. Link, "Plasmonic nanorod absorbers as orientation sensors", Proceedings of the National Academy of Sciences **107**, 2781–2786 (2010).

[41] A. Gaiduk, P. V. Ruijgrok, M. Yorulmaz, and M. Orrit, "Detection limits in photothermal microscopy", Chemical Science **1**, 343–350 (2010).

[42] A. Arbouet, D. Christofilos, N. Del Fatti, F. Vallée, J. Huntzinger, L. Arnaud, P. Billaud, and M. Broyer, "Direct measurement of the single-metal-cluster optical absorption", Physical review letters **93**, 127401 (2004).

[43] Y.-Y. Cai, J. G. Liu, L. J. Tauzin, D. Huang, E. Sung, H. Zhang, A. Joplin, W.-S. Chang, P. Nordlander, and S. Link, "Photoluminescence of gold nanorods: purcell effect enhanced emission from hot carriers", Acs Nano **12**, 976–985 (2018).

[44] C. M. Hill, R. Bennett, C. Zhou, S. Street, J. Zheng, and S. Pan, "Single ag nanoparticle spectroelectrochemistry via dark-field scattering and fluorescence microscopies", The Journal of Physical Chemistry C **119**, 6760–6768 (2015).

[45] H. Staleva and G. V. Hartland, "Vibrational dynamics of silver nanocubes and nanowires studied by single-particle transient absorption spectroscopy", Advanced Functional Materials **18**, 3809–3817 (2008).

[46] A. Al-Zubeidi, L. A. McCarthy, A. Rafiei-Miandashti, T. S. Heiderscheit, and S. Link, "Single-particle scattering spectroscopy: fundamentals and applications", Nanophotonics **10**, 1621–1655 (2021).

[47] U. Hohenester and A. Trügler, "Mnpbem - a matlab toolbox for the simulation of plasmonic nanoparticles", Computer Physics Communications **183**, 370–381 (2012).

[48] M. Dieperink, A. Skorikov, N. Claes, S. Bals, and W. Albrecht, "Considerations for electromagnetic simulations for a quantitative correlation of optical spectroscopy and electron tomography of plasmonic nanoparticles", Nanophotonics **13**, 4647–4665 (2024).

[49] E. Abbe, “Beiträge zur theorie des mikroskops und der mikroskopischen wahrnehmung”, Archiv für mikroskopische Anatomie **9**, 413–468 (1873).

[50] M. Knoll and E. Ruska, “Das elektronenmikroskop”, Zeitschrift für physik **78**, 318–339 (1932).

[51] L. De Broglie, “The reinterpretation of wave mechanics”, Foundations of physics **1**, 5–15 (1970).

[52] R. Erni, M. D. Rossell, C. Kisielowski, and U. Dahmen, “Atomic-resolution imaging with a sub-50-pm electron probe”, Physical review letters **102**, 096101 (2009).

[53] P. A. Midgley and M. Weyland, “3d electron microscopy in the physical sciences: the development of z-contrast and eftem tomography”, Ultramicroscopy **96**, 413–431 (2003).

[54] W. Albrecht and S. Bals, “Fast electron tomography for nanomaterials”, The Journal of Physical Chemistry C **124**, 27276–27286 (2020).

[55] S. Hata, H. Furukawa, T. Gondo, D. Hirakami, N. Horii, K. I. Ikeda, K. Kawamoto, K. Kimura, S. Matsumura, M. Mitsuhara, H. Miyazaki, S. Miyazaki, M. M. Murayama, H. Nakashima, H. Saito, M. Sakamoto, and S. Yamasaki, “Electron tomography imaging methods with diffraction contrast for materials research”, Microscopy **69**, 141–155 (2020).

[56] A. M. Zak, “Light-induced in situ transmission electron microscopy development, challenges, and perspectives”, Nano Letters **22**, 9219–9226 (2022).

[57] C. Ophus, “Four-dimensional scanning transmission electron microscopy (4d-stem): from scanning nanodiffraction to ptychography and beyond”, Microscopy and Microanalysis **25**, 563–582 (2019).

[58] B. Levin, C. Zhang, B. Bammes, P. M. Voyles, and R. B. Bilhorn, “4d stem with a direct electron detector”, Microscopy and analysis **34**, 20–2 (2020).

[59] G.-S. Park, K. S. Min, H. Kwon, S. Yoon, S. Park, J.-H. Kwon, S. Lee, J. Jo, M. Kim, and S. K. Kim, “Strain-induced modulation of localized surface plasmon resonance in ultrathin hexagonal gold nanoplates”, Advanced Materials **33**, 2100653 (2021).

[60] J. A. Scholl, A. García-Etxarri, A. L. Koh, and J. A. Dionne, “Observation of quantum tunneling between two plasmonic nanoparticles”, Nano letters **13**, 564–569 (2013).

[61] G. Li, C. Cherqui, N. W. Bigelow, G. Duscher, P. J. Straney, J. E. Millstone, D. J. Masiello, and J. P. Camden, “Spatially mapping energy transfer from single plasmonic particles to semiconductor substrates via stem/eels”, Nano Letters **15**, 3465–3471 (2015).

[62] J. Lee, D.-J. Jeon, and J.-S. Yeo, "Quantum plasmonics: energy transport through plasmonic gap", Advanced Materials **33**, 2006606 (2021).

[63] M. Song, G. C. des Francs, and A. Bouhelier, "Influence of an electron beam exposure on the surface plasmon resonance of gold nanoparticles", Plasmonics **9**, 343–348 (2014).

[64] W. Albrecht, A. van de Glind, H. Yoshida, Y. Isozaki, A. Imhof, A. van Blaaderen, P. E. de Jongh, K. P. de Jong, J. Zečević, and S. Takeda, "Impact of the electron beam on the thermal stability of gold nanorods studied by environmental transmission electron microscopy", Ultramicroscopy **193**, 97–103 (2018).

[65] H. Leng, B. Szychowski, M.-C. Daniel, and M. Pelton, "Dramatic modification of coupled-plasmon resonances following exposure to electron beams", The Journal of Physical Chemistry Letters **8**, 3607–3612 (2017).

[66] N. Zohar, L. Chuntonov, and G. Haran, "The simplest plasmonic molecules: metal nanoparticle dimers and trimers", Journal of Photochemistry and Photobiology C: Photochemistry Reviews **21**, 26–39 (2014).

[67] S. Lerch and B. M. Reinhard, "Effect of interstitial palladium on plasmon-driven charge transfer in nanoparticle dimers", Nature Communications **9**, 1608 (2018).

[68] P. Nordlander, C. Oubre, E. Prodan, K. Li, and M. Stockman, "Plasmon hybridization in nanoparticle dimers", Nano letters **4**, 899–903 (2004).

[69] C. P. Byers, H. Zhang, D. F. Swearer, M. Yorulmaz, B. S. Hoener, D. Huang, A. Hoggard, W.-S. Chang, P. Mulvaney, E. Ringe, et al., "From tunable core-shell nanoparticles to plasmonic drawbridges: active control of nanoparticle optical properties", Science advances **1**, e1500988 (2015).

[70] R. Esteban, G. Aguirregabiria, A. G. Borisov, Y. M. Wang, P. Nordlander, G. W. Bryant, and J. Aizpurua, "The morphology of narrow gaps modifies the plasmonic response", ACS photonics **2**, 295–305 (2015).

[71] C. Ciracì, R. Hill, J. Mock, Y. Urzhumov, A. Fernández-Domínguez, S. Maier, J. Pendry, A. Chilkoti, and D. Smith, "Probing the ultimate limits of plasmonic enhancement", Science **337**, 1072–1074 (2012).

[72] T. V. Teperik, P. Nordlander, J. Aizpurua, and A. G. Borisov, "Robust subnanometric plasmon ruler by rescaling of the nonlocal optical response", Physical review letters **110**, 263901 (2013).

[73] K. J. Savage, M. M. Hawkeye, R. Esteban, A. G. Borisov, J. Aizpurua, and J. J. Baumberg, "Revealing the quantum regime in tunnelling plasmonics", Nature **491**, 574–577 (2012).

[74] O. Pérez-González, N. Zabala, A. G. Borisov, N. J. Halas, P. Nordlander, and J. Aizpurua, "Optical spectroscopy of conductive junctions in plasmonic cavities", Nano letters **10**, 3090–3095 (2010).

[75] R. Esteban, A. G. Borisov, P. Nordlander, and J. Aizpurua, "Bridging quantum and classical plasmonics with a quantum-corrected model", Nature communications **3**, 825 (2012).

[76] F. Benz, C. Tserkezis, L. O. Herrmann, B. De Nijs, A. Sanders, D. O. Sigle, L. Pukenas, S. D. Evans, J. Aizpurua, and J. J. Baumberg, "Nanooptics of molecular-shunted plasmonic nanojunctions", Nano letters **15**, 669–674 (2015).

[77] A. N. Koya and J. Lin, "Charge transfer plasmons: recent theoretical and experimental developments", Applied Physics Reviews **4**, 10.1063/1.4982890 (2017).

[78] S. F. Tan, L. Wu, J. K. Yang, P. Bai, M. Bosman, and C. A. Nijhuis, "Quantum plasmon resonances controlled by molecular tunnel junctions", Science **343**, 1496–1499 (2014).

[79] D. Knebl, A. Hörl, A. Trügler, J. Kern, J. R. Krenn, P. Puschnig, and U. Hohenester, "Gap plasmonics of silver nanocube dimers", Phys. Rev. B **93**, 081405 (2016).

[80] W. Yan, M. Wubs, and N. Asger Mortensen, "Projected dipole model for quantum plasmonics", Phys. Rev. Lett. **115**, 137403 (2015).

[81] E. G. Emberly and G. Kirczenow, "Theory of electrical conduction through a molecule", Annals of the New York Academy of Sciences **852**, 54–67 (1998).

[82] C. Toher and S. Sanvito, "Effects of self-interaction corrections on the transport properties of phenyl-based molecular junctions", Phys. Rev. B **77**, 155402 (2008).

[83] A. de Melo Souza, I. Rungger, R. B. Pontes, A. R. Rocha, A. J. R. Da Silva, U. Schwingenschlöegl, and S. Sanvito, "Stretching of bdt-gold molecular junctions: thiol or thiolate termination?", Nanoscale **6**, 14495–14507 (2014).

[84] A. M. Scheer, G. A. Gallup, and P. Burrow, "Unoccupied orbital energies of 1, 4-benzenedithiol and the homo–lumo gap", Chemical Physics Letters **466**, 131–135 (2008).

[85] S. Letardi and F. Cleri, "Interaction of benzene thiol and thiolate with small gold clusters", The Journal of chemical physics **120**, 10062–10068 (2004).

[86] R.-W. Yan, X. Jin, S.-Y. Guan, X.-G. Zhang, R. Pang, Z.-Q. Tian, D.-Y. Wu, and B.-W. Mao, "Theoretical study of quantum conductance of conjugated and nonconjugated molecular wire junctions", The Journal of Physical Chemistry C **120**, 11820–11830 (2016).

[87] R. L. McCreery, “Molecular electronic junctions”, Chemistry of Materials **16**, 4477–4496 (2004).

[88] Y. Kim, T. Pietsch, A. Erbe, W. Belzig, and E. Scheer, “Benzenedithiol: a broad-range single-channel molecular conductor”, Nano Letters **11**, 3734–3738 (2011).

[89] M. Tsutsui, T. Morikawa, Y. He, A. Arima, and M. Taniguchi, “High thermopower of mechanically stretched single-molecule junctions”, Scientific reports **5**, 11519 (2015).

[90] S. Triviño-Sánchez, R. Xu, J. González-Izquierdo, L. Bañares, I. Cano, J. Pérez-Juste, A. Guerrero-Martínez, and G. González-Rubio, “Colloidal gold-palladium-platinum alloy nanospheres with tunable compositions and defined numbers of atoms”, Nanoscale, 10.1039/D4NR04898A (2025).

[91] A.-K. Göppert, G. Gonzalez-Rubio, S. Schnitzlein, and H. Cölfen, “A nanoparticle-based model system for the study of heterogeneous nucleation phenomena”, Langmuir **39**, 3580–3588 (2023).

[92] K. M. McPeak, S. V. Jayanti, S. J. P. Kress, S. Meyer, S. Iotti, A. Rossinelli, and D. J. Norris, “Plasmonic films can easily be better: rules and recipes”, ACS Photonics **2**, 326–333 (2015).

[93] P. Kekicheff and O. Spalla, “Refractive index of thin aqueous films confined between two hydrophobic surfaces”, Langmuir **10**, 1584–1591 (1994).

[94] N. J. Halas, S. Lal, W.-S. Chang, S. Link, and P. Nordlander, “Plasmons in strongly coupled metallic nanostructures”, Chemical Reviews **111**, PMID: 21542636, 3913–3961 (2011).

[95] C. Glasbey, “An analysis of histogram-based thresholding algorithms”, CVGIP: Graphical Models and Image Processing **55**, 532–537 (1993).

[96] N. Otsu, “A threshold selection method from gray-level histograms”, IEEE Transactions on Systems, Man, and Cybernetics **9**, 62–66 (1979).

[97] C. A. Nijhuis, W. F. Reus, J. R. Barber, and G. M. Whitesides, “Comparison of sam-based junctions with ga2o3/egain top electrodes to other large-area tunneling junctions”, The Journal of Physical Chemistry C **116**, 14139–14150 (2012).

[98] J. G. Simmons, “Generalized formula for the electric tunnel effect between similar electrodes separated by a thin insulating film”, Journal of applied physics **34**, 1793–1803 (1963).

[99] C. Bruot, J. Hihath, and N. Tao, “Mechanically controlled molecular orbital alignment in single molecule junctions”, Nature nanotechnology **7**, 35–40 (2012).

[100] J. Ulrich, D. Esrail, W. Pontius, L. Venkataraman, D. Millar, and L. H. Doerrer, "Variability of conductance in molecular junctions", The Journal of Physical Chemistry B **110**, PMID: 16471840, 2462–2466 (2006).

[101] Xiao, Xu, and N. J. Tao, "Measurement of single molecule conductance: benzenedithiol and benzenedimethanethiol", Nano Letters **4**, 267–271 (2004).

[102] W. Albrecht and S. Bals, "Fast electron tomography for nanomaterials", Journal of Physical Chemistry C **124**, 27276–27286 (2020).

[103] J. Frank, "Introduction: principles of electron tomography", in *Electron tomography: methods for three-dimensional visualization of structures in the cell*, edited by J. Frank (Springer New York, New York, NY, 2006), pp. 1–15.

[104] W. Van den Broek, A. Rosenauer, B. Goris, G. Martinez, S. Bals, S. Van Aert, and D. Van Dyck, "Correction of non-linear thickness effects in haadf stem electron tomography", Ultramicroscopy **116**, 8–12 (2012).

[105] W. van Aarle, W. J. Palenstijn, J. De Beenhouwer, T. Altantzis, S. Bals, K. J. Batenburg, and J. Sijbers, "The astra toolbox: a platform for advanced algorithm development in electron tomography", Ultramicroscopy **157**, 35–47 (2015).

[106] E. Y. Sidky, J. H. Jørgensen, and X. Pan, "Convex optimization problem prototyping for image reconstruction in computed tomography with the chambolle–pock algorithm", Physics in Medicine & Biology **57**, 3065 (2012).

[107] A. Paszke, S. Gross, F. Massa, A. Lerer, J. Bradbury, G. Chanan, T. Killeen, Z. Lin, N. Gimelshein, L. Antiga, et al., "Pytorch: an imperative style, high-performance deep learning library. arxiv 2019", arXiv preprint arXiv:1912.01703 **10** (1912).

[108] S. Van der Walt, J. L. Schönberger, J. Nunez-Iglesias, F. Boulogne, J. D. Warner, N. Yager, E. Gouillart, and T. Yu, "Scikit-image: image processing in python", PeerJ **2**, e453 (2014).

[109] W. E. Lorensen and H. E. Cline, "Marching cubes: a high resolution 3d surface construction algorithm", in Proceedings of the 14th annual conference on computer graphics and interactive techniques, SIGGRAPH '87 (1987), pp. 163–169.

[110] S. Valette, J. M. Chassery, and R. Prost, "Generic remeshing of 3d triangular meshes with metric-dependent discrete voronoi diagrams", IEEE Transactions on Visualization and Computer Graphics **14**, 369–381 (2008).

[111] H. Heidari Mezerji, W. Van den Broek, and S. Bals, "A practical method to determine the effective resolution in incoherent experimental electron tomography", Ultramicroscopy **111**, 330–336 (2011).

[112] M. A. Reed, C. Zhou, C. Muller, T. Burgin, and J. Tour, "Conductance of a molecular junction", Science **278**, 252–254 (1997).

[113] T. Kong, A. Liao, Y. Xu, X. Qiao, H. Zhang, L. Zhang, and C. Zhang, "Recent advances and mechanism of plasmonic metal–semiconductor photocatalysis", RSC advances **14**, 17041–17050 (2024).

[114] F. Bhom and Y. M. Isa, "Photocatalytic hydrogen production using tio2-based catalysts: a review", Global Challenges **8**, 2400134 (2024).

[115] K. Chen, W. Dong, Y. Huang, F. Wang, J. L. Zhou, and W. Li, "Photocatalysis for sustainable energy and environmental protection in construction: a review on surface engineering and emerging synthesis", J. Environ. Chem. Eng **13**, 117529 (2025).

[116] M. A. Khan, S. Mutahir, I. Shaheen, Y. Qunhui, M. Bououdina, and M. Humayun, "Recent advances over the doped g-c3n4 in photocatalysis: a review", Coordination Chemistry Reviews **522**, 216227 (2025).

[117] B. M. Rajbongshi, "Photocatalyst: mechanism, challenges, and strategy for organic contaminant degradation", in *Handbook of smart photocatalytic materials* (Elsevier, 2020), pp. 127–149.

[118] S. Ali, P. M. Ismail, M. Khan, A. Dang, S. Ali, A. Zada, F. Raziq, I. Khan, M. S. Khan, M. Ateeq, et al., "Charge transfer in tio 2-based photocatalysis: fundamental mechanisms to material strategies", Nanoscale **16**, 4352–4377 (2024).

[119] A. Fujishima and K. Honda, "Electrochemical photolysis of water at a semiconductor electrode", nature **238**, 37–38 (1972).

[120] N. N. Uyen, N. C. Toan, N. Truong, L. A. Tu, and P. H. Le, "Plasmonic au–tio 2 nanowire/nanotube heterostructures for multifunctional photocatalysis: dye and pesticide degradation, water splitting, and antibacterial activity", Nanoscale Advances **7**, 7317–7332 (2025).

[121] A. P. Manuel and K. Shankar, "Hot electrons in tio2–noble metal nanoheterojunctions: fundamental science and applications in photocatalysis", Nanomaterials **11**, 1249 (2021).

[122] A. Kumar, P. Choudhary, A. Kumar, P. H. Camargo, and V. Krishnan, "Recent advances in plasmonic photocatalysis based on tio2 and noble metal nanoparticles for energy conversion, environmental remediation, and organic synthesis", Small **18**, 2101638 (2022).

[123] V. Pellas, D. Hu, Y. Mazouzi, Y. Mimoun, J. Blanchard, C. Guibert, M. Salmain, and S. Boujday, "Gold nanorods for lspr biosensing: synthesis, coating by silica, and bioanalytical applications", Biosensors **10**, 146 (2020).

[124] X. Li, B. Wu, X. Zhang, A. Chen, J. Wang, H. Wang, A. Ciesielski, J. Liu, and J. Zhang, "Plasmon mediated photocatalysis: engineering interfaces for effective hot carrier utilization", ACS Energy Letters **10**, 1347–1356 (2025).

[125] Y. Li, J. G. DiStefano, A. A. Murthy, J. D. Cain, E. D. Hanson, Q. Li, F. C. Castro, X. Chen, and V. P. Dravid, "Superior plasmonic photodetectors based on au@ mos2 core–shell heterostructures", ACS nano **11**, 10321–10329 (2017).

[126] C. Fang, H. Jia, S. Chang, Q. Ruan, P. Wang, T. Chen, and J. Wang, "(gold core)/(titania shell) nanostructures for plasmon-enhanced photon harvesting and generation of reactive oxygen species", Energy & Environmental Science **7**, 3431–3438 (2014).

[127] J. Luo, Q. Wu, L. Zhou, W. Lu, W. Yang, and J. Zhu, "Plasmon-induced hot carrier dynamics and utilization", Photonics Insights **2**, R08–R08 (2023).

[128] H. Li, S. Wang, F. Hong, Y. Gao, B. Zeng, R. S. Haider, F. Fan, J. Huang, and C. Li, "Effects of the interfacial defects in au/tio2 on plasmon-induced water oxidation", The Journal of Chemical Physics **152**, 10.1063/5.0008382 (2020).

[129] T. Luttrell, S. Halpegamage, J. Tao, A. Kramer, E. Sutter, and M. Batzill, "Why is anatase a better photocatalyst than rutile?-model studies on epitaxial tio2 films", Scientific reports **4**, 4043 (2014).

[130] D. O. Scanlon, C. W. Dunnill, J. Buckeridge, S. A. Shevlin, A. J. Logsdail, S. M. Woodley, C. R. A. Catlow, M. J. Powell, R. G. Palgrave, I. P. Parkin, et al., "Band alignment of rutile and anatase tio2", Nature materials **12**, 798–801 (2013).

[131] D. A. Hanaor and C. C. Sorrell, "Review of the anatase to rutile phase transformation", Journal of Materials science **46**, 855–874 (2011).

[132] J. Rodríguez-Fernández, A. M. Funston, J. Pérez-Juste, R. A. Álvarez-Puebla, L. M. Liz-Marzán, and P. Mulvaney, "The effect of surface roughness on the plasmonic response of individual sub-micron gold spheres", Physical Chemistry Chemical Physics **11**, 5909–5914 (2009).

[133] F. Loth, T. Kiel, K. Busch, and P. T. Kristensen, "Surface roughness in finite-element meshes: application to plasmonic nanostructures", J. Opt. Soc. Am. B **40**, B1–B7 (2023).

[134] A. V. Kildishev, J. D. Borneman, K.-P. Chen, and V. P. Drachev, "Numerical modeling of plasmonic nanoantennas with realistic 3d roughness and distortion", Sensors **11**, 7178–7187 (2011).

[135] L. J. Tauzin, Y.-y. Cai, K. W. Smith, S. A. Hosseini Jebeli, U. Bhattacharjee, W.-S. Chang, and S. Link, "Exploring the relationship between plasmon damping and luminescence in lithographically prepared gold nanorods", ACS photonics **5**, 3541–3549 (2018).

[136] K. Yanagisawa, Y. Yamamoto, Q. Feng, and N. Yamasaki, "Formation mechanism of fine anatase crystals from amorphous titania under hydrothermal conditions", Journal of materials research **13**, 825–829 (1998).

[137] H. Sopha, I. Mirza, H. Turčičova, D. Pavlinak, J. Michalicka, M. Krbal, J. Rodriguez-Pereira, L. Hromadko, O. Novák, J. Mužík, et al., "Laser-induced crystallization of anodic tio 2 nanotube layers", RSC advances **10**, 22137–22145 (2020).

[138] M. Zimbone, M. Cantarella, F. Giuffrida, F. La Via, V. Privitera, E. Napolitani, and G. Impellizzeri, "Laser crystallization of amorphous tio2 on polymer", Materials Science in Semiconductor Processing **157**, 107328 (2023).

[139] J. S. Hoppius, D. Bialuschewski, S. Mathur, A. Ostendorf, and E. L. Gurevich, "Femtosecond laser crystallization of amorphous titanium oxide thin films", Applied Physics Letters **113**, `10.1063/1.5027899` (2018).

[140] L. Noel, A. Khitous, C. Molinaro, H.-W. Zan, D. Berling, F. Grasset, and O. Soppera, "Laser direct writing of crystallized tio2 by photothermal effect induced by gold nanoparticles", Advanced Materials Technologies **9**, 2300407 (2024).

[141] B. Prasai, B. Cai, M. K. Underwood, J. P. Lewis, and D. Drabold, "Properties of amorphous and crystalline titanium dioxide from first principles", Journal of materials science **47**, 7515–7521 (2012).

[142] J. Huang, Y. Liu, L. Lu, and L. Li, "The photocatalytic properties of amorphous tio2 composite films deposited by magnetron sputtering", Research on Chemical Intermediates **38**, 487–498 (2012).

[143] Webmineral, *Rutile mineral data*, (2025) `https://webmineral.com/data/Rutile.shtml` (visited on 01/02/2026).

[144] RefractiveIndex.info, *Refractive index of tio_2 (jolivet-amorphous)*, (2025) `https://refractiveindex.info/?book=TiO2&page=Jolivet-amorphous&shelf=main` (visited on 01/02/2026).

[145] F. de la Peña, E. Prestat, J. Lähnemann, V. T. Fauske, P. Burdet, P. Jokubauskas, T. Furnival, C. Francis, M. Nord, T. Ostasevicius, K. E. MacArthur, D. N. Johnstone, M. Sarahan, J. Taillon, T. Aarholt, pquinn-dls, V. Migunov, A. Eljarrat, J. Caron, T. Nemoto, T. Poon, S. Mazzucco, sivborg, actions-user, N. Tappy, N. Cautaerts, S. Somnath, T. Slater, M. Walls, and pietsjoh, *Hyperspy/hyperspy: v2.3.0*, version v2.3.0, Mar. 2025.

[146] M. Klinger, "More features, more tools, more crystbox", Applied Crystallography **50**, 1226–1234 (2017).

[147] J. Mosquera, D. Wang, S. Bals, and L. M. Liz-Marzán, "Surfactant layers on gold nanorods", Accounts of Chemical Research **56**, 1204–1212 (2023).

[148] G. S. Perera, S. A. Athukorale, F. Perez, C. U. Pittman Jr, and D. Zhang, "Facile displacement of citrate residues from gold nanoparticle surfaces", Journal of colloid and interface science **511**, 335–343 (2018).

[149] S. Salloum, J. Rüther, Z. Celik, and C. Janiak, "Comparative analysis of synthesis techniques for citrate-capped gold nanoparticles: insights into optimized wet-chemical approaches for controlled morphology and stability", Nanoscale **17**, 23373–23386 (2025).

[150] Y. Bessekhouad, D. Robert, and J. Weber, "Preparation of tio2 nanoparticles by sol-gel route", International journal of photoenergy **5**, 153–158 (2003).

[151] F. Loosli and S. Stoll, "Effect of surfactants, ph and water hardness on the surface properties and agglomeration behavior of engineered tio 2 nanoparticles", Environmental Science: Nano **4**, 203–211 (2017).

[152] A. Katoch, H. Kim, T. Hwang, and S. S. Kim, "Preparation of highly stable tio2 sols and nanocrystalline tio2 films via a low temperature sol–gel route", Journal of sol-gel science and technology **61**, 77–82 (2012).

[153] J. D. Yoon, K. Y. Park, and H. D. Jang, "Comparison of titania particles between oxidation of titanium tetrachloride and thermal decomposition of titanium tetraisopropoxide", Aerosol Science & Technology **37**, 621–627 (2003).

[154] G. Oskam, A. Nellore, R. L. Penn, and P. C. Searson, "The growth kinetics of tio2 nanoparticles from titanium (iv) alkoxide at high water/titanium ratio", The Journal of Physical Chemistry B **107**, 1734–1738 (2003).

[155] T.-H. Wang, A. M. Navarrete-López, S. Li, D. A. Dixon, and J. L. Gole, "Hydrolysis of ticl4: initial steps in the production of tio2", The Journal of Physical Chemistry A **114**, 7561–7570 (2010).

[156] Z. Cui, M. Zhao, X. Que, J. Wang, Y. Xu, M. N. Ghazzal, C. Colbeau-Justin, D. Pan, and W. Wu, "Facile vacuum annealing-induced modification of tio2 with an enhanced photocatalytic performance", Acs Omega **6**, 27121–27128 (2021).

[157] A. Arenas-Hernandez, C. Zuñiga Islas, M. Moreno, W. Calleja Arriaga, J. C. Mendoza-Cervantes, N. Carlos, C. R. Ascencio-Hurtado, and A. Heredia Jiménez, "Study of oxygen vacancies in tio2 nanostructures and their relationship with photocatalytic activity", Applied Sciences **12**, `10.3390/app12073690` (2022).

[158] M. Li, Y. Fang, and B. Liu, "The effect of vacuum annealing on the structural, electric, and optical properties, and photocatalytic activities of sputtered tio2 and nb-doped tio2 films", Catalysts **15**, `10.3390/catal15020166` (2025).

[159] D. D. Dunuwila, C. D. Gagliardi, and K. A. Berglund, "Application of controlled hydrolysis of titanium (iv) isopropoxide to produce sol-gel-derived thin films", Chemistry of materials **6**, 1556–1562 (1994).

[160] J. P. Glusker, "Citrate conformation and chelation: enzymic implications", Accounts of Chemical Research **13**, 345–352 (1980).

[161] D.-e. Jiang, S. H. Overbury, and S. Dai, "Interaction of gold clusters with a hydroxylated surface", The journal of physical chemistry letters **2**, 1211–1215 (2011).

[162] S. Atta, A. M. Pennington, F. E. Celik, and L. Fabris, "Tio2 on gold nanostars enhances photocatalytic water reduction in the near-infrared regime", Chem **4**, 2140–2153 (2018).

[163] B. Wu, D. Liu, S. Mubeen, T. T. Chuong, M. Moskovits, and G. D. Stucky, "Anisotropic growth of tio2 onto gold nanorods for plasmon-enhanced hydrogen production from water reduction", Journal of the American Chemical Society **138**, PMID: 26807600, 1114–1117 (2016).

[164] Y. W. Myint, T. T. Moe, W. Y. Linn, A. Chang, and P. P. Win, "The effect of heat treatment on phase transformation and morphology of nano-crystalline titanium dioxide (tio2)", Int. J. Sci. Technol. Res **6**, 293–299 (2017).

[165] L. Palmolahti, H. Ali-Löytty, M. Hannula, T. Tinus, K. Lehtola, A. Tukiainen, J. Reuna, and M. Valden, "Production of mixed phase ti 3+-rich tio 2 thin films by oxide defect engineered crystallization", Nanoscale **16**, 22383–22392 (2024).

[166] S. Cassaignon, M. Koelsch, and J.-P. Jolivet, "From ticl3 to tio2 nanoparticles (anatase, brookite and rutile): thermohydrolysis and oxidation in aqueous medium", Journal of Physics and Chemistry of Solids **68**, 695–700 (2007).

[167] `Citrate%20surface.%20url:%20https://nanocomposix.com/pages/citrate-surface` (visited on 01/02/2026).

[168] B. Contreras-Trigo, V. Díaz-García, E. Guzmán-Gutierrez, I. Sanhueza, P. Coelho, S. E. Godoy, S. Torres, and P. Oyarzún, "Slight ph fluctuations in the gold nanoparticle synthesis process influence the performance of the citrate reduction method", Sensors **18**, 2246 (2018).

[169] Y. Xu, S. Wu, P. Wan, J. Sun, and Z. D. Hood, "Introducing ti 3+ defects based on lattice distortion for enhanced visible light photoreactivity in tio 2 microspheres", RSC advances **7**, 32461–32467 (2017).

[170] M. E. Khan, M. M. Khan, B.-K. Min, and M. H. Cho, "Microbial fuel cell assisted band gap narrowed tio2 for visible light-induced photocatalytic activities and power generation", Scientific reports **8**, 1723 (2018).

[171] D. Bethell, R. E. Fessey, E. Namwindwa, and D. W. Roberts, "The hydrolysis of c 12 primary alkyl sulfates in concentrated aqueous solutions. part 1. general features, kinetic form and mode of catalysis in sodium dodecyl sulfate hydrolysis", Journal of the Chemical Society, Perkin Transactions 2, 1489–1495 (2001).

[172] W. Albrecht, T.-S. Deng, B. Goris, M. A. van Huis, S. Bals, and A. van Blaaderen, "Single particle deformation and analysis of silica-coated gold nanorods before and after femtosecond laser pulse excitation", Nano letters **16**, 1818–1825 (2016).

[173] H. Al-Johani, E. Abou-Hamad, A. Jedidi, C. M. Widdifield, J. Viger-Gravel, S. S. Sangaru, D. Gajan, D. H. Anjum, S. Ould-Chikh, M. N. Hedhili, et al., "The structure and binding mode of citrate in the stabilization of gold nanoparticles", Nature chemistry **9**, 890–895 (2017).

[174] J. K. Nørskov, T. Bligaard, J. Rossmeisl, and C. H. Christensen, "Towards the computational design of solid catalysts", Nature chemistry **1**, 37–46 (2009).

[175] R. Ferrando, J. Jellinek, and R. L. Johnston, "Nanoalloys: from theory to applications of alloy clusters and nanoparticles", Chemical reviews **108**, 845–910 (2008).

[176] J. Liu, P. Li, J. Bi, S. Jia, Y. Wang, X. Kang, X. Sun, Q. Zhu, and B. Han, "Switching between c2+ products and ch4 in co2 electrolysis by tuning the composition and structure of rare-earth/copper catalysts", Journal of the American Chemical Society **145**, 23037–23047 (2023).

[177] C. Wu, H. Li, H. He, Y. Song, C. Bi, W. Du, and H. Xia, "Compressive strain in core–shell au–pd nanoparticles introduced by lateral confinement of deformation twinnings to enhance the oxidation reduction reaction performance", ACS applied materials & interfaces **11**, 46902–46911 (2019).

[178] S. Thota, Y. Wang, and J. Zhao, "Colloidal au–cu alloy nanoparticles: synthesis, optical properties and applications", Materials Chemistry Frontiers **2**, 1074–1089 (2018).

[179] W. Zhan, J. Wang, H. Wang, J. Zhang, X. Liu, P. Zhang, M. Chi, Y. Guo, Y. Guo, G. Lu, et al., "Crystal structural effect of aucu alloy nanoparticles on catalytic co oxidation", Journal of the American Chemical Society **139**, 8846–8854 (2017).

[180] J. Yin, S. Shan, L. Yang, D. Mott, O. Malis, V. Petkov, F. Cai, M. Shan Ng, J. Luo, B. H. Chen, et al., "Gold–copper nanoparticles: nanostructural evolution and bifunctional catalytic sites", Chemistry of Materials **24**, 4662–4674 (2012).

[181] G. Guisbiers, S. Mejia-Rosales, S. Khanal, F. Ruiz-Zepeda, R. L. Whetten, and M. José-Yacaman, "Gold–copper nano-alloy,"tumbaga", in the era of nano: phase diagram and segregation", Nano letters **14**, 6718–6726 (2014).

[182] N. E. Motl, E. Ewusi-Annan, I. T. Sines, L. Jensen, and R. E. Schaak, "Au—cu alloy nanoparticles with tunable compositions and plasmonic properties: experimental determination of composition and correlation with theory", The Journal of Physical Chemistry C **114**, 19263–19269 (2010).

[183] M. Sun, A. Wang, M. Zhang, S. Zou, and H. Wang, "Interband and intraband hot carrier-driven photocatalysis on plasmonic bimetallic nanoparticles: a case study of au–cu alloy nanoparticles", ACS Nanoscience Au **4**, 360–373 (2024).

[184] H. Prunier, J. Nelayah, C. Ricolleau, G. Wang, S. Nowak, A.-F. Lamic-Humblot, and D. Alloyeau, "New insights into the mixing of gold and copper in a nanoparticle from a structural study of au–cu nanoalloys synthesized via a wet chemistry method and pulsed laser deposition", Physical Chemistry Chemical Physics **17**, 28339–28346 (2015).

[185] L. M. Vogl, P. Schweizer, X. Maeder, I. Utke, A. M. Minor, and J. Michler, "Unraveling interdiffusion phenomena and the role of nanoscale diffusion barriers in the copper–gold system", ACS nano **18**, 29658–29666 (2024).

[186] M. T. Candela, S. Triviño-Sánchez, A. Guerrero-Martínez, L. M. Liz-Marzán, and G. González-Rubio, "Pulsed laser-assisted phase engineering of multimetallic colloidal nanocrystals with complex compositions", Advanced Materials, e23683 (2026).

[187] Z. Swiatkowska-Warkocka, A. Pyatenko, F. Krok, B. R. Jany, and M. Marszalek, "Synthesis of new metastable nanoalloys of immiscible metals with a pulse laser technique", Scientific reports **5**, 9849 (2015).

[188] G. González-Rubio, P. Díaz-Núñez, W. Albrecht, V. Manzaneda-González, L. Bañares, A. Rivera, L. M. Liz-Marzán, O. Peña-Rodríguez, S. Bals, and A. Guerrero-Martínez, "Controlled alloying of au@ag core-shell nanorods induced by femtosecond laser irradiation", Advanced Optical Materials **9**, 2002134 (2021).

[189] A. Skorikov, W. Albrecht, E. Bladt, X. Xie, J. E. Van Der Hoeven, A. Van Blaaderen, S. Van Aert, and S. Bals, "Quantitative 3d characterization of elemental diffusion dynamics in individual ag@ au nanoparticles with different shapes", ACS nano **13**, 13421–13429 (2019).

[190] D. L. Jernigan and J. L. McAtee, "The study of carbon-coated grids at elevated temperatures by electron microscopy", Thermochimica Acta **4**, 393–404 (1972).

[191] Z. Zhang and D. Su, "Behaviour of tem metal grids during in-situ heating experiments", Ultramicroscopy **109**, 766–774 (2009).

[192] G. Guisbiers, S. Mejia-Rosales, S. Khanal, F. Ruiz-Zepeda, R. L. Whetten, and M. Jose-Yacaman, "Gold–copper nano-alloy, "tumbaga", in the era of nano: phase diagram and segregation", Nano Letters **14**, 6718–6726 (2014).

[193] A. R. Denton and N. W. Ashcroft, "Vegard's law", Phys. Rev. A **43**, 3161–3164 (1991).

Author contributions and publications

The author acknowledges the use of text-based artificial intelligence tools for assistance with sentence-level improvements in grammar and vocabulary. All intellectual content and scientific conclusions remain the author's own.

Chapter 1

Associated publication:
M. Dieperink*, F. Scalerandi* and W. Albrecht. Correlating structure, morphology and properties of metal nanostructures by combining single-particle optical spectroscopy and electron microscopy. Nanoscale 14, 7460-7472 (2022).
* These authors contributed equally.

Author contributions:
Wiebke Albrecht initiated the project. *Mees Dieperink* and *Francesca Scalerandi* performed an extensive literature research under the supervision of *Wiebke Albrecht*. All authors co-wrote the manuscript.

Chapter 2

Author contributions:
Francesca Scalerandi developed and optimized the protocol to fabricate dimers, performed optical measurements, acquired TEM images, conducted data analysis, and carried out the BEM simulations. *Guillermo González-Rubio* and *Nick Sokov* provided the nanoparticles. *Jon Cottom* and *Emilia Olsson* performed the DFT calculations. *Wiebke Albrecht* supervised the work and edited the text. The author acknowledges *Bart de Nijs* and *Rowena Davies* for valuable discussions on dimers and for sharing their expertise. Special thanks to *Ethan Kensett* and *Mareike Wubbenhorst* for their contribution at the early stage of this project as master students.

Chapter 3

Associated publication:
F. Scalerandi, A. Skorikov, N. Claes, S. Bals, G. González-Rubio, N. Sokov, and W. Albrecht. Reliable determination of sub-nanometer gaps in plasmonic gold dimers for correlation to their optical properties. Physical Review Materials 9, p.105202 (2025).

Author contributions:
Francesca Scalerandi prepared the samples, analyzed the data and wrote the first draft of the manuscript. *Wiebke Albrecht* and *Alexander Skorikov* edited the draft. *Natalie Claes* performed the electron tomography experiments under supervision of *Sara Bals*. *Alexander Skorikov* provided feedback on the project and on the data analysis. *Wiebke Albrecht* supervised the work.

Chapter 4

Author contributions:
Francesca Scalerandi developed and optimized the synthesis of the $TiCl_3$-based $AuTiO_2$, performed electron microscopy experiments, conducted data analysis and wrote the original draft. *Floor van der Kolk* synthesized the TTIP-based $AuTiO_2$ under *Francesca Scalerandi*'s supervision. *Francesca Scalerandi* and *Floor van der Kolk* measured dark field scattering spectra. Special thanks to *Nathan Mowry* and *Igor Hoogsteder* for helping setting up the TEM experiments. *Wiebke Albrecht* supervised the work and edited the text.

Chapter 5

Associated publication:
F. Scalerandi, L. Monin, N.J. Mowry and W. Albrecht. Optically driven AuCu alloying in single nanoparticles revealed by in situ TEM (submitted)

Author contributions:
Francesca Scalerandi synthesized the $AuTiO_2$ samples, performed the experiments and the data analysis with the help of *Nathan Mowry* and *Loriane Monin*. *Loriane Monin* performed Comsol simulations and Hertz–Knudsen equation calculations. *Francesca Scalerandi* wrote the original draft of the manuscript, *Nathan Mowry*, *Loriane Monin* and *Wiebke Albrecht* edited the text. *Wiebke Albrecht* supervised the work.

Other publications

J.S. van der Burgt, F. Scalerandi, J.J. de Boer, S.A. Rigter and E.C. Garnett. Perovskite Plasticity: Exploiting Instability for Self-Optimized Performance. Advanced Functional Materials 32, p.2203771 (2022).

S. Adhikari, Y. Wang, P. Spaeth, F. Scalerandi, W. Albrecht, J. Liu and M. Orrit. Magnetization switching of single magnetite nanoparticles monitored optically. Nano Letters 24, pp.9861-9867 (2024).

Summary

This thesis highlights the importance of correlating optical properties with the nanoscale morphology of hybrid plasmonic systems. Furthermore, it explores how the morphology can be characterized and actively modified. Central to this work is the use of transmission electron microscopy (TEM). The TEM is used not only as a high-resolution structural characterization technique, but also as a platform to probe and engineer nanoscale systems in situ. By integrating pulsed laser excitation into the TEM, it becomes possible to induce controlled structural and compositional changes while directly monitoring their evolution in real time. This approach enables in operando structural control and modification at the single-particle level.

The thesis focuses on two main classes of hybrid plasmonic systems: gold nanoparticles coupled to molecules (Chapters 2 and 3), and gold nanorods coupled to semiconductors (Chapters 4 and 5). Plasmonic metal nanoparticles exhibit unique optical properties. When the nanostructure is much smaller than the wavelength of the incident light, collective oscillations of conduction electrons can be driven by the electromagnetic field. These excitations are called localized surface plasmon resonances (LSPRs). These resonances lead to scattering and absorption cross sections much larger than the particle's physical size, as well as strong enhancement and confinement of the electromagnetic field at the nanoscale. Furthermore, the optical response can be tuned across the visible and near-infrared spectral range by simply changing the nanoparticle's morphology and size. These properties make such systems highly relevant for applications in quantum optics, sensing, catalysis, and energy conversion.

Chapter 2 focuses on the synthesis and optical characterization of gold nanosphere dimers linked by 1,4-benzenedithiol (BDT). Gold nanoparticle dimers bridged by a molecular junction are investigated as model systems for exploring light–matter interactions in extremely confined geometries. When two nanoparticles are brought into close proximity, the electromagnetic field becomes strongly localized within the interparticle gap. At sub-nanometer separations, or when the junction becomes conductive, quantum effects such as charge transfer and tunneling can emerge and strongly modify the optical response. Using correlative single-particle measurements combining dark-field scattering spectroscopy and electron microscopy, we show that extracting physical parameters from optical spectra is inherently ambiguous. Different combinations of gap size, dielectric environment, and junction model can produce indistinguishable spectra, preventing unique parameter determination. We attempt to disentangle these contributions using independent structural characteri-

zation. However, extracting gap sizes from 2D electron microscopy images remains limited due to projection effects and segmentation ambiguities. Together, these findings establish that neither optical spectroscopy nor 2D imaging alone can provide the unambiguous gap size determination needed to break the parameter degeneracy. A more robust approach to extracting the gap size is required in order to disentangle its contribution from other parameters affecting the optical response of the dimers. This is essential for achieving a full understanding of the optical behavior and for tailoring it to specific regimes.

To address these challenges, **Chapter 3** presents a methodology for accurately determining sub-nanometer gap sizes by moving from 2D STEM images to full three-dimensional electron tomography reconstructions. By combining electron tomography with a robust data analysis workflow, complete 3D representations of nanoparticle dimers are obtained. A model based on fitting the convolution of a step function with a Gaussian is introduced to extract gap sizes from reconstructed data. This method is demonstrated to be highly reliable and robust. It is validated against simulated datasets, achieving near pixel-level accuracy. The resulting 3D geometries can then be directly integrated into electromagnetic simulations. Finally, we show that the 3D reconstruction can be used as ground truth for improving gap estimation from 2D imaging.

In Chapters 4 and 5, the focus shifts to hybrid systems composed of plasmonic nanoparticles coupled to semiconductors, specifically Au nanorods coated with TiO_2.

Chapter 4 investigates the synthesis and crystallization pathways of TiO_2 shells grown on Au nanorods. In these systems, the quality of the interface between the metal and the semiconductor plays a critical role in determining the efficiency of charge injection, as well as the back-transfer to the Au core and recombination of the injected carriers within the TiO_2. Beyond the interface, the quality of the TiO_2 (including crystallinity, defect density, phase, and grain size) strongly influences the dynamics of the injected carriers. However, controlling this interface and the TiO_2 crystallinity at the nanoscale remains challenging. Different precursor chemicals and ligand environments are explored to control shell morphology, defect density, and interface quality. Two alternative crystallization strategies are investigated to avoid the structural changes of Au nanorods typically caused by high-temperature annealing: low-temperature hydrothermal treatment and laser-induced crystallization. In situ TEM laser excitation is employed to induce crystallization while monitoring structural evolution in real time. The results demonstrate that precursor chemistry and ligand choice strongly influence impurity incorporation and defect formation within the TiO_2 shell, which in turn determine the crystallization pathway and resulting crystalline phase. These findings highlight the importance of defect engineering in controlling both structure and functionality in hybrid plasmonic–semiconductor systems.

Finally, in **Chapter 5**, we demonstrate that optical excitation can drive the formation of gold–copper alloys in a controlled manner. By using a picosecond pulsed laser inside the TEM, the alloying of $Au@TiO_2$ nanorods with copper is monitored in situ. Under optical excitation, residual copper from the TEM grid becomes mobile and diffuses toward the nanorods, forming Au–Cu alloys. The degree of alloying can be tuned beyond 80% by adjusting the laser fluence. 4D-STEM and diffraction measurements confirm that the resulting alloy is spatially homogeneous throughout the particle, rather than phase-segregated or surface-confined. At higher fluences, when the sublimation temperature of copper is reached, a partial restoration of the original gold-rich composition is observed. The evolution of the alloy composition is followed using EDX, electron tomography, and electron diffraction. Time resolved electron diffraction reveals that the process is reversible but kinetically asymmetric, with incorporation driven by fast interdiffusion and removal limited by surface evaporation. Finally, we show that the driving force behind this alloying process is the heating of the carbon film on the TEM grid onto which the sample is drop-cast, dominating over plasmonic heating. Optical heating offers significant advantages compared to conventional thermal approaches. The ultrafast heating and cooling rates achievable with laser excitation in vacuum enable enhanced compositional control and the stabilization of unstable states that are otherwise inaccessible via traditional colloidal synthesis. This work demonstrates that laser excitation can act as an external control parameter to actively drive and stabilize non-equilibrium material states. This opens new pathways for nanoscale materials design.

Overall, this work provides a foundation for future studies in the field of hybrid plasmonic systems. It advances our understanding of how their optical properties are influenced by nanoscale morphological details and interfaces, and how these can be potentially controlled through precise structural design. By combining electron microscopy with in situ optical excitation and quantitative modeling, it becomes possible to both characterize and actively engineer nanoscale interfaces with high precision. This ability to precisely tailor hybrid nanosystems opens the way for designing plasmonic structures with optimized optical properties, enabling applications in catalysis, sensing, and quantum optics.

Samenvatting

Deze thesis benadrukt het belang van het correleren van optische eigenschappen met de morfologie op nanoschaal van hybride plasmonische systemen. Daarnaast wordt onderzocht hoe deze morfologie kan worden gekarakteriseerd en actief gemodificeerd. Centraal in dit werk staat het gebruik van transmissie-elektronenmicroscopie (TEM). De TEM wordt niet alleen gebruikt als een hoge-resolutie structurele karakterisatietechniek, maar ook als een platform om nanosystemen *in situ* te onderzoeken en te sturen. Door gepulste laserexcitatie in de TEM te integreren, wordt het mogelijk om gecontroleerde structurele en compositionele veranderingen te induceren, terwijl hun evolutie direct in *real-time* wordt gevolgd. Deze aanpak maakt in operando structurele controle en modificatie op het niveau van individuele nanodeeltjes mogelijk.

De thesis richt zich op twee hoofdklassen van hybride plasmonische systemen: gouden nanodeeltjes gekoppeld aan moleculen (Hoofdstukken 2 en 3), en gouden nanostaafjes gekoppeld aan halfgeleiders (Hoofdstukken 4 en 5). Metalen plasmonische nanodeeltjes vertonen unieke optische eigenschappen. Wanneer de nanostructuur veel kleiner is dan de golflengte van het invallende licht, kunnen collectieve oscillaties van geleidingselektronen worden aangedreven door het elektromagnetische veld. Deze excitaties worden gelokaliseerde oppervlakteplasmonresonanties (LSPRs) genoemd. Deze resonanties leiden tot werkzame doorsneden voor verstrooiing en absorptie die veel groter zijn dan de fysieke grootte van het deeltje, evenals tot versterking en confinering van het elektromagnetische veld op nanoschaal. Bovendien kan de optische respons worden afgestemd over het zichtbare en nabij-infrarode spectrum door eenvoudig de morfologie en grootte van het nanodeeltje te variëren. Deze eigenschappen maken dergelijke systemen zeer relevant voor toepassingen in de kwantumoptica, sensortechnologie, katalyse en energieconversie.

Hoofdstuk 2 richt zich op de synthese en optische karakterisatie van dimeren van gouden nanosferen gekoppeld door 1,4-benzeendithiol (BDT). Dimeren van gouden nanosferen verbonden via een moleculaire junctie worden onderzocht als modelsystemen voor het bestuderen van licht–materie-interacties in extreem geconfinieerde geometrieën. Wanneer twee nanodeeltjes dicht bij elkaar worden gebracht, wordt het elektromagnetische veld sterk gelokaliseerd in de interpartikelruimte. Bij subnanometerafstanden, of wanneer de junctie geleidend wordt, kunnen kwantumeffecten zoals ladingsoverdracht en tunneling optreden die de optische respons sterk beïnvloeden. We tonen aan dat het optische gedrag van deze dimeren zeer gevoelig is voor de morfologie, de diëlektrische omgeving en het model dat wordt gebruikt om

de moleculen te beschrijven. Verschillende combinaties van deze parameters kunnen vrijwel identieke optische spectra opleveren. Daardoor kan de afstand tussen de deeltjes (*gap size*) niet eenduidig worden bepaald op basis van uitsluitend optische data. Vervolgens tonen we aan dat het extraheren van *gap sizes* uit tweedimensionale elektronenmicroscopiebeelden onbetrouwbaar is vanwege projectie-effecten en segmentatiefouten. Deze bevindingen laten zien dat noch optische spectroscopie noch 2D-beeldvorming op zichzelf een definitieve karakterisering van de *gap size* kan leveren. Er is een meer robuuste methode nodig om de *gap size* te bepalen en zo het effect ervan te scheiden van andere parameters die de optische respons beïnvloeden. Dit is essentieel om het optische gedrag volledig te begrijpen en gericht te kunnen afstemmen.

Om deze uitdagingen aan te pakken, presenteert **Hoofdstuk 3** een methode voor het nauwkeurig bepalen van *sub-nanometergaps* door over te stappen van 2D STEM-beelden naar volledige driedimensionale reconstructie. Door elektronentomografie te combineren met een robuuste data-analyseworkflow worden volledige 3D-representaties van nanodeeltjesdimeren verkregen. Een model gebaseerd op het fitten van de convolutie van een stapfunctie met een Gaussische functie wordt geïntroduceerd om *gap sizes* uit gereconstrueerde data te extraheren. Deze methode blijkt zeer betrouwbaar en robuust en wordt gevalideerd met gesimuleerde datasets, waarbij een nauwkeurigheid tot op bijna pixelniveau wordt bereikt. De resulterende 3D-geometrieën kunnen vervolgens direct worden geïntegreerd in elektromagnetische simulaties. Ten slotte laten we zien dat de 3D-reconstructie als *ground truth* kan dienen om gapbepalingen uit 2D-beeldvorming te verbeteren.

In Hoofdstukken 4 en 5 verschuift de focus naar hybride systemen bestaande uit plasmonische nanodeeltjes gekoppeld aan halfgeleiders, specifiek Au-nanostaafjes gecoat met TiO_2.

Hoofdstuk 4 onderzoekt de synthese en kristallisatieroutes van TiO_2-schillen gegroeid op gouden nanostaafjes. In deze systemen speelt de kwaliteit van het grensvlak tussen metaal en halfgeleider een cruciale rol bij het bepalen van de efficiëntie van ladingsinjectie, evenals de terugtransfer en recombinatiesnelheden van geïnjecteerde ladingsdragers. Naast het grensvlak heeft ook de kwaliteit van het TiO_2 (inclusief kristalliniteit, defectdichtheid, fase en korrelgrootte) een sterke invloed op de dynamica van de ladingsdragers. Het blijft echter uitdagend om dit grensvlak en het TiO_2 op nanoschaal te controleren. Verschillende precursorchemicaliën en ligandomgevingen worden onderzocht om de schilmorfologie, defectdichtheid en interfacekwaliteit te sturen. Twee alternatieve kristallisatiestrategieën worden bestudeerd om structurele veranderingen van gouden nanostaafjes, typisch veroorzaakt door hogetemperatuur ontlating, te vermijden: lage-temperatuur hydrothermische behandeling en laser-geïnduceerde kristallisatie. *In situ* TEM-laserexcitatie wordt toegepast om kristallisatie te induceren terwijl structurele veranderingen in *real-time* wordt gevolgd.

De resultaten tonen aan dat de keuze van precursorchemie en liganden een sterke invloed heeft op de incorporatie van onzuiverheden en defectvorming in de TiO_2-schil, wat op zijn beurt het kristallisatietraject en de resulterende kristallijne fase bepaalt. Deze bevindingen benadrukken het belang van *defectengineering* bij het sturen van zowel structuur als functionaliteit in hybride plasmonisch–halfgeleidersystemen.

Ten slotte tonen we in **Hoofdstuk 5** aan dat optische excitatie de vorming van goud–koperlegeringen op gecontroleerde wijze kan aandrijven. Door gebruik te maken van een picoseconde gepulste laser in de TEM wordt de legeringsvorming van $Au@TiO_2$-nanostaafjes met koper *in situ* gevolgd. Onder optische excitatie wordt resterend koper op het TEM-grid mobiel en diffundeert het naar de nanostaafjes, waar het Au–Cu-legeringen vormt. De mate van legering kan tot boven 80% worden afgestemd door de laserfluëntie te variëren. Bij hogere fluënties, wanneer de sublimatietemperatuur van koper wordt bereikt, treedt een gedeeltelijk herstel van de oorspronkelijke gouden samenstelling op. De evolutie van de legeringssamenstelling wordt gevolgd met behulp van energie-dispersieve röntgenspectroscopie (EDX), elektronentomografie en elektrondiffractie. *Real-time* elektrondiffractie laat zien dat het proces reversibel maar kinetisch asymmetrisch is, met snelle incorporatie en langzamere verwijdering. Ten slotte tonen we aan dat de drijvende kracht achter dit legeringsproces de opwarming van de koolstoffilm op het TEM-grid is, waarop het monster wordt gedeponeerd, en niet plasmonische verwarming zoals aanvankelijk werd verondersteld. Optische verwarming biedt aanzienlijke voordelen ten opzichte van conventionele thermische methoden. De ultrahoge verhittings- en afkoelsnelheden die met laserexcitatie in vacuüm kunnen worden bereikt, maken een verbeterde controle over de samenstelling mogelijk en maken stabilisatie van metastabiele toestanden mogelijk die anders niet toegankelijk zijn via traditionele colloïdale synthese.

Dit werk toont aan dat laserexcitatie kan fungeren als een externe controleparameter om niet-evenwichtstoestanden van materialen actief te sturen en te stabiliseren. Dit opent nieuwe mogelijkheden voor het ontwerp van materialen op nanoschaal. Over het algemeen biedt dit werk een fundament voor toekomstige studies op het gebied van hybride plasmonische systemen. Het verdiept ons begrip van hoe optische eigenschappen worden beïnvloed door nanoschaalmorfologie en grensvlakken, en hoe deze gecontroleerd kunnen worden door nauwkeurig structureel ontwerp. Door elektronenmicroscopie te combineren met *in situ* optische excitatie en kwantitatieve modellering, wordt het mogelijk om grensvlakken op nanoschaal niet alleen te karakteriseren, maar ook actief te ontwerpen met hoge precisie. Dit vermogen om hybride nanosystemen nauwkeurig af te stemmen opent de weg naar het ontwerpen van plasmonische structuren met geoptimaliseerde optische eigenschappen, met toepassingen in katalyse, sensortechnologie en kwantumoptica.

Sommario

Questa tesi evidenzia l'importanza di correlare le proprietà ottiche con la morfologia su scala nanometrica dei sistemi plasmonici ibridi. Inoltre, esplora come la morfologia possa essere caratterizzata e attivamente modificata. Un elemento centrale di questo lavoro è l'utilizzo del microscopio elettronico a trasmissione (TEM). Il TEM viene impiegato non solo come tecnica di caratterizzazione strutturale ad alta risoluzione, ma anche come piattaforma per investigare e ingegnerizzare sistemi su scala nanometrica *in situ*. Integrando l'eccitazione laser nel TEM, diventa possibile indurre modifiche strutturali e composizionali controllate, monitorandone direttamente l'evoluzione in tempo reale. Questo approccio consente un controllo e una modifica strutturale in operando a livello della singola nanoparticella.

La tesi si concentra su due principali classi di sistemi plasmonici ibridi: nanoparticelle d'oro accoppiate a molecole (Capitoli 2 e 3) e nanorods d'oro accoppiati a semiconduttori (Capitoli 4 e 5). Le nanoparticelle metalliche plasmoniche presentano proprietà ottiche uniche. Quando la nanostruttura è molto più piccola della lunghezza d'onda della radiazione incidente, le oscillazioni collettive degli elettroni di conduzione possono essere guidate dal campo elettromagnetico. Tali eccitazioni sono note come risonanze plasmoniche di superficie localizzate (LSPRs). Queste risonanze determinano sezioni di scattering e assorbimento molto più grandi delle dimensioni fisiche della particella, nonché una forte amplificazione e confinamento del campo elettromagnetico su scala nanometrica. Inoltre, la risposta ottica può essere modulata lungo l'intero intervallo spettrale visibile e nel vicino infrarosso semplicemente variando la morfologia e le dimensioni della nanoparticella. Queste proprietà rendono tali sistemi altamente rilevanti per applicazioni in ottica quantistica, sensoristica, catalisi e conversione dell'energia.

Il **Capitolo 2** si concentra sulla sintesi e sulla caratterizzazione ottica di dimeri di nanosfere d'oro collegati da 1,4-benzeneditiolo (BDT). I dimeri di nanoparticelle d'oro collegati tramite una giunzione molecolare vengono studiati come sistemi modello per esplorare le interazioni luce–materia in geometrie estremamente confinate. Quando due nanoparticelle sono poste in stretta prossimità, il campo elettromagnetico diventa fortemente localizzato nello spazio interparticellare. A separazioni sub-nanometriche, o quando la giunzione diventa conduttiva, possono emergere effetti quantistici quali trasferimento di carica e tunneling, che modificano significativamente la risposta ottica. Dimostriamo che il comportamento ottico di questi dimeri è altamente sensibile alla morfologia, all'ambiente dielettrico e al modello utilizzato per descrivere le

molecole. Diverse combinazioni di questi parametri possono produrre spettri ottici quasi identici. Di conseguenza, la dimensione del gap non può essere determinata in modo univoco unicamente dai dati ottici. Dimostriamo inoltre che l'estrazione delle dimensioni del gap da immagini bidimensionali di microscopia elettronica è inaffidabile a causa di effetti di proiezione ed errori di segmentazione. Questi risultati mostrano che né la spettroscopia ottica né l'imaging 2D, considerati singolarmente, sono in grado di fornire una caratterizzazione definitiva della dimensione del gap. È pertanto necessario un approccio più robusto per determinarne la dimensione della distanza tra le nanoparticelle, al fine di separarne il contributo dagli altri parametri che influenzano la risposta ottica dei dimeri. Ciò è essenziale per ottenere una comprensione completa del comportamento ottico e per adattarlo a regimi specifici.

Per affrontare queste sfide, il **Capitolo 3** presenta una metodologia per la determinazione accurata di gap sub-nanometrici attraverso il passaggio da immagini STEM bidimensionali a una ricostruzione tridimensionale completa. Combinando la tomografia elettronica con un robusto workflow di analisi dei dati, si ottengono rappresentazioni tridimensionali complete dei dimeri di nanoparticelle. Viene introdotto un modello basato sull'adattamento della convoluzione tra una funzione a gradino e una funzione gaussiana per estrarre le dimensioni del gap dai dati ricostruiti. Questo metodo si dimostra altamente affidabile e robusto ed è validato su dataset simulati, raggiungendo una precisione prossima al livello del pixel. Le geometrie tridimensionali risultanti possono quindi essere integrate direttamente in simulazioni elettromagnetiche. Infine, mostriamo che la ricostruzione 3D può essere utilizzata come ground truth per migliorare la stima dei gap a partire da immagini bidimensionali.

Nei Capitoli 4 e 5, l'attenzione si sposta verso sistemi ibridi costituiti da nanoparticelle plasmoniche accoppiate a semiconduttori, in particolare nanorods di oro con struttura core–shell rivestiti con TiO_2.

Capitolo 4 indaga la sintesi e i processi di cristallizzazione dei rivestimenti di TiO_2 depositati su nanorods di oro. In questi sistemi, la qualità dell'interfaccia tra metallo e semiconduttore gioca un ruolo cruciale nel determinare l'efficienza dell'iniezione di carica, nonché la velocita' di retrotrasferimento e ricombinazione dei portatori di carica iniettati. Oltre all'interfaccia, la qualità del TiO_2 (in termini di cristallinità, densità di difetti, fase e dimensione dei grani) influenza fortemente la dinamica dei portatori. Tuttavia, il controllo di tale interfaccia e del TiO_2 su scala nanometrica rimane una sfida. Diverse precursori e agente stabilizzanti dei nanorods vengono esplorati per controllare la morfologia del rivestimento, la densità di difetti e la qualità dell'interfaccia. Due strategie alternative di cristallizzazione vengono investigate per evitare le modifiche strutturali dei nanorods di oro, tipicamente causate da trattamenti termici ad alta temperatura: trattamento idrotermale a bassa temperatura e cristallizzazione indotta da laser. L'eccitazione laser *in situ* nel TEM viene utilizzata per indurre la cristallizzazione monitorando l'evoluzione

strutturale in tempo reale. I risultati dimostrano che la chimica del precursore e la scelta degli agente stabilizzanti influenzano fortemente l'incorporazione di impurità e la formazione di difetti nel guscio di TiO_2, che a loro volta determinano il percorso di cristallizzazione e la fase cristallina risultante. Questi risultati evidenziano l'importanza dell'ingegneria dei difetti nel controllo sia della struttura sia della funzionalità nei sistemi plasmonici–semiconduttori ibridi.

Infine, nel **Capitolo 5**, dimostriamo che l'eccitazione ottica può guidare la formazione di leghe oro–rame in modo controllato. Utilizzando un laser a impulsi di picosecondi all'interno del TEM, la formazione della lega tra nanorods $Au@TiO_2$ e rame viene monitorata *in situ*. Sotto eccitazione ottica, il rame residuo sul supporto del TEM diventa mobile e diffonde verso i nanorods, formando leghe Au–Cu. Il grado di lega può essere modulato oltre l'80% variando la fluenza del laser. A fluenza più elevate, quando viene raggiunta la temperatura di sublimazione del rame, si osserva un parziale ripristino della composizione originale ricca in oro. L'evoluzione della composizione della lega viene seguita mediante spettroscopia a raggi X (EDX), tomografia elettronica e diffrazione elettronica. La diffrazione elettronica in tempo reale rivela che il processo è reversibile ma cineticamente asimmetrico, con incorporazione rapida e rimozione più lenta. Infine, mostriamo che la forza motrice di questo processo di lega è il riscaldamento del film di carbonio sul supporto del TEM, su cui il campione è depositato, piuttosto che il riscaldamento plasmonico inizialmente ipotizzato. Il riscaldamento ottico offre vantaggi significativi rispetto agli approcci termici convenzionali. Le velocità ultrarapide di riscaldamento e raffreddamento ottenibili mediante eccitazione laser in vuoto consentono un preciso controllo composizionale e la stabilizzazione di stati metastabili altrimenti non accessibili mediante sintesi colloidale tradizionale. Questo lavoro dimostra che l'eccitazione laser può agire come parametro di controllo esterno per guidare attivamente e stabilizzare stati di materia fuori equilibrio. Ciò apre nuove prospettive per la progettazione di materiali su scala nanometrica.

Nel complesso, questo lavoro fornisce una base per studi futuri nel campo dei sistemi plasmonici ibridi. Migliora la nostra comprensione di come le proprietà ottiche siano influenzate da dettagli morfologici e interfacce su scala nanometrica e di come queste possano essere controllate attraverso una progettazione strutturale precisa. Combinando microscopia elettronica, eccitazione ottica *in situ* e modellazione quantitativa, diventa possibile non solo caratterizzare ma anche ingegnerizzare attivamente interfacce su scala nanometrica con elevata precisione. Questa capacità di modulare con precisione i nanosistemi ibridi apre la strada alla progettazione di strutture plasmoniche con proprietà ottiche ottimizzate, abilitando applicazioni in catalisi, sensoristica e ottica quantistica.

Acknowledgment

Every day of this PhD journey was only possible thanks to all the people I had around me. Writing this acknowledgments section was probably the hardest chapter of the whole thesis. It is difficult to put into words all the support, kindness, and help I received, and how grateful I am for it. So that is how I want to start: by saying thank you to everyone I had around during the last five years.

Let me start by thanking AMOLF and all the wonderful people I met there. It has been a love-and-hate relationship with this green building, but it became a second home over the years, and I know I will miss it a lot.
The first person I have to thank is the BOSS, **Wiebke**. Thank you for putting your trust in me and deciding to hire me as your first (or second) PhD student. You have been such a supportive group leader, always checking on me whenever you saw me working too late or not taking enough breaks. You also have a unique talent for bringing all of us together and creating a great team spirit. It has been a pleasure working with you, and I definitely learned a lot, not only about TEMs and plasmons, but even more about myself and how to be a better scientist.
Erik, during my master's thesis in your group, your passion for science and enthusiasm were the main reasons why I decided to start a PhD. Whenever I presented my work and you were there, I rediscovered my excitement for research thanks to your genuine interest. You always came up with countless new experiments and ideas to explore, and your curiosity has been motivating. **Albert**, thank you for taking care of the group during Wiebke's maternity leave and for the very fun trip to Schiermonnikoog. I also appreciate how you always kept us updated on the latest developments in PV. **Bruno**, your attention to detail was incredibly helpful in every LMPV talk and poster session. **Esther**, I remember you were there during my first PhD interview. Your genuine interest and smiling face definitely made me less stressed during that interview.

I would also like to thank the members of my committee for their time reading of my thesis: **Sander**, **Stefania**, **Albert**, **Giulia**, and **Andrea**.

Then, I would like to thank the entire Hybrid Nanosystems group. Looking back, it is incredible to see how much each of us has achieved.
I would like to first thank my master students **Ethan**, **Floor**, **Davide**, and **Mareike**. Working with all of you was a pleasure, and your contributions played an important role in this thesis. **Ethan**, thank you for always bringing the most unexpected topics to lunch discussions and making them much more entertaining. And thank you for

introducing me to cherry cola! **Floor**, your genuine curiosity and attention to detail taught me a lot, and your questions often made me think more deeply. **Davide**, I truly appreciated your patience, determination, and calm attitude, even when experiments did not go as planned. **Mareike**, I always enjoyed our conversations about social and environmental topics and your interest in looking beyond the science itself. **Mees**, that is how it all started. Thank you for being such a great colleague. We are very different, maybe even opposites in many ways, but I had so much fun with you. We went to so many conferences together, but my favorites have been the ones in Brno and Houston. I will never forget your terrible jokes that still make me laugh a bit too much. Thank you for worrying about me during the difficult days and for always trying to help me whenever you could. **Quynh**, we became friends after the first conference I attended in Turin. You immediately opened up to me. I am not someone who finds it easy to open up to people, but you made it so much easier. What I appreciate most about you is the genuine interest and care you have for all the people around you. You are always there to help in any way you can. And, of course, your knowledge of the most random facts never fails to surprise me. **Sergio**, I really enjoyed sharing an office with you. Your jokes and constant references to The Office made long working days much lighter. You are a genuinely funny person, and your friendly attitude played a big role in bringing the group closer together. **Anezka**, you have been a great addition to the group. I really appreciate your curiosity, rigor, and commitment to good science, and thanks to your many interests there was always something fun to talk about. I hope I will get the opportunity to hear your band play live someday! Now it is time to thank the TEM crew. **Loriane**, I appreciate so much your attention to detail and the fact that you always ask one more question than anyone else does. You are a very good scientist, and you need to believe that yourself. **Nathan**, Loriane and I were so happy to have a third member of the TEM crew. Your knowledge of the TEM was incredible. I really enjoyed working with you and learning all about 4D-STEM and diffraction, but also about coffee and bikes. You are a very fun person, and you definitely made our lunch breaks much more interesting. **Igor**, the first member and honorary member of the TEM crew. Thank you so much for your patience in teaching us how to use the instruments. I am sorry if I made you walk to the TEM so many times for nothing! Our conference, together with Mees, in Brno was a lot of fun, especially crashing the Thermo Fisher party and bringing sweets to a Nobel laureate. **Devin, Patrick, Iris, Max, Jasper, Ece, Tjom, Marco,** and **Stan**, thank you for all the coffee breaks, lunches, celebrations, and conversations that made everyday life in the group so much more fun. You all contributed to creating a friendly and welcoming atmosphere. I was part of the PV for two years and I want to thank everyone in the PV.

Apart from my group, AMOLF brought me so many wonderful people: **Elaina**, **Larissa vdV.**, **Daphne D.**, **Imme**, **Lucy**, **Susan**, **Julia**, **Yorick**, **Manuel**,

Magda, **Evelijn**, **Jerome**, **Nika**, **Omolara**, **Athira**, **Deba**, **Oleg**, **Agustin**, **Hollie**, **Alvaro**, **Tom**, **Robin**, **Masha**, **Nikolai**, **Antony**, **Sarah**, **Linde**, and many more. Thank you all for the fun times we shared at conferences, during the LMPV Summer School, at bouldering sessions, bike rides, and over countless coffee breaks. You made AMOLF an even more enjoyable place to work.

Another aspect that makes AMOLF such a wonderful place to work is the outstanding support from the technical and support departments, for which I would like to express my special appreciation.

Outside of AMOLF I would first like to thank our collaborators, **Alexander**, **Nathalie**, **Sara**, **Guillermo**, **Jon**, and **Emilia**. In particular, I would like to thank **Bart** and **Rowena** for hosting me in Cambridge and for the many stimulating discussions about dimers, which helped me rediscover my love for science.

Sven, thank you for organizing the Dutch Chemical Plasmonics meeting and to all the people I met through it.

My paranymph Melanie and Rohit. **Melanie**, I am sure I would not be here today without you. You were always there when I needed a push not to give up. I miss our dinner nights, making gnocchi together and drinking wine. Thank you for always being there and believing in me, even when I did not believe in myself. **Rohit**, I must admit that our friendship developed slowly, but after our trip to Italy, with all the ice cream, affogato, pizza rossa, and swimming, we officially went from colleagues to besties. You are such a genuine person. Your energy is unbelievable and can transform me from a tired, stressed PhD student into a crazy Italian lady in a matter of seconds. Our daily long walks complaining about everything, discussing the pizza we were going to make later, or deciding which horror movie to watch made the final months of thesis writing much more bearable. Thank you so much for all the laughs and support. **Jamie**, the third member of the amazing people trio (or gossip gang). You are such a kind, thoughtful, and attentive friend, and I am truly grateful to have you in my life. Thank you for your friendship, your support, and the fun trips. **Moritz**, from bouldering and climbing buddies to horror-movie buddies. You are an amazing person, always there for your friends with a smile and a kind word.

Outside of AMOLF I had the support of many other people. My partynymph and two of my favorite people, Erica and Susanna. **Erica**, you have been my best friend for as long as I can remember. You are the person who knows me best, sometimes even better than I know myself. You are funny, kind, and full of love. The way you care for your friends is truly admirable, and it shows in how much people love and care about you in return. We have traveled the world together, we laughed, we went to concerts, we danced, and we cried. Through it all, you have always been by my side. You are the sun and I love to see you shine. I cannot wait for us to get old and retire, just so we can finally move into our dream retirement house in Rapallo.

Susanna, ever since I saw you at Mezrab, I decided that we would become friends and that is exactly how it went, as creepy as that may sound. You are my *punto fermo* in Amsterdam. Thank you for always being there, for all our conversations and adventures, and for being such an important friend in my life. **Sveva**, every time I feel lost, you are there. We shared so many amazing memories, from our wonderful trip to Portugal to every King's Day over the last three years. You are a certainty in my life, and being with you always feels like being home. Thank you for always listening, supporting me, and being by my side. **Federica**, when I saw you on the first day of primary school, I told my mum that I wanted to be your friend. Since then, we have been inseparable. We have grown and changed a lot, but our friendship has only become stronger. Thank you for supporting me throughout these four years and for always checking in on me with such patience and care.

My high school friends, we grew up together. Now, each of the seven of us lives in a different city and is finding her own path, but it is amazing to know that we will always find each other, wherever life takes us. You are and will always be my home around the world. My biggest dream is that one day, when we are 80 years old, we will all live in the same house, doing face masks and laughing together. Thank you, **Erica**, **Noemi**, **Chachou**, **Sofia**, **Agnese**, and **Elena**.

My bachelor friends, even in this case, we all live in different countries, but I know I can always count on you. The only thing I wish is that we could see each other more often. No matter the distance, I know that we will always be there for each other, always ready with a reassuring *pacca sulla spalla* whenever one of us needs it. I can truly talk to you about everything, and I know I will always find someone who understands me and empathizes with me. Thank you, **Elona**, **Gio**, and **Gaia**.

And now is the time to thank all my dutch friends. You made the city home and I could not be more grateful for this. **Merel**, you made me feel at home in Amsterdam. We share so many hobbies, and our camping and bike trips are definitely some of the best memories I have built here. Thanks to you, I was also able to explore so much of the Netherlands. You are an amazing person, and I am very grateful for your friendship and all the adventures we shared together. I'm already looking forward to the next one to come. **Noemi**, since you left Amsterdam, I have missed you almost every day. You are such a calm and inspiring person. Whenever I am struggling with something, I know I can count on you to have a reassuring word and to help me see things from a better perspective. **Jacqueline** and **Nihan** my flatmates (before a man stole me) and now friends. Thanks for all the long walks, dinner and game nights. **Vlad**, you are such a deep person. Every activity with you is never just a simple game night, creativity night, bike ride, or movie night, it is always something more. Thank you for all the thoughtful conversations, your curiosity, and the unique perspective you bring to everything you do. **Victor** and **Wendy**, I truly miss you guys, but I am also so happy for the new life you are building for yourselves in Mexico. **Hongyu**, I

cherish all our boat trips and car rides around the Netherlands during COVID times. And thank you to everyone else who made my time in Amsterdam so special.

Francesco, meeting you was by far the best part of this PhD journey. During the final months of my PhD, you have been the most caring, patient, and supportive partner I could have wished for. You taught me how to believe in myself when I struggled to do so. I look forward to discovering what the future will bring us and to having you by my side every step of the way.

Sono estremamente fortunata ad avere una famiglia così amorevole e presente. **Mamma**, mi hai insegnato cosa significa prendersi cura degli altri. Sei la persona più gentile, attenta e dolce che io conosca. **Papà**, grazie per avermi trasmesso la passione per la scienza, ma anche per avermi sempre supportato in ogni decisione e per aver sempre creduto in me. I miei fratelli, **Matteo**, **Thao** e **Stefano**, grazie per esserci sempre stati e per tutto l'affetto che mi avete dato. Mi ricordo il giorno in cui ho preso in braccio ognuno di voi per la prima volta, e vedere i ragazzi che siete diventati oggi mi riempie di orgoglio, anche se per me rimarrete per sempre dei bambini. Le mie nonne, siete un esempio di forza, amore e generosità. Le estati passate con voi e i nonni al mare o in campagna sono ricordi indelebili. Nonna **Olga**, l'interesse per la chimica sicuramente viene da te. Nonna **Irma**, grazie per avermi insegnato a cucire e a cucinare e per essere sempre così ottimista e piena di energie. I miei nonni, mi mancate tantissimo. Nonno **Lodo**, grazie per le tue battute, per la tua simpatia e per avermi insegnato ad andare in bicicletta. Nonno **Guido**, grazie per avermi insegnato a guidare e per le lunghe passeggiate a Viatosto. Ricordo ancora la mia prima guida con te al mio fianco.

About the author

Francesca Scalerandi was born in Turin, Italy, on September 18, 1996. She obtained her high school diploma from *Liceo Classico Vittorio Alfieri* and subsequently enrolled in the Materials Science and Technology program at Università degli studi di Torino, where she obtained her Bachelor's degree cum laude in 2018. After completing her bachelor's studies, she took a gap year to gain practical experience and reflect on her future academic and professional path. Interested in the climate crisis and the role of advanced materials in sustainable technologies, she completed a six-month internship in the R&D department of Amer-Sil in Luxembourg, a company developing membrane technologies for redox flow batteries. In 2019, she was selected for the Erasmus Mundus Master's programme *Chemistry, Functional Materials and Surfaces for Sustainability*. Through this programme, she obtained a double Master's degree in Chemistry from Université Paris-Saclay in France and the University of Porto in Portugal. For her master's thesis, she joined the group of Erik Garnett at AMOLF in Amsterdam, where she worked on mixed-halide perovskites and their directional emission properties for applications in luminescent solar concentrators. In 2021, Francesca started her PhD at AMOLF in Amsterdam in the group of Wiebke Albrecht. Her research focused on hybrid plasmonic nanosystems, with a particular emphasis on the relationship between nanoscale morphology and optical properties. Using transmission electron microscopy, she investigated methods for structural characterization and *in situ* modification of nanomaterials through laser excitation.

Outside of research, Francesca has a strong interest in sustainability and environmental issues. She volunteers in several social initiatives. She loves spending time in nature and enjoys cycling, diving, hiking, bouldering, reading, and travelling.